NATIONAL CONFERENCE ON

RECENT RESEARCH TRENDS IN PHYSICS, CHEMISTRY, MATHEMATICS AND BIOLOGICAL SCIENCES

VTM NSS COLLEGE
DHANUVACHAPURAM
THIRUVANANTHAPURAM
Affiliated to University of Kerala with a B+ Grade

Proceedings of the conference held on March 9-30, 2023

ISBN 978-81-962695-0-0

National Conference on Recent Research Trends in Physics, Chemistry, Math's and Biological Sciences

(National Conference on Advanced Functional Materials, Recent Research Trends inMathematics & Recent Research Trends in Biological Sciences)

(09 – 30 March, 2023)

as part of

ARCSSCAL 2023

(Annual Research Conference of Science, Social Sciences, Commerce, Arts and Languages)

Printed and Publishedby

Dr. V M Anandakumar

(Principal, VTM NSS College, Dhanuvachapuram)

Author

Dr. Bijini B R (Convener, R & D Cell) Edition: I

ISBN: 978-81-962695-0-0

PREFACE

Annual Research Conference of Science, Social Science, Commerce, Arts and Literature (ARCSSCAL) is organized every year by the Research and Development Cell of the college in association with the Internal Quality Assurance Cell to provide an opportunity to understand different viewpoints and to assimilate new ideas and trends, to acquaint with modern technology, cutting edge equipment and recent developments in the research field. The conference also provides an invaluable opportunity to broaden the spectrum of expertise by mastering new skills in a scholarly environment. The first edition of the conference was held in 2022, proved to be a great success and this year the second edition of ARCSSCAL was organized from the 23rd of February 2023 to the 28th of March 2023. More than 120 research scholars/faculty members presented their research works in addition to 30 invited talks on various topics of international relevance in diverse academic disciplines and around 1000 delegates participated in ARCSSCAL 2023. All the full paper submissions were peer-reviewed by a panel of expert referees and selected full papers were rewritten by incorporating their suggestions and accepted for publication in two proceedings with ISBN number. This year thirteen departments and the central library of the college organized seven subconferences, National Conference on Recent Trends in Social Sciences: History, Economics and Political Science (NCRTSS), Two-day National Conference on Intellectual Property Rights, National Research Conference on Commerce & Management (NRCCM), National conference on Advanced Functional Materials (NCAFM), National Research Conference on Current Trends in Languages & Literature (NRCTLL), National Conference in Recent Research Trends in Mathematics (NCRTM), National Conference on Recent Trends in Biological Science (NCRTBS), under the banner of ARCSSCAL 2023. Out of these NCAFM 2023 is the fruit of a collaboration between the Undergraduate Departments of Physics and Chemistry and the R&D cell of the institution, co-sponsored by Kerala State Council for Science, Technology and Environment (KSCSTE).

The conference sees participation of renowned academicians, researchers, industrial experts, and scientists from all over India. The academic deliberations have greatly contributed to an epistemic awareness about the recent developments in different niches of science like materials science, biological sciences, mathematics, nanomaterials, biomaterials, energy materials and polymers. I would like to take this opportunity to thank the keynote speakers, presenters, and authors for their contributions towards the success of this event.

Dr. Bijini B R

Convener, ARC

TABLE OF CONTENTS

SPECTROSCOPIC CHARACTERIZATION AND BIOLOGICAL EVALUATION OF 4-ACETYL PIPERAZININE AND MOLECULAR DOCING STUDIES.

W. Abisha[a] D.Arul dhas[b*]

a Research scholar, Register number:20213112132015, Associate professor, Department of physics, Research Centre, Nesamony memorial Christian college, Marthandam,629165, TamilNadu, India

a,b* Affiliated to Manonmaniam Sundaranar University Abishekapatti, Tirunelveli 627012, Tamilnadu, India

Abstract

The optimized geometrical parameters were determined by using Density Functional Theory (DFT) through the B3LYP with the level of 6-31G(d) basis set and compared with the experimental values. Molecular Electrostatic Potential (MEP) energy surface and Fukui function descriptor using Natural atomic Analysis of charges were employed to investigate the most reactive sites of the title compound. Natural bond orbital analysis (NBO) elucidates the delocalization of charge due to intermolecular interactions. The topological studies RDG and molecular docking done were also performed to check the bioactivity of molecule.

Introduction:

Piperazines and substituted piperazines are important pharmacophores that can be established in many biologically active compounds across a number of different therapeutic areas (Berkheij, 2005) such as antifungal (Upadhayaya et al., 2004), anti-bacterial, anti-malarial, and anti-psychotic agents (Choudhary et al., 2006). A valuable insight into recent advances in the antimicrobial activity of piperazine derivatives has been reported (Channappa et al., 2014). The piperazine template forms the molecular backbone, enthralling versatile binding properties with a frequently occurring binding motif that provides potent and selective ligands for a range of different biological targets in medicinal chemistry. Piperazines are hygroscopic compounds that have antibiotic effects. Piperazines are currently the most essential building blocks in drug discovery, with a high number of positive hits confronted in biological screens of this heterocycle and its congeners across a number of different therapeutic areas (M. Berkheij et al., 2005), anticancer (K. Rosen et al., 1995), antifungal (C. Hulme et al., 1999), antibacterial, antimalarial and antipsychotic agents (R.S. Upadhayaya et al., 2004), as well as HIV protease inhibitors (B.D. Dorsey et al., 1994).

Simulation methods

The DFT methodology was implemented to compute the 2APNA molecule at the B3LYP level with 6-31G(d,p) basis sets using Gaussian 09 software (2) Natural Bond Orbital (NBO). Molecular Hirshfeld surface analysis and the related 2D fingerprint plots for the compound were calculated using the Crystal explorer 3.1 programs (6). RDG and Fukui function were carried out by Multiwfn (2) which is a multifunctional wave function analysis program and all iso-surface maps were rendered by the VMD program (1) Docking was performed with three different proteins and the ligand using the molecular docking software Auto Dock 4.2 (7).

Results and Discussion

Molecular Geometry

The optimized molecular structure of 2AP were carrying out by using Gaussian 09 program with B3LYP/6-31G(d) basis set and the acquired structures are manifest in Figs.1. The calculated geometrical parameters (bond lengths, bond angles, and dihedral angles) are listed in Table 1. In acetyl piperazinium cation, the C-N bond lengths (1.508 Å) of ACP increase. The organic piperazinium cation shows non-planar nature and adopts a chair conformation. This was confirmed by the internal bond angles C_{31}-C_{34}-N_{21}, N_{21}-C_{22}-C_{25}, N_{28}-C_{25}-C_{22} and N_{28}-C_{31}-C_{34}. The non-planarity nature of the piperazinium cation attached to acetyl group was confirmed by the dihedral angles O_{19}-C_{20}-N_{21}-C_{22} and C_{31}-C_{34}-N_{21}-C_{20}.

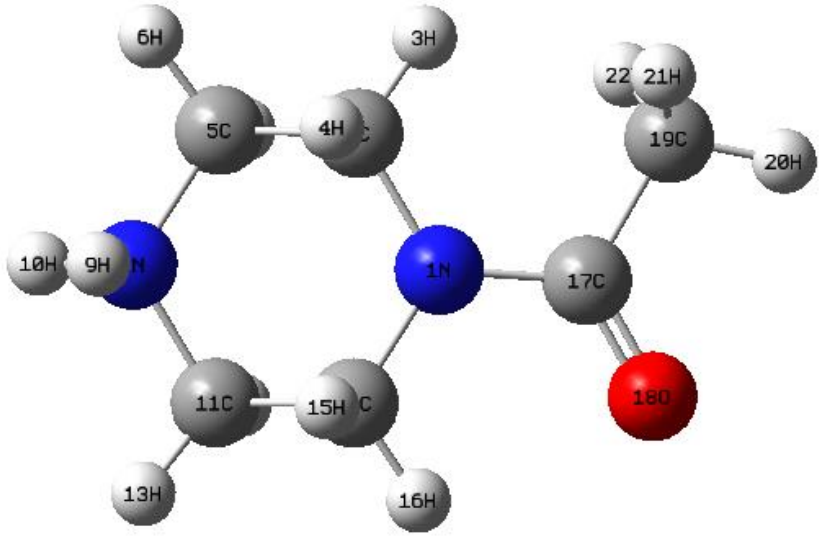

Figure 1 Optimized molecular structure of 2AP

TABLE:1Optimized molecular structure of 2AP

Bond Length	**Experimental value(Å)[a]**	1
		4ACP
C_{20}-N_{21}	1.338	1.387
C_{20}-C_{37}	1.490	1.518
N_{21}-C_{22}	1.451	1.459
N_{21}-C_{34}	1.453	1.456
C_{20}-N_{21}	1.338	1.387
Bond angle	**Experimental (^{0})**	**Calculated Values (^{0})**
		2AP
C_5-N_4-C_9	118.1	122.0
N_4-C_5-C_6	121.5	121.7
N_4-C_5-N_4	118.7	115.5
Dihedral	**Experimental (^{0})**	**Calculated Values (^{0})**
		2AP
C_5-N_4-C_9-C_8	-178.6	-179.8
C_5-N_4-C_9-H_2	-179.2	-0.0
N_4-C_{15}-C_6-C_7	-179.0	179.4
N_4-C_5-C_6-H_3	178.6	-177.9
N_4-C_5-C_6-C_7	-1.3	1.5

MEP

The molecular electrostatic potential (MEP) surface characterizes the interaction energy between the electric charge produced by the electrons and the nuclei of the molecule. It is related to electron density (ED), which recognizes electrophilic and nucleophilic sites as well as hydrogen bonding interactions (F.J. Luque et al., 2000). MEP surface of the 4ACP makes it possible to illustrate the charge distribution of the molecule in 3D. In the MEP surface, there is a spectrum of color ranging from -6.100e-2 (red color) to 6.100e-2 (blue color). Electron rich zone is the negative region concentrated over the carbonyl oxygen atoms and indicate the chemical activity in the 4ACPPA molecule and also confirm the presence of N-H....O interactions in the molecule.

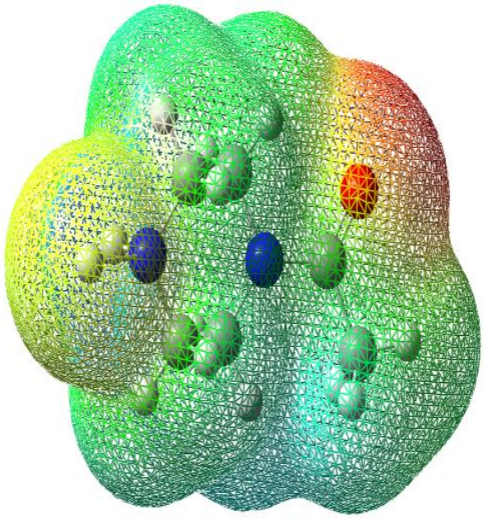

MEP plot of 4ACP

NCI-RDG analysis

The non-covalent interaction (NCI) also known as reduced density gradient (RDG) was a topological tool for analyzing noncovalent interactions such as van der Waals, hydrogen bonds, and steic conflicts. It provides knowledge about the molecular interaction within the molecule, crystallization, and chemical reactivity [3]. Green flaky patches bespeak the presence of weak non-covalent H…H interaction which is also seen from the RDG graph where more green spikes appear between 0.005 to - 0.020 a.u.

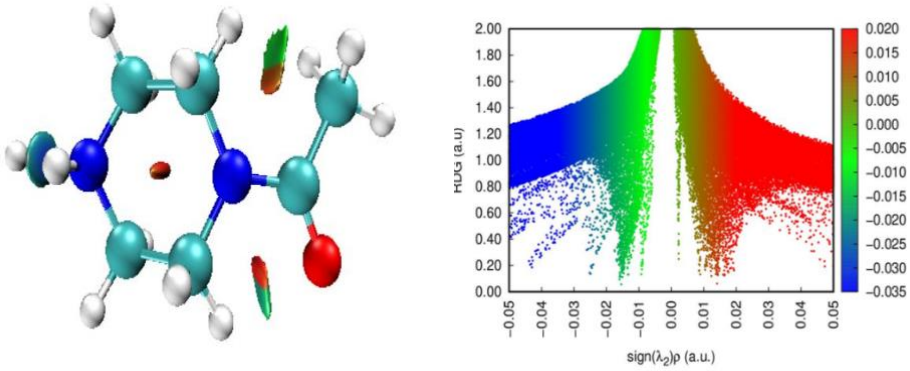

Figure: 2 2D scatter and Is surface density plots illustrating the non-bonded interactions of 2AP

Frontier Molecular Orbital's (FMO)

The HOMO and LUMO plot of 4ACP and its related compounds as implemented within the Gauss view version 5.1 program is shown in fig 4.

The highest occupied molecular orbital (HOMO) and lowest unoccupied molecular orbital (LUMO) are named frontier molecular orbital (FMO). The positive phase of the molecule is represented in red color, whereas the negative phase of the molecule is represented in green color. The conjugated molecules are distinguished by a small HOMO-LUMO separation, which is the result of a significant degree of ICT from the electron-donor groups to the efficient electron-acceptor groups through the π* conjugated path. The HOMO and LUMO energy gap of 4ACP is 3.67eV. The lowest energy gap indicates the highest bioactivity.

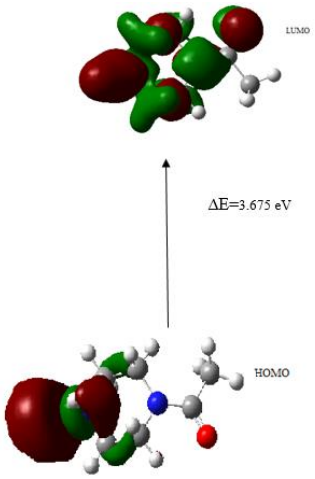

Figure 4: frontier molecular orbitals plot for 2AP

Molecular docking

Molecular docking is an alluring scaffold to know about the drug biomolecular interactions for rational drug design and discovery. It predicts the binding mode and type of interaction between active site proteins and ligand along with their distance and vicinity of functional groups involved [9]. The three-dimensional crystal form of the A.Flaves protein PDB: 6ZD6 was used as a target protein and utilized to choose docking simulation studies. Molecular docking results of 2AP with target protein are shown in Table 13(a). The amino acid residues involved in the hydrogen bond interaction were denoted by green line SER:175 form hydrogen bond interaction with a nitrogen atom of piperazinium ring in the title compound within the bond length of 1.830Å. The residues, LEU A:176 and PRO A:6 form alkyl and Pi-alkyl interaction. The molecular docking contemplation communicates the possible orientation of the 2ACP

Table 13 (a): Antifungal

compound	6ZD6 (anti-fungal)		
	B.E	I.C	RMSD
2ACPPA	-7.34	4.18	49.38

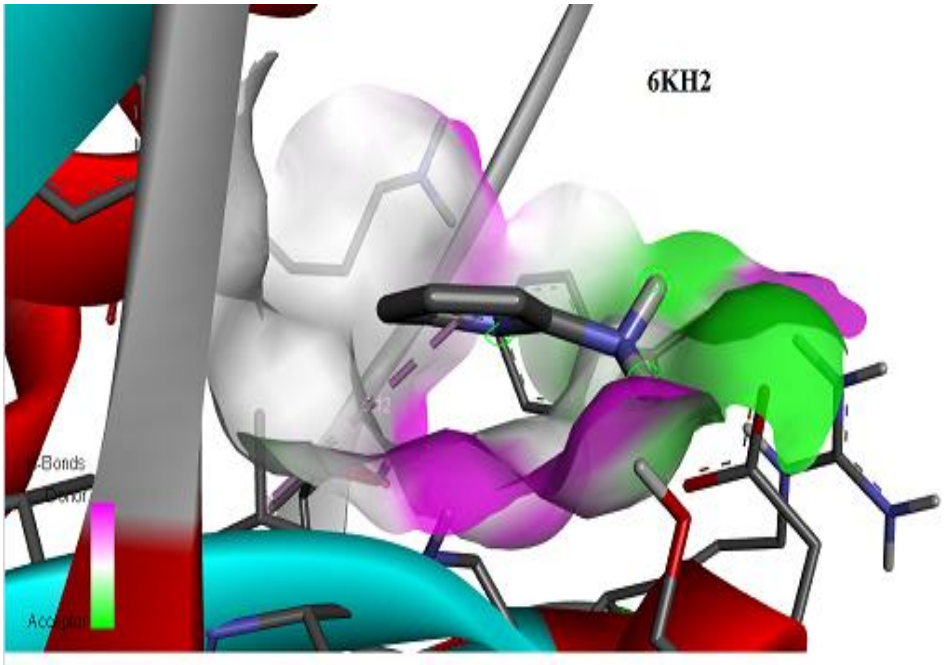

Figure: 5 2AP docked into the binding site of Antifungal

Conclusion

4ACP was synthesized by the slow evaporation method and their molecular structure has been optimized using the DFT technique the calculated bond length, bond angle and dihedral angle sustain good stability with good agreement with the experimental values. The possibility of hydrogen bonding and charge transfer shows the fungicidal nature of the title compound. The lower value of the HOMO-LUMO energy gap confirms charge transfer occurs within the molecule and bioactive nature of 4ACP. The protein-ligand interactions validate the compound's biological activity and can be proposed for antifungal medicines following additional experimental investigations.

Reference

V. Krishnakumar, N. Jayamani b, R. Mathammal, Molecular structure, vibrational spectral studies of pyrazole and 3,5-dimethyl pyrazole based on density functional calculations Spectrochimica Acta Part A 79 (2011) doi:10.1016/j.saa.2011.05.100

D. A.Dhas, I.H. Joe, S.D.D. Roy, T.H. Freeda, DFT computations and spectroscopic analysis of a pesticide: Chlorothalonil, Spectrochimica Acta Part A 77 (2010) 36-44.

D.N. Sathyanarayana, Vibrational Spectroscopy-Theory and Applications, New Age International (P), second ed., Limited Publishers, NewDelhi, 2004.

David Willington. T , Joema. S E , Sindhusha S , Suma V K, Investigation on structural, optical, mechanical, thermal and nonlinear optical activity of 2-methylazinium (2,4,6)-trinitrophenolate – experimental and DFT approach, Journal of Molecular Structure 1230 (2021) 129644 doi.org/10.1016/j.molstruc.2020.129644

N.P.G. Roeges, A Guide to the Complete Interpretation of Infrared Spectra of Organic Structures, John Wiley and Sons Inc, New York, 1994.

D.L. Pavia, G.M. Lampman, G.S. Kriz, Introduction to Spectroscopy, 3rd ed, Brooks/Cole, Thomson Learning, Singapore, 2001.

Spectrometric Identification of Organic Compounds, R.M. Silverstein, F.X. Webster, D. Kiemle, seventh ed., Wiley, New York, 2005.

Vibrational Spectra of Benzene Derivatives G. Varsanyi, , Academic Press, New York, 1969.

Crystal structure, FT-IR, FT-Raman, 1 H NMR and computational study of ethyl 2-{[(Z)3-(4-chlorophenyl)-3-hydroxy-2-propene-1-thione] amino} acetate S. Prasanth, Mary Varughese ,Nirmala Joseph , Paulson Mathew , T.K. Manojkumar , C. Sudarsanakumar journal of Molecular Structure 1081 (2015) 366–374

STUDY OF MOLECULAR INTERACTIONS IN BINARY MIXTURES OF NITRILES WITH TOLUENE USING ULTRASONIC PARAMETER-SPECIFIC ACOUSTIC IMPEDANCE

[a*]Bindu R G and [b]Chaithra B S

[a]Department of Physics, NSS College, Nilamel, Kollam, Kerala, India.

[b]Department of Physics, M G College, Thiruvananthapuram, Kerala, India.

[*]Corresponding author Email: drbindurg@gmail.com

Abstract

Molecular interaction study in binary mixtures of nitriles with toluene has been done by measuring their ultrasonic velocities and densities at room temperature 303K. These direct parameters were used to evaluate the ultrasonic parameter specific acoustic impedance. From the definition of specific acoustic impedance, a concentration dependent relation of this parameter has been derived from the knowledge of concentration coefficients of density and velocity of pure components of liquid mixtures. This empirical relation has been used to study the molecular interactions in binary mixtures of acetonitrile/benzonitrile in toluene.

Keywords: molecular interaction, binary mixtures, specific acoustic impedance

Introduction

Liquid state is considered to be the most complicated among the three states of matter. The study of this state of matter using ultrasonic parameters helps in determining its properties as well as the nature of molecular interactions existing in liquid mixtures [1-3]. The study using derived ultrasonic parameters is found to be more effective than direct parameters in elucidating the properties of liquid mixtures [4-6]. Hence a derived ultrasonic parameter – specific acoustic impedance (Z_A) has been used for the present study. The present study is the continuation of our earlier study of nitriles with methanol – an aliphatic/aromatic nitrile in an aliphatic alcohol. Moreover, nitriles with methanol binary mixtures were of polar + polar type. Here we have chosen the binary mixtures of nitriles with toluene – an aliphatic/aromatic nitrile in an aromatic hydrocarbon [7-9]. Moreover, the mixtures chosen are of polar + non-polar type.

In the present paper, a new concentration dependent relation of specific acoustic impedance has been deduced from the knowledge of concentration coefficients of sound velocity and density of pure components. This relation is then used to estimate the specific acoustic impedance of nitriles with toluene to study the molecular interactions in them.

The binary mixtures chosen for the present study are

Acetonitrile (CH_3CN) + toluene ($C_6H_5CH_3$)

Benzonitrile (C_6H_5CN) + toluene ($C_6 H_5CH3$)

A study of these binary mixtures gives information regarding the molecular interactions taking place between polar and non-polar components.

Materials and methods

The sound velocity and density of the binary mixtures of acetonitrile + toluene and benzonitrile + toluene was determined experimentally at 303 K. Chemicals of AR/BDH grade and distilled water was used for the experimental purpose. The purity of these liquids was tested by comparing their densities with those in literature and found to be in good agreement [10]. Ultrasonic velocities of the pure liquids as well as the binary mixtures were measured using a single-crystal ultrasonic interferometer supplied by Mittal Enterprises at a frequency of 2 MHz The densities were determined using a 12 cm^3 double-stem pycnometer and the masses were recorded using an electronic balance having an accuracy of $\pm$ 0.1 mg.

Theory

The specific acoustic impedance of a liquid is related to sound velocity and density as

$$Z_A = U\,\rho \qquad (1)$$

Since U and ρ depends on concentration, on differentiating Eq. (1) with respect to concentration at constant temperature and dividing throughout by Z_A we get,

$$\frac{dZ_A}{Z_A} = (M + N)\,DC \qquad (2)$$

where $M = \frac{1}{\rho}\left(\frac{\partial \rho}{\partial C}\right)_T$ is the concentration coefficient of density and

$N = \frac{1}{U}\left(\frac{\partial U}{\partial C}\right)_T$ is the concentration coefficient of sound velocity

Integrating Eq. (2) $\ln Z_A = (M + N)\,C + D \qquad (3)$

where D is a constant of integration.

If $Z_A^{'}$ is the specific acoustic impedance at another concentration $C^{'}$ ($C^{'} < C$), then

$$\ln Z_A^{'} = (M + N)\,C^{'} + D \qquad (4)$$

From Eq. (3) & Eq. (4) $$Z_A = Z_A^{'}\, e^{(M+N)\Delta C} \qquad (5)$$

where $\Delta C = C - C^{'}$ is the difference in concentration. This is the concentration dependent relation of specific acoustic impedance. The difference in experimental and estimated (calculated) values gives the excess values of the parameter.

Results and Discussion

Densities and ultrasonic velocities of the pure liquids as well as the binary mixtures of nitriles with toluene were measured at a constant temperature 303 K. Using these parameters the specific acoustic impedance has been determined experimentally using Eq. (1) and estimated using Eq. (5) and are tabulated in Table.1.

Table.1 Variation of U, ρ, Z_A^{Expt}, Z_A^{Cal} and Z_A^E with mole fraction for the binary mixtures of Acetonitrile/ Benzonitrile with toluene at 303K for different concentrations.

X_1	U ms^{-1}	ρ $kg\ m^{-3}$	$Z_A^{Expt} \times 10^{-6}$ $kg\ m^{-2}s^{-1}$	$Z_A^{Cal} \times 10^{-6}$ $kg\ m^{-2}s^{-1}$	$Z_A^E \times 10^{-6}$ $kg\ m^{-2}s^{-1}$
CH_3CN (X_1) + $C_6H_5CH_3$ (X_2)					
0.000	1292	860.1	1.111		
0.1260	1287	854.3	1.099	1.094	0.0050
0.2324	1284	850.8	1.092	1.079	0.0130
0.3293	1281	846.7	1.085	1.066	0.0190
0.4233	1278	841.9	1.076	1.053	0.0230
0.5023	1275	834.7	1.064	1.043	0.0210
0.6588	1270	821.4	1.043	1.023	0.0200
0.7316	1268	815.6	1.034	1.013	0.0210
0.8760	1264	800.2	1.011	0.9951	0.0160
1.000	1255	772.3	0.9692	0.9797	-0.0056
C_6H_5CN (X_1) + $C_6H_5CH_3$ (X_2)					
0.000	1292	860.1	1.111		
0.1034	1305	874.7	1.141	1.140	0.0010
0.2113	1319	890.9	1.175	1.172	0.0030
0.3332	1335	906.9	1.211	1.208	0.0030
0.4090	1344	919.1	1.235	1.231	0.0040
0.5093	1354	933.1	1.263	1.263	0.0000
0.6337	1367	949.8	1.298	1.303	-0.0050
0.7569	1379	967.7	1.334	1.343	-0.0090
0.8790	1392	982.5	1.368	1.385	-0.0170
1.000	1407	999.4	1.406	1.428	-0.0220

Graphs are plotted for the binary mixtures and are depicted in Figs. 1 and 2.

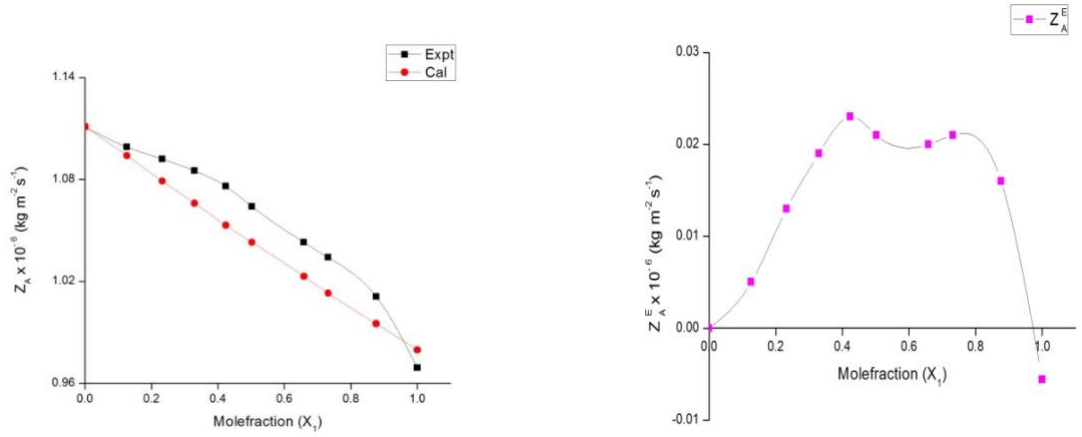

(a) Z_A^{Expt} & Z_A^{Cal} of $CH_3CN + C_6H_5CH_3$ **(b) Z_A^E of $CH_3CN + C_6H_5CH_3$**

Fig.1 Variation of Z_A^{Expt}, Z_A^{Cal} and Z_A^E with mole fraction for $CH_3CN + C_6H_5CH_3$ at 303 K

Analyzing Fig. 1(b), it can be seen that the deviation between the experimental and calculated values of Z_A, denoted as Z_A^E is positive up to $x_1 = 0.9$ mole fraction and thereafter shows a negative trend. Fort and Moore [11] suggests that a positive Z_A^E is an indication of strong hetero molecular interaction in the liquid mixtures which may be attributed due to charge transfer, dipole-dipole, dipole-induced dipole interactions and hydrogen bonding between unlike molecules while a negative Z_A^E is an indication of weak interaction attributed by London forces (dispersive forces). The positive nature of Z_A^E in $CH_3CN + C_6H_5CH_3$ mixture shows that there exists strong molecular interaction between component molecules of acetonitrile and toluene.

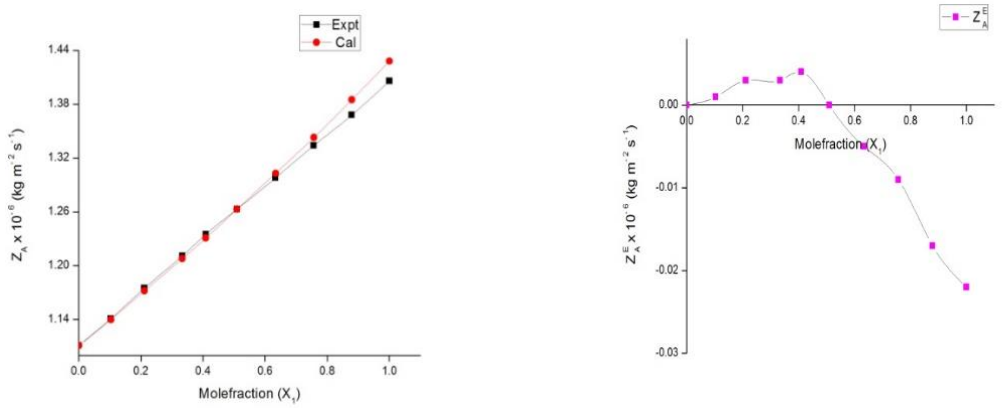

(a) Z_A^{Expt} & Z_A^{Cal} of $C_6H_5CN + C_6H_5CH_3$ **(b) Z_A^E of $C_6H_5CN + C_6H_5CH_3$**

Fig.2 Variation of Z_A^{Expt}, Z_A^{Cal} and Z_A^E with mole fraction for $C_6H_5CN + C_6H_5CH_3$ at 303 K

In the case of C_6H_5CN + $C_6H_5CH_3$ mixture, it can be seen that the excess values of Z_A are positive up to x_1 = 0.5 mole fraction and thereafter becomes negative till x_1= 1 [Fig. 2(b)]. According to Pathania et al [12], the positive values of Z_A^E may be due to molecular association whereas negative values show molecular dissociation. Hence in benzonitrile + toluene mixture, molecular association occurs till the concentration of components become equal and as the concentration of benzonitrile in toluene increases, there occurs dissociation of component molecules. Hence it can be concluded that there exists molecular interactions in binary mixtures of nitriles with toluene which is greater in acetonitrile + toluene mixture than in benzonitrile + toluene mixture.

Conclusions

The concentration dependent relation derived from the knowledge of concentration coefficients of density and sound velocity is helpful in explaining the molecular interactions existing between the component molecules of a liquid mixture of polar and non-polar nature. An added advantage of this relation is that it can be used to estimate the value of specific acoustic impedance at any higher concentration, if its value at a lower concentration is known.

References

Nithin Srivastava, B K Rathour, Sonia Singh & Shashi Singh (2023) Thermo acoustical study of intermolecular interactions in binary mixtures of benzaldehyde with methanol and ethanol. *Chemical Physics Impact*, 6 (100144), 1-6. https://doi.org/10.1016/j-chphi.2022100144.

Manoj Kumar Praharaj & Abhiram Satapathy (2020) Molecular interactions in binary liquid mixtures by ultrasonic technique. *Indian Journal of Natural Sciences*, 10(60), 19721-19725.

N Sathi, P L Sabarathinam, Emayavaramban Mani & C Gopi (2010) Molecular interaction studies in binary liquid mixtures from ultrasonic data. *E-journal of Chemistry*, 7(2), 648-654. DOI: 10.1155/2010/487874.

D Chinnarao, Ch. V. Padmarao, K Raja, M Srilatha & B Venketeswara Rao (2020) Molecular interaction studies on binary liquid mixture of ethyloleate and ethyl methyl ketone at temperature range from 303.15K to 318.15K. *International Journal of Engineering Research and Technology*, 9(4).DOI: 10.17577/IJERT/V9ISO40093.

M Gowrisankar, P Venkateswarlu, K Sivakumar & S Sivarambabu (2013) Ultrasonic studies on molecular interactions in binary mixtures of N-methylaniline with methyl isobutylketone,+3-pentanone and cycloalkanones at 303.15K. *Journal of Solution Chemistry*, 42(5), 916-935

A Ali & A K Nain (2002) Ultrasonic study of molecular interaction in binary liquid mixtures at 30^0C. *Indian Academy of Sciences*, 58(4), 695-701.

N K Karthick, G Arivazhagan & R Shanmugham (2018) FTIR spectroscopic studies and DFT calculations on the toluene-propionitrile binary system. *Journal of Molecular Structure*, 1173, 456-461. http//doi.org/10.1016/j.molstruc.2018.06.046.

K D More, R S Kawale & P G Gawali (2015) Ultrasonic study of binary mixture of acetic acid and toluene. *International Journal of Science and Research*, 4(8), 1-6.

K Rajagopal, S Chenthilnath & A K Nain (2010) Physiochemical studies of molecular interaction in binary mixtures of toluene with some aliphatic nitriles at different temperatures. *Journal of Molecular Liquids*, 151(1), 23-29. https://doi.org/10.1016/j.molliq.2009.10.013.

J A Riddick & W B Bunger (1970). *Organic Solvents*; 3rd ed: Wiley-Interscience: Newyork. Vol (2).

R J Fort & W R Moore (1965). Adiabatic compressibilities of binary liquid mixtures. *Trans Faraday Soc*., 61, 2102-2111

V Pathania, S Sharma, B K Vermani & D S Gill (2022) A study of some excess thermodynamic properties in binary mixtures of non-aqueous solvents at variable temperatures. *Physical Chemistry Research*, 10(3), 439-453.

SYNTHESIS, SPECTROSCOPIC, STRUCTURAL INVESTIGATION, CHEMICAL REACTIVITY AND MOLECULAR DOCKING ANALYSIS OF 3-AMINO-N-PHENYLBENZENESULFONAMIDE

Bravanjalin Subi E [a,b], D. Arul Dhas[b]

[a]Research scholar, Register Number: 20213112132016, Manonmanium Sundaranar University, Abishekapatti, Tirunelveli – 627 012, Tamil Nadu, India

[b]Department of Physics and Research Centre, Nesamony Memorial Christian College, Marthandam – 629 165, Kanyakumari District, Tamilnadu, India

**Corresponding author: aruldhas2k4@gmail.com*

Abstract

The prospective antimicrobial molecule 3-amino-N-phenylbenzenesulfonamide (3PBS) has been synthesized and characterized by XRD, FT-IR, FT-Raman spectra. The quantum chemical computations of energies, geometrical structure, charge transfer and vibrational wavenumbers were carried out using density functional method (DFT/B3LYP) with 6-311G (d, p) basis set. The complete vibrational assignment for the vibrational modes were performed with vibrational energy distribution analysis (VEDA4) and these assignments were compared with the experimental FT-IR and FT-Raman spectrum. The strength of N-H…O and C-H…O intermolecular interactions were analyzed using reduced density gradient (RDG) analysis. The frontier molecular orbital analysis reveals the possibility of charge transfer within the molecule. Molecular docking shows that sulfonamide and hydroxyl groups are biologically active through their hydrogen bonding interaction with amino acids, which reveals the antimicrobial activity of the compound.

Introduction

Sulfonamides are a very important class of compounds in medical and pharmaceutical chemistry with several biological applications [1]. Sulfonamides continue to attract the attention of structural and pharmaceutical chemist because of their drug-like properties [2]. Sulfonamides, or sulfa drugs, are antibiotics that treat bacterial infections. Other conditions treated with them include urinary tract infections (UTIs), bronchitis, eye infections, bacterial meningitis, pneumonia, ear infections, severe burns, and traveler's diarrhea. Sulfonamides do not kill the bacteria but they will prevent growths of bacteria. In addition, sulfa drugs have been administered to food producing animals to increase their growth for therapeutic and prophylactic purposes [3].

Results and Discussion

Synthesis of N-(2-Hydroxyphenyl) 4-toluenesulfonamide

Single crystal of 3PBS was prepared by dissolving aniline (2mmol) and 3-aminobenzene-1-sulfonylchloride (2mmol) in 30 ml of acetone and the solution was refluxed for 2 hours. The resultant solution was cooled, filtered and allowed for slow evaporation at room temperature. Brown needle like crystals were grown after 2 weeks and are shown in Figure 1.

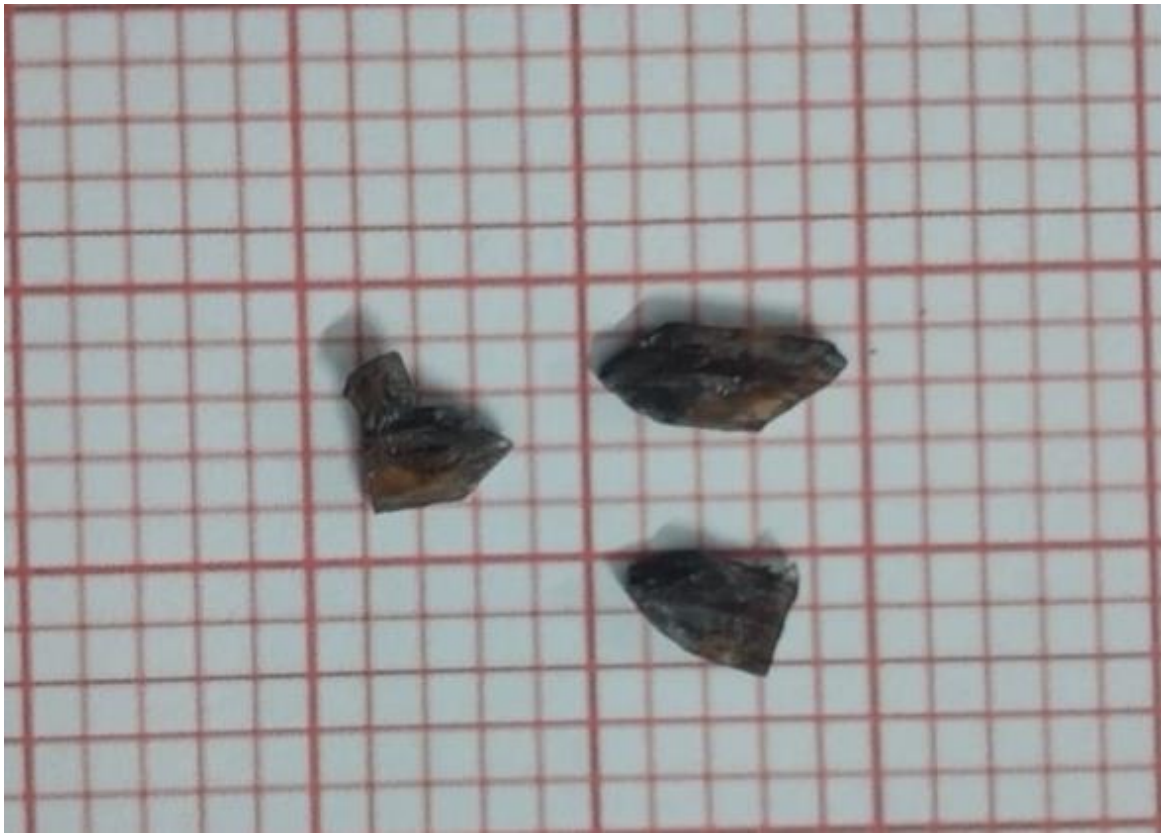

Figure: 1 Photograph of grown crystal

Optimized Geometry

The optimized structure of the title compound using DFT/B3LYP method with 6311G (d, p) basis set is shown in Figure 2. The aniline ring of 3PBS appear to be little distorted due to the substitution of NH-SO_2 group, which is evident from the bond angles C_{13}-C_{12}-C_{17} (119.3˚) and C_{12}-C_{17}-C_{16} (120.2˚) [4]. Similarly, the asymmetry of the aminobenzene ring is evident from the bond angles C_7-C_6-C_{11} and C_7-C_8-C calculated as 122.5˚ and 118.4˚ for 3PBS, which was due to the NH_2 and SO_2 substitution at C_8 and C_6 atoms. In 3PBS, the bond length S_1-O_3 (1.456A˚) [8] was increased due to C_{13}-H_{23}…O_3 hydrogen bonding and the bond length S_1-N_5 (1.697A˚) [8] was increased due to electron delocalization.

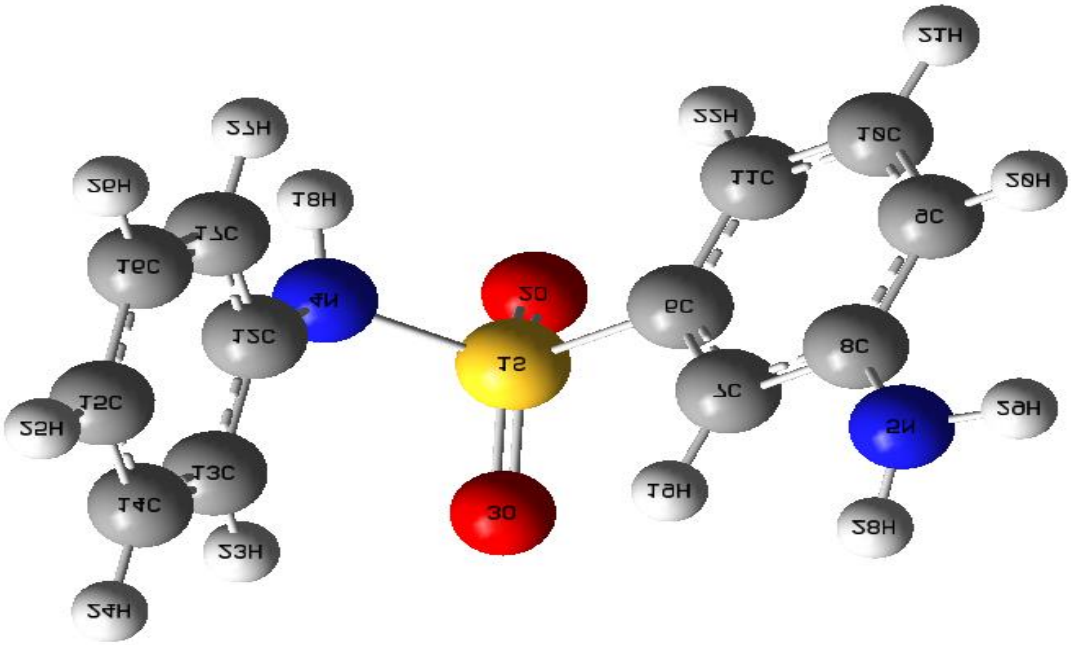

Figure: 2 Optimized figures of 3PBS

Vibrational analysis

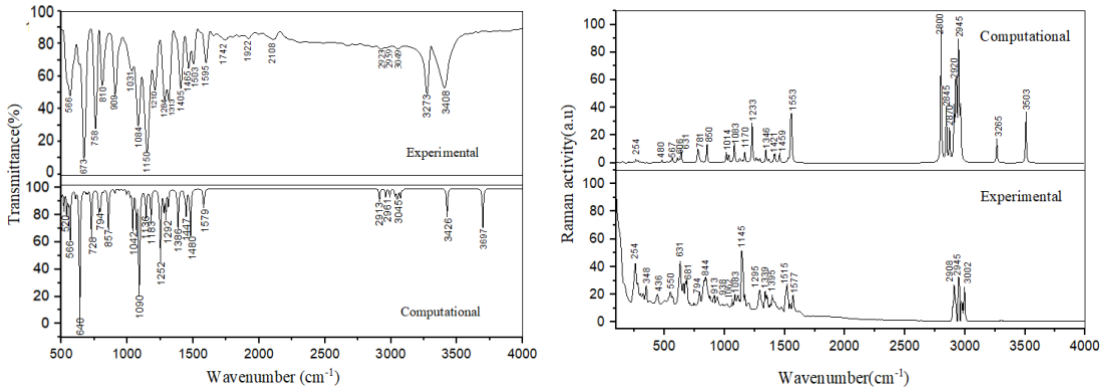

Figure: 3 Experimental and Simulated IR and Raman spectra.

The harmonic frequency by DFT calculation is usually higher than the corresponding experimental frequencies due to the facts of the electron correlation, the anharmonicity effect and basis set deficiency etc. [9]. Vibrational analysis of theoretical and experimental approaches provides deeper knowledge in determining the functional groups, predicting their spectral features and assessment of structural changes. Experimental and simulated IR and Raman spectra of 3PBA was shown in Figure 3.

In heterocyclic aromatic compounds, the N-H stretching vibrations have been measured in the region 3000-3500cm^{-1}[10]. The N-H in-plane bending vibration is expected near 1400cm^{-1}. In the title molecule, this bond was observed at 1405cm^{-1} in FT-IR and 1395cm^{-1} in FT-Raman spectrum. The N-H in-plane bending mode was computed at 1386cm^{-1}. The asymmetric SO_2 stretching vibrations are generally observed in the region 1310-1360cm^{-1}, while the SO_2 symmetric stretching vibration appears in the region 1135-1165 cm^{-1} [11]. In the title molecule, the asymmetric stretching band was observed as a medium band at 1339 cm^{-1} in FT-Raman spectrum and was calculated at 1362 cm^{-1}.

Frontier Molecular Orbital analysis

The frontier molecular orbitals are most useful in determining the properties such as chemical reactions, chemical reactivity, molecular stability and biological activity [12]. The HOMO represents the ability to donate an electron, LUMO as an electron acceptor represents the ability to obtain an electron. A molecule with less HOMO-LUMO band gap is more chemical reactive and has less kinetic stability [13]. HOMO and LUMO energy gap explain the external charge transfer interaction taking place within the molecule. The low band gap energy is determined as 2.6248eV shows the highest bioactivity of the molecule.

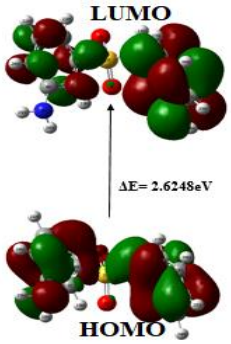

Figure: 4 HOMO-LUMO band Gap of 3PBS

Reduced density gradient (RDG) analysis

Reduced density gradient (RDG) analysis were performed using multiwfn [14] package to ascertain the noncovalent interaction in the title compound. Reduced density gradient (RDG) is an extension of AIM analysis to explain non-covalent weak interactions such as van der Waals (vdW), steric effect and hydrogen bond. The 2D scatter graph and 3D RDG isosurface of 3PBS are depicted in figure 5, which shows the presence of various non-covalent interaction in 3PBS. RDG scatter graph is generated between reduced density gradient and sign $(\lambda)\rho$. The sign $(\lambda)\rho < 0$ for attractive interaction, sign$(\lambda)\rho > 0$ for repulsive interaction and sign $(\lambda)\rho \approx 0$ for van der Waals interaction (weak interaction).

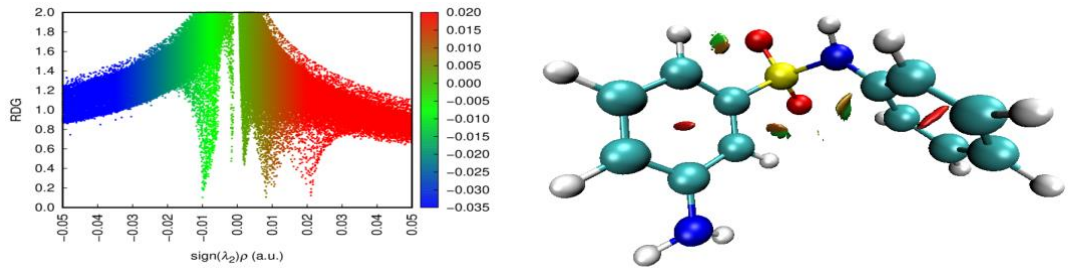

Figure: 5 2D scatter graph and 3D is surface map of 3PBS

Molecular Docking analysis

Molecular docking plays an important role in calculating the mode of action, mechanism and binding capability between the drug and protein. The title compound was docked into the active site of proteins 3D8W associated with anticancer activity. The ligand was docked individually at the functional site of the respective proteins and the docking energy was investigated to achieve the minimum value. The pictorial representation shows best ranked ligand-target protein complexes with hydrogen bond interaction as displayed in Figure 6. Protein-ligand interaction with binding energy -6.76 kcal/mol claims that the synthesised compound can be developed as an antimicrobial drug.

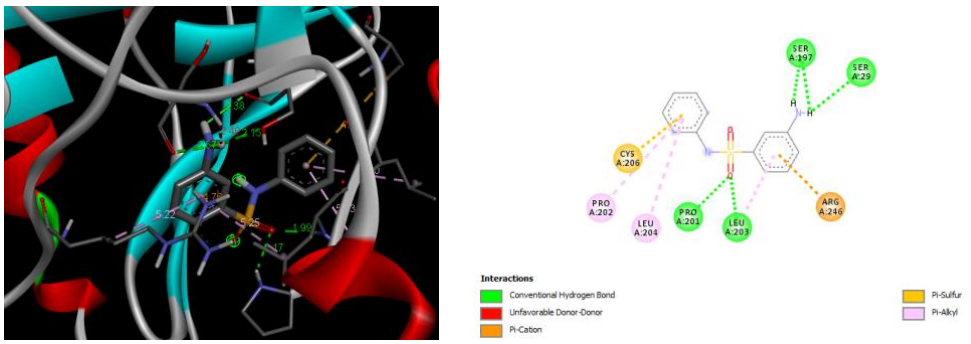

Figure: 6 Molecular docking of protein (3D8W) with ligand 3PBS

Conclusion

The complete study on synthesis, spectroscopic, structural investigation, chemical reactivity of N-3-amino-N-phenylbenzenesulfonamide were carried out with the aid of quantum chemical calculation. The calculated result of optimized geometry shows good agreement with the related experimental data. The RDG analysis indicates the presence C_{13}-$H_{23}\ldots O_3$ hydrogen bonding, which was substantiated by optimized geometry. The HOMO-LUMO band gap energy 2.6248eV reflects the chemical reactivity and highest bioactivity of the molecule. The band gap energy of 3PBS was compared with reported data reveals the significant bioactivity of the title molecule. The lowest binding energy (-7.58 kcal/mol) of the title molecule against protein reveals that the title molecule can be developed as an anticancer drug.

References

H. Schiff, “Mittheilungen Aus Dem Universitatslaboratorium in Pisa: Eine Neue Reihe Organischer Basen,” *Annalen Der Chemie Und Pharmacie* 131, no. 1 (1864): 118–9.

Elias E. Elemike, Henry U. Nwankwo, and Damian C. Onwudiwe, *Heliyon* 4, no. 7 (2018): e00670.

C. Desfrancois, S. Carles, and J. P. Schermann, “Weakly Bound Clusters of Biological Interest,” *Chemical Reviews* 100, no. 11 (2000): 3943–62.

A. D. Becke, *Physical Review A, General Physics* 38, no. 6 (1988): 3098–100.

Chengteh. Lee, Weitao. Yang, and Robert G. Parr, *Physical Review. B, Condensed Matter* 37, no. 2 (1988): 785–9.

Peter Pulay, Geza Fogarasi, Gabor Pongor, James E. Boggs, and Anna Vargha, *Journal of the American Chemical Society* 105, no. 24 (1983): 7037–e7047.

Garrett M. Morris, Ruth Huey, William Lindstrom, Michel F. Sanner, Richard K. Belew, David S. Go odsell, and Arthur J. Olson, *Journal of Computational Chemistry* 30, no. 16 (2009): 2785–91.

A. Subashini, C. Arunagiri, and M. Saranya, *Chemical Data Collections* 30 (2020): 100549.

Sapna Pathak, Anuj Kumar, and Poonam Tandon, *Journal of Molecular Structure* 981, no. 1–3 (2010): 1–9.

D. Arul Dhas, I. Hubert Joe, S. D. D. Roy, and S. Balachandran, *Spectrochimica Acta Part A: Molecular and Biomolecular Spectroscopy* 108 (2013): 89–99.

B. Lakshmaiah, and G. Ramana. Rao, “Vibrational Analysis of Substituted Anisoles,” *Journal of Raman Spectroscopy* 20, no. 7 (1989): 439–48.

Peter Politzer, Pat Lane, Keerthi Jayasuriya, and Linda N. Domelsmith, *Journal of the American Chemical Society* 109, no. 7 (1987): 1899–901.

L. S. Anju, D. Aruldhas, I. Hubert Joe, and S. Balachandran, *Journal of Molecular Structure* 1201 (2020): 127201.

T. Sasitha, and Winfred Jebaraj. John, *Heliyon* 7, no. 2 (2021): e06127.

EVALUATING THE EFFECT OF DIFFERENT IONIZATION CHAMBER VOLUMES IN MEASURING THE ABSORBED DOSERATE IN WATER PHANTOM USING GAMMA EMITTING Co-60 RADIONUCLIDE

Niju Thankachan T[1], Sumimol K S[2], Mary Vinaya[2], Bijini B R[2*]

[1,2]Radiation Physics, Department of Radiation Oncology, Government Medical College, Thrissur

[2]Associate Professor, Department of Physics, VTMNSS College, Dhanuvachapuram*

[*]Corresponding author: Dr.Bijini.B.R, bijinijyothis@gmail.com, Tel: 9496253673

Abstract

The dose rate measurement from a Co-60 radioactive source loaded in telecobalt equipment was measured by ionization chambers placed in a radiation field analyser (RFA).In this study, using gamma radiation, the variation of absorbed dose rate with three ionization chambers having different volumes was evaluated and it was inferred that, as the volume of the chamber increases, the percentage error in the measured absorbed dose rate decreased significantly.

Keywords: *farmer chamber, semiflex chamber, pinpoint chamber, absorbed dose rate*

Introduction

The gamma rays emitted from a Co-60 radioactive source housed in a Bhabhatron II TAW telecobalt machine was primarily used for the purpose of radiation treatment [8]. As the radiation interacts with matter, electrons liberated by photons will deposit energy in medium and absorbed dose varies with depth. This depends on beam energy, depth, field size and distance from the radionuclide to the surface [4]. Absorbed dose, a radiation quantity is the energy absorbed per unit mass and its SI unit is gray (Gy), defined as one joule of energy absorbed per kilogram of matter, J/kg. The absorbed dose rate (cGy/min) of the source at the depth of maximum dose in a medium was precisely measured using the principle of radiation detection with gas filled detectors. Ionization occurs in the gas cavity and ions were collected by applied potential difference. A cylindrical gas ionization chamber measures the charge from the number of ion pairs . The motion of ion pairs under the effect of electric field generates an ionization current which was measured by an electrometer circuit and this is proportional to the radiation dose. Ion chambers were used because of their flat energy response and precision. Water was taken as the standard medium for the measurement of absorbed dose rate. The code

of practice prescribed in the International Atomic Energy Agency (IAEA) Technical Report Series (TRS) 398[3] is used worldwide for the in- phantom dosimetry before the actual irradiation to clinical applications. TRS 398 is an International code of practice for dosimetry based on standards of absorbed dose to water. Cylindrical chambers, especially farmer chambers, are well characterized and are considered the gold standard of clinical reference dosimetry. Semiflex chamber is a vented, waterproof, fully guarded and is an ideal *chamber* for relative and reference dosimetry measurements in water, air or solid phantoms. Pinpoint ion chamber is an ultra small-sized therapy chamber with 3D characteristics for dosimetry in high-energy photon beams. Because of the axial design of the cylindrical chambers, the effective point of measurement is upstream of the central axis of the chamber by $0.6r_{cav}$ for photons. A water phantom that scans ionization chambers in the radiation field is required for acceptance testing and commissioning of the high energy radiation generating telecobalt treatment unit. This type of water phantom is the radiation field analyzer (RFA).

Methods and materials

Three different types of Ionization chambers were used for the precise dose rate measurement along with a calibrated electrometer (PTW Unidos E) in Bhabha Tron telecobalt unit loaded with a 207RMM Co-60 radioactive source having an activity of 8371.64 Ci as on 09-03-2023. The ionization chambers used were farmer chamber, semi flex field chamber and pinpoint chamber of volume 0.6cc, 0.07cc and 0.015cc respectively. All the chambers were of PTW made. The individual chambers were positioned at 5cm depth inside RFA based on TRS 398 protocol for each measurement. The Co-60 source position to the surface of the water phantom was maintained at 80 cm for the measurement. The gamma radiation of average energy 1.25 MeV emitted from the source was shaped to a square field of size 10 x 10 cm^2 using collimator jaws and directed towards RFA. The central axis of the radiation beam was aligned with the centre of cavity volume of chambers. Charge produced due to ionization in the detector volume was collected by electrometer. The meter reading of dosimeter with the reference point of chamber placed at 5cm were corrected for timer error due to transit of radionuclide and influence quantities such as temperature and pressure correction factor (k_{TP}), electrometer calibration (k_{elec}), polarity effect (k_{pol}), ion recombination (k_s) and beam quality correction factor (k_{QQ0}) [3]. The mass of air in the cavity volume will be subjected to atmospheric variations. The correction factor k_{TP} should be applied to convert the cavity air mass to the reference conditions. When the ionization chamber and the electrometer are calibrated separately, an electrometer calibration factor k_{elec} given by the calibration laboratory should be applied during the measurement. A polarity correction factor k_{pol} should be used for considering the variation in the meter reading due to polarizing potentials of opposite polarity. The ion recombination correction factor k_s is applied to consider the incomplete collection of charges in ionization chamber. k_{QQ0} is the correction factor which corrects for the difference between reference beam quality Q_0 and actual quality Q being used.

Gamma rays from a doubly encapsulated Co-60 radionuclide which was well shielded with lead and titanium was used for the measurement of absorbed dose rate in water. The depth

of maximum dose for a Co-60 beam in water was 5mm. The standard absorbed dose rate at the depth of maximum dose when the radionuclide was first loaded into telecobalt machine was 295.8372 on 08-06-2022. The value obtained by manual calculation using radioactivity decay formula was 268.03 on 09-03-2023. As per TRS 398 protocol, reading for the measurement of dose rate for 10 x 10 cm^2 field was taken at reference depth of 5cm. The dose rate calculated at 5cm for each ionization chamber was converted to absorbed dose rate at depth (5mm) of maximum dose using percentage depth dose (PDD) of 5cm, which is defined as the quotient, expressed as a percentage, of absorbed dose at any depth d to the absorbed dose at a reference depth d_0, along the central axis of the beam.

The chambers were calibrated along with PTW Unidose E and hence, electrometer calibration k_{elec} = 1.Since the radiation quality of gamma rays used in the secondary standard dosimetry laboratory for calibration of ionization chambers was performed with Co-60 source and all measurements taken for this study was also carried out using Co-60 radionuclide, the radiation quality correction factor, k_{QQ0} = 1

The timer error, **τ** considering the transit of radionuclide from OFF to ON and back to OFF shielded position and the influence quantities like k_{TP}, k_{pol} & k_s , for each ionization chamber is detailed below. The calculation method for each influence quantity is

$$\tau = \frac{M_B\, t_A - M_A\, t_B}{n\, M_A - M_B} \qquad k_{TP} = \frac{(273.2+T)}{(273.2+T_o)}\frac{P_o}{P}$$

$$k_{\text{pol}} = \frac{|M_+| + |M_-|}{2M} \qquad k_s = \frac{(V_1/V_2)^2 - 1}{(V_1/V_2)^2 - (M_1/M_2)}$$

Where, M_A is the integrated reading in a time t_A & M_B is the integrated reading in **n** short exposures of time t_B/n each. T_0 and T is the standard and measured temperature respectively, P_0 and P is the standard and measured atmospheric pressure respectively.

M_+ and M_- is the electrometer readings for positive (V_+) and negative (V_-) polarity respectively and M is the reading at the user polarity.

M_1 and M_2 are the readings at polarizing voltages V_1 and V_2 respectively. V_1 is the normal operating voltage and V_2 is a lower voltage

Dose rate at 5 cm depth, $\mathbf{D = M \times N_{D,W} \times k_{TP} \times K_{pol} \times K_s \times K_{elec} \times K_{QQ0}}$, where $M = \frac{M_A}{t_A + \tau}$

is the corrected meter reading for timer error.

$N_{D,W}$ is the calibration factor in terms of absorbed dose to water for the dosimeter provided by secondary standard dosimetry laboratory (SSDL), BARC, Mumbai.

PDD for 5cm depth, 10 x10 cm^2, 80cm SSD from a Co-60 beam = 78.56

Results and discussion

Attempts were made with the intention of comparing the volume effect by measuring ions produced in active gas region of the chamber. Eight sets of meter reading were taken for each setup with all the three chambers and standard deviation was measured.

The temperature in irradiated medium was 21^0C and atmospheric pressure on the day of measurement (09-03-2023) was 1013mbar and temperature pressure correction factor, k_{TP} for all the chamber setting was

Standard temperature, T_0 (^{0}C)	Standard atmospheric pressure, P_0 (mbar)	Measured temperature, T (^{0}C)	Measured atmospheric pressure, P (mbar)	calculated k_{TP} value
20	1013.2	21	1013	1.00361

For farmer chamber (0.6cc volume)

Timer error,τ

V = -300V	V = -300V	t_A = 1 min	n = 2	calculated τ value
M_A = 40.763	M_B = 40.92	t_B = 1 min		0.00385

Polarity effect, k_{pol}:

V_+ = 300V	V_- = -300V	M = 40.763	calculated k_{pol} value
M_+ = 40.9066	M_- = 40.763		1.00175

Ion recombination, k_s

V_1 = -300V	V_2 = -150V	calculated k_s value
M_+ = 40.763	M_- = 40.76	1.000027

The calibration factor $N_{D,W}$ for the farmer chamber provided by SSDL was 5.16 x 10^7 Gy/C. The average electrometer reading for charge collected when farmer chamber exposed to radiation was 40.763 ± 0.007 nC. Dose rate at 5cm= 210.7436 cGy/min and dose rate at the depth (5mm) of maximum dose = 268.2582 cGy/min

B. For semiflex chamber (0.007cc volume)

Timer error,τ

V = 400V	V = 400V	t_A = 1 min	n = 2	calculated τ value
M_A = 3.631	M_B = 3.645	t_B = 1 min		0.00387

Polarity effect, k_{pol}

V_+ = 400V	V_- = -400V	M = 3.631	calculated k_{pol} value
M_+ = 3.631	M_- = 3.615		0.9977

Ion recombination, k_s

V_1 = 400V	V_2 = 200V	calculated k_s value
M_+ = 3.631	M_- = 3.632	0.9998

The calibration Factor $N_{D,W}$ for the semi flex chamber provided by SSDL was 5.85 x 10^8 Gy/C. The average electrometer reading for charge collected when farmer chamber exposed to radiation was 3.632 ± 0.008nC. Dose rate at 5cm = 211.8281 cGy/min and dose rate at the depth (5mm) of maximum dose = 269.6386 cGy/min

C. For pin point chamber (0.015cc volume)

Timer error, τ

V = 200V	V = 200V	t_A = 1 min	n = 2	calculated τ value
M_A= 0.876	M_B = 0.878	t_B = 1 min		0.00385

Polarity effect, k_{pol}

V_+ = 200V	V_- = -200V	M = 0.876	calculated k_{pol} value
M_+ = 0.876	M_- = 0.858		0.9893

Ion recombination, k_s

V_1 = 200V	V_2 = 100V	calculated k_s value
M_+ = 0.876	M_- = 0.87	1.0025

The calibration factor $N_{D,W}$ for the pinpoint chamber provided by SSDL was 2.44 x 10^9 Gy/C. The average electrometer reading for charge collected when pinpoint chamber exposed to radiation was 0.876 ± 0.009 nC. Dose rate at 5cm = 212.3566 cGy/min and dose rate at the depth (5mm) of maximum dose = 270.3114 cGy/min.

From the readings obtained for farmer, semiflex and pinpoint chambers, it was observed that, the corresponding absorbed dose rate values at the depth of maximum dose were 268.2582 cGy/min, 269.6386 cGy/min and 270.3114 cGy/min and the percentage error of the absorbed dose rate at depth of maximum dose in water phantom when compared with the standard dose rate are 0.086%, 0.603% and 0.85% respectively. The influence of different detector volumes on the dose rate were studied and found that, there is a gradual increase in the measured absorbed dose rate with decreasing detector volume. Since the energy of radiation emitted by a radionuclide is constant and all the influence factors were included for the calculation, the variation of measured dose rate must be due to the change in volume of the chamber.

Conclusion:

In this study, it was inferred that, as the volume of the chamber increases, percentage error in measured absorbed dose rate decreased significantly. Hence, farmer chamber with 0.6cc volume had less percentage error in dose rate reading compared to the other two chambers. This is because of the phenomenon in which detector averages the dose over its finite size measuring the volume, the volume averaging effect and hence farmer chamber is more precise in dose rate measurement for a standard field size of 10 x 10 cm^2. However absorbed dose rate measured at 5cm in water phantom for 10 x 10 cm^2 field size using three ionization chambers of different volumes are within tolerance limit from the actual value and hence these three ionization chambers can be used for reference dosimetry depending on field size in the irradiated medium.

Acknowledgement: *The authors would like to thank Prof. Dr. Suresh Kumar K, Department of Radiation Oncology for providing the facility of the Department like telecobalt unit, ion chambers and RFA for the measurements.*

References

Ahmad, Iftikhar. (2012). Measurements of output factors using different ionization chambers and build up caps. Iranian Journal of Radiation Research. 10. 95-98.

Wegener, Sonja & Sauer, Otto. (2019). The effective point of measurement for depth-dose measurements in small MV photon beams with different detectors. Medical Physics. 46. 10.1002/mp.13788.

IAEA. TRS-398, 2000, Absorbed Dose Determination in External Beam Radiotherapy, Dosimetry and Medical Radiation Physics Section. International Atomic Energy Agency; Wagramer Strasse 5, A-1400 Vienna, Austria: [Google Scholar]

Khan FM. The Physics of Radiation Therapy. William and Wilkins; Baltimore MD: 2003. p. 451. [Google Scholar]

Güngör, G., Aydın, G., Mustafayev, T. Z., & Özyar, E. (2019). Output factors of ionization chambers and solid state detectors for mobile intraoperative radiotherapy (IORT) accelerator electron beams. Journal of applied clinical medical physics, 20(2), 13–23. https://doi.org/10.1002/acm2.12522

Sharma R, Sharma SD, Agarwal P, Avasthi DK, Verma R. Evaluating the Impact of Ionization Chamber-Specific Beam Quality Correction Factor in Dosimetry of Filtered and Unfiltered Photon Beams. J Med Phys. 2022 Apr-Jun;47(2):159-165. doi: 10.4103/jmp.jmp_101_21. Epub 2022 Aug 5. PMID: 36212211; PMCID: PMC9542991.

Saminathan S, Godson HF, Ponmalar R, Manickam R, Mazarello J, Fernandes R. Dosimetric Performance of Newly Developed Farmer-Type Ionization Chamber in Radiotherapy Practice. Technology in Cancer Research & Treatment. 2016;15(6):NP113-NP120. doi:10.1177/1533034615621635

Sharma SB, Sarma G, Barthakur M, Goswami P, Yadav B, Goswami S. Installation, commissioning, and performance evaluation of Bhabhatron-II TAW – An Indian-made telecobalt unit. J Radiat Med Trop [serial online] 2020 [cited 2023 Jul 9];1:38-42. http://www.jrmt.org/text.asp?2020/1/1/38/296108

Baba MH, Mohib-Ul-Haq M, Khan AA. Dosimetric Consistency of Co-60 Teletherapy Unit-a ten years Study. Int J Health Sci (Qassim). 2013 Jan;7(1):15-21. doi: 10.12816/0006016. PMID: 23559901; PMCID: PMC3612411.

Reza, Md & Islam, Md. Rakibul & Rahman, Md & Shamsuzzaman, Md & Rahman, Rashedur & Khan, H R. (2018). Calibration of Therapy Level Ionization Chamber at 60Co Teletherapy Beam Used for Radiation Therapy. International Letters of Chemistry, Physics and Astronomy. 79. 1-8. doi:10.18052/www.scipress.com/ILCPA.79.1.

EFFECT OF DY DOPING ON THE STRUCTURAL AND OPTICAL PROPERTIES OF RF SPUTTERED ZINC SULFIDE FILMS

Dr. Chalana S R

Department of Physics, T K Madhava Memorial College, Nangiarkulangara,

Alappuzha, 690513, Kerala, India

chalanatkmm@gmail.com

Introduction

Nanoscience is one of the most compelling and technologically relevant areas of condensed matter physics [1]. Thin films and nanostructured materials possess lot of research impetus due to the interesting inordinate properties, applications and capabilities of low dimensional material systems [2]. II–VI compound semiconductor thin films have received an intensive attention due to their application in thin film solar cells, optical coatings, optoelectronic devices and light emitting diodes [3]. Among the II–VI compound semiconductor materials, zincsulfide (ZnS) is a direct transition semiconductor with the widest energy bandgap (3.7 eV) [4] and this wide band gap makes it a suitable material for visible-blind ultraviolet (UV)-light based devices such as sensors and photodetectors [5]. It has high refractive index of 2.35 and wide wavelength pass band (0.4-13μm) [6] and good environmental durability [7]. The binding energy for excitons in ZnS is 40 meV, which is much higher than the thermal energy at room temperature (~ 26 meV) [8], which makes ZnS an ideal candidate for efficient excitonic laser action at room temperature [8]. ZnS is a luminescent material well known for its photoluminescence and electroluminescence, which enable it for wide applications in the fields of displays, sensors, and lasers [9]. It is also widely used in photocatalysis [10]. Properties in nanoforms are significantly different from those of their bulk counterparts and hence, nanocrystalline ZnS attracted much attention in recent years [9].

There has been increasing interest in the field of doped ZnS nanostructures since ZnS has a wide direct band (3.7 eV) gap with a large exciton binding energy (40 meV) [11], [12]. ZnS is widely employed as a host material for both transition metal and rare earth ions [13]. Due to the similar ionic radii and the valence state of the transition metal ions and Zn^{2+} ions, an efficient doping of ZnS with transition metal ions is easily obtained compared to the rare earth ions [14]. Semiconductors doped with rare earth ions are excellent phosphors of high efficiency and low degradation in addition to their unique physical and chemical properties [15]. Even though, it absorbs only UV radiation due to its large band gap, the absorption and emission bands can be altered by suitable doping with metal ions such as Mn, Ni, Cu, Pb, etc [16]. ZnS phosphors have a broad-band luminescence from the near ultraviolet (UV) to the near infrared (IR). When doped with a small amount of metallic ions, it can emit light in the

visible region characteristic of the incorporated impurity [17]. The nature and concentrations of dopants in semiconductor nanoparticles play key roles in the luminescence efficiency and emission bands position. Therefore, investigating the role of dopant concentration of doped semiconductor nanoparticles, which affects the optical properties is very important [11]. Furthermore, the introduction of magnetic elements into nonmagnetic ZnS host lattice can result in the generation of dilute magnetic semiconductors (DMS), which shows interesting magnetic and magneto-optical properties [18].

Experimental details

Pure ZnS film and Dy doped zinc sulfide (ZnS) films are prepared by RF magnetron sputtering technique and the influence of dysprosium (Dy) doping concentration (0, 1, 3, 5 and 7 wt. %) on the structural and optical properties is systematically analyzed.

The mixture of ZnS and dysprosium powder was thoroughly ground for 2 h using an agate mortar and pestle in order to get homogeneous mixing. The thoroughly mixed powder was used as the sputtering target. The depositions were carried out at room temperature inside a vacuum chamber evacuated initially to a base pressure of 3.0×10^{-6} mbar using a diffusion pump and a rotary pump. Pure argon gas was admitted into the chamber and the argon pressure was maintained at 0.1 mbar during the deposition. The target was powered through a magnetron power supply (Advanced Energy, MDX 500) operated at an RF frequency of 13.56 MHz. The films were deposited for a deposition time 30 minutes on quartz substrate kept at a distance of 4 cm from the target using an RF power of 150 W. The as-deposited films thus obtained were used for the structural, morphological and optical characterizations. Structural analysis has been done by XRD and Raman analysis. Optical characterizations of the present films were done by UV-visible spectroscopy.

Results and discussions

The X-ray diffraction data of pure and Dy doped ZnS films revealed polycrystalline nature for all the films. Fig.1(a) and 1(b) shows the XRD patterns of pure ZnS film and 7wt % Dy doped ZnS film respectively. The pure ZnS film shows preferential orientation of crystalline growth along (111) lattice reflection plane of cubic sphalerite phase of ZnS [JCPDS 79-0043]. It is very interesting to notice that XRD patterns of all the Dy doped ZnS films present as mixed phases of cubic sphalerite and hexagonal wurtzite [JCPDS 89-2145]. It can also inferred from the XRD analysis that the intensity of XRD peaks show significant reduction with increase in Dy doping concentration, which indicates that Dy doping in ZnS deteriorates the crystalline quality of RF sputtered ZnS films. The average size of the crystallites in the pure and doped films is in the range 30 nm, which shows the nanocrystalline nature of the developed films.

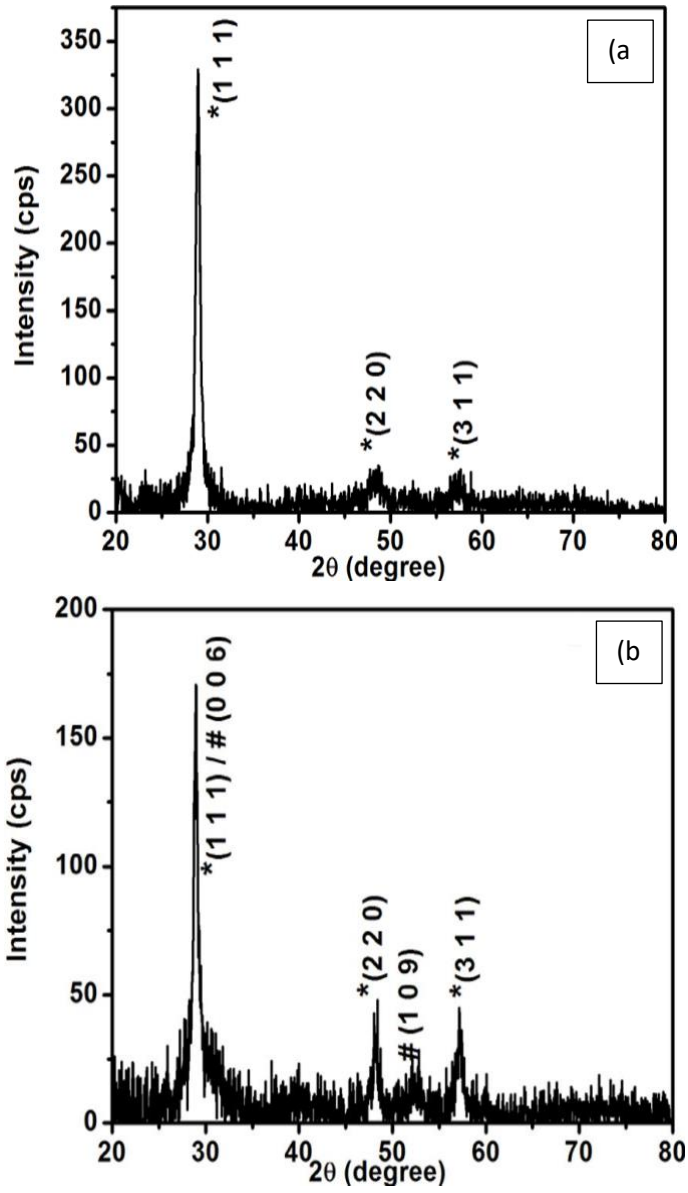

Fig.1 (a) XRD pattern of pure ZnS film, (b) XRD pattern of 7wt % Dy doped ZnS film

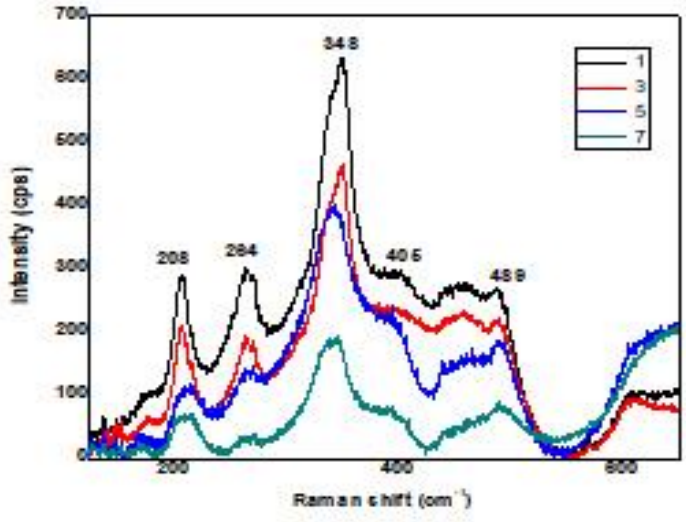

Fig.2. Micro Raman spectra of Dy doped ZnS films

Micro-Raman spectra of the pure and Dy doped ZnS filmsare shown in Fig 2, which shows the characteristic Raman bands of ZnS.

For all the Dy doped ZnS films, a sharp intense band at 348 cm^{-1} was observed and several weak to medium intense bands at 208, 264, 405, 489 and 660 cm^{-1} are also observed. Earlier reports on the Raman studies in ZnS films show that the longitudinal optical (LO) mode and the transverse optical (TO) mode in both cubic and hexagonal phases of ZnS are observed at 350 cm^{-1} and 272 cm^{-1} respectively [19]. Thus, the intense Raman band at 348 cm^{-1} obtained in all the films can be assigned to longitudinal optical (LO) phonon mode and the medium intensity band at 264 cm^{-1} in all the films can be assigned to transverse optical (TO) phonon mode. Raman band observed at 208 cm^{-1} corresponds to first order longitudinal acoustic (LA) mode [20]. Weak and broad Raman band around 405 cm^{-1} present in all the Dy loaded films can be attributed to longitudinal acoustic (LA) overtone [21]. A much broader band observed near 660 cm^{-1} in all the films is associated with the second order LO phonons [19]. Comparatively weak Raman band around 489 cm^{-1} can be due to spectral contributions from quartz substrate.

It can see that the prominent Raman bands observed in the doped films reduces its sharpness and get broadened with increase in Dy doping concentration. This trend of systematic reduction in the sharpness of Raman bands along with the systematic increase in their broadness is attributed to the drop of crystallinity observed in the ZnS film with increase in Dy doping concentration.

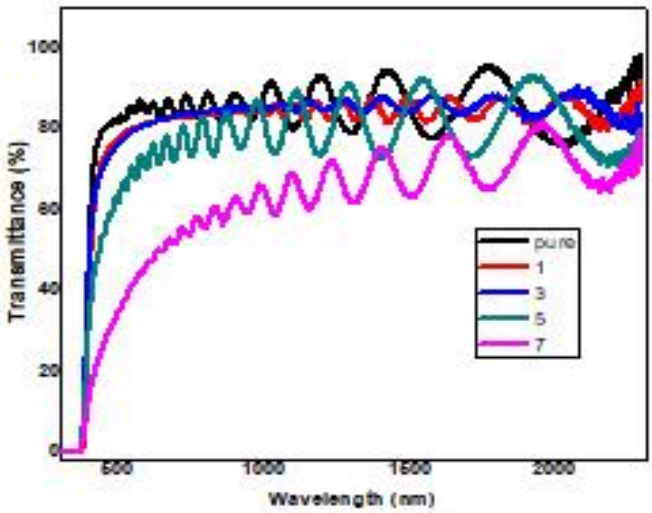

Fig. 3. Optical transmittance spectra of Dy doped

Optical transmittance spectra of pure and Dy doped ZnS films with in the wavelength range 250-2300 nm are recorded using UV-visible spectroscopy and shown in Fig.3. Average value of transmittance of these films in the wavelength regions 400-900 nm and 900-2300 nm were calculated. From this we can inferred that the pure ZnS film exhibit very high transmittance of > 80 % in the visible and near infrared (NIR) regions, whereas all the Dy doped films exhibit lower values for average transmittance than the pure film. It is also noticed that the average value of transmittance shows a trend of systematic reduction with increase in Dy doping concentration throughout the measurement wavelength range (250-2300 nm). The comparatively lower values of transmittance along with its systematic reduction seen in the Dy doped films can be correlated with the deterioration of crystalline nature in the Dy doped films which corroborates the XRD and Raman findings. The observed oscillations in the transmittance spectra of pure and Dy doped ZnS films are mainly due to the interference of light arising from the change in thin film refractive indices and the substrate material.

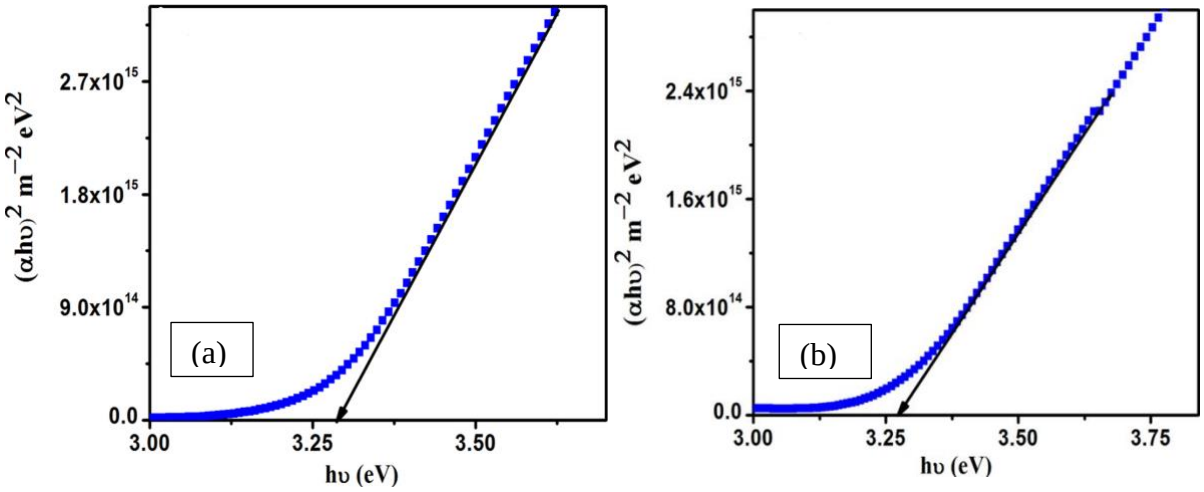

The band gap energy of the films were calculated from the extrapolation of the $\alpha^{1/n}$ v/s hν curve to the energy axis. The best fit is obtained for n=1/2 for all the films, which indicates that the transition in the pure and Dy doped ZnS films are direct allowed. The calculated values of band gap energy are in the range 3.26 eV. Typical Tauc plots of pure ZnS film and 7wt % Dy doped ZnS film are shown in Fig.4(a) and 4(b).

Conclusion

Pure and Dy doped ZnS films were grown by RF magnetron sputtering technique and the effect of Dy doping concentration on the structural and optical properties of ZnS films is studied.

The Dy doping deteriorates the crystalline quality of RF sputtered ZnS films and substantially reduces the average optical transmittance.

References

M. Taherian, A. A. Sabbagh Alvani, M. A. Shokrgozar, R. Salimi, S. Moosakhani, H. Sameie, F. Tabatabaee, Electron. Mater. Lett. 10 (2014) 393–400, http://dx. doi.org/10.1007/s13391-013-3211-2.

K. J. Lethy, D. Beena, V. P. Mahadevan Pillai, K. A. Suresh, J. Nanosci. Nanotechnol. 9 (2009) 1–10, http://dx.doi.org/10.1166/jnn.2009.1156.

G. Nabiyoni, S. Sahrae, M. Toghiany, M. H. Majles Aa, K. Hedayati, Rev. Adv. Mater. Sci. 27 (2011) 52–57

S. Lee, D. Song, D. Kim, J. Lee, S. Kim, I. Y. Park and Y. D. Choi, Effects of synthesis temperature on particle size/shape and photoluminescence characteristics of ZnS:Cu nanocrystals, Mater Lett, 58 (2004) 342-346.

X. Fang, T. Zhai, U. K. Gautam, L. Li, L. Wu, Y. Bando, D. Golberg, ZnS nanostructures: From synthesis to applications, Prog. Mater Sci, 56, 2011, 175-287.

M. D. Himel, J. A. Ruffner and U. J. Gibson, Stress modification and reduced waveguide losses in ZnS thin films, Appl Opt, 27, 1988, 2810-2811.

R. R. Willey, Practical design and production of optical thin films, Marcel Dekker, INC, New York-1996

UV-VIS and Photoluminescence Spectroscopy for Nanomaterials Characterization, C. S. S. R. Kumar, Springer Heidelberg, New York, 2013.

S. Kar and S. Chaudhuri, Controlled Synthesis and Photoluminescence Properties of ZnS Nanowires and Nanoribbons, J. Phys. Chem. B, 109, 2005, 3298-3302

Focus on nanomaterials research, B. M. Karuta, Nova Science Publishers Inc, New York, 2006

W. Q. Peng, G. W. Cong, S. C. Qu and Z. G. Wang, Synthesis and photoluminescence of ZnS:Cu nanoparticles, Opt Mater, 29 (2006) 313-317

A. K. Kole and P. Kumbhakar, Effect of manganese doping on the photoluminescence characteristics of chemically synthesized zinc sulfide nanoparticles, Appl Nanosci, 2, 2012, 15-23.

A. L Donne, S. K. Jana, S. Banerjee, S. Basu and S. Binetti, Optimized luminescence properties of Mn doped ZnS nanoparticles for photovoltaic applications, J. Appl. Phys, 113, 2013, 014903 (1-5).

R. M. K. Whiffen, D. J. Jovanovic, Z. Antic, B. Bartova, D. Milivojevic, M. D. Dramicanin, M. G. Brik, Structural, optical and crystal field analyses of undoped and Mn2p-doped ZnS nanoparticles synthesized via reverse micelle route, j. lumin, 146, 2014, 133-140.

N. Rakov, F. E. Ramos, G. Hirata and M. Xiao , Appl. Phys. Lett., **83** (2003) 272

M. Hafeez, S. Rehman, U. Manzoor, M. A. Khan and A. S. Bhatti, Catalyst driven optical properties of the self - assembled ZnS nanostructures , Phys.Chem. Chem. Phys, 15, 2013, 9726- 9734.

A. N. Yazici, M. Oztas, V. E. Kafadar, M. Bedir and H. Toktamis, .The analysis of thermoluminescent glow peaks of copper doped ZnS thin films after β-irradiation, J. Lumin, 124, 2007, 58-66

A. Goktas and I. H. Mutlu, Room temperature ferromagnetism in Mn-doped ZnS nanocrystalline thin films grown by sol-gel dip coating process, J. Sol-Gel. Sci. Technol, 69, 2014, 120-129.

1M. Lin, T. Sudhiranjan, C. Boothroyd, K. P. Loh, Chemical Physics Letters, 2004, 400 175

A.G. Milekhin, N.A. Yeryukov , L.L. Sveshnikova, T.A. Duda, C. Himcinschi, E. I. Zenkevich and D. R. T. Zahn, Appl. Phys. A, 2012, 107, 275

Q. Xiong, J. Wang, O. Reese, L. C. L. Y. Voon and P. C. Eklund, Nanoletters, 2004, l4 1991

QUANTUM CHEMICAL INVESTIGATIONS OF 2-HYDROXY-1,2-DIPHENYLETHANONE: A DFT APPROACH

M. Jini Pramila [a,b], D. Arul Dhas[b*]

[a]Research scholar, Register Number: 20213112132017, Manonmanium Sundaranar University, Abishekapatti, Tirunelveli – 627 012, Tamil Nadu, India

[b,b]Department of Physics and Research Centre, Nesamony Memorial Christian College, Marthandam – 629 165, Kanyakumari District, Tamilnadu, India*

Abstract

The molecular geometry has been optimized at B3LYP density functional theory (DFT) with the standard 6-31G(d,p)basis set using Gaussian '09 program package. The stability of the molecule arising from hyperconjugative interaction and charge delocalization has been analysed using NBO analysis along with molecular electrostatic potential (MEP) analysis. The HOMO- LUMO energy level pictogram addressed the intramolecular charge transfer (ICT) interaction between donor and acceptor moieties and their impact on the energy gap were determined. The theoretical calculation shows that 2HDE have NLO efficiency. Topological features electron localization function (ELF) and localized orbital locator (LOL) have been also performed. The predicted NLO properties of the title compound are much greater than ones of urea.

Keywords: DFT, NBO, HOMO-LUMO, MEP, NLO.

Introduction

Recently efforts have been made to synthesize optically good quality single crystals because of their application in telecommunication, optical information processing, photonics, optical data storage, opto-electric switches and frequency conversions. Researchers have paid much attention to synthesize materials with high stability and optical non linearity. Organic complexes show higher non linearity in device fabrication but their use is limited because of their poor mechanical and low thermal stability. To overcome these difficulties, a new class of hybrid crystalline framework has been proposed and this type of material show high stability, large nonlinearity and good thermal and mechanical behaviour [1].

Computational techniques

In computational methods, Gaussian 09 software program package is used. The quantum chemical calculations are performed by density functional theory with 6-31G (d,p) basis set. Gaussview 5.0.8 visualization program [2] has been utilized to shape the FMO and MEP analysis. Furthermore, multiwfn software has been used to explain electronic and chemical properties by localized orbital locator (LOL), electronic localized functions (ELF). NBO analysis, polarizability, first and second order polarizability has been evaluated using Gaussian' 09 software package at B3LYP/6-31G (d,p) basis set level.

Result and Discussion

Molecular Geometry

The molecular structure of 2HDE was optimized by the DFT and B3LYP method with 6-31G (d,p) basis set. The bond length, bond angle and dihedral angle of 2HDE molecule were listed in Table.1, while the optimized structures with numbering of atoms are shown in Fig.1. The experimental data for 2HDE is correlated with the XRD data. In the phenyl ring of 2HDE, the C-C bond distance of ring varies in the narrow range 1.393-1.405 A°. In 2HDE, O_1-H_{25} bond length (0.967A°) is increased due to the influence of intermolecular C_7-H_{18}…O_2 hydrogenbonding interaction. The bond length C_4-C_7 (1.489A°) and C_4-C_8 (1.533A°) have altered due to the influence of electronegative oxygen atom attached in the C_3 position. In addition, the C_{16}-H_{21} bond length is decreased in phenyl ring due to the possibility of intermolecular C_{16}-H_{21}…O_2 hydrogen bonding interaction.

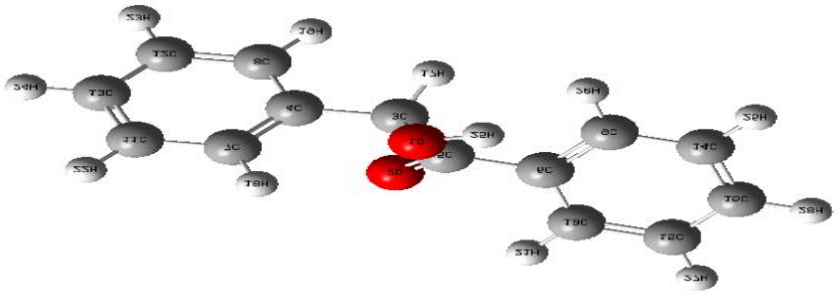

Fig.1 Optimized structure of 2HDE

Natural bond orbital (NBO) analysis

Natural bond orbital analysis provides an efficient method for studying intra and intermolecular bonding and interaction among bonds. Investigation of charge transfer, conjugative interaction and hydrogen bonding in molecular system is efficiently provided by NBO analysis. The donating tendency from electron donors to electron acceptors is reflected by the $E^{(2)}$ values, the larger is the $E^{(2)}$ the more intensive in the interaction [3].

In the present study, the NBO analysis has been performed using Gaussian 09 program at the DFT/B3LYP level in order to understand the filled orbital of one subsystem and vacant orbital of another subsystem, which is a measure of delocalization. The weakening of O_3-H_{19} bond is

due to the rehybridization which is revealed by low ED (0.031e) in the σ*(O_3-H_{19}) orbital. The interaction between lone pair $n_1(O_1)$ and it's antibonding σ*(C_{17}-H_{18}) show the existence of C_7-H_{18}…O_1 intramolecular hydrogen bonding interaction, which has the stabilization energy 8.124 kJ/mol.

Table:2 Possible hydrogen bond interactions

Donor NBO(i)	E.D(e)	Acceptor NBO(j)	E.D(e)	$E^{(2)}$ $kJmol^{-1}$	H..O	D-H (A°)	H…A (A°)	D…A (A°)	D-H…A(°)
$n_1(O_1)$	1.93214 -0. 4014	C_7-H_{18}	0.03024 0.4547	8.124	$Sp^{1.00}$	1.853	0.952	2.480	56.0

Frontier molecular orbital analysis

Energies of HOMO and LUMO orbitals play a crucial role in quantum chemistry, along with photonic and electrical properties. HOMO-LUMO separation in conjugated compounds is the consequence of a considerable degree of inter and intramolecular charge transfer (ICT) from the end-capping electron-donating group to competent electron-accepting group through the π-conjugated pathway [4]. The HOMO and LUMO energy gap was calculated at the B3LYP/6-31G(d,p) level, which reveals that the energy gap reflects the NLO activity of the molecule. The simulated FMO's were depicted in Fig.2, in which a green colour lobes represent the positive charge that is mainly HOMO orbitals whereas red colour lobes represent the negative charge that is LUMO orbitals. The distribution of HOMO and LUMO over the majority of the atoms of the molecular system suggested that the charge transfer takes place within the molecule. The smaller energy gap between the HOMO and LUMO orbitals suggested ease of transition among these orbitals which leads to the high reactivity of the compound.

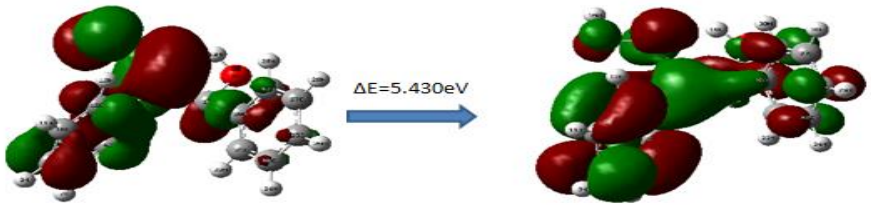

Fig 2: -Frontier molecular orbitals plot for 2HDE

Molecular electrostatic potential (MEP) analysis

The molecular electrostatic potential mapping has been visualized by using Gaussview 5.0.8 software package and the generated map was illustrated in Fig 3. This analysis helps to predict the electron density, hydrogen bonding interaction, charge transfer, the reactive site for electrophilic and nucleophilic attack and the total electron density for the 2HDE crystal were found between -6.106e^{-2} (red) to 6.106e^{-2}(blue) [5]. The spreading of red colour over the oxygen atom confirms the presence of C-H…O interaction present in the molecule. Hence the presence of effective charge transfer interaction present in the molecule was confirmed and this makes the material be an effective candidate in NLO devices.

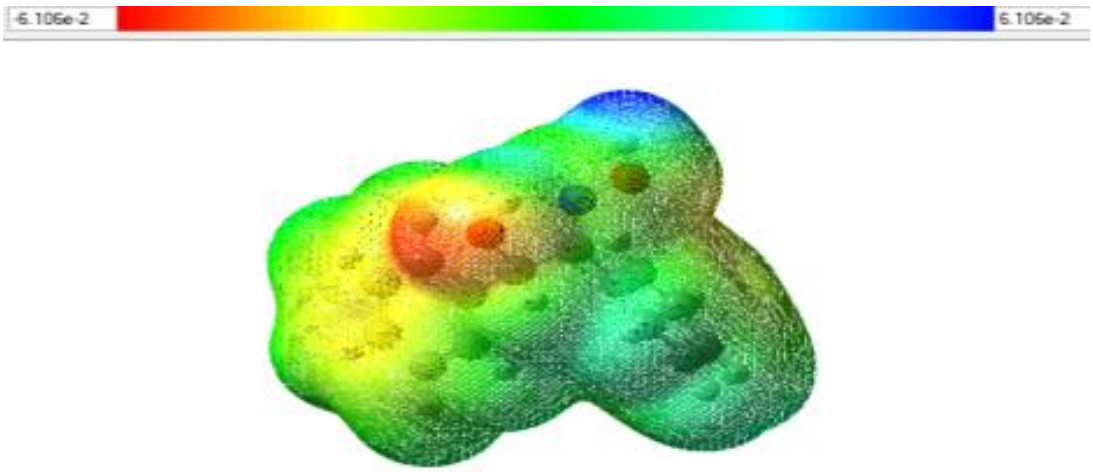

Fig. 3 MEP plot of 2HDE

Electron localization function (ELF) analysis

In this investigation, we investigate the value of ELF based on Pauli repulsion theory which results in the excess of kinetic energy density. Important information about the molecules such as chemical structure, reactivity and molecular bond is obtained through the analysis of the ELF, which has been widely used for the quantitative analysis of aromaticity. The ELF value ranges from 0 to 1. When Pauli repulsion is 1, that region is called maximum Pauli repulsion and represented by red colour whereas the value of ELF is 0, that region is called minimum Pauli repulsion and showed in blue colour [6]. The maximum Pauli repulsion resembled to well localized electrons, whereas minimum Pauling repulsion resembled to the delocalized electron and we can investigate with atomic shell, chemical bonds and lone pairs. ELF analysis gives the vital data of the chemical structure, molecular bonding and reactivity with vital use of quantitative analysis of aromaticity. The high value of ELF was represented by red colour, the middle ELF value represented by yellow to green colour and the lowest value of ELF is represented by blue colour.

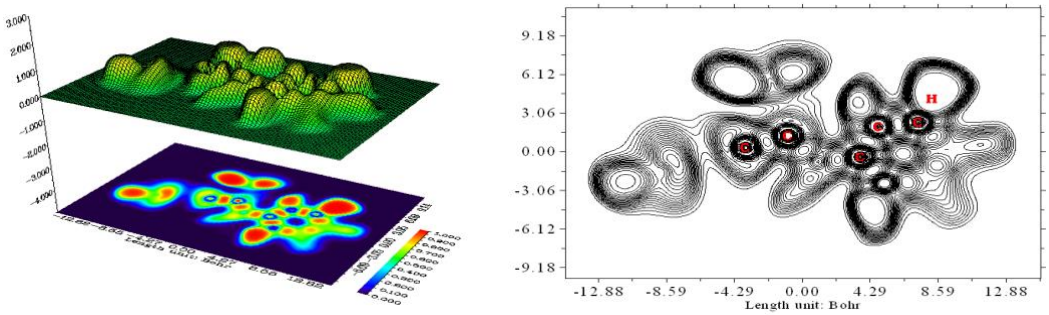

Figure: -4 ELF colour filled map and contour map

Localized orbital locator (LOL) analysis

The localized orbital locator (LOL) was similar to electron localization function (ELF), that originates on the basis of electron pair density while LOL originates when the localized orbitals overlap resulting in high gradients that indicate localized orbitals [7]. The colour filled LOL map with surface projection and contour map of 2HDE was depicted in Fig.5. The LOL map was plotted in the range 0.0 to 0.8, in which the highest LOL value was indicated by red colour while the low LOL value by blue colour, representing the highest localized bonding and nonbonding electrons and delocalized electron cloud respectively. The path of the topological critical points in 2HDE was illustrated by green coloured region. The appearance of white colour existing in the central part of hydrogen atoms indicates that the electron density was higher than the scaling limit (0.8). The covalent region was mainly located between carbon – carbon atom and few between carbon – oxygen atoms, indicated by the presence of red colour.

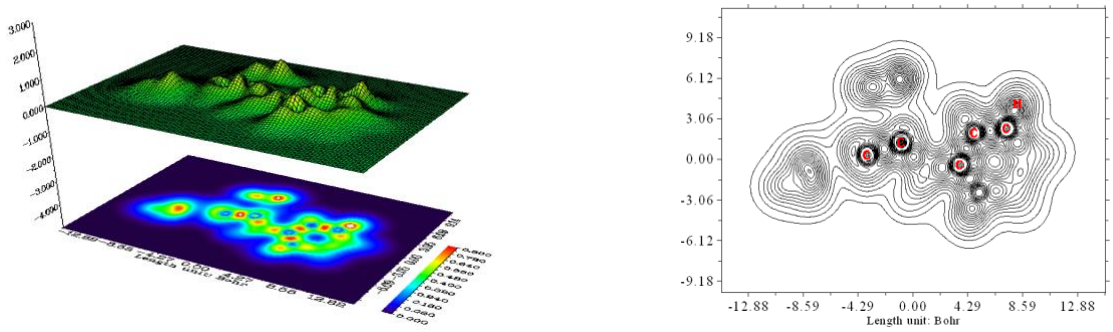

Figure: -5 LOL colour filled map and contour map

NLO analysis

Nonlinear optics corresponds to optical phenomena involving intense electric field and playing an important role in many field of application such as medicine, optoelectronics, and telecommunication [8]. For the title compound, polarizability and first hyperpolarizability are 1.36×10^{-23} esu and 3.214×10^{-30} esu and the first hyperpolarizability is 10 times that of the standard NLO material urea. The second order hyperpolarizability is found to be 32.14×10^{-36} esu. The higher values of dipole moment, molecular polarizability and hyperpolarizabilities are important for NLO applications. From these theoretical results, it can be observed that 2HDE molecule can be used as a good non-linear optical material.

Conclusion

Optimized structural parameters of 2HDE was calculated and compared with experimental data. The C_{16}-H_{21} bond length was shorter than the expected value, which is due to the influence of C_{16}-H_{21}…O_2 hydrogen bonding interaction. The calculated HOMO and LUMO energies authenticate the charge transfer occurs in the molecule when it is excited. The MEP shows the negative potential sites on electronegative oxygen atoms as well as the positive potential sites are around the hydrogen atom. The various types of intramolecular electron interactions and their stabilization energies were determined by NBO analysis. The first and second hyperpolarizability value calculated was about 3.214×10^{-30} esu and 32.14×10^{-36} esu. The calculated values were compared with non-linear optical material urea, the title compound was 10 times higher. The high value of first and second hyperpolarizability shows that the title compound can be used as a new material in non-linear optical studies.

References

S. Sindhusha, C.M. Padma, B. Gunasekaran, H. Marshan Robert, Structural, optical and thermal analysis of creatininium borate e A new semi organic nlo single crystal, Journal of Molecular Structure 1209 (2020) 127981.

A. Frisch, A.B. Nielsen, A.J. Holder, Gaussview User's Manual, Gaussian Inc., Pittsburg, PA, 2000.

Jeyavijayan S and Arivazhagan M, Indian J Pure and Applied Phys 48 (2010) 869.

Shashi Janeoo, Reenu, Amandeep Saroa, Rakesh Kumar, Harminder Kaur, Computational investigation of bioactive 2,3-diaryl quinolines using DFT method: FT-IR, NMR spectra, NBO, NLO, HOMO-LUMO, transitions, and quantum-chemical properties, J. of molecular structure, 1253 (2022) 132285.

Abdul-Malek S. Al-Tamimi, Y.Sheena Mary, Hanan M. Hassan, K.S. Resmi, Ali A. El-Emam, B. Narayana, B.K. Sarojini, Study on the structure, vibrational analysis and molecular docking of fluorophenyl derivatives using FT-IR and density functional theory computations, J. Mol. Struct. 1164 (2018) 172–179.

Olfa Noureddine, Sofian Gatfaoui, Silvia Antonia Brandan, Abir Sagaama, Houda Marouni, Noureddine Issaoui, Eperimental and DFT studies on the molecular structure, spectroscopic properties, and molecular docking of 4-phenylpiperazine-1-ium dihydrogen phosphate, 1207(2020) 127762.

Seema S. Khemalapure, Vinay S.Katti, Chidanandayya S. Hiremath, Suthir M. Hiremath, Mahantesha Basanagouda, Shivaraj B.Radder, Spectroscopic (FT-IR, NMR and UV-Vis), ELF, LOL, NBO, and Fukui function investigations on (5-bromo-benzofuran-3-yl)-acetic acid hydrazide (5BBAH): Experimental and theoretical approach, J. Mol.Struc., 1196 (2019) 280-290.

G. Rajasekar, G. Maheshwaran, N. Swarna Sowmya, A. Bhaskaran, R. Mohan Kumar, S. Jayavijayan, M. Krishna Kumar, S. Sudhakar, Studies of crystal growth, structural, spectral, and optical properties of solution grown 2-phenylethylaminium p-nitrophenolate monohydrate single crystals for efficient nonlinear optical applications, J. Mol. Struct. 1225 (2021) 129304.

INVESTIGATIONS ON THE STRUCTURAL, OPTICAL AND DIELECTRIC PROPERTIES OF $LaMnO_3$ AND $La_{0.5}Sr_{0.5}MnO_3$

Sandhya Suresh[1], Kavitha V T[1, 2 *]

[1]Post Graduate and Research Department of Physics, Mahatma Gandhi College, Thiruvananthapuram-695004, Kerala, India.
[2]NSS College for Women, Thiruvananthapuram-695040, Kerala, India.
Corresponding author E-mail: kavithavasant@gmail.com

Abstract

Rare earth manganite perovskite oxides exhibit ostensible electrical, optical and magnetic properties. In this study, pure and strontium-doped lanthanum manganites were obtained by the solution combustion method using metal oxides and nitrates as oxidants and citric acid as the fuel. XRD results confirmed the rhombohedral structure of lanthanum manganite ($LaMnO_3$) and lanthanum strontium manganite ($La_{0.5}Sr_{0.5}MnO_3$). The FTIR spectra of the synthesized samples clearly show the MnO_6 octahedral bond of the perovskite structure. SEM micrographs reveal the porous structure of synthesized samples. UV-Visible absorption spectra show increased absorbance as a result of Sr ion doping in the host lattice. From Tauc's plot, bandgap values were obtained as 1.4 eV and 2.4 eV for $LaMnO_3$ and $La_{0.5}Sr_{0.5}MnO_3$ respectively. The frequency dependant dielectric properties such as dielectric constant, dielectric loss, loss tangent, ac conductivity and capacitance were studied using broad band dielectric spectrometer (BDS) at room temperature.

Key words: Combustion synthesis, perovskites, dielectric study

Introduction

Perovskite nanomaterials show promising and potential properties due to excellent storage characteristics and these group exhibiting unusual magnetic properties. The $LaMnO_3$ and $La_{0.5}Sr_{0.5}MnO_3$ belongs to the perovskite family of compounds which are formulated as AMO_3.Lanthanum manganite, which is an electrical insulator and an A-type antiferromagnet. It is the main compound of several important alloys, termed as rare-earth manganite's or colossal magneto resistance oxides [1]. Perovskite like Lanthanum Manganite is an interesting material for application in solid oxide fuel cells (SOFC) due to chemical and thermal stability, mechanical strength and high electrical conductivity [2]. Present study focused on the synthesis and optical, dielectric characterizations of $LaMnO_3$ and $La_{0.5}Sr_{0.5}MnO_3$

Experimental Procedure

Lanthanum manganite ($LaMnO_3$) and lanthanum strontium manganite ($La_{0.5}Sr_{0.5}MnO_3$) nano powders were synthesized through the solution combustion method. Lanthanum oxide (La_2O_3), strontium nitrate $Sr(NO_3)_2$ and manganese nitrate tetrahydrate ($Mn(NO_3)_2.4H_2O$) were used as the oxidisers and citric acid is used as the fuel.

Characterizations

The powder XRD analysis was conducted to determine the purity, structure and crystalline size of the $LaMnO_3$ nanoparticles. The XRD patterns were recorded using a D8 Advance Bruker X ray diffractometer equipped with a CuK_α radiation source. Samples were scanned over 2θ range from 10° to 90°.. FTIR was recorded by using Thermo Nicolet Avatar360. The surface morphology was analysed using high resolution scanning electron microscopy(Hitachi,S-3400N). The optical absorption was characterized by using UV-Visible absorption spectroscopy in the wavelength range 200 to 1200nm. The dielectric properties of the samples are observed by Broad band Dielectric Spectrometer (BDS) (NOVOCONTROL Technologies GmbH & Co. Germany Model: Concept 80) at room temperature.

Results and Discussion

XRD Analysis

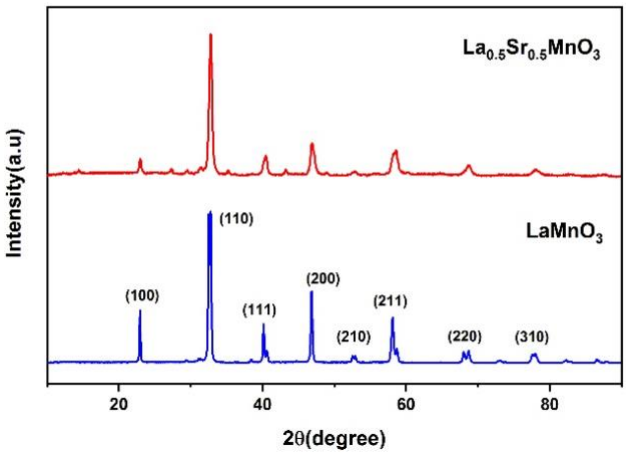

Fig 1. XRD pattern of $LaMnO_3$ nanoparticles

The Powder XRD pattern of LaMnO3 and La0.5Sr0.5MnO3 nanoparticles are shown in fig:3. XRD results have proved that synthesized materials were formed in rhombohedral perovskite structure and is in agreement with PCPDF-00-50-0298 and PCPDF-00-50-0308. The sharp distinct peaks remarked good crystallinity of the synthesized nano powders. The crystalline size of the prepared samples was calculated with Scherrer equation and the obtained crystalline sizes of LaMnO3 and La0.5Sr0.5MnO3 is about 30nm and 17 nm respectively.

FTIR Analysis

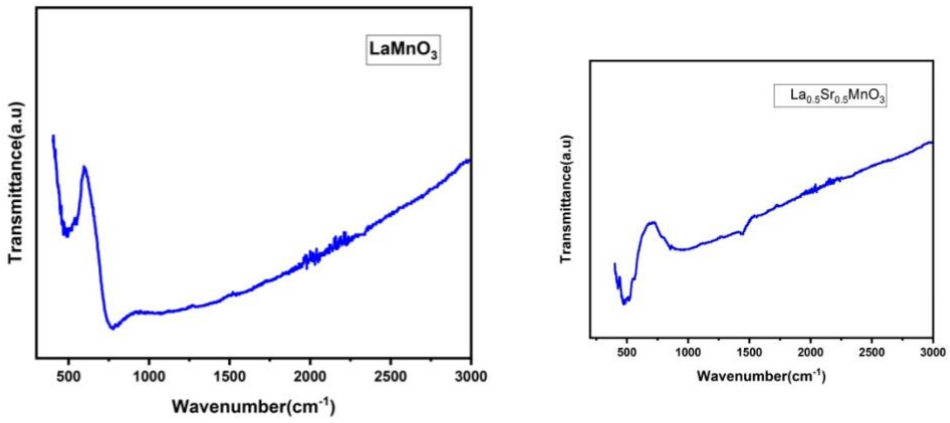

Figure: u2. FTIR spectrum of $LaMnO_3$ and $La_{0.5}Sr_{0.5}MnO_3$ nanoparticles

Fig 2. displays the infrared spectra of the synthesized nanoparticles calcinated at 800°C. The obtained peak in the 500- 600 cm^{-1} range is allotted to the stretching mode, which involves the internal motion of a change in Mn-O-Mn bond length [3]. This is an indication that the metal-oxygen (m-o) bonds are subsequently organized into a MnO_6 octahedral structure, representing the formation of crystalline $LaMnO_3$ and $La_{0.5}Sr_{0.5}MnO_3$ nano powders containing the perovskite structure.

SEM Analysis

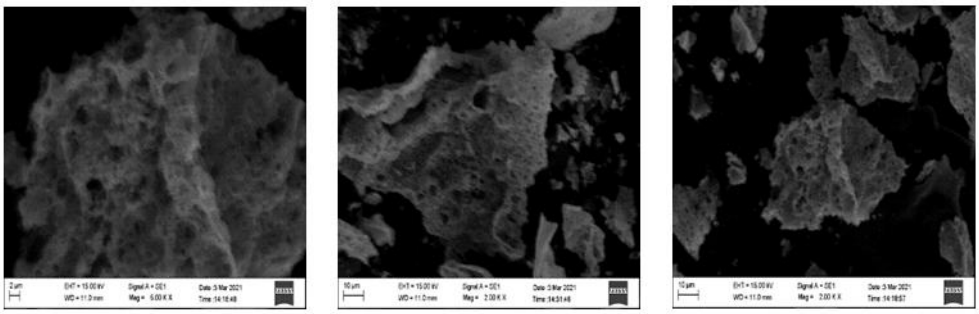

Fig 3. $LaMnO_3$

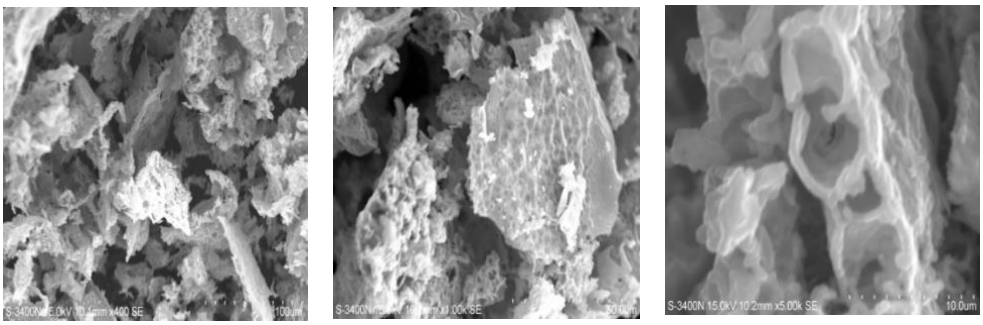

Fig4. $La_{0.5}Sr_{0.5}MnO_3$

SEM micrograph fig 3. and fig 4. of $LaMnO_3$ and $La_{0.5}Sr_{0.5}MnO_3$ sample shows that the synthesized powder has spongy structure, fine primary particles forming agglomerates with different shapes [4]. Also, the synthesized samples show voids, might be due to escaping large number of gases during combustion.

UV-VIS Spectra Analysis

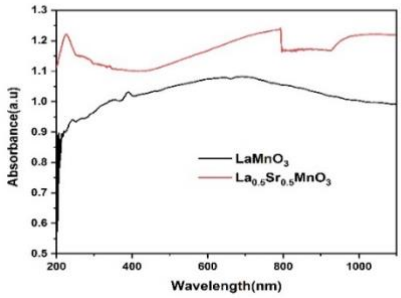

Fig 5. Absorption spectra

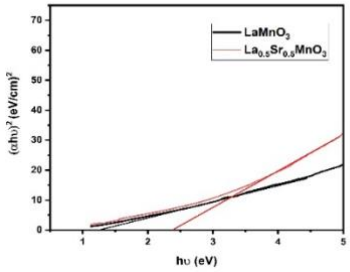

Fig 6. Tauc's plot

The optical absorption Spectra of $LaMnO_3$ and $La_{0.5}Sr_{0.5}MnO_3$ are shown in fig 5. The synthesized nano perovskites possess good optical absorbance in the wavelength range 200-1000nm. The optical bandgap E_g is shown in fig 6.. The obtained bandgap of $LaMnO_3$ and $La_{0.5}Sr_{0.5}MnO_3$ nano powders were found to be 1.4eV and 2.4eV respectively. The increase in band gap is due to the Burstein- Moss effect. The refractive index of the sample is calculated using moss relation and its values are 2.87 and 2.50 respectively

Dielectric Studies

Fig 7. (a) shows the variation of dielectric constant of $LaMnO_3$ and $La_{0.5}Sr_{0.5}MnO_3$ with frequency at room temperature. As frequency increases, the dielectric constant rapidly decreases and then remains constant. The sudden decrease is due to the space charge polarization effect [5]. Figure 8(b) shows the variation of dielectric loss with frequency. The

dielectric loss decreases exponentially as the frequency increases and attain constant at higher frequencies. The energy dissipation factor tan δ is shown in figure 8(c) is caused by the domain wall resonance. From the figure it is clear that tan δ decreases with increase in frequency. Figure 8(d) represents the frequency response of ac conductivity. As frequency increases, the ac conductivity increases due to bound carriers trapped in the sample and the flat response in low frequency region may be attributed the dc part of conductivity. The variation of capacitance with frequency is shown in figure 8(e). In the low frequency region capacitance is high and it decreases with increase in frequency.

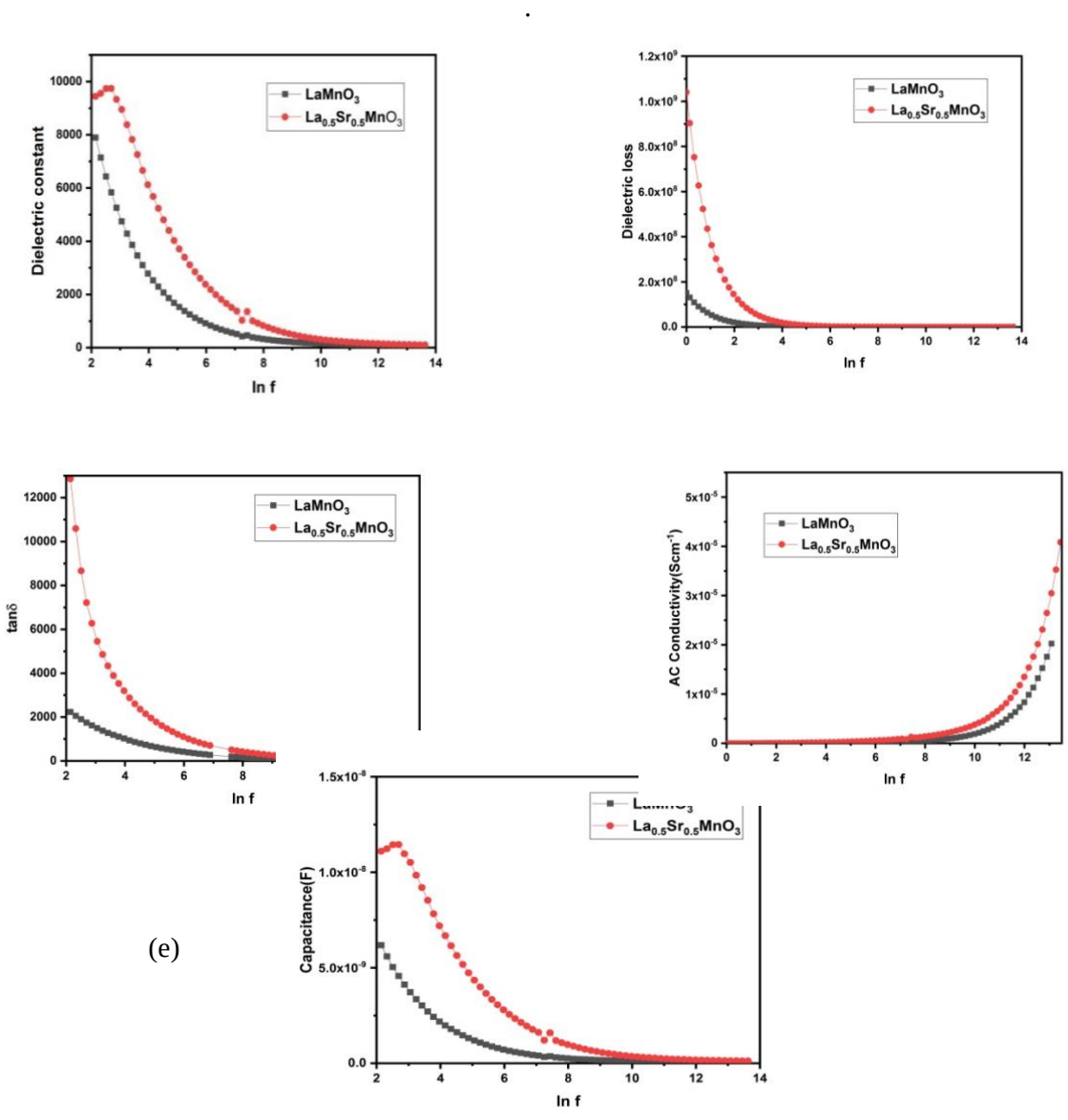

(e)

Fig 7. Variation of (a) dielectric constant, (b) dielectric loss (c) loss tangent (d) AC conductivity and (e) capacitance of $LaMnO_3$ and $La_{0.5}Sr_{0.5}MnO_3$ nanoparticles with function of frequency

Conclusion

The XRD results confirmed the formation of rhombohedral perovskite structure of the synthesized samples. FTIR analysis illustrates the perovskite structure of Mn-O stretching bond. Direct band gap value of 1.4 eV and 2.4eV were obtained using Tauc Model and this band gap is very much suitable for solar cell applications. Increase in band gap is observed due to Sr ion doping. The BDS analysis clearly explains the behavior of $LaMnO_3$ and $La_{0.5}Sr_{0.5}MnO_3$ nanoparticles with frequency. The material possess comparatively high value of dielectric constant and it decreases with increase in frequency. Moreover, its ac conductivity increases with Sr ion content and also it increases with increase in frequency.

References

S.Gong, B.G.Liu,Electronic energy gaps and optical properties of $LaMnO_3$, Phys.Lett.Sect.A Gen.At. Solid State Phys.375(2011)1477-1480, https://doi.org/10.1016/j.physleta 2011.02.027

C, Ma, W, Ren, L.Wang, J, Xu, A, Chang, L Bian, Structural, optical, and electrical properties of (Mn1.56Co0.96Ni0.4804)1-x(LaMnO3)x composite thin films, J, Eur. Ceram. Soc.36(2016) 4059-4064.https://doi.org/10.1016/j.jeurceramsoc 2016.06.019.

T. Ha, T.Huong, H.Nam, N.Hai, C.Viet, Results in Physics Sr doped LaMnO3 nanoparticles prepared by microwave combustion method: A recyclable visible light photocatalyst,ResultsPhys.19(2020)103417.https://doi.org/10.1016/j.rinp.2020.103417

V.A Khomchenko, D.A.Kiselev, J.M. Vieira, L Jian, A.L.Kholkin, A.M.L.Lopes, Y.G.Pogorelov, J.P.Araujo, M.Maglione, Effect of diamagnetic Ca, Sr, Pb, and Ba substitution on the crystal structure and multiferroic properties of the BiFeO3 perovskite, J.Appl.Phys.103(2008). https://doi.org/10.1063/1.2836802.

N Özbay, RZY Şahin-Preparation and characterization of $LaMnO_3$ and $LaNiO_3$ perovskite type oxides by the hydrothermal synthesis method - AIP Conference Proceedings, 2017 - aip.scitation.org

STRUCTURAL INVESTIGATION, CHEMICAL REACTIVITY, RDG, NBO, NLO, AND CHARGE ANALYSIS OF 2-PYRAZINECARBOXYLIC ACID

Sukanya R[1, 2], D. Aruldhas[2*]

[1] Register No: 20213112132018, Manonmaniam Sundaranar University, Tirunelveli.

[2]Department of Physics & Research Centre, Nesamony Memorial Christian College, Marthandam-629165, TamilNadu, India.

**corresponding mail id : aruldhas@nmcc.ac.in*

Abstract

The theoretical analysis of 2-pyrazine carboxylic acid (2PCA) are detailed in the present study. The B3LYP method with a 6-311G (d, p) basis set was used to obtain the optimal structure. The MESP recognizes the nucleophilic and electrophilic regions about inter and intra-non-covalent interaction. The interactions between donor and acceptor are revealed by natural bond orbital analysis. The natural bond orbital (NBO) analysis enabled in comprehending the stability and charge delocalization in the title molecule. Nonlinear optical (NLO) behavior of the 2PCA compound was investigated by the computed value of the first order hyperpolarizability.

Keywords: DFT, RDG, NBO

Introduction

During past years, there has been a growing attraction towards non-linear optical (NLO) materials because of their emerging applications such as frequency conversion, colour displays, optical switching, optical communications, data storage, dynamic holography etc. Organic aromatic π conjugated compounds have been widely identified as NLO materials due to their distinct structural flexibility, functionality, and featuring enlarged π-electron delocalization interconnection with the donor and acceptor and also frequently consistent with their symmetry properties and inherent intra-molecular charge transmits features compared to the inorganic materials [1].The literature review reveals that there is no detailed study on the chemical, computational and structural calculations for 2-pyrazine carboxylic acid (2PCA) has been performed.

Computational Techniques

All theoretical calculations for the title compound were carried out with Gaussian 09 [2] quantum chemistry program. Gauss view 5.0.8 visualization program has been utilized to shape the FMO analysis. The chemical behavior of the molecules including the strength of the hydrogen bonds are predicted using Bader's Theory of atoms in molecules. The analysis are done using AIMALL program suite [3] which is developed by Todd A Keith, and its molecular graph is visualized by multiwfn [4].

Geometry Optimization

The optimized geometry with atomic numbering scheme for 2-pyrazine carboxylic acid (2PCA) and is shown in figure 1. To compare with experimental data, the optimized parameters of the title compound using DFT/B3LYP method with 6-31G (d, p) basis set are given in table 1. As the theoretical values belong to the isolated molecule in gas phase and the experimental values are attributed to the molecule in solid state. The experimental data agrees well with almost all values.

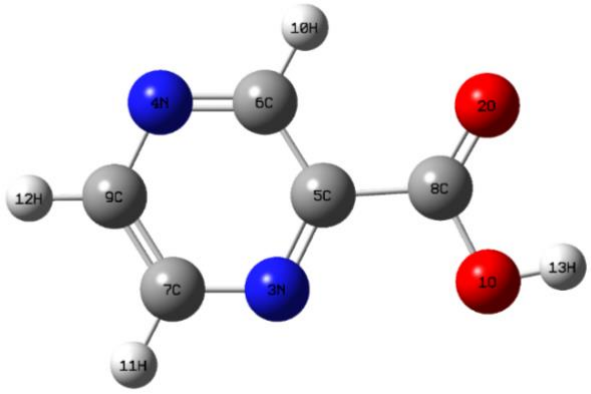

Figure: 1 Optimized molecular structure of 2-pyrazinecarboxylic acid

In 2PCA, the ring reveals that the C-C bond lengths are different, which is confirmed by the presence of hydrogen bonding. In the pyrazine ring, the bond length C_9-N_4(1.342 Å) is increased from the expected value (1.339 Å) [10]. Similarly, the bond length N_3-C_6 (1.345 Å) is increased from the expected value (1.339 Å) [10]. This is due to the attachment of the carbonyl group. C_6-H_{10} bondlength is decreased compared to other C-H bond lengths in 2PCA, this is because of C_6-H_{10}…O_2 hydrogen bonding. From the geometry of bond angle, the pyrazine ring endocyclic angles C_6-N_4-C_8 and C_5-N_3-C_7 are 115.8° and 116.9° respectively. The exocyclic angle of pyrazine ring N_4-C_6-H_{10} and N_3-C_7-H_{11} are 117.1° and 117.2° respectively. The decreased endocyclic and exocyclic angles reveal a high electronegative nitrogen atom present inside the ring.

Table: 1 Optimized bond length, bond angle, and dihedral angle of 2PCA

Bondlength(Å)			**Bond angle(˚)**		
	Expt.	**Calculated**		**Expt.**	**Calculated**
$C_9 – N_4$	1.340	1.342	C_6-N_4-C_8	115.2	115.8
$N_3 – C_6$	1.333	1.343	C_5-N_3-C_7	116.6	116.9
O_2- C_8	1.384	1.368	N_4-C_6-C_{10}	117.7	117.1
$C_6 – H_{10}$	0.940	1.084	N_3-C_7-H_{11}	117.3	117.2

Homo-Lumo analysis

The HOMO represents the ability to donate an electron, LUMO as an electron acceptor represents the ability to obtain an electron. LUMO is located over the entire compound and HOMO is especially located on the pyrazine. HOMO-LUMO transition implies an electron density transfer from pyrazine group to carboxylic group.

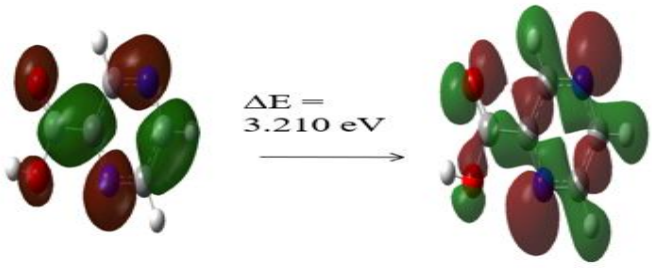

Figure 2

Molecular Electrostatic potential

Molecular electrostatic potential is a tool which gives information about the electrophilic and nucleophilic sites of a molecule. The different values of the electrostatic potential at the surface increases in the order red<orange<yellow<green<blue: red represent most negative and blue represent most positive potential, which was shown in figure 3. The potential surface with red region having the most electrostatic potential, that is electronegative atoms are rich in electrons, blue region with most positive electrostatic potential and green depicts the region of zero potential.

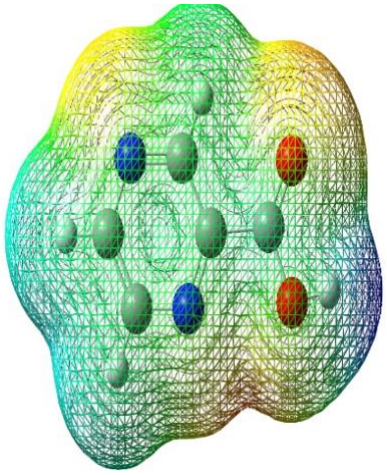

Figure 3: 3D plots of the molecular electrostatic potential [MEP] for 2PCA

Reduced density gradient (RDG) analysis

Reduced density gradient (RDG) is a method to investigate weak interactions. The RDG is calculated by the following relation

$$\mathrm{RDG(r)} = \frac{1}{2(3\pi^2)^{\frac{1}{3}}} \frac{|\nabla\rho(r)|}{\rho(r)^{4/3}}$$

RDG plots against ρ(r), the NCI index can be well organized to identify the noncovalent interaction regions as RDG approaches zero at low level densities. The λ_2 sign is used to differentiate the bonding ($\lambda_2 < 0$) interactions from non-bonding ($\lambda_2 > 0$) interaction [7]. Figure 4 shows the strength of noncovalent interaction and their strengths are point up using colour code: blue implies strong hydrogen bonds and halogen bonds, green for very weak interaction such as van der Waals interaction and red for steric repulsion [8].The peaks or spikes that appear in the 2D scatter plot are associated with the interaction of critical points (ICP). In 2PCA, the peak region -0.01 to 0.01 represent the presence of $O_2\cdots H_{10}$ van der Waals attraction within the molecule. The peak at $(\lambda_2)\rho(r) \simeq 0.02$ in title compound represent C6-$H_{10}\cdots O_2$ intermolecular hydrogen bonding.

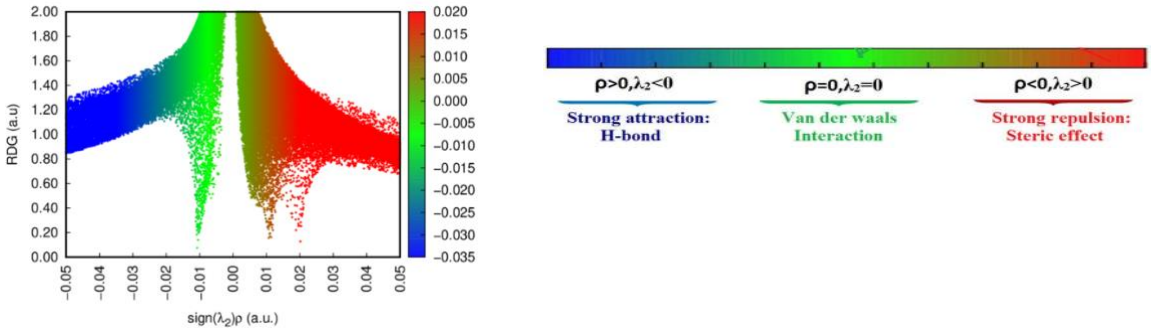

Figure: 4 Plots of the RDG versus the electron density

ELF analysis

The localization of electron in atomic or molecular systems is calculated using the Electron localization function (ELF). It can be defined as the property of the same spin pair density. The difference in kinetic energy density resulting from Pauli repulsion forms the root for measuring ELF. It is a powerful tool to understand qualitatively the behavior of electrons in a nuclei system. Some of its applications include the confirmation of geometry and bond types, explanation of reactions that yield aromatic products [5]. For the 2PCA compound, the red color corresponds to high values of ELF, N-H present in the positive region and it indicates red color. The blue represents the region with the low-end of ELF value. The ELF value present in a positive region shown in Fig 5. The title compound 2PCA having a high value of electron localization function.

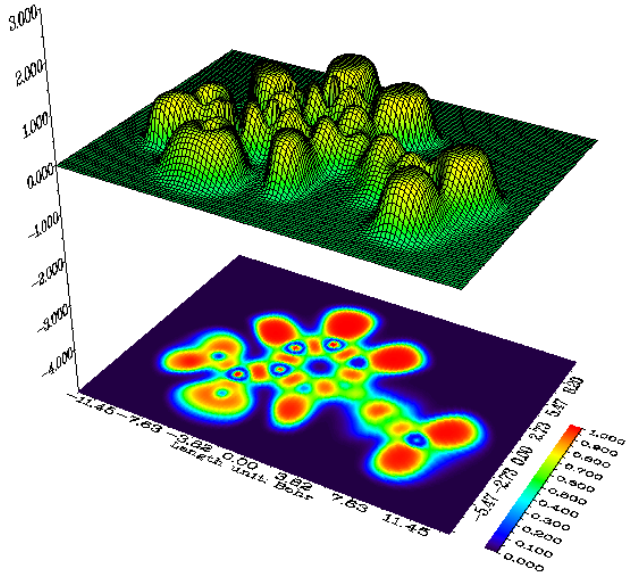

Fig 5 : ELF representation of 2PCA

NBO

The NBO approach of Weinhold and co-workers has been frequently used in the evaluation of the anomeric effect and the origin of internal rotation barrier [7]. The NBO analysis allows estimating the energy of the molecule with the same geometry in the absence of electronic delocalization. It is also used to elucidate the intramolecular, rehybridization and delocalization of electron density within the molecule. The highest E (2) value of 21.19kJ/mol corresponding to C_5-C_8 which indicate the strongest charge interaction. In 2PCA the most intra molecular interaction energy in σ(C_9-C_{10}) bond to antibonding σ*(C_9-C_{12}) leads to the stabilization energy 21.19kJ/mol respectively.

SECOND ORDER PERTURBATION THEORY ANALYSIS OF 2PCA:

Donor	E.D(e)	Acceptor NBO(j)	E.D(e)	E(2)Kjmol
σ(C7-C9)	1.97564 -0.67556	σ*(C5-N3)	0.02134 0.59286	2.77
σ(C5-C6)	1.97452 -0.67321	σ*(N3-C7)	0.02134 0.59286	3.31
σ(C12-C9)	1.97239 -0.59527	σ*(N4-C9)	0.02420 0.58638	2.17
σ(C5-C8)	1.97984 -0.67755	σ*(N4-C6)	0.02913 0.42668	21.19

Nonlinear optical calculation

The relationship between molecular structure and nonlinear optical properties were analysed theoretically by using quantum chemical computational approach and it also provides the way to examine the efficiency of NLO properties of the materials before being synthesized. The charge transfer interactions from donor to acceptor through π conjugated framework and the fabrication of nonlinear optical devices have been related to the higher polarizability values [11-12]. The dipole moment, isotropic and anisotropic hyperpolarizability were calculated as 6.178 Debye, 1.4597×10^{-23} e.s.u and 4.5469×10^{-24} e.s.u. The first and second order hyperpolarizability values were evaluated as 3.4646×10^{-30} e.s.u and 5.0704×10^{-39} e.s.u. These high values depicts that the title compound have efficient contribution in the field of nonlinear optics.

Conclusion

In the present work, the optimized geometric parameters of 2PCA had been theoretically determined using DFT calculations and are compared with the experimental result. The distribution of electrons and the position on the surface of the designated compound were analysed using MEP. Thus, from the above investigations, it can be concluded that syringaldehyde is a good NLO agent and further work can be responsible for NLO activity. It is believed that the results of the current experimental and theoretical investigations could strongly support the development of a new NLO applications.

References:

Elias E. Elemike, Henry U. Nwankwo, Damian C. Onwudiwe, Synthesis and characterization of Schiff bases NBBA, MNBA and CNBA, Heliyon 4 (2018) 00670.

M.J. Frisch, G.W. Trucks, H.B. Schlegel, G.E. Scuseria, M.A. Robb, B. Mennucci, Caricato, X. Li, et al., Gaussian 09, Revision C.01, Gaussian, Inc., Wallingford, CT, 2009.

T.A. Keith, AIMAll (Version 16.10.31); TK Gristmill Software, Overland Park KS, USA (aim.tkgristmill.com), 2016.

T. Lu, F. Chen, Multiwfn: Multiwfn: A multifunctional wavefunction analyzer, J. Comput. Chem. 33 (2012) 580-592.

Michal Hricovini, James Asher and Milos Hricovini, Photochemical anti-syn isomerization around the –N- N=bond in hetrocyclic imines, Rsc Adv., 2020, 10,5540.

A.subashini, C.Arunagiri, M.Saranya, Crystal structure, Hirshfeld surface analysis, PIXEL energy and molecular electronic properties on [2-(2-nitrobenzylidene)-amino naphthalene], Chemical Data Collections,30 (2020) 100549.

Assem Barakat, Hany J. Al-Najjar, Abdullah Mohammed Al-Majid, Saied M. Soliman, Yahia Nasser Mabkhot, ,Journal of Molecular Structure, 2014.

S. Sangeetha Margreat, S. Ramalingam DFT, spectroscopic, DSC/TGA, electronic, biological and molecular docking investigation of 2,5-thiophenedicarboxylic acid: A promising anticancer agent, J.Mol.Structure, 1200, 2020, 127099.

Nyiang Kennet Nkungli and Julius Numbonui Ghogomu, Theoretical analysis of the binding of iron(III) protoporphyrin IX to 4-methoxyacetophenone thiosemicarbazone via DFT-D3, MEP, QTAIM, NCI, ELF, and LOL studies, J Mol Model (2017) 23:200

V. Chis, A. Piranau, T. Jurca, M. Vasilescu, S. Simorn, O. Cozar, L. David, Experimental and DFT study of pyrazinamide, *Chem. Phys.* 316 (2005) 153-163. https://scihub.tw/10.1016/j.chemphys.2005.05.

G. Maroulis, C. Pouchan, Size and electric dipole (hyper) polarizability in small cadmium sulfide clusters: an ab initio study on (CdS)n, n= 1, 2, and 4, *J. Phys.Chem. B* 107 (2003) 10683–10686.

V. Nalla, R. Medishetty, Y. Wang, Z. Bai, H. Sun, J. Wei, J.J. Vittal, Second harmonic generation from the ‘centrosymmetric’ crystals, *IUCrJ* 2 (2015) 317–321.

GROWTH AND CHARACTERIZATION OF BIS(DIAMINOMETHANIMINIUM) PYRROLIDINE-1,2-DICARBOXYLATE SINGLE CRYSTAL

Annusha T L[a], Jebamalar A S[b*]

[a]Research scholar, Register number: 19113112132008, Department of Physics & Research centre, Nesamony Memorial Christian College, Manonmaniam Sundaranar University, Tirunelveli 627012, Tamilnadu, India

[b]Assistant Professor, Department of Physics & Research centre, Nesamony Memorial Christian College, Marthandam 629159, Tamilnadu, India*

Abstract

Single crystal of bis(diaminomethaniminium) pyrrolidine-1,2-dicarboxylate (DP12C) was grown by the slow evaporation technique by using double distilled water at room temperature. Single crystal X-ray diffraction determined that the crystal structure of DP12C as orthorhombic and the lattice parameters are confirmed to be a = 8.3580(4) Å, b = 10.3479(4) Å, c = 15.1833(5) Å, α = β = γ = 90°, Volume V= 1313.17(9) A^3. The optimized geometrical parameters such as bond length, bond angle and dihedral angle of DP12C are computed theoretically by DFT method. Hirshfeld surface (HS) analysis was performed to explore the intermolecular interactions. The optical absorption spectrum of DP12C crystal has been recorded using UV-Visible spectral analysis. The functional groups of the grown crystal were identified and confirmed by Fourier transform infrared spectroscopic study (FTIR) and Fourier transform Raman spectroscopy (FT-RAMAN). The thermal stability of the crystal was investigated by the thermogravimetric- differential thermal analysis (TG-DTA). Vickers micro hardness test was carried out to determine the mechanical stability and the hardness parameters of the crystals. The luminescence property of the grown DP12C crystal was determined by the photoluminescence (PL) spectroscopy.

Keywords: Slow evaporation, crystalline, thermal, luminescence.

Introduction

The nonlinear optic single crystals play a vital role in the area of immense science and technological excellence in various fields. Optical materials with effective nonlinearity have good potential implementations like optical data storage, optical information processing, optical computing and telecommunication. The extended field of nonlinear optical (NLO) applications has stimulated search for the highly nonlinear optical materials [1–3].Organic materials has been of particular interest because of their high order of optical nonlinearity, large electro-optic co-efficient with low frequency dispersion, large nonlinear response over abroad frequency range and large structural diversity. Urea is the organic nonlinear optical material used in the processing of generation and mixing of frequencies in a spectrum including the UV because of its unique properties such as transparency and large birefringence. Lack of large sized optically single crystals prevents the utilization in the NLO applications; moreover growth process is difficult to control. In order to overcome these draw-backs, a variety of dopants like L-alanine, L-valine, L-histidine, etc., have been incorporated for investigation, thereby giving quality bulk single crystals with better properties than pure. Amino acid family crystals are playing an important role in the field of non-linear optical organic molecular crystal. L-proline is a heterocyclic compound that contains secondary amine group which is also a part of pyrrolidine ring, making it rigid and directional in biological systems. L-proline have been used in the investigation of synthesizing various compounds with organic and inorganic salts of L-proline lithium bromide monohydrate [6], dichloro (4-hydroxyl-L-proline) cadmium(II) [7], dichlorobis (L-proline) zinc(II), bis L-proline hydrogen nitrate, L-prolinium trichloroacetate were reported earlier.

Guanidine is a strong base material that easily reacts with all organic acid and gives good quality crystals. The presence of six potential donor sites for hydrogen bonding interactions and a delocalized electron system have made guanidine compounds potentially interesting materials for nonlinear optical applications. Guanidine compounds which shows good nonlinearity are guanidinium 4-hydroxy benzoate, guanidinium tetraflouroborate, bis (guanidinium) hydrogen phosphate monohydrate, guanidinium 3-nitrobenzoate, guanidinium chlorochromate, guanidinium L-glutamate, zinc guanidinium sulphate, guanidinium perchlorate, guanidinium cinnamate and guanidinium propionate have been reported earlier [8]. In the present work, a single crystal of L-proline guanidine carbonate was grown by slow evaporation technique. Based on the analysis of various characterization techniques such as single crystal X-ray diffraction, UV-Visible spectra, Fourier transform infrared spectra (FTIR), thermogravimetry/differential thermal analysis, photoluminescence spectra, Vicker's microhardness test, dielectric analysis, laser damage threshold analysis, Z-scan analysis, the structural, optical, thermal, electrical and its mechanical properties were investigated.

Experimental procedure

Crystallization method

The bis(diaminomethaniminium) pyrrolidine-1,2-dicarboxylate (DP12C) crystals were synthesized from a high purity (2*S*)-pyrrolidine-2-carboxylic acid and bis(diamino me than iminium) bicarbonate taken in 1:1 stoichiometric ratio which was dissolved in 50 ml of double distilled water, stirred for 5 hours in a magnetic stirrer. The saturated solution is filtered in a transparent beaker and covered for slow evaporation without any disturbance at room temperature. The DP12C crystals were collected after 44 days. The harvested crystal is shown in the figure 1.

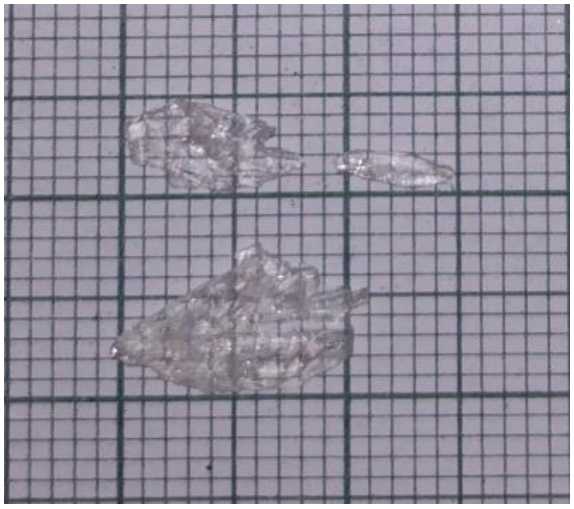

Fig 1. Single crystals of DP12C

Results and discussion

Structural analysis

Single X-ray Diffraction analysis

The crystallographic structural information of the grown single crystals was analyzed by the single crystal diffraction analysis. The grown crystal belongs to orthorhombic non-centro symmetric system with the $P2_12_12_1$ space group. The observed unit cell lattice parameters are a = 8.3580 Å, b = 10.3479 Å, c = 15.1833 Å, $\alpha = \beta = \gamma = 90^o$, Volume V = 1313.17 A^3. The ORTEP diagram of DP12C crystal is shown in figure 2.

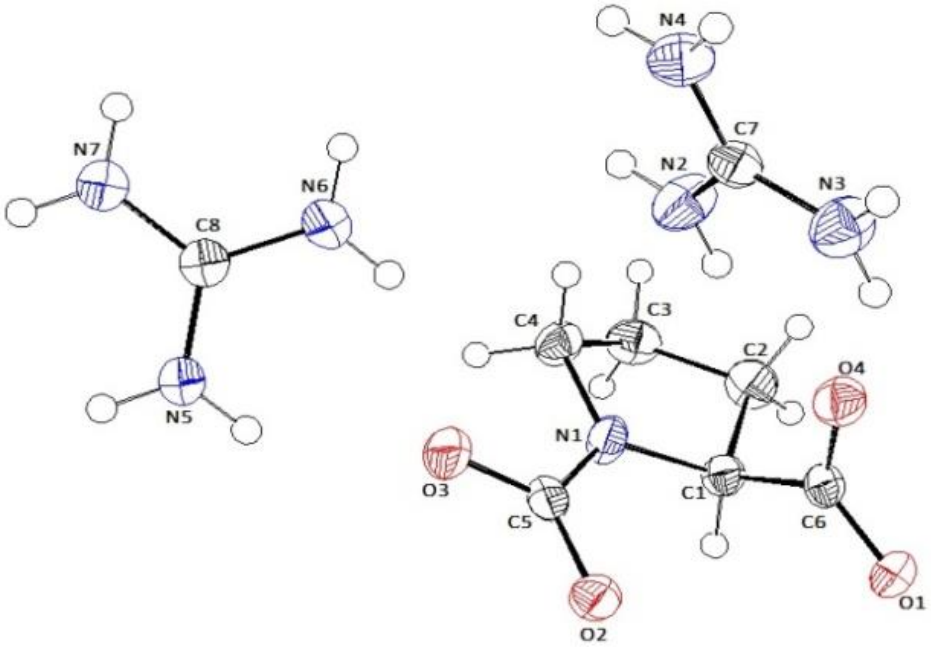

Fig 2. ORTEP diagram of DP12C crystal

Optimized geometry

The grown material comprises a protonated (2*S*)-pyrrolidine-2-carboxylic acid anion and diaminomethaniminium cation and it was observed that the five membered ring anion planar nature. The optimized geometrical parameters such as bond length, bond angle and dihedral angle of DP12C are computed theoretically by DFT method using Guassian 09 B3LYP/6-311++G(d,p) basis set. The obtained theoretical values for C_{12}–N_{14} the calculated bond length value 1.345Å is slightly lower than the experimental value 1.358Å due to the substitution of carboxylate group. For the grown crystal, the bond angle of N_{14}–C_{12}–O_{17} = 118.2º, 113.1º and C_9–N_{14}–C_{12} = 124.9º, 124.3º depicted slight variations between the experimental and calculated value. The dihedral angle for O_{16}–C_{12}–N_{14}–C_1 = -8.1º, -7.5º shows the protonated anion [9].

Hirshfeld surface analysis

Hirshfeld surface (HS) analysis was performed using Crystal Explorer software, version 3.1 to explore the intermolecular interactions. The Hirshfeld surface is plotted over the values of d_{norm} and it was normalized by the van der Waals radius. The d_{norm} represents the internal (d_i–the distance from the nearest nucleus outside the Hirshfeld surface to the surface itself) and the external (d_e–the distance from the nearest nucleus inside the Hirshfeld surface to the surface itself. The Hirshfeld surface mapped across d_{norm} and Shape index, are shown in the figure 4.

In the crystal packing of the grown crystal, the major percentage contribution appears as 46.6% for the H···H interatomic contacts. The percentages of intermolecular contributions

for the various H···H, O···H and N···H contacts to the Hirshfeld surface of the grown crystal are shown in table 1. The two-dimensional fingerprint plot of H···H, O···H, C···H and N···H is shown in the figure 5 [10].

Table 1. Percentages of intermolecular contributions for the grown crystal DP12C

Contact	Percentage contribution %
H···H	46.6%
O···H	17.8%
N···H	6.5%

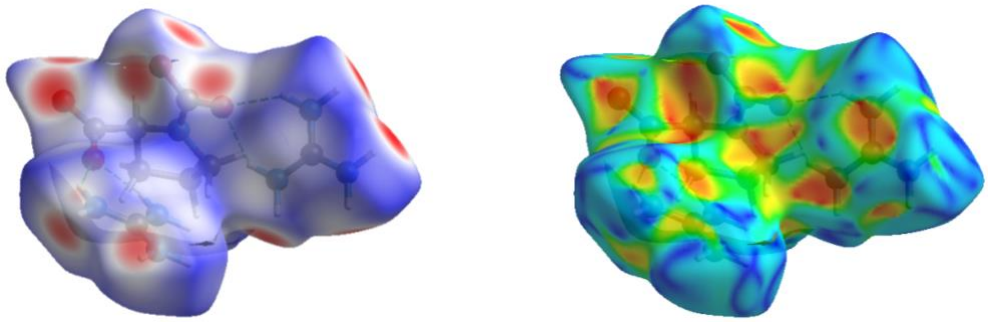

d_{norm} **Shape index**

Fig 4. Hirshfeld surfaces of the grown crystal mapped across (a) d_{norm} , (b) Shape index

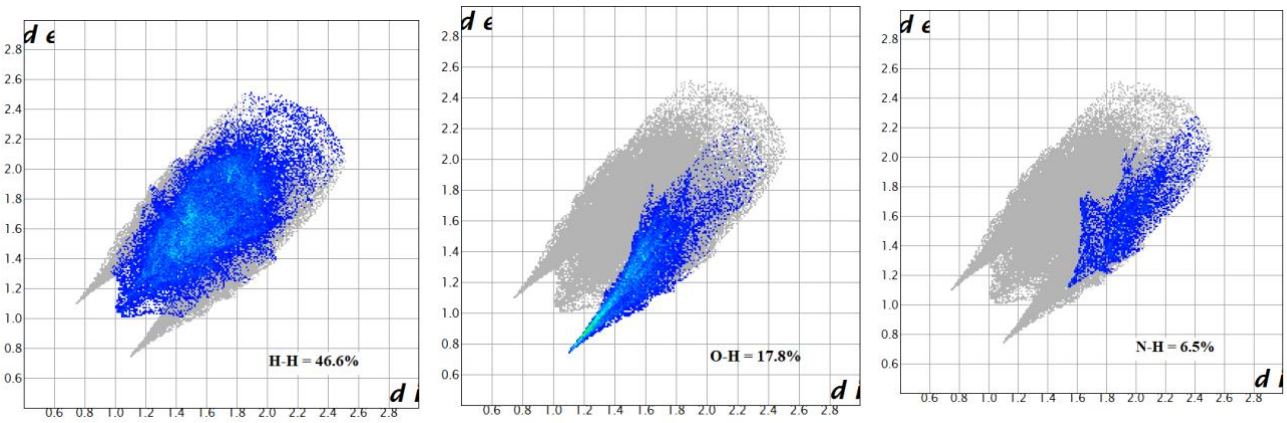

Fig 5. Fingerprint plot of H···H, O···H and N···H interactions

FTIR spectral analysis and FT- RAMAN analysis

Fourier transform infrared spectroscopy was performed in order to understand more concerning the chemical bonds and FT-Raman spectroscopy provides the information about

inter and intra molecular vibrations. The recorded FTIR and FT-Raman spectrum of the grown crystal is shown in the figure 6,7.

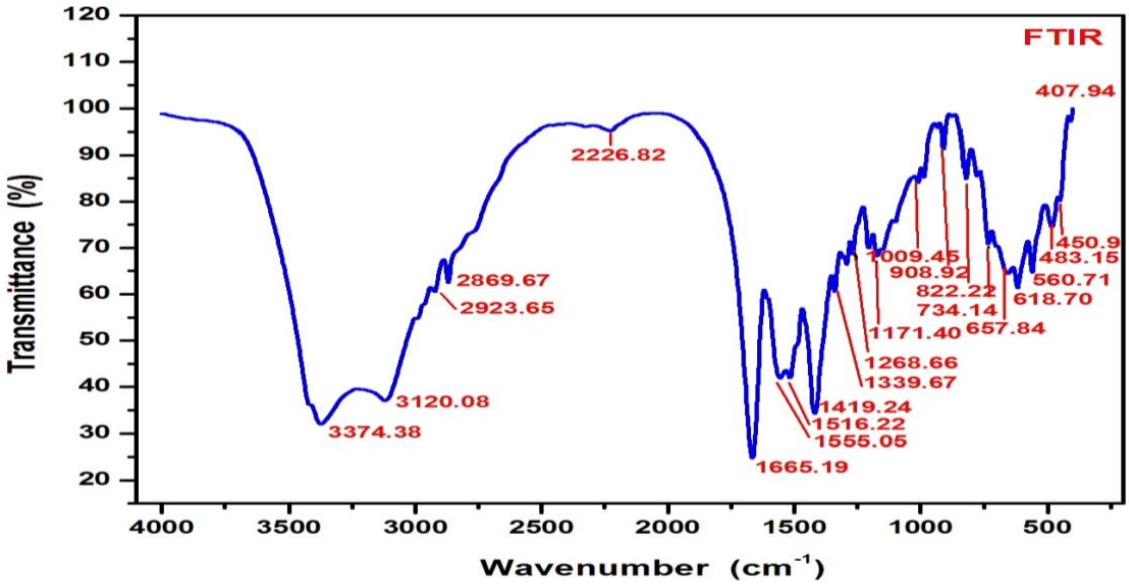

Fig 6. FTIR spectrum of grown crystal

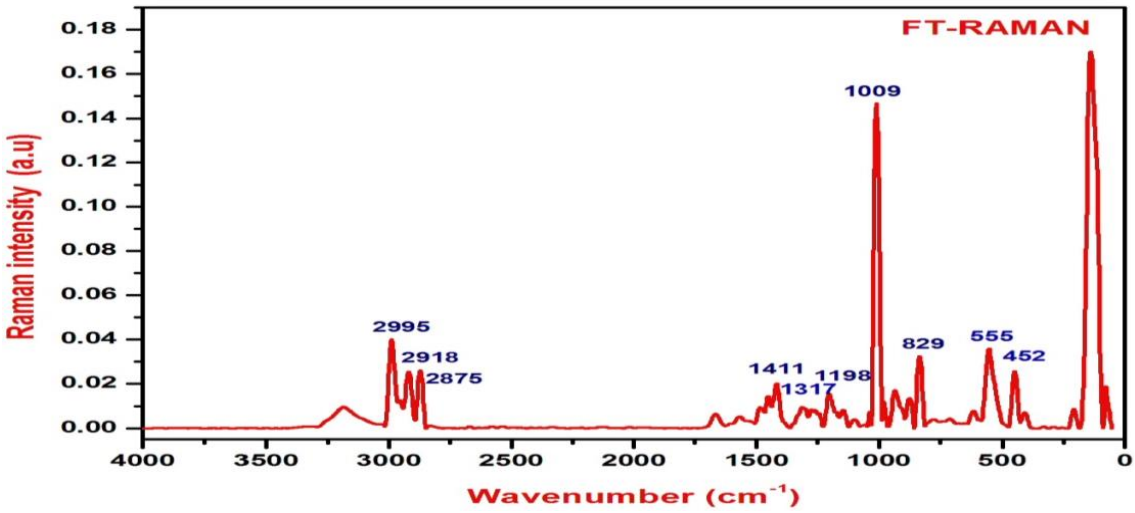

Fig 7. FT-Raman spectrum of grown crystal

The strong symmetric stretching vibration of NH group is observed at 3374 cm^{-1}. The presence of C=N vibration strong band is observed at 1555 cm^{-1}. The obtained carboxylate group of COO^- rocking vibration is observed at 560 cm^{-1}. In case FT-Raman, the band appears at 452 cm^{-1} and 555 cm^{-1} are attributed to rocking NH_2 vibration and O–H stretching vibrations respectively. The peak at 829 cm^{-1} describes the CH_2 stretching vibration.

UV-Visible spectral analysis

The optical absorption spectrum of the DP12C crystals was recorded in the range of 190 – 900 nm shown in figure 8.

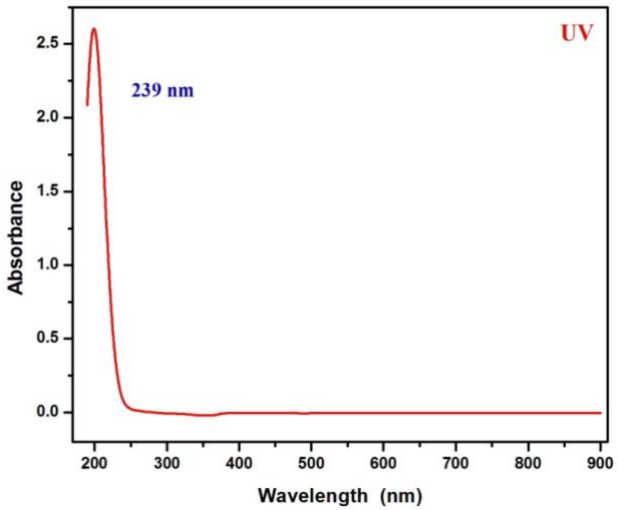

Fig 8. UV-Vis absorption spectrum of grown crystal

The grown DP12C crystal has good transparency in nature. The lower cutoff wavelength is found to be 239 nm which is confirmed to be a predominant material for optoelectronic applications [3].

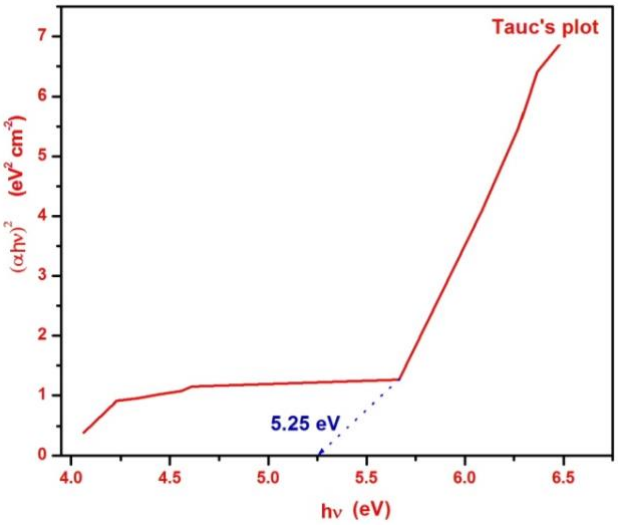

Fig 9. Tauc's plot of grown crystal

The Tauc's plot is drawn between $(\alpha h\nu)^2$ and $h\nu$ is shown in figure 9. The obtained optical energy band gap 5.25 eV denotes that the crystal is a suitable material for optoelectronics applications.

Photoluminescence (PL) analysis

Photoluminescence (PL) spectroscopy deals with the optical properties of the materials at the molecular level and the crystalline quality of the material. For the grown DP12C crystal, the PL spectrum was recorded in the range of 200 - 900 nm is shown in figure 10.

The observed emission spectrum indicated the sharp intense peak occurs at 478 nm in the blue visible region which is a most appropriate candidate for photonic applications [18]. The above results indicate that the grown crystal acts as best material for optical data storage applications.

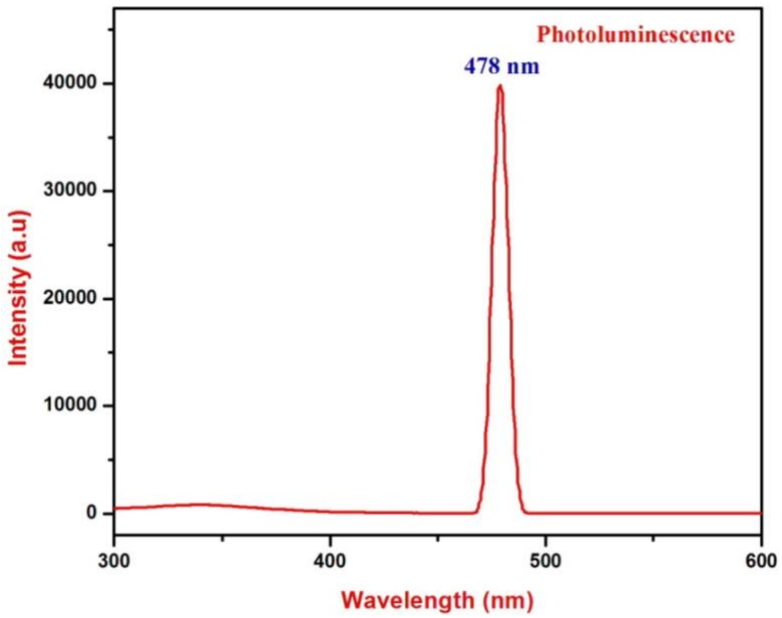

Fig 10. Photoluminescence spectrum of grown crystal

Mechanical analysis

The mechanical property of a grown material was analyzed by using Vicker's microhardness tester indented using diamond indenter. The load of 5 g, 10 g, 25 g and 50 g are applied and indented on a grown crystal at room temperature. The hardness number (H_V) value was estimated by the formula,

$$H_v = \frac{1.8544\ P}{d^2} \quad kg/mm^2 \qquad (9)$$

where,

P = load indented on DP12C in kg,

d = the average diagonal indentation length in mm.

The graph between load applied (P) and Vicker's hardness value (H_v) is shown in the figure 16. It is noted that the hardness value increases when the applied load increases depicted the Reverse Indentation Size Effect (RISE). The work hardening coefficient (n) was determined by using the relation of Meyer's law which is given by,

$$P = A\, d^n \quad (10)$$

$$\log P = \log A + n \log d \quad (11)$$

where,

A= the material constant,

n = work hardening coefficient

.

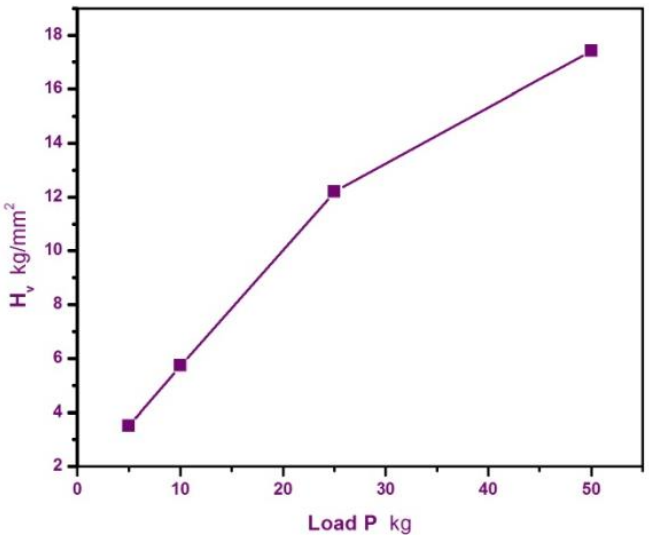

Onitsch and Hannesman suggested the limitations of a material to be a soft material or hard material. The work hardening coefficient (n) between 1-1.6 is for hard materials and above 1.6 will be considered as soft materials [21]. The grown crystal has the work hardening coefficient (n) as 2, it clearly indicates a soft material. From the Wooster's empirical formula, the expression for the yield strength (σ_y) and elastic stiffness constant (C_{11}) can be written as,

$$\sigma_y = \frac{H_v}{3} (0.1)^{n'-2} \quad (12)$$

where,

$n' = n + 2$.

$$C_{11} = H_v^{7/4} \quad (13)$$

Fig 11. Plot between Load P vs H_v

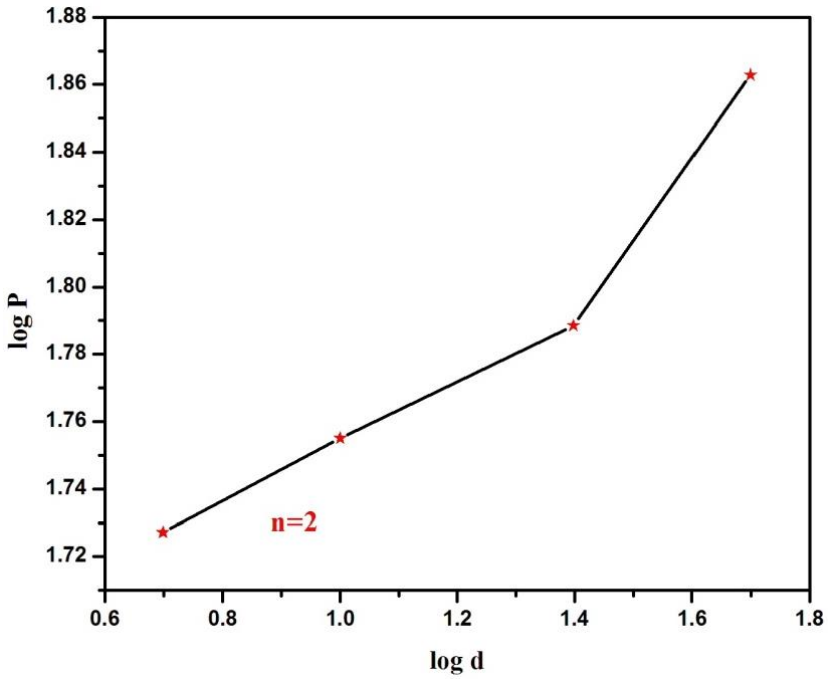

Fig 12. Plot between log d vs log P

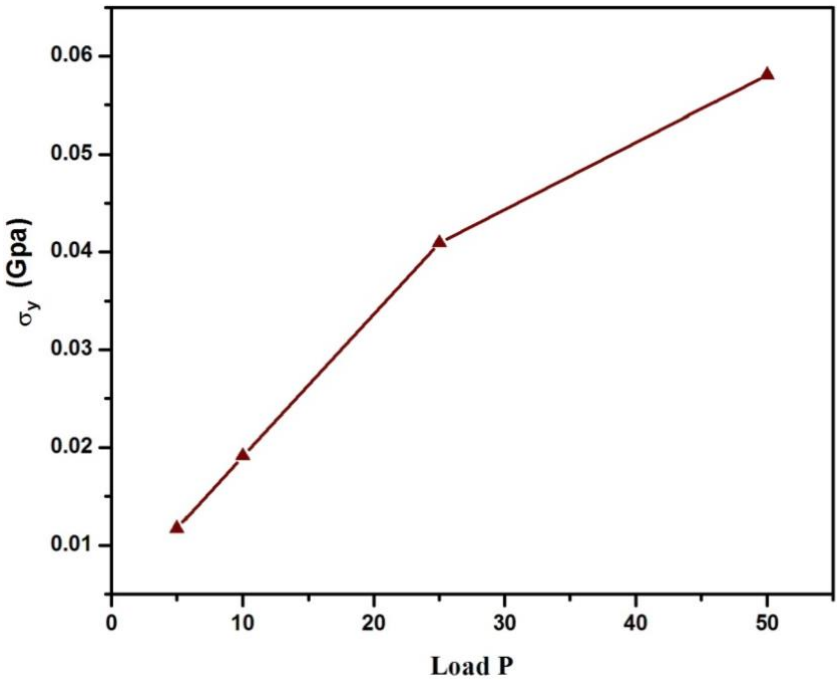

Fig 13. Plot between Load P vs σ_y

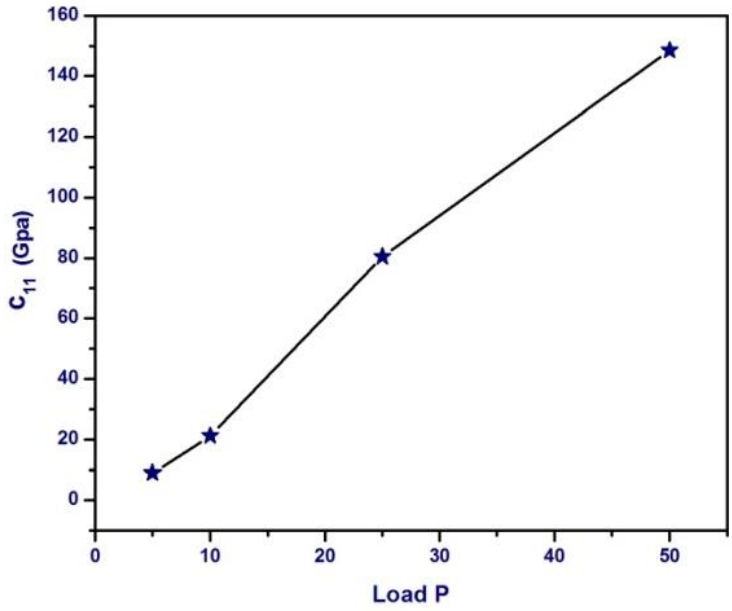

Fig 14. Plot between Load P vs C_{11}

6 Thermal analysis

The grown crystal DP12C is analyzed using Thermal Analyzer STA 6000 heating at a rate of 20 ^{o}C/min from 50 to 900 ^{o}C.

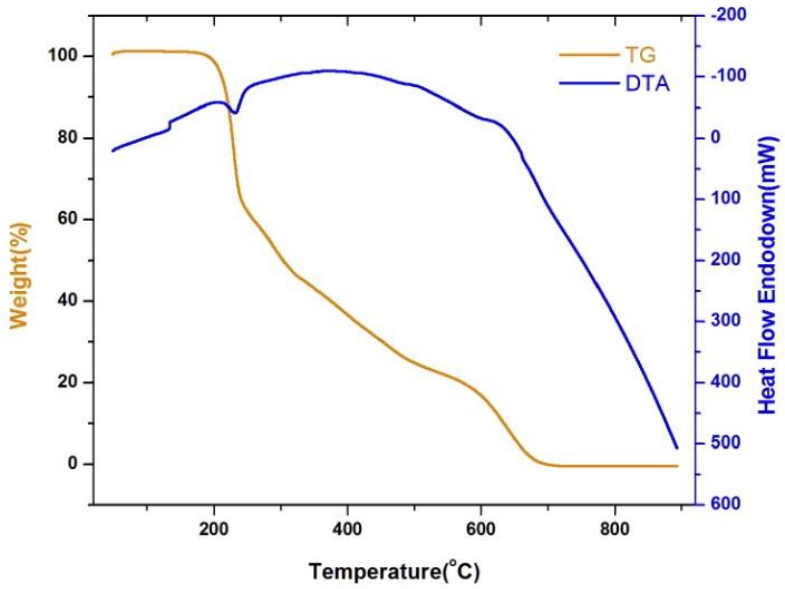

Fig 20. TG/ DTA curve of grown crystal

It is concluded that the grown crystal DP12C is stable upto 233 ^{o}C and the weight loss occurs drastically upto 700 ^{o}C [9]. From the observed DTA curve, the endothermic peak is observed at 233 ^{o}C, which indicates the stability of the crystal.

Conclusion

Good quality single crystals of DP12C were grown by slow evaporation technique. Single crystal X-ray diffraction determined the crystal structure, space group and the cell parameters of crystal. The obtained optical transmittance spectrum of crystal was discussed. The functional groups of the grown crystal including the lowest modes of vibration were identified and confirmed by Fourier transform infrared spectroscopic study (FTIR) and Fourier transform Raman spectroscopy (FT–RAMAN). The thermal stability of the grown crystal was analyzed by the thermogravimetric-differential thermal analysis (TG–DTA). Vickers micro hardness test determined the mechanical stability and the hardness parameters of the crystal. The luminescence activity of the grown crystal was determined by the photoluminescence (PL) spectroscopy. Thus, it is confirmed that the synthesized and grown crystal has better optical property which can be a suitable candidate for the optical applications, fabrication of sensible devices and in the photonic industry.

References

P. Karuppasamy, Muthu Senthil Pandian, P. Ramasamy, S.K. Das, Growth and characterization of semi-organic nonlinear optical (NLO) guanidinium trichloroacetate (GTCA) single crystal, Optik, Volume 156, 2018, Pages 707-719, ISSN 0030-4026, https://doi.org/10.1016/j.ijleo.2017.12.012.

B. Deepa, P. Philominathan, Optical, mechanical and thermal behaviour of Guanidinium Carbonate single crystal, Optik, Volume 127, Issue 3, 2016, Pages 1507-1510, ISSN 0030-4026, https://doi.org/10.1016/j.ijleo.2015.10.159.

M. Nageshwari, P. Jayaprakash, C. Rathika Thaya Kumari, G. Vinitha, M. Lydia Caroline, Growth, spectral, linear and nonlinear optical characteristics of an efficient semiorganic acentric crystal: L-valinium L-valine chloride, Physica B: Condensed Matter, Volume 511, 2017, Pages 1-9, ISSN 0921-4526, https://doi.org/10.1016/j.physb.2017.01.027.

Aarthi, J. & Dhanasekaran, Perumal. (2020). Growth and characterization study of L-glutamic acid α-polymorphs in the presence of L-aspartic acid. AIP Conference Proceedings. 2220. 060004. 10.1063/5.0001617.

The American Chemical Society is a scientific society based in the United States that supports scientific inquiry in the field of chemistry. https://www.acs.org/content/acs/en/molecule-of-the-week/archive/p/proline.html

Shkir, Mohd & Al-Faifi, Salem & Khan, M. & Dieguez, Ernesto & Perles, Josefina. (2014). Synthesis, growth, crystal structure, EDX, UV-vis-NIR and DSC studies of L-proline lithium bromide monohydrate A new semiorganic compound. Journal of Crystal Growth. 391. 104–110. 10.1016/j.jcrysgro.2014.01.012.

K. Mohana Priyadarshini, A. Chandramohan, G. Anandha Babu, P. Ramasamy, Synthesis, crystal growth, spectral, optical, thermal and dielectric studies of dichloro(4-hydroxy-l-proline)cadmium(II) single crystals, Optik, Volume 125, Issue 3, 2014, Pages 1390-1395, ISSN 0030-4026, https://doi.org/10.1016/j.ijleo.2013.08.008.

Rajan, Rejeena & George, Merin & D R, Leenaraj & Ittyachan, Reena & Sajan, Davidson & Vinitha, G.. (2020). Growth, Z-scan and density functional theoretical study for investigating the NLO properties of Guanidinium L-glutamate for optical limiting applications. Journal of Molecular Structure. 1222. 128937. 10.1016/j.molstruc.2020.128937.

Abisha W., D. Arul Dhas, S. Balachandran & Hubert Joe I. (2022) Structural, Spectroscopic, and C-H…O Hydrogen Bonding Interaction on Structure (Monomer and Dimer) Vibrational Spectroscopic, Fukui, NCI, AIM, and RDG Analysis Molecular Docking and Molecular Dynamic Simulation of Biological Active Pencycuron, Polycyclic Aromatic Compounds, DOI: 10.1080/10406638.2022.2149563

S. Devi, Deepa Jananakumar, Structural, optical and thermal studies of novel nonlinear optical materials – L-Valine doped Guanidine carbonate single crystals, Materials Today: Proceedings, Volume 42, Part 2, 2021, Pages 1353-1355, ISSN 2214-7853, https://doi.org/10.1016/j.matpr.2020.12.1207.

N. Sudha, R. Mathammal, R. Shankar, G. Sharon Benita, A comprehensive experimental and computational study of highly efficient organic NLO crystal: Anilinium -L-Tartrate, Optics & Laser Technology, Volume 137, 2021, 106800, ISSN 0030-3992, https://doi.org/10.1016/j.optlastec.2020.106800.

N. Saravanan, Geetha Palani, S. Shanmugan, V. Chithambaram, Investigation of third-order nonlinear optical semi organic potassium bromide malate single crystals for optoelectronic applications, Materials Today: Proceedings, Volume 30, Part 1, 2020, Pages 115-122, ISSN 2214-7853, https://doi.org/10.1016/j.matpr.2020.04.887.

ENHANCING THE MECHANICAL PROPERTIES OF HYDROXYAPATITE/TiO_2 NANOCOMPOSITES BY RESISTIVE COUPLED MICROWAVE SINTERING FOR BIOMEDICAL APPLICATIONS

Swapna Y V*, Mathew C T and Jijimon K Thomas

Department of Physics, Mar Ivanios College, Nalanchira, Thiruvananthapuram 695015, Kerala, India.

****presenting author e-mail: swapnamct08@gmail.com***

Abstract

Hydroxyapatite (HA) has been widely used in bone tissue engineering due to its biocompatibility, bioactivity, osteoinduction, and osteoconduction. But the synthetic HA based bone substitutes lack enough mechanical properties required for load-bearing applications. Tailoring the mechanical properties of HA by forming its composites or by adopting various processing techniques have evoked the interest of researchers all over the world. In this work nanostructured HA/TiO_2 bio composite in the weight ratio 75:25 was prepared using an auto ignited single step combustion technique. The XRD pattern revealed that the samples contain hexagonal phases of hydroxyapatite and tetragonal phase of titania in the nanometer regime. Scherrer formula was used to find the crystallite size. A novel sintering strategy called resistive coupled microwave sintering was used to sinter the samples. This sintering method effectively couples the conventional heating and microwave heating in definite proportions to yield samples with improved mechanical properties. The resistive heating and microwave heating can be controlled independently to yield reliable results. The new sintering strategy showed a substantial reduction in sintering temperature (~170 ^oC) and soaking duration (20 min). The X-ray diffraction technique was used to identify the phases contained in the sintered sample and EDS spectrum was used to study the elemental composition. The samples sintered via the new method showed better compressive strength of 162 MPa compared to the sample sintered by conventional resistive heating. The results indicate that by adopting a suitable low-temperature sintering strategy like resistive coupled microwave sintering, one can tailor the mechanical properties of hydroxyapatite/TiO_2 nano-biocomposite, a potential candidate of hard tissue substitutes.

Keywords: Resistive coupled microwave sintering; Hydroxyapatite/TiO_2 nano-biocomposite; compressive strength.

Introduction

Synthetic hydroxyapatite (HA) is widely used in bone tissue engineering as it mimics extra cellular matrix of natural bone [1]. HA is well known for its bioactivity, biocompatibility, osteoconduction and osteoconduction properties [2]. It stimulates osteoblast adhesion and proliferation [3]. But the mechanical properties of HA are not up to the mark for load bearing applications [4]. Enhancing the strength of HA without compromising the biological properties is one of the major challenges in the fabrication of bone tissue substitutes [5]. The mechanical properties of HA can be improved by incorporating biocompatible metal oxides to get reinforced matrices or by choosing suitable processing strategies [6].

This work is an effort to enhance the compressive strength of HA by incorporating TiO_2 in HA matrix and by using a novel sintering strategy called resistive coupled microwave sintering.

Materials and Methods

Phase pure HA and titania were synthesised using a single step auto ignited combustion technique [7]. For synthesising HA stoichiometric amounts of Ca $(NO_3)_2.4H_2O$ (Merck, India) and $(NH_4)_2HPO_4$ (Merck, Germany) were used. To prepare TiO_2 titanium isopropoxide (Merck, Germany) was used. The metal salts were dissolved in suitable solvents and to the precursor solution citric acid was added as fuel. To prepare HA the Ca/P ratio 1.67 was maintained in the solution. Nitric acid was added to the precursor and ammonium hydroxide solution was added to it to adjust the pH to ~7. The ammonium nitrate formed in the reaction acts as an extra oxidant without changing the proportion of the other reactants in the mixture. The clear solution was then kept on a hot plate till boiling and foaming and finally was auto-ignited to yield nanocrystalline powder.

X-ray diffraction (XRD) technique (X'pert pro, PANalytical, the Netherlands) was used to analyses the phases present in the as prepared sample. The sample powders of HA and TiO_2 were mixed in the ratio 75:25 to prepare HA/ TiO_2 nanocomposite. The nanocomposite sample powder was pelletized into discs of 12 mm diameter and 2 mm thickness using a hydraulic press under 20 MPa pressure. A novel resistive coupled microwave sintering strategy was used to sinter HA/TiO_2 nanocomposite. Both HA and TiO_2 have low microwave absorption capacity as they have low dielectric loss at low temperature. But as temperature increases their microwave absorbance increases. So, in the present work the sample is fired to 800 ^oC by keeping the resistive power and microwave power in the ratio 65:35 and thereafter the ratio was reversed as 35:65. The switching and controlling of the resistive and microwave powers were found to have a significant role in the densification of the samples. In the present work an indigenously made resistive coupled microwave furnace was used (VBCC/HMF/71,VB Ceramics Consultants, India). It possesses a pair of molybdenum disilicide heating elements were used for resistive heating and a pair of 2.5 GHz magnetrons with a power of 1.1 kW each were used for microwave heating. Hence the heating power rate could be regulated effectively as per the processing requirements. The pellet sintered via resistive coupled microwave sintering was coded as $HT25_{RM}$ and that sintered using the conventional resistive heating was

coded as $HT25_R$. Conventional sintering was carried out in a conventional furnace (TE-4050,Therelek, India).

The density calculations were done using the Archimedes method. The morphology of the sample powders raised to the sintering temperature and the top surface of the sintered samples were examined using a scanning electron microscope (NOVA NANOSEM-450, FEI, USA). A universal testing machine (Shimadzu, AGS-X, Kyoto, Japan) was used to study the stress-strain relationship of samples as a response to uniaxial compressive load as per ASTM standard C1424-15. The compressive strength of the sintered pellets was calculated from the experimental data.

Results and Discussion

Figure 1 shows the XRD patterns of the as-prepared HA, TiO_2 and HA/TiO_2 composites. The XRD patterns of HA and TiO_2 reveal that the required phases were formed during the combustion itself. The XRD data of as-synthesized HA was indexed with JCPDS file no: 74-0565 for the hexagonal phase of HA. The Scherrer formula was used to estimate the crystallite size [8]. The average crystallite size was found to be 22 nm. The XRD data of as-synthesized titania was indexed with JCPDS file no:89-4920 for the tetragonal phase of rutile TiO_2 and the average crystallite size was estimated to be 14 nm.

The XRD pattern of the samples sintered via resistive heating and resistive coupled microwave heating reveal that HA completely decomposes in the presence of TiO_2 to β-$Ca_3P_2O_8$ (β-Tricalcium phosphate, TCP), $CaTiO_3$ (Calcium titanate, CT), and TiO_2 (titania). The XRD patterns of the sintered samples were indexed with JCPDS file 702065 for rhombohedral phase of TCP, 653287 for cubic phase of CT and 894920 for tetragonal phase of rutile Titania. The formation of TCP during sintering is advantageous for biomedical applications as its biodegradability is high compared to HA[9,10]. It was reported that the decomposition of HA to TCP occurs at 1400 ^oC [11]. But in the presence of TiO_2 this decomposition temperature drops below 1150 ^oC [12].

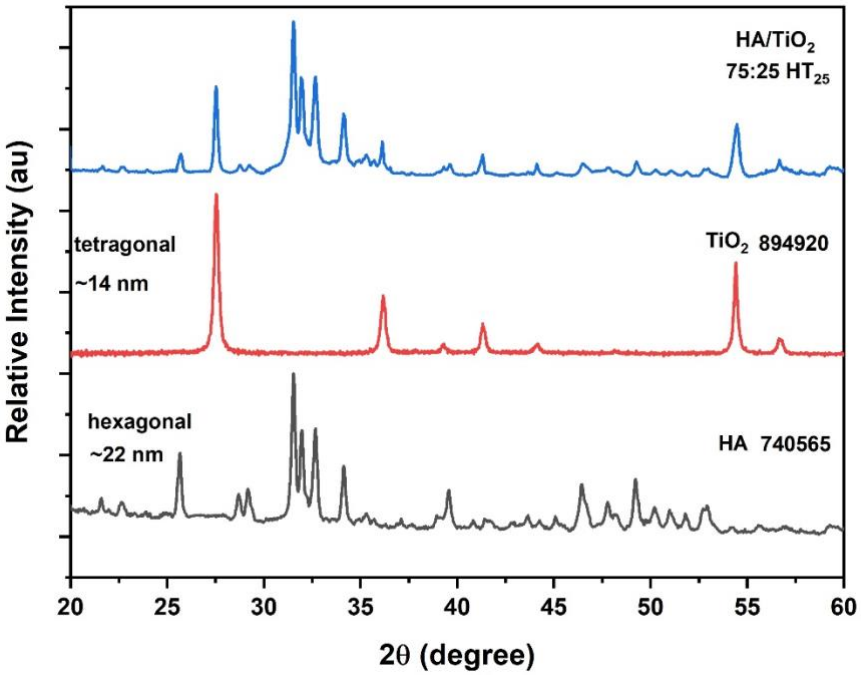

Fig 1 : XRD patterns of as-prepared sample powders of HA, TiO_2 and HA/TiO_2 composites

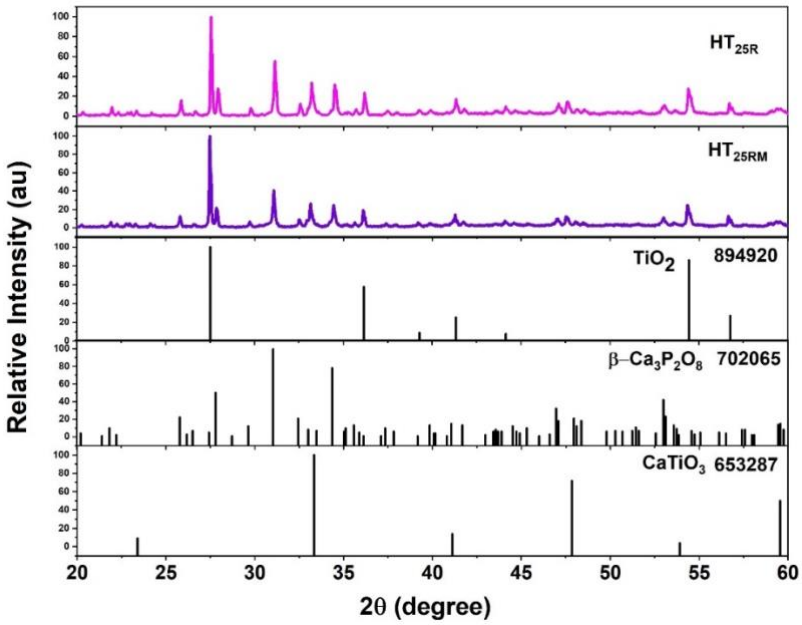

Fig 2 : XRD patterns of HA/TiO_2 composites sintered via conventional heating and resistive coupled microwave sintering.

The sample sintered using conventional resistive heating achieved 97.7 % of the theoretical density at 1198 ^{o}C for a soaking duration of 120 min. Figure 3 shows the scanning electron microscopic image of HT_{25R} sintered via conventional resistive heating. The grains are well defined, and their size varies from 0.1 µm to 0.8µm. The grain size distribution on the surface of the well-sintered pellet is shown inset of the figure 3. It reveals that the maximum number of grainsize lies in the size range 0.3 - 0.4 µm and the average grain size of the distribution is 0.31± 0.01µm.

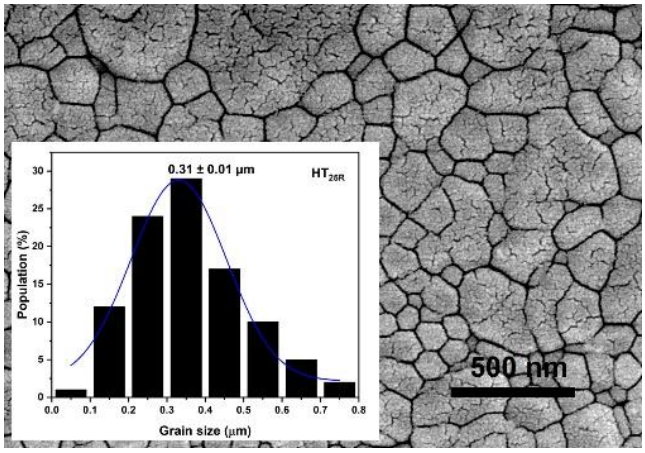

Fig 3 : SEM micrograph of HT_{25R} . Grain size distribution is shown inset.

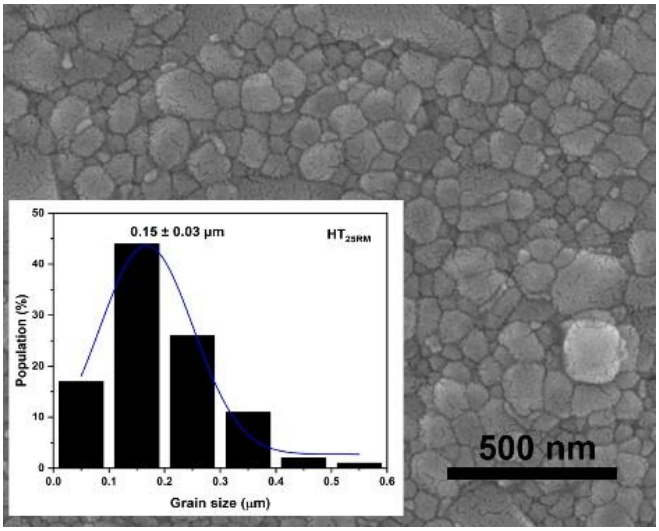

Fig 4 : SEM micrograph of HT_{25RM} . Grain size distribution is shown inset.

The sample sintered using conventional resistive heating achieved 98.1 % of the theoretical density at 1030 ^{o}C for a soaking duration of 20 min. The SEM image of HT_{25RM} sintered via resistive coupled microwave sintering is presented in figure 4. The grain size distribution is shown inset. Here also the grain size varies from 0.1 µm to 0.6 µm but the majority of grains lie in the size range 0.1 - 0.2 µm and the average grain size of the distribution is 0.15± 0.03 µm. The fast heating, reduction in sintering temperature and the reduction in soaking duration achieved by the resistive coupled microwave sintering are the reason behind the reduction in grain size.

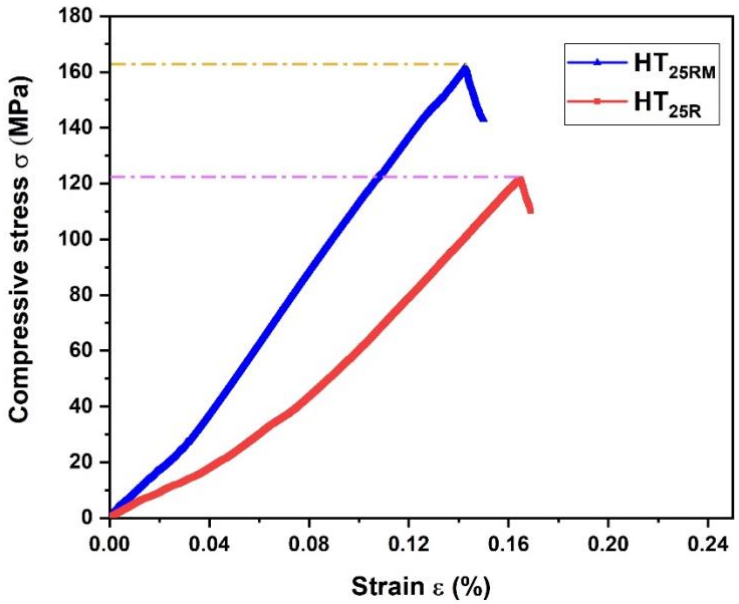

Fig. 5: Stress-strain relationship in HT_{25RM} , HT_{25R} samples.

The compressive strength of the samples was determined. The stress-strain relationship in HT_{25RM} and HT_{25R} are presented in figure 5. The compressive strength of the HT_{25R} sample was found to be 121 MPa and that of HT_{25RM} sample was 162 MPa. The HT_{25RM} sample showed significantly high compressive strength compared to HT_{25R} sample which attributed to the reduced grain size resulted from the effective coupling of resistive and microwave heating. The reduction ingrain size increases the percentage of grain boundaries which hinders the crack propagation. In addition to this the titania present in the sample cause pinning of grain boundaries which effectively hinders the grain growth [13]. The reduction in grain size attributes to the enhancement in the mechanical properties [14]. It is evident from the results that resistive coupled microwave sintering is a reliable sintering strategy to reduce the grain growth in bioceramics and tune the mechanical properties.

Conclusions

XRD results of the as prepared samples show that the sample synthesised using the method is phase pure and in nano regime. The XRD patterns of the sintered samples reveals that the TiO_2 present in the samples triggers the decomposition of HA and the phases in the samples were β-Tricalcium phosphate, Calcium titanate, and rutile phase of titania. The novel sintering strategy effectively couples the resistive power and microwave power in definite proportion. It reduces the sintering temperature ~170 and soaking duration by 100 min. The samples sintered using the novel method showed reduce grain size of 0.15± 0.03 µm and better compressive strength 162 MPa compared to the sample sintered using conventional methods. It can be concluded that resistive coupled microwave sintering is a reliable sintering strategy to reduce the grain growth in bioceramics and tune the mechanical properties.

References

Mingzu, D., Jingdi, C., Kaihua, L., Huaran, X., Cui, S., Recent advances in biomedical engineering of nano-hydroxyapatite including dentistry, cancer treatment and bone repair, Compos. Part B, 215 (2021) 108790. https://doi.org/10.1016/ j.compositesb.2021.108790.

Anita, L.J., Suresh, S., Fathimah, I., Enamul, H.M., Yogeswaran, L., Estelle, L., Solhe, F.A., Romana, S., Won, C.O., Recent advances in natural polymer-based hydroxyapatite scaffolds: properties and applications, Eur. Polym. J.,148 (2021) 110360. https://doi.org/10.1016/j.eurpolymj.2021.110360.

Hongjian, Z., Jaebeom, L., Nanoscale hydroxyapatite particles for bone tissue engineering, Acta Biomater. 7 (2011) 2769-2781. https://doi.org/10.1016/j.actbio.2011.03.019.

Chin, S.H., Stephanie, L.H., Matthew, T.B., Quizhen, L., Effects of chloride substitution on physical, mechanical and biological properties of hydroxyapatite, Ceram. Inter. 47 (2021) 13207-13215. https://doi.org/10.1016/j.ceramint.2021.01.186.

Mythili, P., Janis, L., Kristine, S.A., Dagnija, L., Alain, L., Liga, B.C., Fabrication, Properties and applications of dense hydroxyapatite: A Review , J. Func. Biomater., 6 (2015) 1099-1140. https://doi.org/10.3390/jfb6041099.

Singh, R.P., Mehta, M.S., Singh, P., Verma, R., Singh, B., In-vitro performance of titania reinforced hydroxyapatite nanopowders- a microstudy, J.Aust. Ceram. Soc., 53 (2017) 235-243. https://doi.org/10.1007/s41779-017-0029-7.

Swapna, Y.V., Mathew, C.T., Thomas, J.K., Resistive coupled microwave sintering- A promising technique to fabricate bioceramics with improved properties, J. Mech. Behav. Biomed., 136 (2022) 105488. https://doi.org/10.1016/j.jmbbm.2022.105488.

Langford, L.I., Wilson, A. J. C., Scherrer after Sixty Years: A Survey and Some New Results in the Determination of Crystallite Size, J. Appl. Crystallogr., 11 (1978) 102-113. https://doi.org/10.1107/S0021889878012844.

Ogose, A., Tetsuo, H., Hiroyuki, K., Naoki, K., Wenguang, G., Takeshi, K., Naoto, E., Comparison of hydroxyapatite and beta tricalcium phosphate as bone substitutes after excision of bone tumors, J. Biomed. Mater. Res. B, 72 B[1] (2005) 94-101. https://doi.org/10.1002/jbm.b.30136.

Kunio, I., Youji, M., Akira, T., Koichiro, H., Kanji, T., Go, O., Physical and histological comparison of hydroxyapatite, carbonate apatite, and β-tricalcium phosphate bone substitutes, Mater.,11 (2018) 1993. https://doi.org/10.3390/ma11101993.

Jong, K.L., Hang, C.J., Dong, S.S., Hwan, K., Kyu, H.H., Preparation of β-TCP/TiO2 composite by hot-pressing, Solid State Phenom., 121-123 (2007) 983-986. https://doi.org/10.4028/www.scientific.net/SSP.121-123.983.

Kumar, A., Biswas, K., Basu, B., Hydroxyapatite-titanium bulk composites for bone tissue applications, J. Biomed. Mater. Res. A, 103[2] (2015) 791-806. https://doi.org/10.1002/jbm.a.35198.

Fan, D., Chen, L.Q., Chen, S.P.P., Numerical simulation of Zener pinning with growing second phase particles, J. Am. Ceram. Soc., 81 [3] (1998) 526-532. https://doi.org/10.1111/J.1151-2916.1998.TB02370.X.

Orlovskii, V.P., Komlev, V.S., Barinov, S.M., Hydroxyapatite and hydroxyapatite-based ceramics, Inorg. Mater., 38 (2002) 973-984. https://doi.org/10.1023/A:1020585800572.

ANNUAL EFFECTIVE DOSE FROM ENVIRONMENTAL GAMMA DOSE LEVELS

[a]S. Monica, [b]PJ Jojo, [c]BR Bijini

[a]Assistant Professor ,Department of Physics,
St.Joseph's college for women, Alappuzha, India
[b]Fatima Mata National College ,Kollam
[c]Assistant Professor and HOD, VTM NSS College Dhanuvachapuram, Thiruvananthapuram
E-mail:monicakollam@gmail.com

Abstract

Indoor and outdoor gamma dose rates were evaluated along the coastal regions of Kollam district, Kerala through direct measurements using a GM(Geiger Muller) based gamma dose survey meter, time integrated measurement using $CaSO_4$:Dy based thermo luminescent dosimeters (TLDs). The mean value of total annual effective dose rate observed were 0.26 ± 0.01mSv/yr , respectively with an indoor to outdoor dose ratio of 0.54. Correlation study showed that the dose estimated from the TLDs is better correlated with that measured directly using the portable survey meter. The results of natural radioactivity levels in the soil samples has been compared with the levels reported in other Indian cities as well as other parts of the world.

Keywords: Terrestrial gamma dose, Extraterrestrial gamma dose, TLD (Thermoluminescent Dosimeter)

Introduction

Environmental gamma dose refers to the amount of ionizing radiation that an individual may be exposed to from natural sources in their environment, such as rocks, soil, and cosmic rays. This type of radiation is often referred to as background radiation.

The amount of environmental gamma dose can vary depending on a number of factors, including altitude, geology, and climate.Areas with higher levels of naturally occurring radioactive materials in the soil and rock, such as granite or shale formations, may have higher levels of environmental gamma dose.

The average annual environmental gamma dose varies around the world, with values ranging from less than 1 millisievert (mSv) in some areas to over 10 mSv in others. The annual limit of radiation exposure for the general public is typically set at 1 mSv, although this may vary by country or region.

It's important to note that while environmental gamma dose is a source of ionizing radiation exposure, the majority of an individual's exposure to radiation comes from medical procedures, such as X-rays and CT scans, and other human-made sources, such as nuclear power plants and industrial facilities.

Terrestrial gamma dose refers to the amount of gamma radiation that an individual may be exposed to from naturally occurring radioactive isotopes in the Earth's crust, such as uranium, thorium, and potassium-40. This type of radiation is a form of background radiation that is present everywhere on Earth, and contributes to an individual's overall radiation exposure.

Extra-terrestrial gamma dose, on the other hand, refers to the amount of gamma radiation that an individual may be exposed to from sources outside of Earth, such as cosmic radiation from the sun or from other stars in the galaxy. This type of radiation is typically more intense at higher altitudes, and can be a concern for astronauts and aircrew who are exposed to higher levels of cosmic radiation.

While both terrestrial and extra-terrestrial gamma radiation contribute to an individual's overall radiation exposure, the amount of extra-terrestrial gamma radiation is generally much lower than terrestrial gamma radiation. This is because the Earth's atmosphere provides some shielding from cosmic radiation, and most of the high-energy particles are absorbed or scattered before they reach the Earth's surface.

The average annual dose from terrestrial gamma radiation is typically in the range of 0.1 to 1 millisievert (mSv), while the average annual dose from cosmic radiation at sea level is about 0.3 mSv. At higher altitudes, such as during air travel or space missions, the dose from cosmic radiation can be much higher, potentially reaching levels of several millisieverts per year.

TLD stands for Thermoluminescent Dosimeter, which is a type of radiation dosimeter used to measure and record the amount of radiation exposure that a person receives. TLDs work by measuring the amount of light emitted by a crystal within the dosimeter when it is heated, which is proportional to the amount of radiation absorbed.

A survey meter, on the other hand, is a portable radiation detection instrument that is used to measure the levels of radiation in a particular area. Survey meters typically use a Geiger-Muller tube or other radiation detection device to detect and measure the levels of radiation in the environment [3,5].

While both TLDs and survey meters are used to measure radiation, they are used for different purposes. TLDs are typically worn by workers who may be exposed to radiation in their jobs, such as nuclear power plant workers, to monitor their exposure over time. Survey meters, on the other hand, are used by emergency responders, first responders, and others to quickly assess the radiation levels in a particular area to determine if it is safe for people to enter or if there is a potential radiation hazard.

There are regions in the world where the outdoor terrestrial radiation exceeds substantially the average value due to the enrichment of certain radioactive minerals leading to the formation of what are known as high background areas. The presence of high background areas has been reported in several countries like China, Iran, Germany, USA, Brazil, and India [1]. The main objective of the present study is to determine the indoor and outdoor gamma dose rate along the coastal regions of Kollam district,Kerala.

Materials and methods

Selection of the measurement sites

The gamma background radiation measurements were performed both indoor and outdoor along the coastal region of Kollam district, Kerala. Here the area chosen for the present study contains monazite bearing sands.

Gamma absorbed dose measurements using portable dose surveymeter

The ambient gamma absorbed dose rates were measured in the sampling locations using GM tube based gamma dosimeter (POLIMASTER PM 1405). This device can detect gamma rays in the energy range of 0.05–3 MeV and the dose rate measurement range is 0.1 μSv/h to 100mSv/h. The gamma radiation levels were measured both inside and outside the dwellings at 1 m above the ground. About 20 readings were taken at different points in each location.

Gamma absorbed dose measurements using Thermoluminescent dosimeter (TLD)

A thermoluminescent dosimeter (TLD) is a device used to measure the dose of ionizing radiation received by an object or person. TLDs are commonly used in medical, industrial, and environmental settings where radiation exposure needs to be monitored. A TLD consists of a small piece of crystalline material, such as lithium fluoride, that is able to absorb energy from ionizing radiation. When the TLD is heated, the absorbed energy is released in the form of visible light, which is detected by a photomultiplier tube or other light-sensitive device [6].

The dosimeters were specially designed to measure the environmental gamma radiation by the Bhabha Atomic Research Centre (BARC), Mumbai Chougaonkar et al. [4]. The details of the preparation of the TLD dosimeters and calibration are published elsewhere by Chougaonkar et al. [4]. The TLDs were deployed inside 20 dwellings and 20 outdoor locations for a time period of 90 days. Inside the dwellings, they were installed at least 1 m away from the walls and about 3 m above the floor. In the outdoors they were installed just outside the dwelling at a similar height. The retrieved dosimeters were analyzed using the automatic TLD reader (LLRRL, Kollam) and the absorbed dose was arrived using standardized methodology [4].

Results and Discussion

Gamma absorbed dose rates

The indoor and outdoor gamma absorbed dose rates along the coastal region of Kollam district measured using portable dose survey meter, are presented in Table 1, and the doses measured using the TLDs are also presented in Table 1. Also, the mean value of the dose for the entire region was higher when compared to the values (mean of 59 nGy h^{-1} in the range of 18–93 nGy h^{-1}) given in UNSCEAR(United Nations Scientific Committee on the Effects of Atomic Radiation) [9] for different countries and with the all India mean value (89 nGy h^{-1} in the range of 27–3051 nGy h^{-1}) reported by Nambi et al. [2].

Indoor and outdoor annual effective dose

From the hourly dose rate, the annual effective dose was computed using the indoor occupancy factor of 0.8 and the outdoor occupancy factor of 0.2 [1] and these are also presented in Tables 1. The total annual effective dose thus calculated from the survey meter data had mean values of 0.26 $\pm$0.01mSv y^{-1}(Table 1) and the corresponding dose values computed from TLD data had mean values of 0.28$\pm$0.09 mSv y^{-1} (Table 1). Nambi et al. [2] found the dose levels in India, except HBRAs in the states of Kerala and Tamil Nadu, to be 0.44 ± 0.13 mSv a^{-1}. Thus, the total gamma ray dose is higher than the average value for normal background regions of India [7,8]

Table 1: Indoor and outdoor gamma absorbed dose rates (measured using portable survey meter and TLDs).

Location	Sample code	Gamma dose rate(nGy/h) (measured using Surveymeter)		Gamma dose rate(nGy/h) (measured using TLD)		Annual effective dose (mSv/y)		Reduction Co-efficient
		Indoor	outdoor	Indoor	outdoor	Surveymeter	TLD	
Kollam	KL1	56.2	119.5	56.3	119.3	0.27	0.27	0.45
	KL2	58.5	124.5	60.6	123.3	0.29	0.29	0.47
	KL3	52.9	132.5	54.1	131.3	0.25	0.26	0.39
	KL4	60.2	134.8	61.3	133.7	0.29	0.31	0.44
	KL5	65.2	115.8	66.3	114.6	0.31	0.32	0.56
	KL6	69.5	117.6	70.6	116.4	0.34	0.34	0.59
	KL7	54.2	126.4	55.3	125.2	0.26	0.27	0.42
	KL8	50.2	130.4	51.3	129.2	0.24	0.25	0.38
	KL9	52.8	148.6	54.5	147.4	0.25	0.26	0.35
	KL10	55.5	145.7	56.6	144.6	0.27	0.27	0.38
	KL11	62.8	150.2	64.4	149.1	0.31	0.31	0.41
	KL12	64.8	119.8	66.9	118.6	0.31	0.32	0.54
	KL13	67.9	136.5	69.1	135.3	0.33	0.33	0.49
	KL14	68.4	145.5	69.5	144.3	0.33	0.34	0.47
	KL15	54.8	147.8	56.4	146.6	0.26	0.27	0.37

Comparison of dose measured by survey meter and TLDs

The correlation between the dose rate values measured using TLD and portable survey meter is plotted, which indicates a significant positive correlation (R^2=0.98) between the results of the two different methods. The agreement between the two techniques is good for low dose values and the deviation increases at higher dose values.

Conclusion

The total annual effective dose thus calculated from the survey meter data had mean values of 0.26 $\pm$0.01mSv y^{-1} and the corresponding dose values computed from TLD data had mean values of .28$\pm$0.09 mSv y^{-1} . Nambi et al. [2] found the dose levels in India, except HBRAs in the states of Kerala and Tamil Nadu, to be 0.44 ± 0.13 mSv a^{-1}. Thus, the total gamma ray dose is higher than the average value for normal background regions of India .

References

United Nations Scientific Committee on the Effects of Atomic Radiation(UNSCEAR).Report to the General Assembly, vol. 1, Annex. B;2008.

Nambi KSV, Bapat VN, David M, Sundaram VK, Santa CM, Soman SD. Natural background radiation and population dose distribution in India. India: HPD,BARC; 1986.

United Nations Scientific Committee on the effects of Atomic Radiation(UNSCEAR). Exposures resulting from nuclear explosions. New York, AnnexE: United Nations Publication; 1982.

Chougaonkar MP, Shetty PG, Mayya YS, Puranik VD, Kushwaha HS.Performance characteristics of newly modified CaSO4:Dy based indigenous thermoluminescent dosimeters for environmental radiation monitoring. J NuclSci Technol 2008(Suppl. 5):610–3.

Lu, X. and Zhang, X (2006). Measurement of natural radioactivity in sand samples collected from the Baoji Weihe Sands Park, China. Environ. Geol. 50, 977–982 .

Ramasamy, V., Suresh, G., Meenakshisundaram, V.andPonnusamy, V. Horizontal and vertical characterization of radionuclides and minerals in river sediments. Appl. Radiat. Isot. 69, 184–195 (2011).

Mamont-Ciesla, K., Gwiazdowski, B., Biernacka, M. andZak, A. Radioactivity of building materials in Poland. In:Vohra, G., Pillai, K. C. and Sadavisan, S., Eds. Natural Radiation Environment. Halsted Press, p. 551 (1982).

Chougaonkar MP, Eappen KP, Ramachandran TV, Shetty PG, Mayya YS, Sadasivan S, Venkat S, Raj V. Profiles of doses to the population living in the high background radiation areas in Kerala, India. J Environ Radioact2004;71:275–97

United Nations Scientific Committee on the Effects of Atomic Radiation(UNSCEAR). Sources and effects of ionizing radiation. Report to the GeneralAssembly, Annexe B; 2000.

Ramachandran TV. Review article on background radiation, people and the environment. Iran J Radiat Res 2011;9:63-76.

SYNTHESIS AND CHARACTERIZATION OF ZnO, BARIUM DOPED ZnO AND BARIUM COPPER Co-DOPED ZnO NANOPARTICLES FOR ENHANCED STRUCTURAL AND MAGNETIC PROPERTIES VIA Co-PRECIPITATION METHOD

M.Abshana Begam

Assistant Professor,Department of Chemistry,
Khadir Mohideen College,Adirampattinam,61470,Thanjavur District,
Tamil Nadu,India.

Abstract

Nanotechnology is an emerging technology for future requirements and applications of materials with their fundamental new properties and functions. Nanosensor devices based on nanomaterials provide a very faster response, low-cost and long-life time. They are user friendly and provide higher-efficiency.In this study,three sets of nanoparticles Zinc Oxide (ZnO), Barium doped ZnO (Ba:ZnO) and Barium-Copper co-doped ZnO (BaCu:ZnO) were synthesized using co-precipitation metod.The X-ray diffraction pattern confirms that the synthesized ZnO nanoparticles have a hexagonal wurtzite structure.The lattice constant ‘a’ and ‘c’ for the doped and co-doped ZnO nanoparticles decrease due to the substitution of Ba and Cu ions in place of Zn ions.The FESEM images show that the synthesized ZnO nanoparticles have a spherical shape nanostructure.The EDAX spectra confirm the presence of Zn, Ba, Cu and O in the samples without any impurities.The FT-IR spectra of synthesized ZnO, Ba:ZnO and BaCu:ZnO nanoparticles were analysed using the KBr Pellet method in the wave number range 400-4000 cm^{-1}.It was confirmed that the dopant ions are incorporated in that ZnO matrix.The photoluminescence studies showed that the doping of ZnO altered the band emission, which is due to zinc vacancies, oxygen vacancies and surface defects.Additonaly, magnetic measurements using Vibrating Sample Magnetometer showed that doped and co-doped nanoparticles exhibited ferromagnetic behavior at room temperature.Overall, this study provides important insights into the synthesis , characterization and magnetic properties of different types of nanoparticles which could have potential applications in various field such as bio medicine and electronics.

Introduction

Zinc oxide is a highly important semiconductor with valuable properties for various applications. To optimize its performance, surface modification is a key factor that must be considered. One approach is to use different surface coatings, such as metal oxides or polymers, to enhance the material's stability and reactivity. Another effective method is to dope the material with different impurities to alter its electronic and optical properties[1-3]. This can be achieved through sol-gel synthesis, hydrothermal synthesis, or chemical vapor deposition techniques. Additionally, controlling the synthesis conditions can help regulate the morphology of the ZnO nanoparticles, leading to particles with different sizes and shapes, which can influence their properties such as surface area and optical absorption. Co-precipitation is a widely used method for the synthesis of nanopowders, which offers advantages such as reduced reaction temperature due to homogeneous mixing of reactant precipitates and highly reactive metal powders that can be sintered at low temperatures, resulting in the formation of smaller particles[5]. Overall, modifying the surface of ZnO is crucial for enhancing its performance in areas such as photocatalytic activity and conductivity[4]

Crystals cannot be perfect as they have a finite size and cannot extend infinitely in all directions. As a result of this imperfection, the diffraction peaks become broadened. The broadening of the diffraction peaks is used to determine two important properties,the crystallite size and the lattice strain. The crystallite size refers to the size of coherently diffracting domains, which is not necessarily the same as the particle size due to the formation of polycrystalline aggregates [6]. The lattice strain measures the distribution of lattice constants caused by crystal imperfections, such as lattice dislocations. To analyze micro-strain, X-ray diffraction is performed on the samples.

In this study, co-precipitation method is used to synthesize ZnO, Ba:ZnO, and BaCu:ZnO NPs. This investigation focused on the structural, morphological, chemical composition, optical properties and magnetic properties of these NPs.

Experimental Methods

The experimental methods involved the use of high purity chemicals including Zinc (II) nitrate hexahydrate, Copper (II) nitrate hexahydrate, Barium nitrate and Sodium hydroxide as precursors without purification.

For the preparation of ZnO nanoparticles, a solution was made by dissolving 0.1 M of Zinc nitrate in double distilled water, followed by the addition of 0.8 M of NaOH solution. The resulting white precipitate was stirred at 60 ^{o}C for 4 h and then washed with double distilled water and ethanol. The obtained ZnO nanopowder was dried at 120 °C.

To prepare Ba doped ZnO NPs, 0.006 M of Barium nitrate was dissolved in 100 ml of double distilled water and then mixed with 0.094 M of Zinc (II) nitrate hexahydrate solution. NaOH was added as a precipitating agent and the white precipitate was stirred at room

temperature for 20 minutes followed by 4 hours at 60 °C. The resulting precipitate was washed with double distilled water and ethanol before being dried at 120 °C.

Similarly, for BaCu codoped ZnO NPs, 0.003 M each of Barium nitrate and Copper (II) nitrate Hexahydrate were dissolved in 100 ml of double distilled water and mixed with 0.094 M of Zinc (II) nitrate hexahydrate solution. NaOH was added as a precipitating agent and the resulting precipitate was stirred at room temperature for 20 minutes followed by 4 hours at 60 °C. The precipitate was washed with double distilled water and ethanol before being dried at 120 °C. All samples were annealed at 800 °C for 5 h to enhance atomic rearrangement and remove residual impurities.

The ZnO, Ba:ZnO and BaCu:ZnO NPs were characterized by X-ray diffractometer (model: X'PERT PRO PANalytical). The diffraction patterns were recorded in the range of 25^{o}-80^{o} for the ZnO, Ba:ZnO and BaCu:ZnO samples where the monochromatic wavelength of 1.54 Å was used. The samples were analyzed by Field Emission Scanning Electron Microscopy (Carl Zeiss Ultra 55 FESEM) with EDAX (model: Inca).

Photoluminescence spectra was taken using a spectrometer JASCO spectroflurometer FP-8200. VSM measurements were performed for ZnO, SrBa:ZnO and BaCu:ZnO NPs with M Vs H @ constant T using Lakeshore VSM 740 instruments.

Results And Discussions

Figure1 shows the XRD patterns of ZnO, Ba:ZnO, and BaCu:ZnO NPs show that they have a hexagonal wurtzite structure, which is confirmed by JCPDS data (Card No: 36-1451). There is no impurity phase observed in Ba and BaCu codoped ZnO NPs. The diffraction peaks for ZnO NPs show a lower angle shift compared to the Ba and BaCu codoped ZnO NPs, which may be due to the substitution of an impurity phase. The intensity of Ba and BaCu codoped ZnO NPs is higher than that of pure ZnO NPs due to impurity effects.

The particle grain size of ZnO, Ba:ZnO, and BaCu:ZnO NPs is determined using the X-ray line broadening method and the Scherrer's equation. The average particle sizes are 44, 53, and 42 nm for ZnO, Ba:ZnO, and BaCu:ZnO NPs, respectively. The strain-induced broadening is given by the Wilson formula, and the observed line width is the sum of the strain-induced broadening and the instrumental broadening[7].

The Williamson-Hall equation is used to calculate the strain values, which are 0.0025, 0.00355, and 0.00285 for ZnO, Ba:ZnO, and BaCu:ZnO NPs, respectively. These strain effects can change the size and shape of the particles. Overall, the XRD analysis provides important information about the structure, size, and strain of the NPs, which is useful for understanding their properties and potential applications.

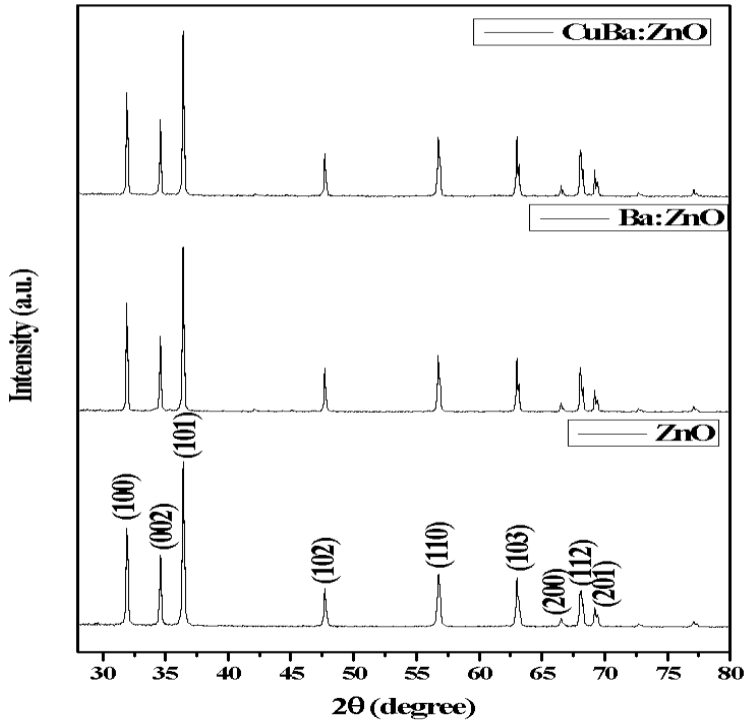

Figure 1 X-ray diffraction pattern of ZnO, Ba:ZnO and BaCu:ZnO NPs.

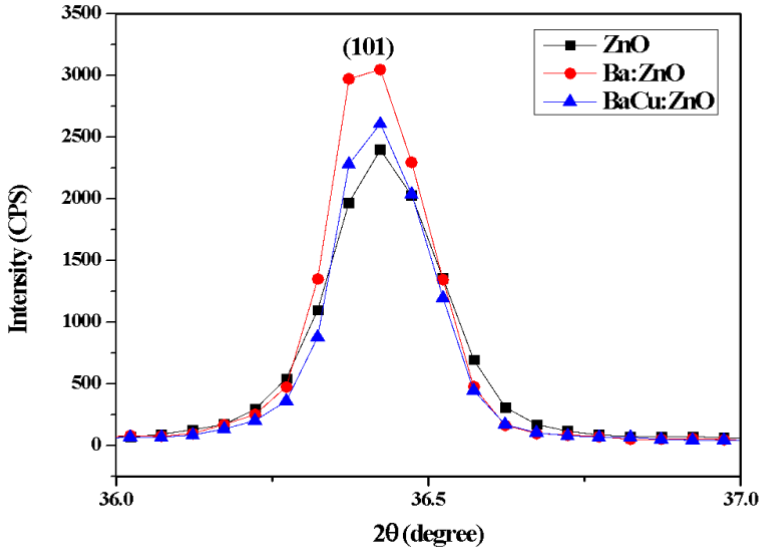

Figure 2 X-ray powder diffraction patterns of the doping-induced peak shift for ZnO, Ba:ZnO and BaCu:ZnO NPs

Morphology and chemical composition

Figure 3 shows the surface morphology of the ZnO, Ba:ZnO and BaCu:ZnO NPs were investigated by FESEM analysis. FESEM clearly display the synthesized ZnO, Ba:ZnO and BaCu:ZnO NPs formed spherical structure. The atomic percentage was identified by EDAX spectra is shown in Fig. 4. The EDAX data display the expected elements Zn, Ba, Cu and O are present in the nanoparticles.

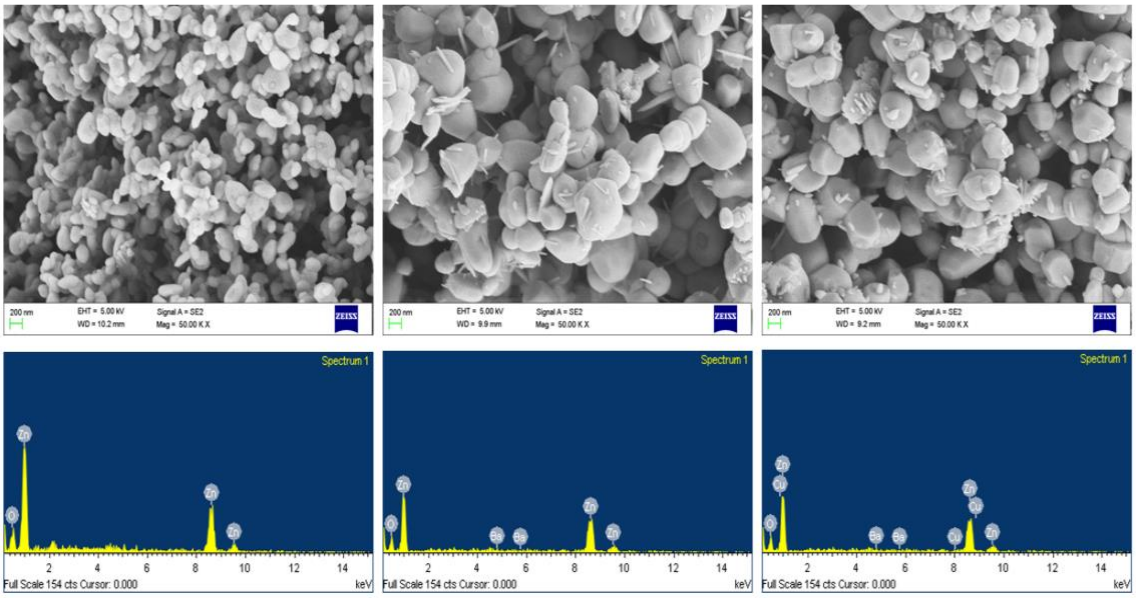

Figure 3 FESEM and EDAX spectra of ZnO, Ba:ZnO and BaCu:ZnO NPs.

Photoluminescence (PL) spectroscopic studies

Photoluminescence (PL) spectra of ZnO, Ba:ZnO and BaCu:ZnO NPs are shown in Fig. 4. Which excitation wavelength at 320 nm. The PL spectra of ZnO, Ba doped ZnO and BaCu Codoped NPs, UV emission observed at 360 nm, (360 nm and 389 nm) and (360 nm and 392 nm) , which is recombination corresponding to the near band edge (NBE) exciton emission of the wide band gap ZnO NPs [8, 9]. The violet emission centered at 415 nm for BaCu codoped ZnO NPs is attributed to radiative defects of interstitial (Zn_i) and Zn vacancies (V_{Zn}) related to the interface traps existing at the grain boundaries [10]. The blue emission observed at 479 and 480 nm for Ba:ZnO and BaCu:ZnO NPs, respectively, which is corresponding to singly ionized Zn vacancies. The green emission peak at 524 nm is ascribed to the recombination of electrons in singly ionized oxygen (Vo) vacancy with photo-excited holes in the valence band .

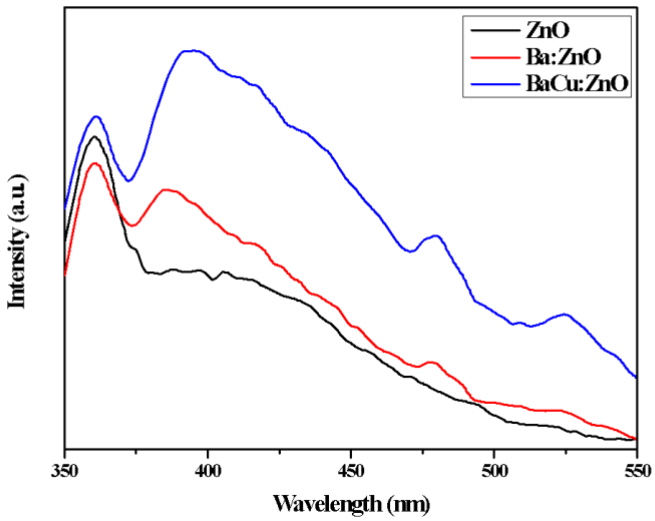

Figure 4 PL spectra of ZnO, Ba:ZnO and BaCu:ZnO NPs

Fourier transforms infra-red spectroscopic studies

The FT-IR spectra of ZnO, Ba:ZnO, and BaCu:ZnO NPs were analyzed using the KBr pellet method in the frequency range of 400-4000 cm $^{-1}$(Figure 5). The broad absorption band observed between 3750-3000 cm^{-1} is attributed to the O-H stretching of residual alcohols, water, and Zn-OH[11]. The absorption peaks observed at 3422, 3433, and 3439 cm $^{-1}$ for ZnO, Ba:ZnO, and BaCu:ZnO NPs, respectively, correspond to the H-OH bending vibration. The stretching frequency of Zn-O is observed at 1483 and 1457cm $^{-1}$ for Ba:ZnO and BaCu:ZnO NPs. No carbonated phase impurity was detected in the XRD pattern of the doped and co-doped ZnO samples. The Zn-O stretching bands were observed at 618, 490, and 503 cm $^{-1}$ for ZnO, Ba:ZnO, and BaCu:ZnO NPs, respectively. The intense broad absorption band observed between 600-400 cm $^{-1}$ is attributed to the stretching vibration of ZnO NPs.

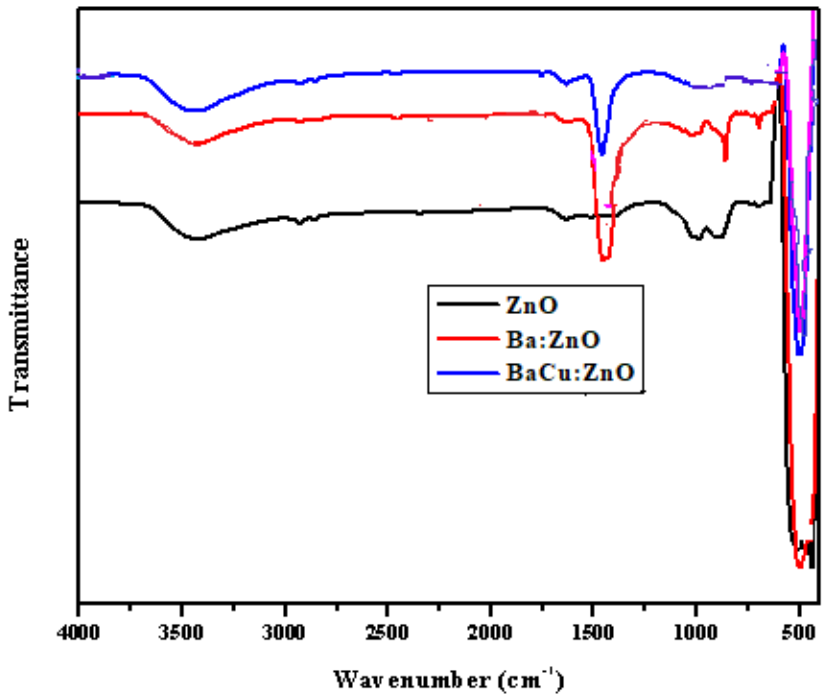

Figure 5 FTIR spectra of ZnO, Ba:ZnO and BaCu:ZnO NPs.

Vibrating Sample Magnetometer Studies

The magnetization of synthesized ZnO, Ba:ZnO, and BaCu:ZnO NPs was investigated using a vibrating sample magnetometer (VSM) with an applied magnetic field range of 0 to ±15 kOe at 300 K. The M-H loop of ZnO NPs exhibited diamagnetic behavior [Zhou et al., (2007)], while Ba:ZnO and BaCu:ZnO NPs showed clear indications of ferromagnetic behavior. The magnetization values observed were 100.06 E-6 emu/g, 276.92 E-6 emu/g, and 342.63 E-6 emu/g for ZnO, Ba:ZnO, and BaCu:ZnO NPs, respectively. The magnetization values of Ba:ZnO and BaCu:ZnO co-doped NPs were found to be higher compared to pure ZnO NPs due to the exchange interaction between localized spin moments resulting from the oxygen vacancies at the surface of nanoparticles.

The changes in the M-H loop can be explained based on the magnetic contribution from the orientation of the strong exchange interaction in d-d couple with respect to the dopant ions. The variation in dopants and their ionic radii also increases the linear behavior of the M-H loop. This suggests that metal-metal superexchange dominates and varies the magnetization values at room temperature [12].

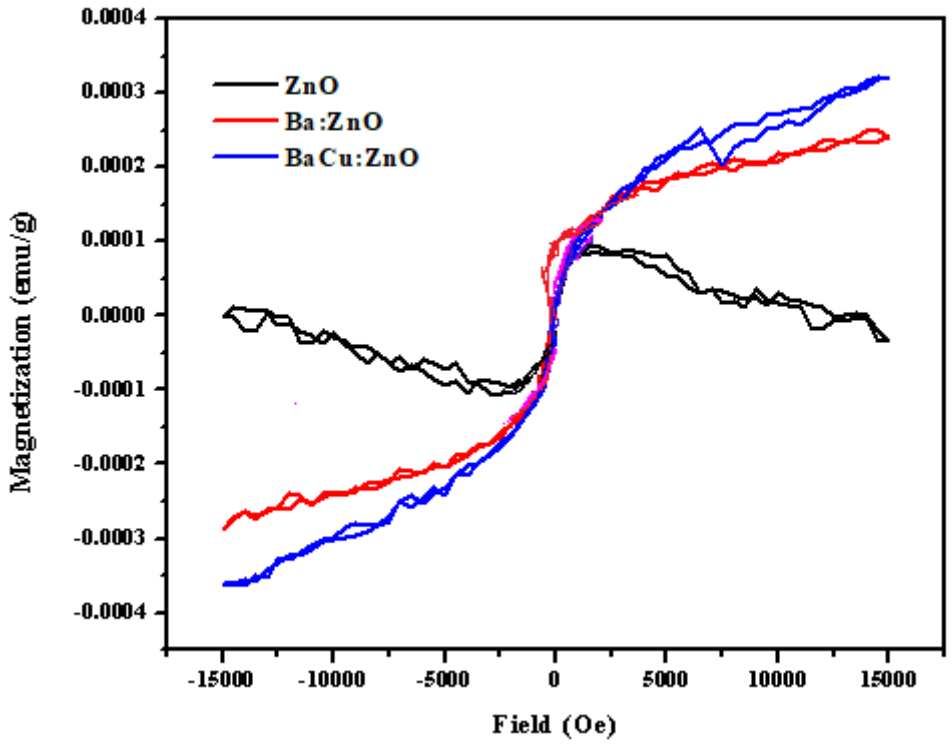

Figure 6 VSM analysis of ZnO, Ba : ZnO, BaCu :ZnO and BaNi :ZnO NPs.

Conclusions

The ZnO, Ba:ZnO and BaCu:ZnO NPs were prepared through co-precipitation method. From the XRD patterns, the synthesis ZnO, Ba:ZnO and BaCu:ZnO NPs exhibits the hexagonal structure. The XRD broadening of ZnO, Ba:ZnO and BaCu:ZnO NPs, barium and copper doping effects which may be small crystallite size and lattice strains. XRD broadening was analyzed through scherrer formula and modified forms of W-H analysis. FESEM images show the synthesized nanoparticles were spherical structure for ZnO, Ba:ZnO and BaCu:ZnO NPs respectively. Chemical composition were identified through EDAX spectra. The recorded FT-IR spectra were used to assign various vibrational frequencies for ZnO, Ba:ZnO, BaCu:ZnO, and NPs samples, confirming the incorporation of dopant ions in the ZnO matrix. Additionally, photoluminescence studies revealed that the band emission, which is due to zinc vacancies, oxygen vacancies, and surface defects, was altered by the doping of ZnO. The magnetization behavior of the synthesized ZnO, Ba:ZnO, and BaCu:ZnO NPs was also studied using a vibrating sample magnetometer (VSM). The results showed that Ba:ZnO and BaCu:ZnO NPs exhibit ferromagnetic behavior at room temperature, indicating a modification of the magnetic properties compared to pure ZnO NPs.

References

Dietl, Tomasz, H. Ohno, F. Matsukura, J. Cibert, and E. D. Ferrand. "Zener model description of ferromagnetism in zinc-blende magnetic semiconductors." *science* 287, no. 5455 (2000): 1019-1022.

Özgür, Ü., Ya I. Alivov, Chunli Liu, A. Teke, M. A. Reshchikov, S. Doğan, V. C. S. J. Avrutin, S-J. Cho, and H. Morkoç. "A comprehensive review of ZnO materials and devices." *Journal of applied physics* 98, no. 4 (2005): 11.

Srinet, Gunjan, Prateek Varshney, Ravindra Kumar, Vivek Sajal, P. K. Kulriya, M. Knobel, and S. K. Sharma. "Structural, optical and magnetic properties of Zn1− xCoxO prepared by the sol–gel route." *Ceramics International* 39, no. 6 (2013): 6077-6085.

Uskoković, Vuk, and Miha Drofenik. "Synthesis of materials within reverse micelles." *Surface Review and Letters* 12, no. 02 (2005): 239-277.

Kumaran, Nimisha N., and K. Muraleedharan. "Photocatalytic activity of ZnO and Sr2+ doped ZnO nanoparticles." Journal of water process engineering 17 (2017): 264-270.

Rogers, K. D., and P. Daniels. "An X-ray diffraction study of the effects of heat treatment on bone mineral microstructure." *Biomaterials* 23, no. 12 (2002): 2577-2585.

Ramakanth, K., Basics of diffraction and its application, I. K. International Publishing house PVT. LTD. New Dehli, 2007.

S.Mahamuni, K. Borgohain, B. S. Bendre, Spectroscopic and Structural Characterization of Electrochemically Grown ZnO Quantum Dots. J. Appl. Phys., 85 (1999) 2861-2865.

Samanta K, Bhattacharya P, Katiyar RS, Iwamoto W, Pagliuso PG, Rettori C. Raman Physical Review B. 2006 Jun 26;73(24):245213.

Wang H, Wang HB, Yang FJ, Chen Y, Zhang C, Yang CP, Li Q, Wong SP. Nanotechnology. 2006 Aug 8;17(17):4312.

Xu XL, Lau SP, Chen JS, Chen GY, Tay BK. Journal of Crystal Growth. 2001 Feb 28;223(1):201-5.

Senthilkumaar, S., K. Rajendran, S. Banerjee, T. K. Chini, and V. Sengodan."Influence of Mn doping on the microstructure and optical property of ZnO." Materials Science in Semiconductor Processing 11, no. 1 (2008): 6-12.

Singh, S.B., Limaye, M. V., Date, S.K., Gokhale, S. Kulkarni, S.K. “Ferromagnetism as a universal feature of nanoparticles of the otherwise nonmagnetic oxides ” Phys. Rev. B: Condens. Matter Mater. Phys., 80 (2009) 235421.

RECENT DEVELOPMENTS IN THE MATERIALS USED FOR SENSORS

Ansiya A

Department of Physics, Sunrise University
Alwar, Rajasthan, INDIA
ansiyavadooth@gmail.com

Abstract

Sensors are devices that respond to stimuli and are used to identify and quantify motion, chemicals, sound and light. Wireless sensor network has evolved as an emerging technology, which provides various prospects to different applications used for communication. Recent advancement in the area of sensing material categorizes sensors into two classes; direct sensors and complex sensors.

Direct sensors employ change in electrical signals like current, potential, capacitance or resistance. Generally, these signals are influenced by chemical reaction phenomena up to a measurable quantity. On the other hand, the chemical affected phenomena used by complex sensors utilize does not affect electrical features. Therefore, these sensors require a conversion process.

Different kind of materials are used to fabricate these various types of sensors. One of the primary requisites for fabrication of a sensor for a designer is, to have the knowledge of the different kinds of sensing material suitable for these sensors.

This paper discusses the different types of sensors used in multidisciplinary areas and the main novel materials used for the fabrication of different types of sensors. Different types of sensors include temperature sensors, proximity sensors, water quality sensors, optical sensors, chemical sensors, gas sensors, accelerometer sensors, gyroscope sensors. Materials used for fabrication of sensors include metals, metal oxides, metal organic framework, solid electrolytes, carbon nanotubes, graphene, sol-gel materials, mass sensing materials, light sensing materials, motion sensing materials.

Keywords: Sensors, direct sensors, complex sensors, materials for sensors, fabrication of sensors.

Introduction

Sensors are evolved as an emerging technology, which provides various prospects to different applications used for communication. They play a critical role in quality control of produced goods and online operations management. Internet of things systems use a range of sensors to function and supply various types of information along with processing data to deliver particular intelligence.

Pressure, temperature and flow have all been monitored using physical devices called sensors for a long time. Chemical sensors, are required for detection of species such as gas particles in smells. Recent advances in semiconductors such as silicon nanomembranes, metal oxides, and organic materials have made possible the creation of large and high-performance systems capable of on-site sensor conditioning. Chemical sensors and biosensor manufacturing for the detection of hazardous chemicals, chemical warfare agents, industrial waste, biological indicators, and environmental pollutants has been an active research area in analytical sciences over the past several decades.

Recent advancements in the area of sensing materials categorizes sensors into two classes direct sensors and complex sensors. Direct sensors employ change in electrical signals like current, potential, capacitance or resistance. Chemical affected phenomena used by complex sensors utilize does not affect electrical features. Therefore, these sensors require a conversion process.

Types Of Sensors

Temperature sensors

To estimate the degree of heat energy.It permits to sense a difference in temperature of a specific source.

Proximity Sensors

To discover the appearance or non-availability of a close by object, or features of the identity and translates it as signal.

Water Quality Sensors

To measure the quality of water and ion monitoring.

Optical Sensors

To estimate the substantial number of light rays. Also, to measure different things simultaneously in the form of electromagnetic energy, which includes light, electricity etc.

Chemical Sensors

The objective of chemical sensors is to ascertain variations in liquid or to discover air chemical differences.

Gas Sensors

To keep track in variation of the quality of air and determine the appearance of numerous gases.

Humidity Sensors

To measure humidity which is the quantity of water mist in a climate of various gases including air.

Smoke Sensors

To sense the presence of smoke with its levels. Smoke is a collection of airborne particulates and gases.

IR Sensors

They use either detection or emission of infrared radiation. Also have the capability of estimating the heat being released by the entity.

Image Sensors

To save optical image files electronically, translates image into electronic signals .

Motion Detection Sensors

To indicate the physical movement of any object in a given area.

Accelerometer Sensors.

To estimate the tangible or quantifiable acceleration encountered by an entity because of inertial forces.

Gyroscope Sensors

To measure the angular rate or angular velocity.

Materials Used for Sensors

Metals

Metals like gold, platinum and silver are chosen by sensor industry due to their suitable properties. Gold is a nonreactive and very soft metal and used for ozone sensors. Platinum nanoparticles demonstrate greater electrocatalytic response in favor of small molecule oxidation and reducing oxygen. Silver is malleable and shows a high corrosion resistance and enjoys of having highest thermal and electrical conductivity.

Metal Oxides.

For gas detection applications, metal oxides play a vital role as sensing material. Apart from gas sensing, a few metal oxides are also utilized to detect other types of fluids.

Solid Electrolyte Materials.

Liquid and solid electrolytes are available. Hydrogen sensors are extremely important, which are made with protonic solid electrolytes. Solid electrolyte advances are anticipated to lead to smaller devices with lower power requirements and faster reaction times.

Carbon Nanotubes and Graphene.

Carbon nanotubes have outstanding inherent features due to its exceptional structure, including unique physical properties, large surface area, high electrical conductivity, thermal stability and so on, leading to a large variety of applications in nanoelectronics and energy storage. Different types of sensors have shown interest in using carbon nanotubes as sensing material.

A deeper knowledge of graphene's chemistry and physics, as well as its interactions with biomolecules will be critical for its use in catalysis and sensor technologies.

Sol-Gel Materials

Sol-gel glass reflects many superior properties than organic polymers that includes photo and thermal stability, chemically intern, highly pure, porous and optically transparent.

Conclusions

In recent years there has been an emphasis on the design and improvement of sensors in various sectors. The internet of things is made up of numerous sensors that connect with one another and with outside world to convey data and information. The sensors are classified into various classes according to technology used and their use. Fabrication of these sensors employs different kinds of materials.

Acknowledgements

I would like to thank god, and my parents, teachers and everyone who has given great support on me.

Reference

Materials today: proceedings 62(2022)

Recent advances in 2D inorganic nanomaterials

Review of recent developments in sensing materials (2014)

Recent advance in graphene and other 2D materials

Semiconducting metal oxides as sensors for environmentally hazardous gases.

Recent advances in graphene-based biosensors.

Ce-DOPED COPPER-COBALT FERRITE NANOPARTICLES: PREPARATION AND ASSESSMENT OF STRUCTURAL, MORPHOLOGICAL AND OPTICAL PROPERTIES

Sheena T.V, John Jacob*

Assistant Professor, Department of Physics, Christian College, Kattakada, Thiruvananthapuram, Kerala, India.
sheenatvarun@gmail.com
Corresponding Author: E-mail: john.jacob@mic.ac.in
Assistant Professor, Department of Physics, Mar Ivanios College, Nalanchira Thiruvananthapuram, Kerala, Pin-695015, India.

Abstract

Ce^{3+} doped mixed Cobalt-Copper nanoferrites with nominal composition of $Co_{0.5}Cu_{0.5}Ce_xFe_{2-x}O_4$ were synthesized by surfactant-assisted chemical Co-precipitation method. The crystalline structure, morphology, elemental composition and optical properties of the ferrite samples calcinated at 600^0C were analysed using powder XRD, FT-IR, FE-SEM, EDX and UV-visible spectrometer. PXRD spectra confirmed the formation of spinel ferrites with cubic structure. Morphology and elemental composition of the synthesized samples were analysed by FE-SEM and EDX spectra. FT-IR spectra also confirmed the formation of spinel ferrites. Tauc plot was drawn from the UV-visible studies to estimate the band gap energy of the synthesized nanoferrites.

Keywords: Co-Cu ferrite, Chemical Co-precipitation.

Introduction

Among the spinel ferrites, copper and cobalt ferrite nanoparticles possess excellent magnetic, semiconducting and electrical properties such as high coercivity, strong magneto-crystalline anisotropy, moderate saturation magnetization, high electrical resistance, high thermal and chemical stability and low eddy current losses(1,2). The synthesized ferrites can either exist in cubic or tetragonal structures depending on the method of preparation and the calcination temperature and also in accordance with concentration of Jahn-Teller Cu^{2+} ions in B sites of the spinel structure(3). Also, the flexibility in tuning its properties make it possible to use in different types of sensors, as photocatalysts, in high density storage devices, ferrofluids, hyperthermia, drug delivery, magnetic resonance imaging etc(4,5). In recent times, the study of substituted complex nano ferrite materials such as Copper-Cobalt has become the focus point in search of novel materials with high potential for controlled and desired magnetic and electrical properties for a tremendous impact on the application areas of s biomedicine, catalysts and environmental remediation.

Doping with rare earth (Ce, Dy, Gd, Er, etc.) can alter the overall properties of the nano ferrites by inducing strain in the lattice due to their large ionic radii (2,6,7). Studies on RE-doped ferrites are very limited and they are promising candidates for tuning the overall properties of spinel ferrites.

Experimental Section

Synthesis of Ce^{3+} doped $Co_{0.05}$ Cu $_{0.05}$ Fe_2O_4 nanoparticles

The $Co_{0.5}Cu_{0.5}Ce_xFe_{2-x}O_4(0\leq x\leq 0.05)$ nanoparticles were synthesized via chemical co-precipitation method. Stoichiometric amount of material nitrates such as copper nitrate (Cu $(NO_3)_3.6H_2O$), cobalt nitrate (Co $(NO_3)_3.6H_2O$) ferric nitrate (Fe $(NO_3)_3.9H_2O$), cerium nitrate $(Ce(NO_3)_3.6H_2O)$ were used as raw materials. Polyethylene glycol (PEG) was used as the capping agent, and NH_4OH will act as the precipitating agent and was added slowly until the pH of about 8 was reached. All the chemicals used in this study were analytical grade with 99.99% purity. The precipitate formed was separated and washed several times in deionized water and finally, in acetone. The precipitate obtained was dried in an oven at 75^0C for about 3 to 4 hrs. Finally, the powdered sample was calcinated at 600^0C for 4hrs to stabilize the crystalline spinel phase. Further, it was milled with a mortar to get the fine sample in powder form.

Characterization techniques

The phase identification & crystallographic analysis of the samples were carried out by means of an X-ray diffractometer (Brucker, D8 Advance with DAVINCI design) at 40 mA and 40 kV equipped with CuK_α radiation with a step size of 0.02^0 in the 2θ range from 15^0 to 70^0. The surface morphology and compositional elemental analysis of the samples were done using field emission scanning electron microscope (FESEM, ZEISS, Germany) and Carl Zeiss EVO 18 SEM-EDX instrument. Fourier transform infrared (FTIR) spectra of the nano ferrites were recorded using NICOLET iS50 (Thermo scientific, America) spectrometer in the wavelength range (4000-400$cm^{-1)}$ using KBr as a background. The UV-Vis spectrums of the samples were recorded using a high-performance Cary 5000 UV-Vis-NIR spectrometer in the 200-800nm range.

Results and discussion

PXRD analysis of the samples

The XRD pattern of Co $_{0.5}$Cu $_{0.5}Ce_xFe_{2-x}O_4$(x=0.03,0.05) nano ferrites sintered at 800^0C are shown in Fig (1). The diffraction pattern showed sharp peaks that matches well with the standard values for $CuFe_2O_4$ (JCPDS card no: 75-1517) and this indicates the formation of cubic(fcc) spinel phase with Fd/3m space group. Secondary phases were also observed in the diffraction pattern which attributes to Fe_2O_3 and CeO_2 phases.The average crystalline sizes of the NPs corresponding to the most intense peak were estimated by Scherrer's equation and was found to be 24.08nm for3% doped sample and 26.49nm for 5% doped sample.

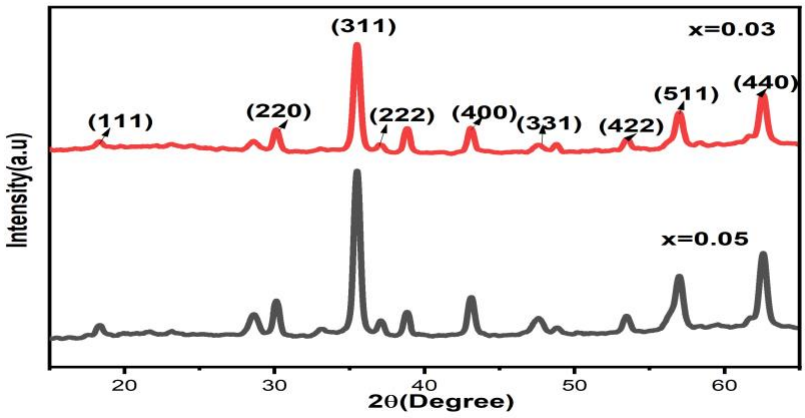

Fig 1. PXRD spectrum of $Co_{0.5}Cu_{0.5}Ce_xFe_{2-x}O_4$ (x= 0.03 &0.05) nanoparticles

FTIR Analysis

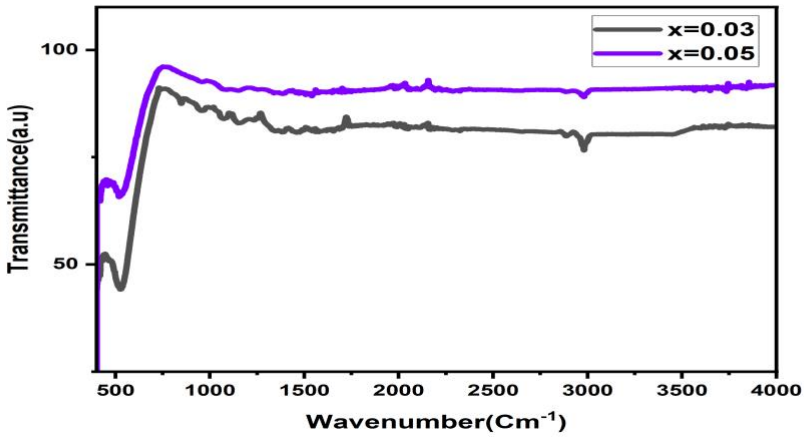

Fig 2. FTIR analysis of $Co_{0.5}Cu_{0.5}Ce_xFe_{2-x}O_4$ (x= 0.03 &0.05) nanoparticle

Fig (2) displays the FT-IR spectra to analyse absorption bands and the functional groups present in the as-prepared samples of $Co_{0.5}Cu_{0.5}Ce_xFe_{2-x}O_4$. Generally, FT-IR provides structural information, rather it is also related to the distribution of cations and any defects or distortions in the chemical structure of synthesized samples. In Ce-doped samples, FTIR spectra were recorded at room temperature in the 400 $cm^{-1}$to 4000 cm^{-1} range. Usually, in the case of ferrites, the absorption bands in the FTIR spectra exhibits two obvious absorption bands, as shown in fig, which are in the 499 cm^{-1} to 619 cm^{-1} range. The absorption band at approximately 499 cm^{-1} corresponds to metal ion stretching at octahedral sites (ν1) and absorption band at approximately 619 cm^{-1} represents the low-frequency M − O vibration at tetrahedral sites (ν2), which corresponds to the spinel structure.

Optical properties

For the present $Co_{0.5}Cu_{0.5}Ce_xFe_{2-x}O_4$, ferrite nanoparticles, an absorption band is formed in the UV region as shown in fig 3(a). For direct allowed transitions, the E_g values of $Co_{0.5}Cu_{0.5}Ce_xFe_{2-x}O_4$ were calculated as given in figure by extrapolating the linear portion curve of $(\alpha h\gamma)^2$ against photon energy ($h\gamma$) to $(\alpha h\gamma)^2 = 0$(Tauc's plot) for the samples. The band gap energy shows an increase with increase in doping concentration and is shown in Fig 3(b) and 3(c).

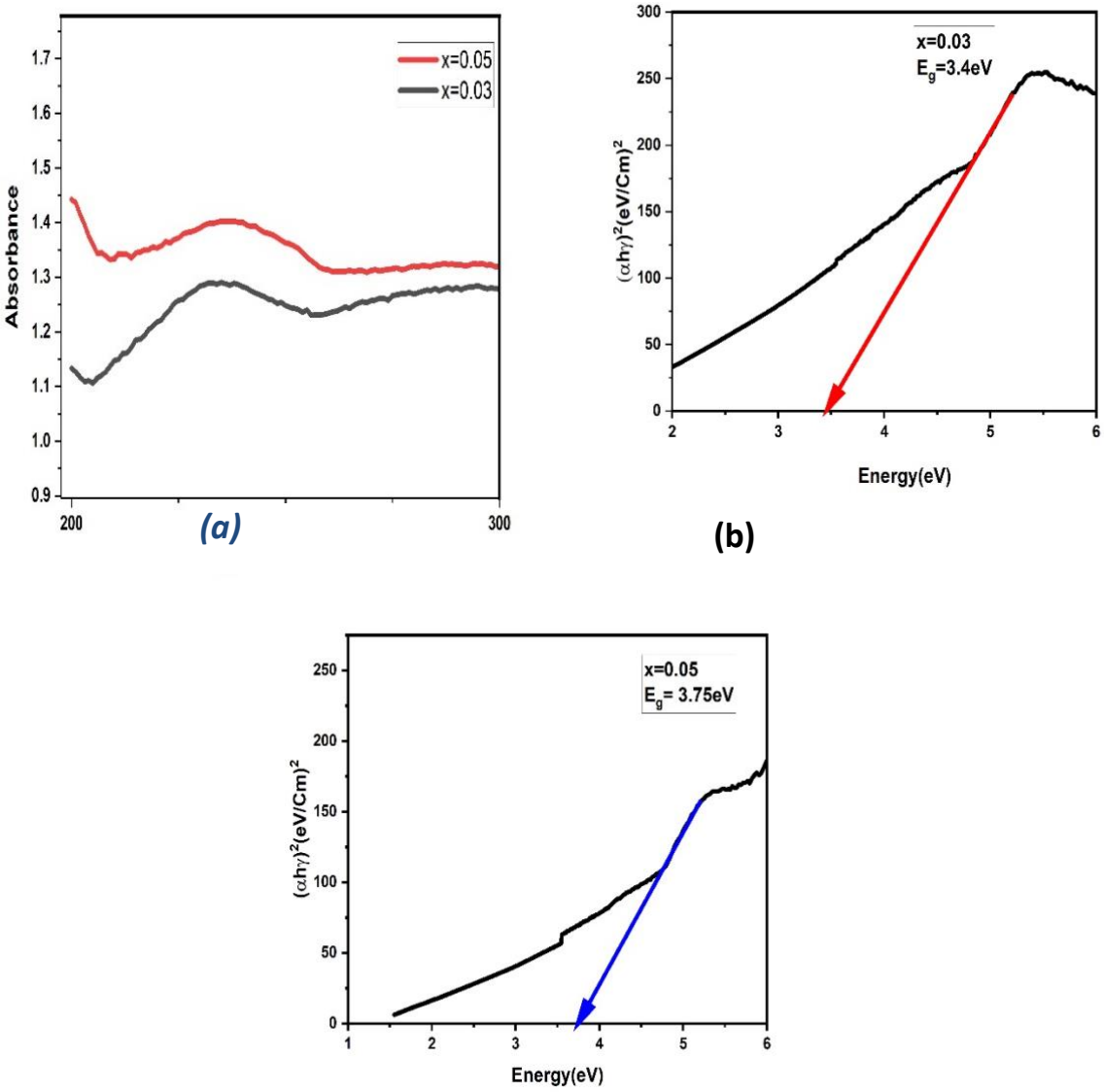

Fig 3(a) UV-Visible absorbance spectrum, 3(b) and 3(c) are Tauc plot of $Co_{0.5}Cu_{0.5}Ce_xFe_{2-x}O_4$ (x=0.03 &0.05) sample

3.4 FE-SEM analysis of Co0.5Cu0.5$Ce_xFe_{2-x}O_4$(x=0.03,0.05) nanoparticles

The morphology and elemental composition of $Co_{0.5}Cu_{0.5}Ce_xFe_{2-x}O_4$ (x=0.03,0.05) nanoparticles have been analysed by FE-SEM and EDX are shown in Fig 4. From the fig, it is clear that the NPs have a spherical morphology. EDX shows peaks corresponding to Cu, Co, Fe, O, and Ce elements in the nanoparticles. This confirms the purity of prepared $Co_{0.5}Cu_{0.5}$ $Ce_xFe_{2-x}O_4$(x=0.03) nanoparticles.

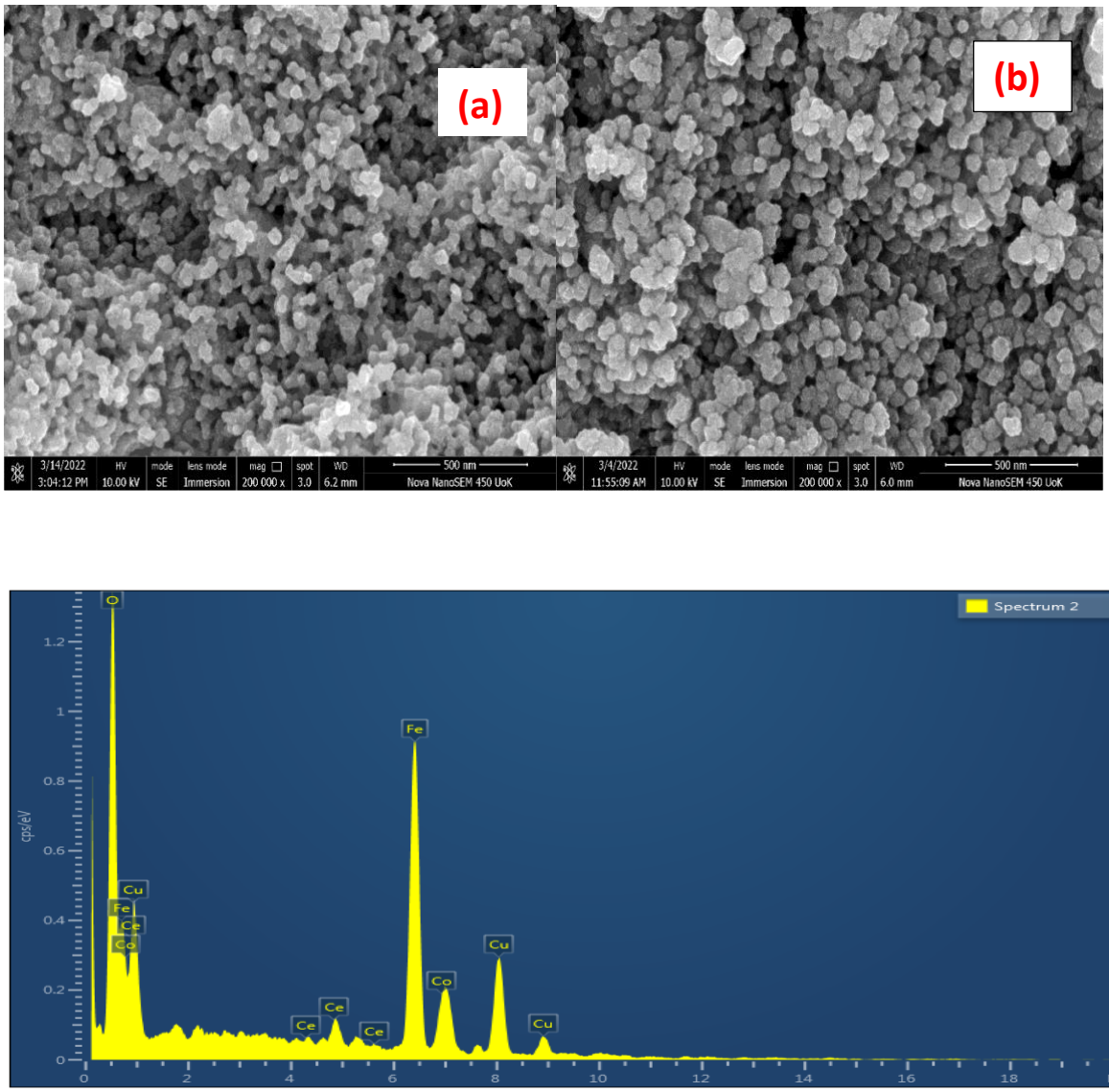

Fig 4. FE-SEM images and EDX spectrum of $Co_{0.5}Cu_{0.5}$ $Ce_xFe_{2-x}O_4$ (x= 0.03 &0.05) nanoparticles

Conclusions

Cerium-doped Co-Cu nanoparticles with the general formula $Co_{0.5}Cu_{0.5}Ce_xFe_{2-x}O_4$ (x= 0.03 &0.05) were synthesized by promising co-precipitation method and calcined at 600^0C. The structural properties of the NPs were analysed using XRD and it confirmed the formation of cubic spinel ferrite with Fd/3m space group. The morphological and compositional analysis of the samples were done using FESEM and EDX. FTIR analysis also confirms the formation of nano ferrites. The synthesised material can be studied further for its photocatalytic and biomedical applications.

Acknowledgement

We are grateful to the authorities of CLIF, the University of Kerala, Karyavattom, and STIC CUSAT.

Reference

Shakil M, Inayat U, Khalid NR, Tanveer M, Gillani SSA, Tariq NH, et al. Enhanced structural, optical, and photocatalytic activities of Cd–Co doped Zn ferrites for degrading methyl orange dye under irradiation by visible light. J Phys Chem Solids. 2022 Feb 1;161:110419.

Yousaf M, Nazir S, Akbar M, Akhtar MN, Noor A, Hu E, et al. Structural, magnetic, and electrical evaluations of rare earth Gd3+ doped in mixed Co–Mn spinel ferrite nanoparticles. Ceram Int. 2022 Jan 1;48(1):578–86.

Soufi A, Hajjaoui H, Elmoubarki R, Abdennouri M, Qourzal S, Barka N. Spinel ferrites nanoparticles: Synthesis methods and application in heterogeneous Fenton oxidation of organic pollutants – A review. Appl Surf Sci Adv. 2021 Dec 1;6:100145.

Tatarchuk T, Bououdina M, Judith Vijaya J, John Kennedy L. Spinel Ferrite Nanoparticles: Synthesis, Crystal Structure, Properties, and Perspective Applications. In: Fesenko O, Yatsenko L, editors. Nanophysics, Nanomaterials, Interface Studies, and Applications [Internet]. Cham: Springer International Publishing; 2017 [cited 2023 Apr 3]. p. 305–25. (Springer Proceedings in Physics; vol. 195). Available from: http://link.springer.com/10.1007/978-3-319-56422-7_22

Valenzuela R. Novel Applications of Ferrites. Zhukov A, editor. Phys Res Int. 2012 Mar 15;2012:591839.

Irfan M, Ayyaz M, Naz MY, Shukrullah S, Munir MM, Kamran K, et al. Testing of optical, dielectric and photocatalytic properties of Ce3+ doped cobalt–cadmium nanocomposite for high frequency devices and wastewater treatment. Ceram Int. 2022 Mar 15;48(6):8517–28.

Roman T, Ghercă D, Borhan AI, Grigoraș M, Stoian G, Lupu N, et al. Nanostructured quaternary Ni1-xCuxFe2-yCeyO4 complex system: Cerium content and copper substitution dependence of cation distribution and magnetic-electric properties in spinel ferrites. Ceram Int. 2021 Jul 1;47(13):18177–87.

STRUCTURAL AND OPTICAL PROPERTIES OF SAMARIUM DOPED $MgTiO_3$ PEROVSKITES

Meenu Venugopal[1*], Sajin S B[2], Riya Amado[2], Ancy Richard[2] and R. Satheesh[3a,b]

[1]Department of Physics, Christ Nagar College, Maranalloor, Koovalassery PO, Thiruvananthapuram, Kerala, India-695512
[2]Department of Physics, St. Xavier's College, Thumba, Thiruvananthapuram, Kerala, India-695568
[3a]Department of Physics, Research Centre-University of Kerala, Mar Ivanios College, Bethany Hills, Nalanchira, Thiruvananthapuram, Kerala 695015
[3b]Department of Physics, V.T.M.N.S.S College, Dhanuvachapuram, Thiruvananthapuram, Kerala, 695503
[*]Corresponding author: Meenu Venugopal, E-mail: drmeenuvenugopal20@gmail.com
Phone: 7012165805

Abstract

This study investigates the structural and optical properties of Samarium doped Magnesium Titanate perovskites. The X ray diffraction studies reveals the presence of anatase as well as rutile phase of the as prepared samples. Weight percentage of anatase phase is calculated to be 82.30% with cell volume 114.847 Å3. SEM analysis confirmed the uniform nature of the sample and the elemental analysis as well as concentration of chemical elements were obtained from EDS spectrum. EDS shows the presence of Ti and O without any other impurity. The photoluminescence spectra reveal the presence of emission peaks due to oxygen related defect states and charge transfer from Ti3+ to TiO_6^{2-} octahedra in Samarium doped $MgTiO_3$ samples. CIE coordinates shows that the emission from the sample is in the blue region of electromagnetic spectrum and the coordinates show a shift when doping concentration increases.

Keywords: TiO_2; Magnesium Titanate; Photoluminescence

Introduction

Recently, inorganic perovskite films find a wide range of applications in various optoelectronic devices, display devices, photovoltaic devices and solar cells. Titanium dioxide (TiO_2) is a versatile transition metal oxide with a wide variety of applications varying from optoelectronics to drug release [1-5]. The wide band gap of titanium dioxide makes it a suitable candidate in many optoelectronics applications including solar cells [6,7]. Recently, researchers have given much importance to the tailor the luminescent properties of TiO_2 using suitable rare earth doping. Doping of metal ions will result in the weakening of the bonding between oxygen ions which will result in the creation of oxygen vacancies. This will affect electronic and optical properties of the TiO_2 powder [8,9]. The present work discusses the structural and emission properties of undoped and Samarium doped $MgTiO_3$ perovskites.

Methods

The samples were prepared via solid state ceramic route method. The starting materials used for the synthesis of samples were Titanium Dioxide (HiMedia, India), Magnesium Oxide, 99% (CDH, India), Samarium Oxide, 99.9% (HiMedia, India). The starting materials for the preparation of undoped and Samarium doped MgTiO3 ceramic compounds are were taken in stochiometric ratios. The starting materials were weighed and were mixed thoroughly in acetone medium in an agate mortar for 2 hours. The as prepared samples were then dried and calcined at 1250°C for about 5 hours in an electrically heated furnace. The calcined powders were later grinded well. The as prepared samples were then analyzed for their structural properties.

The X-ray diffraction studies of the prepared film systems were studied using Philips XPERT PRO instrument using Cu-Kα radiation. The Scanning Electron Microscopy and Energy Dispersive Spectroscopy of the sample carried out using JEOL (Model JSM - 6390LV) instrument. The Photoluminescence spectra of the samples were measured using a Spectrofluorometer (Model FP 8500, Jasco International). The CIE colour coordinates based on CIE 1931 chromaticity calculations of the luminescence spectra were also discussed.

Results and discussion

Figure 1 and 2 shows the XRD patterns of TiO_2, Samarium doped $MgTiO_3$ ceramic compounds ceramic powder respectively. XRD peaks reveals the presence of anatase as well as rutile phase which is in agreement with JCPDS 21-1272 and JCPDS 21-1276 respectively. The diffraction peaks 25.40^0, 35.65^0, 48.64^0, 55.06^0, 57.05^0 for anatase correspond to the crystal planes (101), (004), (200), (211), (118). The peaks 27.88^0, 45.63^0, 58.82^0 corresponding to rutile crystal planes (110), (210), (002). The weight percentage of anatase phase is calculated using the equation [8,9]:

$$W_A = \frac{1}{1+1.26\,(I_R/I_A)} \qquad (1)$$

where I_A denotes the intensity of the strongest anatase reflection and I_R is the intensity of the strongest rutile reflection. In our case, the TiO_2 particles have a percentage of the anatase

phase equal to 82.30% as calculated by Eq. (1). The peaks corresponding to $MgTiO_3$ (indicated as * in the graph) were present at 30.55^0, 41.54^0, 51.22^0 which is in agreement with the JCPDS card number 02-0874. At high temperature, Ti ions reacted with Mg ions and formed new phases like Mg_2TiO_4. Peaks corresponding to Mg_2TiO_4 are present at 37.89^0 and is in agreement with the JCPDS card number 79-0830. For $MgTi_{0.90}Sm_{0.10}O_3$ and $MgTi_{0.95}Sm_{0.05}O_3$ ceramic powders the diffraction peaks show slight shift towards lower 2 theta values and it increases with doping concentration of Sm^{3+} ions. Also, for $MgTi_{0.90}Sm_{0.10}O_3$ sample the anatase peak corresponding to (101) shows a decrease in intensity. This shift and intensity variation is associated to TiO_2 lattice enlargement induced by Sm^{3+} doping. The ionic radii of Ti^{4+} and Sm^{3+} are 0.68 Å and 0.95 Å, respectively, and the possible outcomes of doping are, substitution of Ti^{4+} sites by Sm^{3+} or Sm^{3+} occupy interstitial sites of anatase structure. In our case, the shift towards the lower angle suggests a substitution of Ti^{4+} by Sm^{3+} [9]. The SEM image of TiO_2 in figure 3 reveals the uniform and regular sample surface. The average particle size is calculated from SEM analysis and is found to be about 282 µm. EDS spectrum in figure 4 provide the elemental analysis of sample, showing the chemical elements that are characteristic of TiO_2 ceramic compound. EDS shows the presence of Ti and O without any other impurity. Multiple regions in the surface were analyzed and revealed comparable concentrations of the chemical elements at the specimen's surface. Figure 5 gives the photoluminescence spectra of undoped and Samarium doped $MgTiO_3$ ceramic powders at 407nm excitation. A sharp peak is observed at 458 nm for samarium doped samples. For undoped samples the peak at 458 nm is having less intensity. After photoexcitation at 407 nm, the electrons in conduction band move through the ionic lattice, interact with the lattice ions and then localizes on a lattice site. The localized electron captures a hole and generates self-trapped excitons (STE). The localization of the STE depends on the length and compactness of the TiO_6 octahedra chain. The emission peak at 457 nm is with oxygen related defect states. The broad emission peak at 474 nm is ascribed to charge transfer transition from Ti^{3+} to TiO_6^{2-} octahedra. The broad emission at 537 nm can be attributed to oxygen defect centers [10]. The CIE chromaticity diagrams were calculated from the luminescence spectra of undoped and samarium doped $MgTiO_3$ ceramic powders. CIE chromaticity diagram of blue emitting $MgTiO_3$ ceramic powders for excitation under 407 is given in figure 6. It is evident from the figures that for samarium doped samples there is shift in the CIE coordinates from that of the undoped samples.

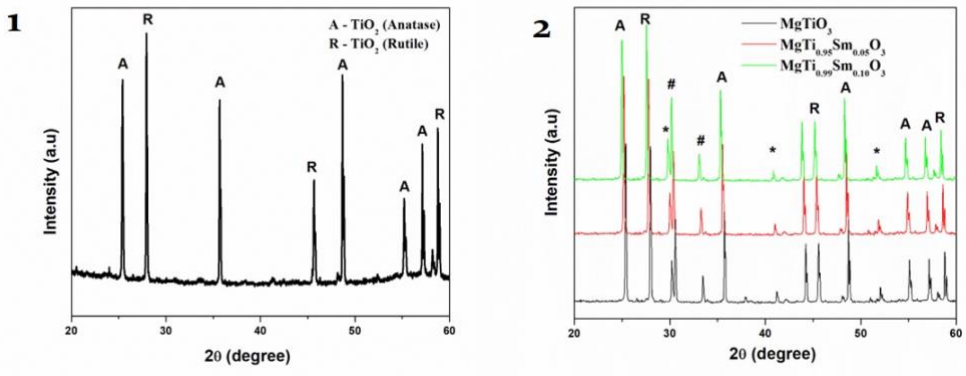

Figure 1) XRD pattern of TiO_2 2) Undoped and Samarium doped $MgTiO_3$

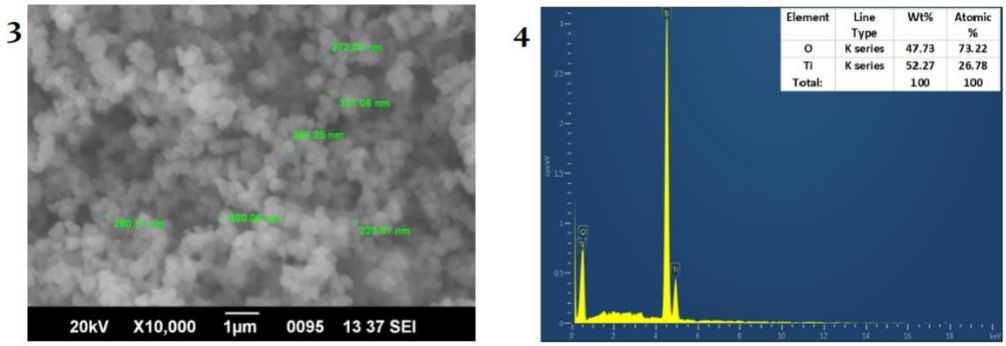

Figure 3) SEM analysis of TiO_2 ceramic powder 4) EDS spectrum of TiO_2

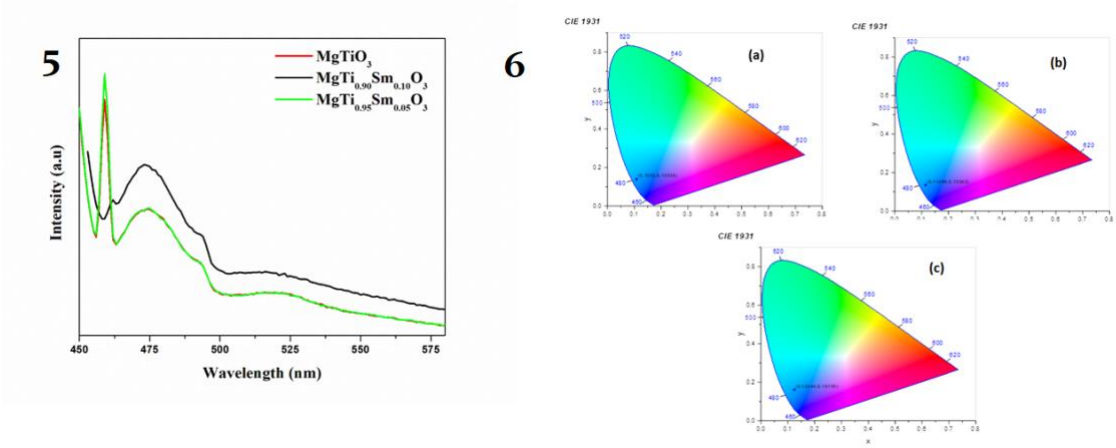

Figure 5) Photoluminescence spectra of undoped and Samarium doped $MgTiO_3$ 6) CIE coordinates of (a) $MgTiO_3$ (b) $MgTi_{0.90}Sm_{0.10}O_3$ and (c) $MgTi_{0.95}Sm_{0.05}O_3$

Conclusions

$MgTiO_3$, $MgTi_{0.90}Sm_{0.10}O_3$ and $MgTi_{0.95}Sm_{0.05}O_3$ ceramic powders were synthesized by the solid-state ceramic route method which is a comparatively easiest and low-cost method. Structural studies using Xray diffraction techniques reveals the presence of TiO_2, MgO, $MgTiO_3$ and Mg_2TiO_4 phases. For samarium doped samples the diffraction peaks show slight shift towards lower 2 theta values and it increases with doping concentration of Sm^{3+} ions. This shift and intensity variation is associated to TiO_2 lattice enlargement induced by Sm^{3+} doping that suggests a substitution of Ti^{4+} by Sm^{3+}. The photoluminescence spectra reveal the presence of emission peaks due to oxygen related defect states and charge transfer from Ti^{3+} to TiO_6^{2-} octahedra. CIE coordinates shows that the emission from the sample is in the blue region of electromagnetic spectrum and the coordinates show a shift when doping concentration increases. The intense blue emission of the samples makes it a suitable candidate for optoelectronic applications.

Acknowledgements

The authors acknowledge VTMNSS College, Dhanuvachapuram and STIC, Cochin University of Science and Technology for the analysis support.

References

W. Thitsartarn and S. Kawi, Green Chem., (2011) 13, 3423–3430

Kawashima, K. Matsubara, K. Honda, Bioresource Technology., 99 (2008) 3439–3443

X. Yu, Z. Wen, H. Li, S.Tu, J. Yan, Fuel., 90 (2011) 1868–1874

L. L. Hench, Int. J. Non-Cryst. Sol., (1970)250.

Afzal, Mater. Express, Vol. 4, No. 1, 2014

H. Li, H. Xu, J. Wang, J. Nat. Gas Chem., (2011), 20, 1-8

H. J. Beie, A. Gnörich, Sens. Actuators, B (1991), 4, 393-399

P. Z. Zambare, K. D. Girase, K. V. R. Murthy, O. H. Mahajan, Adv. Mat. Lett., (2013) 4, 577-581.

Ye M, Jia J, Wu Z, Qian C, Chen R, O'Brien PG, Sun W, Dong Y, Ozin GA. Advanced Energy Materials., (2017) 7(4),1601811

Gajdics M, Spassov T, Kovács Kis V, Béke F, Novák Z, Schafler E, Révész. Energies., (2020)13(3),563.

STUDY OF DOUBLE ALPHA DECAY PROPERTIES OF $^{221-232}$Pu ISOTOPES

G.M.Carmel Vigila Bai[1], M.Thenmozhi[2] and R. Racil Jeya Geetha[2]

1. Department of Physics, Government Arts and Science College, Konam, Nagercoil – 629 004.
2. Department of Physics, Nesamony Memorial Christian College, Marthandam- 629 165.
mthenmozhi9696@gmail.com
Affliated to Manonmaniam Sundaranar University, Abhishekapatti, Tirunelveli-12. Tamil nadu, India.

Abstract:

An identical alpha particles are simultaneously emitted from an unstable parent nucleus is known as double alpha radioactivity. The concept of double alpha decay was initially predicted by Yu. N. Novikov in 1979. Various theoretical models have been proposed to study the double alpha decay. Our Cubic plus Yukawa plus Exponential Model (CYEM) has already been used to compute the half life time of alpha decay, cluster decay, and spontaneous fission of radioactive nuclei. In this paper, we have predicted 2α-decay half lives for Plutonium isotopes $^{221-232}$Pu using our well known CYE model. Our predicted half life values are well-agreement with other theoretical models.

Keywords: Double alpha decay, CYEM, Half life time.

Introduction:

A radioactive nucleus will attempt to reach stability by ejecting nucleons (protons, neutrons) as well as other particles, or by releasing energy in the form of radiation is called radioactivity. An atomic nucleus spontaneously emits a single particle as well as double particles during radioactive decay. Some instance of double particle emissions are 2α, 2β[3,4], 2γ[5,6,7], 2p[8], 2n[8] radioactivities. Concurrent emission of two alpha particles of same nature, from radioactive nuclei is called double alpha decay. In 1979, Yu. N. Novikov[1] predicted the half life time of double alpha decay of various isotopes ^{148}Sm, ^{152}Gd, ^{156}Dy, ^{190}Pt and ^{234}U for the first time[2]. Multiple theoretical models exist to expound upon the properties of double alpha decay[9-11,13-19]. V.I. Tretyak [10,11] has reported, for the first time, an experimental half-life limit of double alpha decay of ^{209}Bi as 2.9×10^{20} years, utilizing data obtained from an experiment conducted by Marcillac[12].

In our previous paper[20], we have calculated the half-life values of radioactive nuclei with Z=89-91 and Z=126 by performing calculations for Double alpha decay and Beryllium

decay using our well known Cubic plus Yukawa plus Exponential Model (CYEM)[21]. Our current paper focuses, the feasibility of double alpha radioactivities from parent isotopes $^{221-232}$Pu, utilizing our CYE model with a two-sphere approximation.

Cubic Plus Yukawa Plus Exponential Model (Cyem):

To explore the decay characteristics of super heavy elements, we have used our realistic model called CYE model[21], in which we use a cubic potential in the pre-scission region which is connected by a Yukawa plus Exponential potential in the post scission region. Here the zero-point vibration energy is explicitly included without breaking the law of conservation of energy. The alpha particle pre-exists within the nucleus at a certain distance from the nucleus and the potential encountered by this alpha particle is purely coulomb. This potential as a function of r which is the centre of mass distance of the two fragments for the post scission region is given by,

$$V(r) = \frac{Z_1 Z_2 e^2}{r} + V_n(r) - Q \quad ; \qquad r \geq r_t$$

Where, nuclear interaction energy is denoted by the symbol $V_n(r)$ is expressed as

$$V_n(r) = -D\left[F + \frac{r - r_t}{a}\right]\frac{r_t}{r}\exp\left[\frac{r_t - r}{a}\right]$$

And $r_t = R_1 + R_2$ is the sum of their equivalent sharp surface radii. The depth constant D and the constant F.The shape of the potential barrier in the overlapping region which connects the ground-state and the contact-point is approximated by a third order polynomial in r suggested by Nix having the form

$$V(r) = -E_v + [V(r_t) + E_v]\left\{s_1\left[\frac{r - r_i}{r_t - r_i}\right]^2 - s_2\left[\frac{r - r_i}{r_t - r_i}\right]^3\right\} \; ; \qquad r_i \leq r \leq r_t$$

Where r_i is the distance between the centres of mass of two portions of a parent nucleus cut by a planar section into two pieces with volume asymmetry of the decay. Let a planar section cut the parent nucleus into two unequal portions with the masses of the heavy and light nuclei of the decay. If h_1 and h_2 are the heights of the heavy and light segments and R_0 is the radius of the parent nucleus, then

$$r_i = \frac{3}{4}\left[\frac{h_1^2}{R_0 + h_1} + \frac{h_2^2}{R_0 + h_2}\right]$$

For calculating the zero - point vibration energy E_v,

$$E_v = \frac{\pi\hbar}{2}\left[\frac{\left(\frac{2Q}{\mu}\right)^{1/2}}{(C_1 + C_2)}\right]$$

The central radii C_1 and C_2 of the fragments are given by

$$C_i = 1.18\,A^{1/3} - 0.48 \qquad (i = 1, 2)$$

And $\mu = \frac{m_1 m_2}{m_1 + m_2}$

Where μ is the reduced mass of the system and m is the mass of the nucleon. Half-life time value is calculated by using the formula

$$T = \frac{1.433 \times 10^{-21}(1 + \exp K)}{E_v}$$

Result and Discussion:

In nuclear transition, double alpha decay is an important mechanism and is studied in the framework of our CYE model. In this paper, Table denotes the computed half-lives using CYE model and its comparison with UDL values of double alpha decay from parent nuclei with the mass range is 221≤ A ≤232. Subsequently figure showing the relation connecting logarithm of the 2α half-life in seconds Vs the mass number of daughter nuclei $^{213\text{-}224}$Th of CYEM and UDL.

Conclusion:

Nuclear decay (A,Z) ⟶(A-8, Z-4)+2α with simultaneous emission of two alpha particles is studied using our well known CYE model with two sphere approximation. In our present work, we have estimated the double alpha radioactivity half lives of Plutonium isotopes with mass number varying from 221 to 232 using our model without inclusion of deoformation effects. Our predicted half life values are align well with Universal Decay Law (UDL). We anticipate that our current predictions will prove beneficial for future research in this field.

Table: Calculated half life of Plutonium 228-232 isotopes using CYEM.

Parent nuclei	Daughter nuclei	$Q_{2\alpha}$ (MeV)	Log $T_{1/2}$ (s)	
			UDL	CYEM
^{221}Pu	^{213}Th	18.96017	11.96093	12.13
^{222}Pu	^{214}Th	19.51517	10.63326	10.69
^{223}Pu	^{215}Th	20.34917	8.753466	8.66
^{224}Pu	^{216}Th	20.12117	9.218781	9.15
^{225}Pu	^{217}Th	19.24417	11.17328	11.25
^{226}Pu	^{218}Th	18.41317	12.15346	13.37
^{227}Pu	^{219}Th	17.46017	15.60335	16.01
^{228}Pu	^{220}Th	16.56817	18.08625	18.68
^{229}Pu	^{221}Th	15.60017	21.02378	21.84
^{230}Pu	^{222}Th	14.87917	23.39071	24.38
^{231}Pu	^{223}Th	14.07417	26.25163	27.46
^{232}Pu	^{224}Th	13.51517	28.38043	29.76

Figure: Graphical representation between Mass number of daughter nuclei Vs Log $T_{1/2}$ (s)

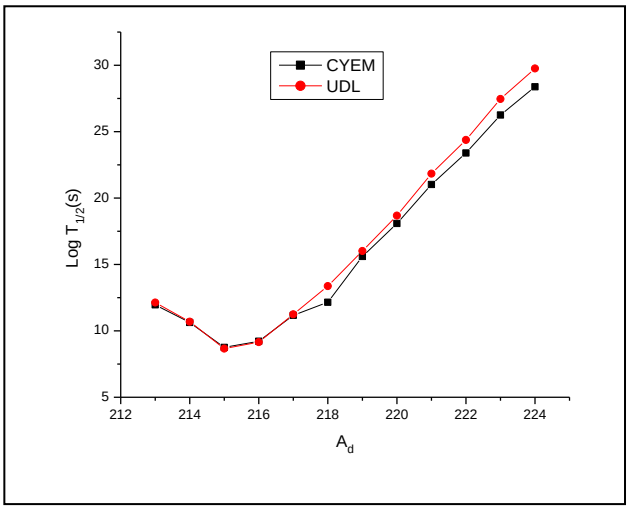

Reference:

Yu.N.Novikov, Workshop on U-400 Program.JINR (1979)p.15.

E.E.Berlovich, Yu.N.Novikov, Modern Methods of Nuclear Spectroscopy 1986, Nauka (Leningrad, 1988) p.107.

M. Goeppert-Mayer, Double beta-disintegration, Phys. Rev. 48 (1935) 512.

W.H. Furry, On transition probabilities in double beta-disintegration,

Phys. Rev. 56 (1939) 1184.

M. Goeppert, Uber die Wahrscheinlichkeit des Zusammenwirkens zweier Lichtquanten in

einem Elementarakt, Naturwissenschaften 17 (1929) 932.

M. Goeppert-Mayer, Uber Elementarakte mit zwei Quantensprungen,

Ann. Phys. (Leipz.) 401 (1931) 273.

G. Sutter, Etude experimentale de la double emission gamma dans les transitions monopo-laires des noyaux 16O, 40Ca et 90Zr, Ann. Phys. (Paris) 13 (1963) 323

M. Pfutzner et al., Radioactive decays at limits of nuclear stability,

Rev. Mod. Phys. 84 (2012) 567.

D.N.Poenaru and M.Ivascu, J.Physique Lett.46(1985) L-591-L-594.

V.I.Tretyak, Nucl.Phys.At.energy 22,121 February (2021).

V.I.Tretyak, Nucl.Phys.At.energy 22,121 September (2021).

P.de Marcillac et.al., Nature 422(2003) 876.

K.P.Santhosh and Tinu Ann Jose, PHYSICSL REVIEW C 104, 064604 (2021).

F. Mercier, J.Zhao, J.P.Ebran, E.Khan, T.Niksic, D.Vretner, Phys.Rev. Lett.127 (2021) 012501.

F. Mercier, J.Zhao, J.P.Ebran, E.Khan, T.Niksic, D.Vretner, Nuovo Cimento 45 C (2022) 59.

Ch. Theisen, E. Khan, CERN-INTC-2022-016 / INTC-CLL-049, https://cds.cern.ch/record/2809125/files/INTC-CLL-049.pdf, May 2022.

K.P.Santhosh, Tinu Ann Jose, and N.K. Deepak, PHYSICAL REVIEW C, 105, 054605 (2022).

K.P.Santhosh, Megha chandran, Anusree Radhakrishnan, Proceedings of the DAE Symp. On Nucl. Phys. 66 (2022).

V.Yu. Denisov, Physics Letters B 835 (2022) 137569.

G.M.Carmel Vigila Bai, M.Thenmozhi, Proceedings of ICIRC (2023).

G.Shanmugam, G.M.Carmel Vigila Bai and B. Kamalaharan, Phys. Rev. C51, 2616 (1995).

INVESTIGATION OF THE STRUCTURAL PARAMETERS OF METHAMPHETAMINEUSING DENSITY FUNCTIONAL THEORY

Arya B[1,2], P Sachidanandan[3,4], and AnandaKumar V M[1,5]

[1]Mahatma Gandhi College, Thiruvananthapuram, Kerala
[2]University College, Thiruvananthapuram, Kerala
[3]Kerala Police Academy, Thrissur, Kerla
[4]State Forensic Science Laboratory, Thiruvananthapuram, Kerla
[5]VTMNSS College, Dhanuvachapuram, Kerala

Abstract

The structural parameters of methamphetamine, an important psychoactive drug, are analysed experimentally and computationally using spectroscopic and DFT methods. The molecular structureis optimized using B3LYP functional with 6-311+G(2d,p) and augmented cc-pVTZ basis sets andthe values are compared with those of the published crystal data. **Quantum Theory of AtomsIn Molecules** is used to analyse the electron density distributions of the molecule. The molecular electrostatic potential surface, frontier orbital analysis, and global and local reactivity descriptors are used to predict the reactivity of the molecule. Electron localization function and NCI analysis has been carried out to visualize the covalent and non-covalent interaction of the molecule inorder to havea comprehensive understanding of the nature and strength of chemical bonds. NBO analysis has also been carried out to investigate the hybridisation, charge transfer and correlation effects. The results from this study can be used for the development of novel chemical sensors for drug detection and to predict the structure-activity relationship of the amphetamine derivatives. Also these findings offer valuable insights into the nature and strength of chemical bonds, allowing scientists to optimize drug molecules and improve their efficacy.

Introduction

Methamphetamine is a central nervous system(CNS) stimulant that is used in the treatment of attention deficit hyperactivity disorder (ADHD), narcolepsy, and obesity. It exists as two enantiomers: levom- methamphetamine and dextromethamphetamine. Methamphetamine activates receptors in the brain and increases the activity of many neurotransmitters, especially norepinephrine and dopamine [1]. It is a pre- scription drug in many countries and unauthorized possession and distribution of methamphetamine are of- ten tightly controlled due to the significant health risks associated with recreational use. N methylphenethy- lamine or methamphetamine is a positional isomer of amphetamine that differs only in the placement ofthe methyl group. Methamphetamine is also an indirect sympathomimetic amine, but its effects are more powerful than those of amphetamine [2]. It produces greater stimulation of the central nervous system andis a more potent stimulant and euphoric drug than amphetamine. It is highly addictive, and its abuse hasbeen linked to many serious health problems.

Density functional theory (DFT) is the most successful and promising quantum chemical approach to calculate the ground-state properties of atoms and molecules. The density functional approach allows thecalculation of the entire energy surface, the structure and related properties from knowledge of the electron density distribution alone. DFT technique can theoretically predict the chemical shifts in NMR, structural parameters, and chemical reactivity with good accuracy. Other advantages of DFT methods include low computational cost, good accuracy for structures and thermochemistry, and use of conceptually simple electron density term which is dependent on just three variables as compared to the more complicated anddifficult to interpret electronic wave function[3] The present study explores the structural properties of the methamphetamine molecule using DFT and TD-DFT techniques. Molecular electrostatic potential (MEP) surface analysis, Frontier molecular orbitals analysis, and NBO analysis have also been carried out. NBO analysis will provide more insight into the possible intermolecular interaction of the title molecule which is useful for studying pharmacological action as well as for sensor development. Calculation of global and local reactivity descriptors is done to predict the reactivity sites and type of the molecule. NCI analysis andElectron localization function analysis have been carried out to understand the covalent and non covalentinteraction of the molecule.

The above investigation helps in understanding the biological mechanism of action like drug-receptor interaction and the binding mechanism of various amphetamine derivatives. This molecule and its deriva-tives are under international regulation and control. In most countries, they are regulated under drug laws and hence their detection from various matrices is essential for law enforcement. DFT studies are provedto be useful for this purpose [4].

Computational Details

All quantum mechanical calculations were performed with Guassian-16 program[5]. The density functional theory with the exchange correlational functional B3LYP [6](three-parameter hybrid functional for the ex- change part and the Lee-Yang-Parr correlational functional)is used for computational calculations[7]. The 6-311 +G set supplemented with two sets of diffuse functions and one set of polarisation functions and augmented cc-pVTZ set have been utilized for the optimization of molecular structure.

The molecular electrostatic potential surface is developed by the B3LYP/6-311+G(2d,p) method whichdescribes the charge distribution of the molecule and helps to find out the reactive sites of the molecule [8,9].NBO analysis has been carried out to analyse the hyper conjugative and delocalized charge interactionsof the molecule [10]. The ionisation potential(I) and the electron affintiy(E) have been calculated using the delta SCF method[11]. Various global reactivity descriptors such as chemical potential, chemical hardness,softness, electrophilicity and nucleophilicity have also been calculated using finite difference approximation. To find out the site selectivity of a system, the Fukui function is also calculated which is one of the most commonly used local reactivity descriptors [12, 13, 14]. “Quantum theory of Atoms In Molecules” [15]wasemployed to analyse the Electron Localized Function and Non-covalent interaction using multiwfn and VDM softwares.

Results and Discussion

Geometrical optimization

The molecular structure of the compound in the ground state has been optimized using Gaussian-16 software using density functional theory with B3LYP functional and 6-311+G(2d,P)/ccPVTZ basic set.The optimized structure and the scheme of the numbering of atoms are shown in figure 1. Comparisonof the geometrical parameters of methamphetamine with experimental values[16] are presented in Table 1The thermodynamic parameters of the compound such as total thermal energy, the rotational constantsand the dipole moment values obtained from B3LYP/6-311+ G(2d,p) basic sets are shown in table 2.

Frontier Molecular Orbitals (FMO)

The “Highest Occupied Molecular Orbital (HOMO) and the Lowest Unoccupied Molecular Orbital (LUMO)”are the most important orbitals that determine the chemical reactivity, which are called frontier orbitals[17]. The energy of HOMO determines its electron giving capacity and LUMO energy describes its electron accepting abilty[18]. That means HOMO energy characterizes the nucleophilic component and LUMO en- ergy characterizes electrophilc component of a molecule. The energy difference between HOMO and LUMO is called energy gap which is a critical parameter in determining the chemical

stability of a molecule and eventual charge transfer interactions within a molecule. Hence the determination of energies of HOMO and LUMO and their energy gap are very important in quantum chemical calculations for determining the chemical reactivity of a molecule.

The 3D plots of the frontier orbitals and their energies are shown in figure 2 and it shows that the HOMO of the molecule is concentrated more on the NH group and lumo is concentrated on the phenyl group. Thus NH group has more nucleophilic character and act as a favorable site for the electron deficient groups. The calculated frontier molecular energy gap is 5.7604 eV and the lower value in the

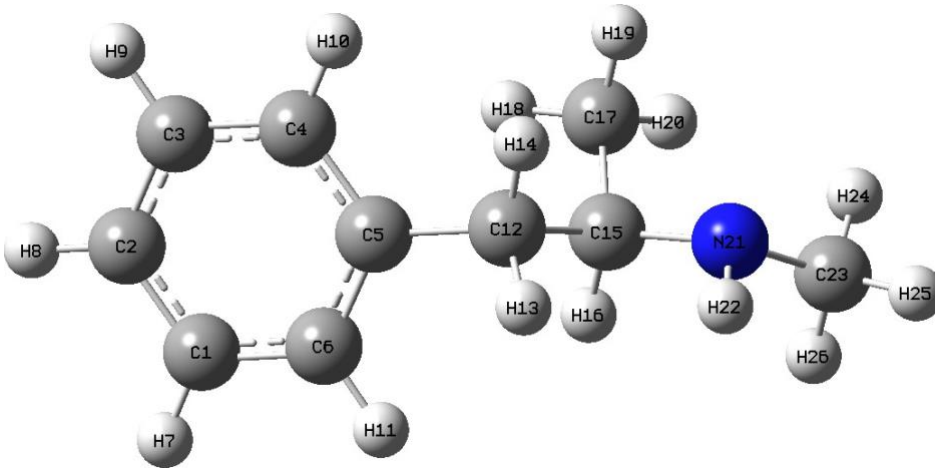

Figure 1: The optimized structure of methamphetamine

Table 1: Structural parameters of methamphetamine calculated using "B3LYP/6.311+G(2d,p)" and"B3LYP/cc-pVTZ" methods

Structural parameters	B3LYP/6-311+G(2d,p)	B3LYP/cc-pVTZ	Exptl.value
Bond distance			
$C_1 - C_2$	1.39	1.39	1.38
$C_2 - C_3$	1.39	1.39	1.39
$C_3 - C_4$	1.39	1.39	1.39
$C_4 - C_5$	1.4	1.4	1.39
$C_5 - C_6$	1.4	1 .4	1.39
$C_1 - C_6$	1.39	1.39	1.39
$C_5 - C_{12}$	1.51	1.51	1.51
$C_{12} - C_{15}$	1.54	1.54	1.51
$C_{15} - N_{21}$	1.47	1.47	1.5
$C_{15} - C_{17}$	1.53	1.53	1.51
$N_{21} - C_{25}$	1.47	1.47	1.48
$C_6 - H_{11}$	1.08	1.08	1.0
$C4 - H_{10}$	1.08	1.08	0.90
$C_3 - H_9$	1.08	1.08	0.95
$C_2 - H_8$	1.08	1.08	0.9
$C_1 - H_7$	1.08	1.08	0.98
$C_{12} - H_{14}$	1.09	1.09	1.0
$C_{12} - H_{13}$	1.09	1.09	1.0
$C_{15} - H_{16}$	1.05	1.1	0.9
$C_{17} - H_{18}$	1.09	1.09	1.0
$C_{17} - H_{19}$	1.09	1.09	0.94
$C_{17} - H_{20}$	1.09	1.09	0.93
$N_{21} - H_{22}$	1.01	1.01	0.91
Bond Angle			
$C_1C_2C_3$	119.4	119.4	119.3
$C_2C_3C_4$	120.1	120.1	120.5
$C_3C_4C_5$	120.1	120.1	120.5
$C_4C_5C_6$	118.09	118.09	118.7
$C_5C_6C_1$	121.1	121.1	120.8
$C_6C_1C_2$	120.2	120.2	120.2
$C_6C_5C_{12}$	121.3	121.3	120.8
$C12C_15C_{17}$	111.87	111.87	113.9
$C_4C_3H_9$	119.8	119.8	119.6
$C_{12}C_{15}N_{21}$	108.05	108.05	106.2
$C_{17}C_{15}N_{21}$	110.63	110.63	109.9

Table 2: The thermodynamic parameters of methamphetamine calculated using theB3LYP/6.311+G(2d,p) basic set

Thermodynamic parameters	B3LYP/6-311+G(2d,p)
SCF energy(Hartree)	-444.7983
Total thermal energy((Kcal.mol^{-1})	151.32
Vibrational energy((Kcal.mol^{-1})	149.354
Zeropoint Vibrational energy (Kcal.mol^{-1})	144.1054
Heat capacity at constant volume (cal.mol^{-1}K^{-1})	37.924
Entropy ((cal.mol^{-1}K^{-1})	104.905
Rotational Constants(GHz)	
A	2.8593
B	0.5432
C	0.5057
Dipole moment (Debye)	
μ_x	0.0460
μ_y	-0.8819
μ_z	-0.2317
$\mu Total$	0.9130

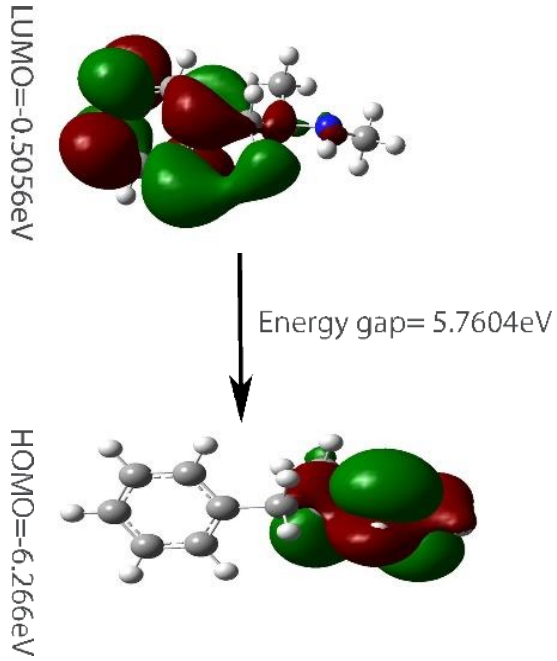

Figure 2: Frontier orbitals of methamphetamine

HOMO and LUMO energy gap enhances intra molecular charge transfer interactions within the moleculewhich influences its chemical and biological activities.

Table 3: Calculated values of ionization potential, electron affinity and global reactivity descriptors ofmethamphetamine using B3LYP/6-311+G(2d,p) method

Parameters	Values
Ionization potential (I) (eV)	7.59
Electron Affinity(A) (eV)	-0.7586
Chemical Hardness (η)	4.1729
Chemical Softness(s)	0.1198
Chemical Potential (μ)	-3.4143
Electronegativity (χ)	3.4143
Electrophilicity Index (ω)	1.3968

Global reactivity descriptors

The global reactivity descriptors such as chemical hardness, softness, chemical potential, electronegativ- ity and electrophilicity index are important parameters for understanding the reactivity and stability of molecular systems. The global reactivity descriptors of the title molecule have been calculated using B3LYP/6-311+G(2d,p) basic set using finite difference approximations [19, 20, 21].

The hardness of the molecule is ;

$$\eta = \frac{I - A}{2} \quad (1)$$

The softness of the molecule is ;

$$S = \frac{1}{2\eta} \quad (2)$$

The chemical potential of the molecule is;

$$\mu = -\frac{I + A}{2} \quad (3)$$

The electronegativity of the molecule is;

$$\chi = \frac{I + A}{2} \quad (4)$$

The electrophilicity index of the molecule is;

$$\omega = \frac{\mu^2}{2\eta} \quad (5)$$

where I is the ionization potential and A is the electron affinity of the molecule.

Ionization potential is the energy needed to remove an electron from a molecule and hence high ion- ization energy indicates high stability and chemical inertness. Electron affinity is the amount of energy released when an electron is added to a neutral atom. The ionization potential(I) and the electron affin- ity(E) have been calculated using the delta SCF method[22].

$$I = E(N - 1) - E(N) \quad (6)$$

$$E = E(N) - E(N + 1) \quad (7)$$

where E (N) , E (N 1) andE (N + 1) are the energies of N, N-1 and N+1 electron systems.

The chemical potential(μ) describes the escaping tendency of an electron and as chemical potential becomes more negative, it is more difficult to lose an electron. Electronegativity (χ), represents the abilityof molecules to attract electrons. Hardness (η) and softness (S) are useful concepts for understanding the behaviour of chemical systems. A hard molecule has a large energy gap and a soft molecule has a small energy gap. Therefore, soft molecules will be more polarizable than hard molecules. Electrophilicity (ω) is a measure

of the stabilization energy when the system gets saturated by electrons. A more reactive nucleophile is characterized by a lower value of ω, while higher values indicate the presence of a good electrophile [23].

The electron affinity,ionization potential [23] and global reactivity descriptors of the title molecule arecalculated and tabulated in table 3.The values of global reactivity descriptors showed that the molecule under study is a soft molecule and a reactive nucleophile.

Molecular Electrostatic Potential Analysis

The molecular electrostatic potential map illustrates the charge distribution of a molecule three-dimensionally.So it is a critical factor for understanding the reactive sites of electrophilic and nucleophilic attacks of a molecule. This map also help to understand the different polar regions of a molecule. This is a useful tool to identify the net electrostatic effect caused due to total charge distribution. The molecular electrostaticpotential at a point in the space can be expressed as

$$V(r) = \sum_A \frac{Z_A}{|R_A - r|} - \int \frac{\rho(r)dr'}{\vec{r}' - \vec{r}.} \qquad (8)$$

where Z_A is the charge on nucleus A located at R_A and ρ(r) is the electron density function. The first and second terms represent the contribution by the nuclei and electrons of the molecule to the electrostatic potential produced at the point r. The electron density surface mapped with electrostatic potential revealsthe shape, size, charge density distribution and site of chemical reactivity of a molecule [24, 25]. Using

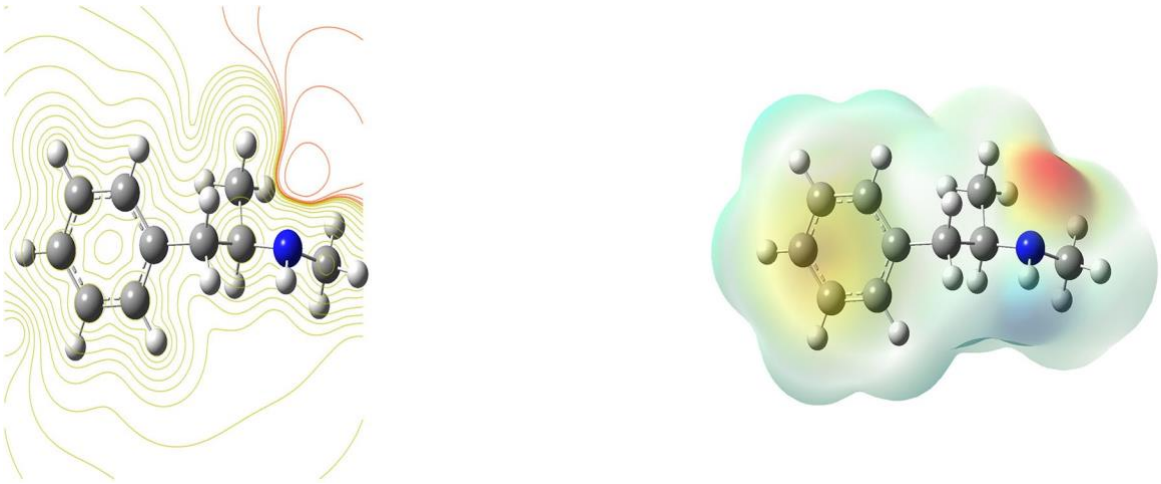

Figure 3: Electron density and Electrostatic potential map of the title molecule using the B3LYP/6-311+G(2d,p) in the range -4.207e-2 to +4.207e-2

Gaussview program, the molecular electrostatic potential surface have been visualized. A high electrostatic potential represents the relative lack of electrons and a low electrostatic potential indicates an abundance of electrons in that region. The surface is colour coded according to the variation in the electrostatic potential [26]. The red colour indicates the lowest electrostatic potential, blue colour represents the highest electrostatic potential and green colour indicates zero electrostatic potential. The electrostatic potential increases in the order red<orange<yellow<green<blue. The total electron density and the electrostatic potential surface of the molecule are constructed by using the B3LYP/6-311+G(2d.p) method. The total electron density surface mapped with the electrostatic potential and the contour map of the electrostatic otential is shown in figure 3. According to the result, the lowest electrostatic potential region is over the nitrogen atom due to the presence of lone pair electrons while the positive potential sites are around the hydrogen atoms. The negative potential regions or the lowest electrostatic potential regions of the molecule are expected to be the sites of nucleophilic attack while the positive potential regions are expected to be the sites of electrophilic attack. The green area over the aromatic ring represents zero electrostatic potential region leaving a more electrophilic region in the plane of hydrogen atoms.

Electron localized function and NCI analysis

"Electron localized function" provides a detailed description of the electron density distribution in a molecule, which is useful in understanding the chemical bonding and reactivity of molecules. ELF is based on the idea that the distribution of electrons in a molecule can be described in terms of a series oflocal electron pairs [27] These local electron pairs are defined as regions in the molecule where the electron density is relatively high and the probability of finding an electron is high. It is an alternative way to represent electron pair probability which is six dimensional and hence difficult to visualize.[28]

Non-covalent interactions play a crucial role in various biological, chemical, and physical processes, including protein folding, molecular recognition, and drug design. NCI analysis aims to provide a detailed understanding of the strength and directionality of non-covalent interactions, such as hydrogen bonding, -stacking, van der Waals forces, and electrostatic interactions. NCI analysis is based on the electron densitydistribution in a molecule and is used to identify and quantify the non-covalent interactions that contributeto the stability of the molecule.[29] NCI Anaysis together with Electron Localized function is particularly

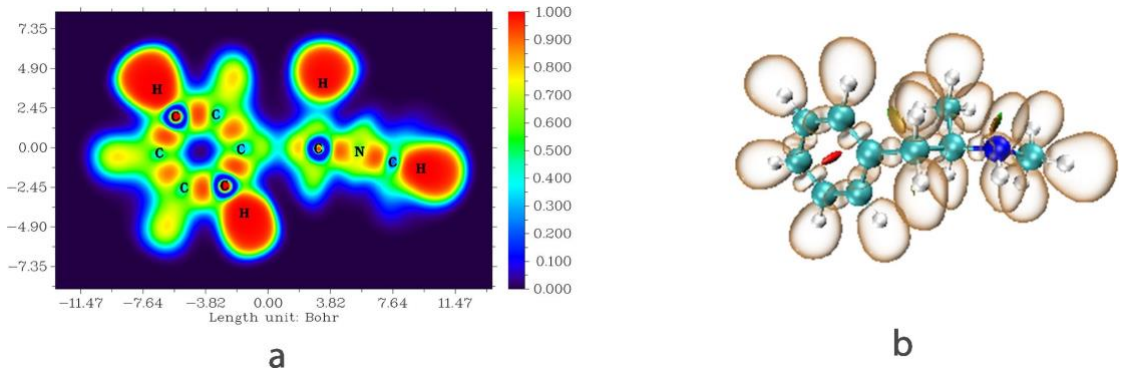

Figure 4: Electron Localized Function and NCI analysis of methamphetamine

Useful in rational drug design and materials science, where the understanding of covalent/non-covalent interactions is critical to developing effective drugs and materials. Figure 4 presents electron localization function and NCI analysis results calculated using multiwfn and VMD. The red colored region of the ELF map represents highest ELF value which indicates the presence of a covalent bond or a lone pair and the violet region represents lowest ELF. Both maps show the presence of a bond attractor between the core attractors which indicates a shared electron attraction. Hydrogen has no core attractor and large domain around hydrogen indicates the presence of more negative character and high electron localization. In theNCI analysis map, the red colour region at the centre of benzene ring represents strong repulsion region due to steric interaction. The green colour region represents the vdW interction region where the electron density is minimum. Methamphetamine has one strong repulsion region and two weak interaction regionsas marked in the figure.

NBO Analysis

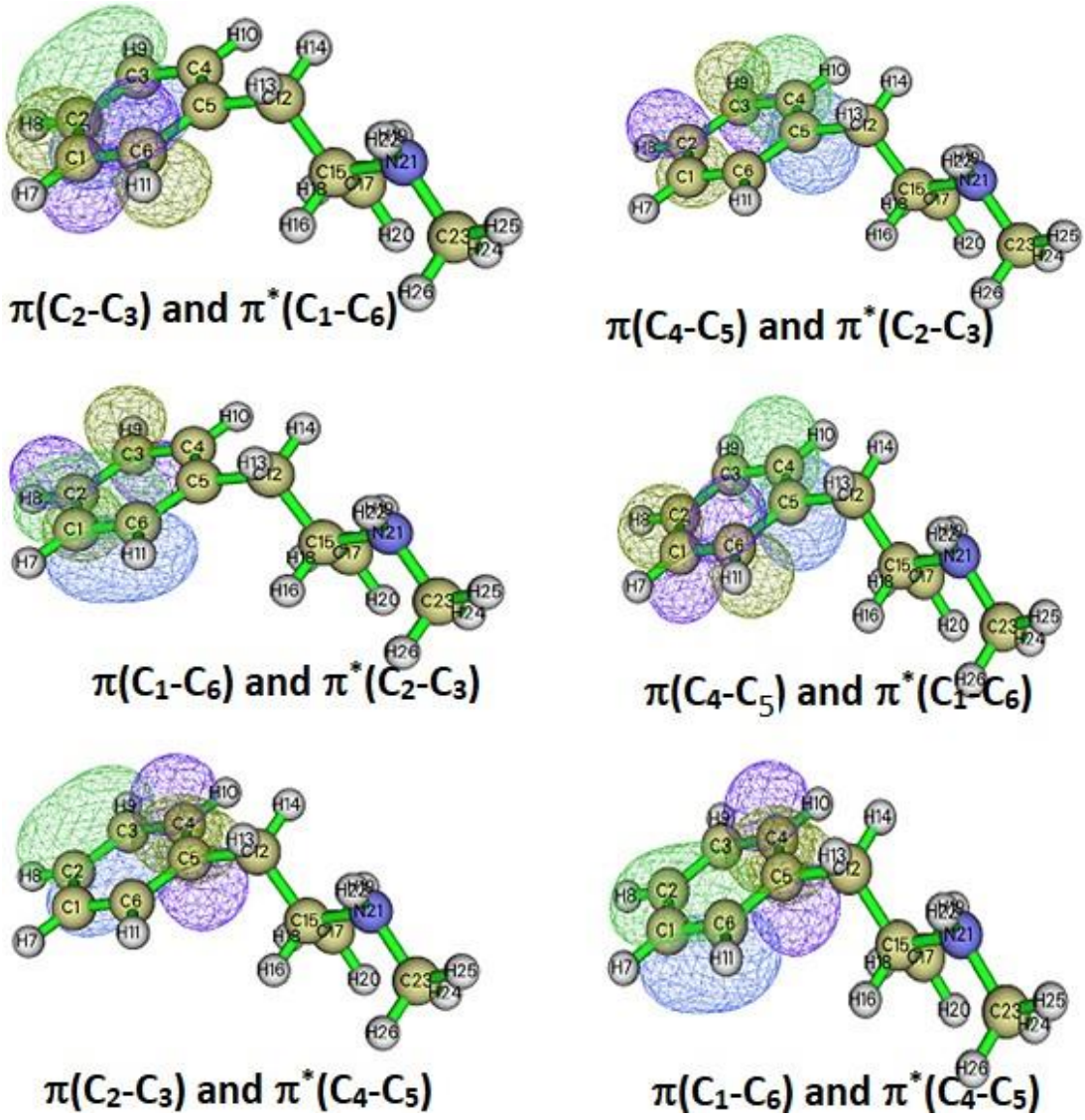

Figure 5: Highly overlapping acceptor and donor natural bonding orbitals of methamphetamine “Natural bonding Orbital Analysis” is most efficient tool for analysing charge transfer, hybridization and

Table 4: Second Order Perturbation Theory

Sl.No	Donor NBO(i)	Acceptor NBO (j)	E(2) (Kcal/mol)	E(j)-E(i) (a.u)	F(i,j) (a.u)
1			1.27	0.060	
2.			1.12	0.057	
3.			0.28	0.067	
4.			0.29	0.070	
5.			1.09	0.057	
6.	$\sigma (C_1 - C_6)$	$\sigma^* (C_5 - C_6)$	1.08	0.058	
7.	$\sigma (C_1 - C_6) \pi (C_1 - C_6) \pi (C_1 - C_6) \sigma (C_1 - H_7) \sigma (C_1 - H_7) \pi (C_4 - C_5) \pi (C_4 - C_5) \sigma (C_2 - H_8) \sigma (C_2 - H_8) \sigma (C_3 - C_4) \sigma (C_3 - C_4) \sigma (C_3 - H_9) \sigma (C_3 - H_9) \sigma (C_4 - C_5) \pi (C_2 - C_3) \pi (C_2 - C_3) \sigma (C_5 - C_6) \sigma (C_5 - C_6) \sigma (C_6 - H_{11}) \sigma (C_6 - H_{11}) \sigma (C_{12} - H_{13}) \sigma (C_{12} - H_{14}) \sigma (C_{17} - H_{20}) \sigma (C_{23} - H_{25})$ LP(1)(N_{21}) LP(1)(N_{21})	$\sigma^* (C_5 - C_{12}) \pi^* (C_2 - C_3) \pi^* (C_4 - C_5) \sigma^* (C_5 - C_6) \sigma^* (C_5 - C_6) \pi^* (C_1 - C_6) \pi^* (C_2 - C_3) \sigma^* (C_1 - C_6) \sigma^* (C_3 - C_4) \sigma^* (C_4 - C_5) \sigma^* (C_5 - C_12) \sigma^* (C_1 - C_2) \sigma^* (C_4 - C_5) \sigma^* (C_3 - C_4) \pi^* (C_4 - C_5) \pi^* (C_1 - C_6) \sigma^* (C_1 - C_6) \sigma^* (C_4 - C_5) \sigma^* (C_1 - C_2) \sigma^* (C_4 - C_5) \sigma^* (C_{15} - C_{17}) \sigma^* (C_5 - C_6) \sigma^* (C_{12} - C_{15}) \sigma^* (C_{15} - N_{21}) \sigma^* (C_{15} - H_{16}) \sigma^* (C_{23} - H_{26})$	0.28	0.068	
8.			0.29	0.067	
9.			1.09	0.058	
10.			1.09	0.058	
11			1.27	0.060	
12.			1.12	0.058	
13.			1.09	0.057	
14.			1.09	0.058	
15.			1.27	0.057	
16.			0.28	0.066	
17.			0.29	0.07	
18.			1.27	0.058	
19.			1.26	0.058	
20.			1.09	0.057	
21.			1.09	0.063	
22.			0.88	0.048	
23.			1.06	0.060	
24.			0.87	0.047	
25.			0.86	0.049	
26.			0.67	0.065	
27.			0.67	0.064	

delocalization effects. Instead of using unlocalized electron representations, this method utilizes localized forms based on electron density to describe the system [30] A set of high occupancy NBO's are employed to represent the molecular system with each NBO being doubly occupied. Small deviations from this idealized stucture appears as delocalization effects. As detailed in "NBO-7 Program manual" by Frank Weinhold and Eric D. Glendening[31] "NBO program offers a comprehensive analysis of NBO interactions, based on the second-order perturbation theory . The NBO program provides an estimation of the stabilization energy associated with electron delocalization between donor and acceptor NBOs using the following equation is the Fock matrix element between NBOs i and j,

with energies ϵ_σ and ϵ^*_{σ}. n_σ represents the population of the donor orbital, and δE represents the energy difference between donor and accept or orbitals. The larger $E^{(2)}$ value indicates the strong interaction between the corresponding donor andacceptor natural bonding orbitals and a greater tendency for delocalization effects".

Table 4 presents the results of the second order perturbation theory analysis of the NB0's. Only stabilization energy values greater than 3 KJ/mol are listed in the table. The analysis reveals that the interaction of $\pi\,(C_1 - C_6)$ and $\pi\,(C_4 - C_5)$ with $\pi^*\,(C_2 - C_3)$ results in stabilization energy values (E^2)of 19.75 and 19.32 KJ/mole, respectively. Similarly, the interaction of $\pi\,(C_1 - C_6)$ and $\pi\,(C_2 - C_3)$ with

Table 5: Hirshfeld charges, condensed Fukui functions and dual descriptors of methamphetamine calculatedusing B3LYP/6-311+G(2d,p) basic set with Multiwfn

atom	Hirshfeld charges			Condensed Fukui Functions			CDD
q(N)	q(N+1)	q(N-1)	f-	f+	f0		
1(C)	-0.0414	-0.0750	0.0185	0.0599	0.0336	0.0467	-0.0263
2(C)	-0.0446	-0.0841	0.0355	0.0801	0.0395	0.0598	-0.0406
3(C)	-0.0410	-0.0734	-0.0047	0.0363	0.0324	0.0344	-0.0039
4(C)	-0.0410	-0.0631	0.0098	0.0507	0.0221	0.0364	-0.0287
5(C)	0.0084	-0.0013	0.0563	0.0479	0.0097	0.0288	-0.0382
6(C)	-0.0434	-0.0704	-0.0184	0.0250	0.0270	0.0260	0.0020
7(H)	0.0391	-0.0336	0.0711	0.0320	0.0728	0.0524	0.0408
8(H)	0.0391	-0.0303	0.0749	0.0358	0.0694	0.0526	0.0337
9(H)	0.0395	-0.0290	0.0674	0.0279	0.0685	0.0482	0.0405
10(H)	0.0379	-0.0096	0.0637	0.0258	0.0475	0.0367	0.0218
11(H)	0.0362	-0.0605	0.0583	0.0221	0.0967	0.0594	0.0746
12(C)	-0.0487	-0.0679	-0.0352	0.0135	0.0193	0.0164	0.0058
13(H)	0.0291	-0.0320	0.0491	0.0200	0.0610	0.0405	0.0410
14(H)	0.0312	0.0007	0.0548	0.0237	0.0304	0.0270	0.0067
15(C)	0.0262	0.0171	0.0490	0.0228	0.0090	0.0159	-0.0138
16(H)	0.0121	-0.0187	0.0581	0.0460	0.0307	0.0384	-0.0153
17(C)	-0.0918	-0.1082	-0.0794	0.0125	0.0163	0.0144	0.0039
18(H)	0.0279	0.0146	0.0410	0.0131	0.0133	0.0132	0.0002
19(H)	0.0270	0.0063	0.0483	0.0212	0.0208	0.0210	-0.0004
20(H)	0.0282	0.0093	0.0453	0.0172	0.0189	0.0180	0.0017
21(N)	-0.1488	-0.1658	0.0095	0.1583	0.0169	0.0876	-0.1414
22(H)	0.0875	0.0194	0.1419	0.0545	0.0681	0.0613	0.0136
23(C)	-0.0458	-0.0826	-0.0064	0.0394	0.0368	0.0381	-0.0026
24(H)	0.0302	0.0156	0.0616	0.0314	0.0146	0.0230	-0.0169
25(H)	0.0333	-0.0265	0.0654	0.0321	0.0598	0.0459	0.0277
26(H)	0.0142	-0.0367	0.0645	0.0503	0.0509	0.0506	0.0006

π^* (C_4 C_5) results in stabilization energy values (E^2) of 21.05 and 19.6 KJ/mole, respectively. Moreover, the interaction of π (C_2–C_3) and π (C_4 C_5) with π^* (C_1 C_6) gives stabilization energy values (E^2) of

19.32 and 20.73 KJ/mole, respectively. These high stabilization energy values indicate significant delocal- ization effects, resulting in a high tendency of charge transfer between the "acceptor and donor NBO's". These highest interactions of the molecule around the ring enhance the biological activity of the molecule,as described in [32]. The interaction between acceptor and donor NBO's can be visualized using multiwfnas shown in figure 5

3.7 Hirshfeld surface charge and Local Reactivity Decriptor

The Fukui function is a highly valuable local reactivity descriptor used for modeling chemical reactivity and site selectivity. High values of 'f' at a particular site suggest a greater propensity for reactivity at that site. To calculate the Hirshfeld Charge and Local reactivity descriptors, "Conceptual Density Functional Theory" is employed using Multiwfn. According to Parr et al [33] "Fukui function is defined as the change in electron density ρ(r) at a given point r in response to a change in the total number of electrons, or alternatively, as the sensitivity of a system's chemical potential to an external perturbation at a specific point r". By utilizing the Fukui function, researchers are able to gain valuable insights into the local activity of a system, allowing for the rational design of new compounds with desired properties.

$$f(r) = \left(\frac{\partial \rho(r)}{\partial (N)}\right)_{v(r)} \quad \text{or} f(r) = \left(\frac{\partial \mu}{\partial (v(r))}\right)_{N} \tag{10}$$

Due to the derivative discontinuity, "Fukui function" is approximated using the finite difference method, which can be expressed as follows [34]

$$\begin{aligned} f_-(r) &= \rho_N(r) - \rho_{N-1}(r) = \rho^{Homo}(r) \\ f_+(r) &= \rho_{N+1}(r) - \rho_N(r) = \rho^{Lumo}(r) \\ f_0(r) &= \frac{f_-(r) + f_+(r)}{2} = \frac{\rho^{Homo}(r) + \rho^{Lumo}(r)}{2} \end{aligned} \tag{11}$$

ρ_N (r), ρ_{N-1}(r), ρ_{N+1}(r) represent separately the electron densities of the system with N, N-1 and N+1 elec- trons. ρ^{Homo}(r) and ρ^{Lumo}(r) are the electron-densities of "Highest Occupied Molecular Orbital (HOMO) and Lowest unoccupied molecular orbital (LUMO)", respectively. A large value of "Fukui function" at asite indicates its higher reactivity [35]. Thus, the Fukui function is a crucial tool for identifying the reac- tive sites. By integrating the Fukui function equation over individual atoms in a molecule, we obtained "Condensed Fukui Function (CFF)" [36, 37], which offers an easier way to detect the electrophilic and nucleophilic attack sites.Depending on the way of electron transfer, three "Condensed Fukui functions" can be defined for each atom "K" within a molecule [38].

For nucleophilic attack,

$$f_k^+(r) = [q_k(N+1) - q_k(N)] \quad (12)$$

For electrophilic attack,

$$f_k^-(r) = [q_k(N) - q_k(N-1)] \quad (13)$$

For radial attack,

$$f_k^0(r) = \frac{1}{2}[q_k(N+1) - q_k(N-1)] \quad (14)$$

"q_k" represents the total electronic population of atom "k"

In 2005, Morell et al. proposed "Dual Descriptor (DD)" [39] which is a more practical tool for predicting sites' reactivity as it can simultaneously reveal both nucleophilic and electrophilic reactive sites and is expressed as follows

$$f(r) = \frac{\partial \eta(r)}{\partial V(r)}_N \quad or f(r) = \frac{\partial \eta(r)}{\partial N}_{V(r)} \quad (15)$$

where η represents "chemical hardness".
" Condensed dual descriptor(CDD)" can be expressed as:

$$f^2(r) = f^+(r) - f^-(r) = \rho^{Lumo}(r) - \rho^{HOmo}(r) \quad (16)$$

Table 5 presents the "Hirshfeld charges, condensed Fukui functions, and Dual Descriptor (DD) values" calculated using Multiwfn for the three molecules. The DD reveals the reactive sites by indicating positive values in electrophilic regions dominated by $\rho^{Lumo}(r)$ and negative values in nucleophilic regions where $\rho^{Homo}(r)$ dominates.

The condensed Fukui function values show the highest nucleophilic attack site is the area around nitrogen and nucleophilicity decreases in the order 21N > 1C > 4C > 22H > 5C > 16H > 23C > 2C > 24H > 15C > 19H

Conclusion

The structural parameters of methamphetamine, a psychoactive drug, were analyzed using Density Func- tional Theory and Quantum Theory of Atoms in Molecules. The optimized structure's geometrical pa- rameters, such as bond length, bond angle, and dihedral angle, were compared with experimental values and found to be in good agreement. Further analysis was conducted using frontier orbital analysis, MEP analysis, and reactivity descriptors, which confirmed that the nitrogen atom had the highest electrophilic attack sites in the molecule. Additionally, NBO analysis revealed that the phenyl ring had the highest interactions and delocalization effects between the donor and acceptor orbitals, which contributed to the molecule's enhanced biological activity.

In the field of rational drug design, ELF and NCI analysis have emerged as indispensable techniques. By utilizing ELF analysis, researchers can precisely locate and characterize electron-rich and electron-poor regions within a molecule. This information is vital for identifying reactive sites and understanding the reactivity of drug molecules. Moreover, ELF analysis assists in elucidating the mechanisms underlying chemical reactions, enabling scientists to predict and optimize drug-target interactions.

The HOMO-LUMO energy gap is a key parameter in evaluating the charge transfer interactions of amolecule, which can significantly influence its pharmacological activity. By utilizing various parameters, including the results of Electron Localized Function and NCI analysis, researchers can propose new drugswith finely-tuned biological activity, minimizing side effects and enhancing therapeutic outcomes. Thesefindings can also be leveraged in the development of efficient and cost-effective sensors. By identifying electron-rich and electron-

deficient regions within a molecule as well as the energy gap, appropriate binding groups can be selected that interact specifically with the target analyte. This selectivity is crucial for achieving accurate and reliable sensing capabilities.

Acknowledgement

The authors wish to express their sincere gratitude to the Department of Chemistry, University College, Thiruvananthapuram for providing access to the Gaussian-16 programme.

References

Mohamed M Abdou. A molecular approach to the study of structure activity correlation for someamphetamines. *Journal of psychoactive drugs*, 33(3):295–300, 2001.

Lewis Nelson. Acute cyanide toxicity: mechanisms and manifestations. *Journal of Emergency Nursing*,32(4):S8–S11, 2006.

P. Hohenberg and W. Kohn. Inhomogeneous electron gas. *Phys. Rev.*, 136:B864–B871, Nov 1964.

Aron Hakonen, Kaiyu Wu, Michael Stenb k Schmidt, Per Ola Andersson, Anja Boisen, and Tomas Rindzevicius. Detecting forensic substances using commercially available sers substrates and handheld raman spectrometers. *Talanta*, 189:649–652, 2018.

M. J. Frisch, G. W. Trucks, H. B. Schlegel, G. E. Scuseria, M. A. Robb, J. R. Cheeseman, G. Scalmani,

V. Barone, G. A. Petersson, H. Nakatsuji, X. Li, M. Caricato, A. V. Marenich, J. Bloino, B. G.Janesko, R. Gomperts, B. Mennucci, H. P. Hratchian, J. V. Ortiz, A. F. Izmaylov, J. L. Sonnenberg,

D. Williams-Young, F. Ding, F. Lipparini, F. Egidi, J. Goings, B. Peng, A. Petrone, T. Henderson,

D. Ranasinghe, V. G. Zakrzewski, J. Gao, N. Rega, G. Zheng, W. Liang, M. Hada, M. Ehara,

K. Toyota, R. Fukuda, J. Hasegawa, M. Ishida, T. Nakajima, Y. Honda, O. Kitao, H. Nakai, T. Vreven,

K. Throssell, J. A. Montgomery, Jr., J. E. Peralta, F. Ogliaro, M. J. Bearpark, J. J. Heyd, E. N. Brothers, K. N. Kudin, V. N. Staroverov, T. A. Keith, R. Kobayashi, J. Normand, K. Raghavachari,

A. P. Rendell, J. C. Burant, S. S. Iyengar, J. Tomasi, M. Cossi, J. M. Millam, M. Klene, C. Adamo,

R. Cammi, J. W. Ochterski, R. L. Martin, K. Morokuma, O. Farkas, J. B. Foresman, and D. J. Fox.Gaussian˜16 Revision C.01, 2016. Gaussian Inc. Wallingford CT.

W. Kohn and L. J. Sham. Self consistent equations including exchange and correlation effects. *Phys. Rev.*, 140:A1133–A1138, Nov 1965.

Axel D Beeke. Density-functional thermochemistry. iii. the role of exact exchange. *J. Chem. Phys*, 98(7):5648–6, 1993.

W. J. Hehre L. Radom P. v. R. Schleyer J.A. Pople. *Ab initio Molecular Orbital theory*. Wiley Newyork, 1986.

Murray Jane and Politzer Peter. The electrostatic potential:an overview. *Computational Molecular Science*, 1:153–163, 03 2011.

John E. Carpenter Frank Weinhold. The natural bond orbital lewis structure concept for molecules, radicals, and radical ions. In *The Structure of Small Molecules and Ions*. Springer, 1988.

Ramaniah LM. Kumar V, Kishor S. Understanding the antioxidant behavior of some vitamin molecules: a first-principles density functional approach. *J Mol Model*, 19(8):3175–86, August 2013.

Robert G. Parr, László v. Szentpály, and Shubin Liu. Electrophilicity index. *Journal of the American Chemical Society*, 121(9):1922–1924, 1999.

Robert G. Parr and Ralph G. Pearson. Absolute hardness: companion parameter to absolute elec- tronegativity. *Journal of the American Chemical Society*, 105(26):7512–7516, 1983.

P. Geerlings, F. De Proft, and W. Langenaeker. Conceptual density functional theory. *Chemical Reviews*, 103(5):1793–1874, 2003. PMID: 12744694.

Richard FW Bader. Atoms in molecules. *Accounts of Chemical Research*, 18(1):9–15, 1985.

Wayne Ouellette, Jon Zubieta, and Timothy Korter. Redetermination of (+)- methamphetamine hydrochloride at 90 k. *Acta Crystallographica Section E: Structure Reports Online*, 64(5):o940–o940, 2008.

Iam Fleming. *Frontier orbitals and organic chemical reactions*. Wiley, 1976.

Jun-ichi Aihara. Reduced homolumo gap as an index of kinetic stability for polycyclic aromatic hydrocarbons. *The Journal of Physical Chemistry A*, 103(37):7487–7495, 1999.

Robert G. Parr and Ralph G. Pearson. Absolute hardness: companion parameter to absolute elec- tronegativity. *Journal of the American Chemical Society*, 105(26):7512–7516, 1983.

Ralph G. Pearson. The principle of maximum hardness. *Accounts of Chemical Research*, 26(5):250– 255, 1993.

Robert G. Parr and Pratim K. Chattaraj. Principle of maximum hardness. *Journal of the American Chemical Society*, 113(5):1854–1855, 1991.

Robert G. Parr, Laszlo v. Szentpaly, and Shubin Liu. Electrophilicity index. *Journal of the AmericanChemical Society*, 121(9):1922–1924, 1999.

R. Vijayaraj, V. Subramanian, and P. K. Chattaraj. Comparison of global reactivity descriptors calculated using various density functionals: A qsar perspective. *Journal of Chemical Theory and Computation*, 5(10):2744–2753, 2009. PMID: 26631787.

Laurence P. R. Politzer P. and Jayasuriya K. Molecular electrostatic potentials: an effective tool for the elucidation of biochemical phenomena. *Environmental health perspectives*, 61:191–202, 1985.

E. Scrocco and J. Tomasi. Electronic molecular structure, reactivity and intermolecular forces: An eu- ristic interpretation by means of electrostatic molecular potentials. *Advances in Quantum Chemistry*,11:115–193, 1978.

E. Scrocco and J. Tomasi. The electrostatic molecular potential as a tool for the interpretation of molecular properties. 1973.

Savin A. Silvi B. Classification of chemical bonds based on topological analysis of electron localizationfunctions. *Nature*, 371:683–86, 1994.

CHEN Fei Wu LU Tian. Meaning and functional form of the electron localization function. *Acta Physico Chimica Sinica*, 27(12):2786, 2011.

Erin R. Johnson, Shahar Keinan, Paula Mori-Sánchez, Julia Contreras-García, Aron J. Cohen, and Weitao Yang. Revealing noncovalent interactions. *Journal of the American Chemical Society*, 132(18):6498–6506, 2010. PMID: 20394428.

Eric D Glendening, Clark R Landis, and Frank Weinhold. Natural bond orbital methods. *Wiley interdisciplinary reviews: computational molecular science*, 2(1):1–42, 2012.

Frank Weinhold and Eric D. Glendening. *NBO 7.0 Program Manual Natural Bond Orbital Analysis Programs*.

Sara Yousefnejad, SH Reza Shojaei, Filippo Morini, and Abolfazl Shiroudi. A theoretical study of potential energy surface and some chemo-physical descriptors of aspirin, coupling the rotation of the ester and carboxyl groups. *Journal of the Indian Chemical Society*, 99(9):100644, 2022.

Kenichi Fukui. Role of frontier orbitals in chemical reactions. *Science*, 218(4574):747–754, 1982.

Chen F Cao J., Ren Q. Comparative study on the methods for predicting the reactive site of nucle-ophilic reaction. *Science China Chemistry*, 58:1845–1852, Ocober 2015.

Robert G. Parr and Weitao Yang. Density functional approach to the frontier-electron theory of chemical reactivity. *Journal of the American Chemical Society*, 106(14):4049–4050, 1984.

Paul Geerlings, Frank De Proft, and Wilfried Langenaeker. Conceptual density functional theory.

Chemical reviews, 103(5):1793–1874, 2003.

Mortier WJ. Yang W. The use of global and local molecular parameters for the analysis of the gas- phase basicity of amines. *Journal of American Chemical Society*, 108(19):108(19):5708–11, September 1986.

Weitao Yang and Wilfried J Mortier. The use of global and local molecular parameters for the analysis of the gas-phase basicity of amines. *Journal of the American Chemical Society*, 108(19):5708–5711, 1986.

Toro-Labbé A Morell C, Grand A. New dual descriptor for chemical reactivity. *Journal of Physical Chemistry A*, 109(1):205–12, January 2005.

FABRICATION OF BENT ROD-SHAPED HYBRID SILICA BY AN AUTO-CATALYZED HYDROLYTIC CONDENSATION OF 3-AMINOPROPYLTRIETHOXYSILANE

Shiji E. [a,b] and Bindu P. Nair[b,c]*

[a] Department of Chemistry, Christian College, Kattakkada, University of Kerala, Thiruvananthapuram
[b] Department of Chemistry and Research Center, Mahatma Gandhi College, University of Kerala, Thiruvananthapuram
[c] Department of Chemistry, Velu Thampi Memorial Nair Service Society College, Dhanuvachapuram, University of Kerala, Thiruvananthapuram
[*]Corresponding author, Phone: 9747511925, E-mail: bindumelekkuttu@gmail.com

Abstract

Bent-rod-shaped hybrid silica was prepared through a surfactant-free auto-catalyzed hydrolytic condensation of 3-aminopropyltriethoxysilane in an ethanol/water mixture. Characterization using FT-IR revealed that the hybrid silica contains fully and partially condensed siloxanes. X-ray diffractogram revealed a short-range order of the siloxanes into a bilayer/two-dimensional arrangement in the hybrid silica. Thermogram of the sample indicated a char yield of 55 wt% at 800 ^{o}C, due to the loss of structural hydroxyl groups and the organic content. The release characteristic of Rhodamine B encapsulated in the hybrid silica indicated its use for controlled delivery applications.

Keywords: Hybrid silica, hydrolytic condensation, siloxanes, POSS.

Introduction

Synthesis of hybrid silica of defined morphology is being extensively explored in recent years due to the wide possibility of these materials for various applications such as separation,[1] sensor design,[2] catalysis,[3] and drug delivery.[4] The preparative method for obtaining hybrid silica with regular morphology includes hydrothermal synthesis, synthesis from layered silicates, hydrolysis, and poly-condensation of alkoxysilanes using a surfactant, etc. The formation of regular morphology and ordered structure is attributed to the ordering of surfactants to form micelles of various shapes in most cases. An important application of this ordered siloxane is its porosity which will find application in various fields such as catalysis, drug delivery, etc. However, pores are sometimes blocked by surfactant moieties and their complete removal is not possible; a surfactant-free synthetic strategy is attractive in this regard.[5] Lin et al obtained rod-shaped silica through a co-condensation method based on sodium hydroxide-catalyzed reactions of tetraethoxysilane (TEOS) with 3-aminopropyltrimethoxysilane in the presence of a low concentration of cetyltrimethylammonium bromide (CTAB) surfactant.[6] Kaneko et al explored acid-catalyzed

hydrolytic poly-condensation of aminopropyltrimethoxysilane under a non-surfactant route in aqueous medium for producing ordered polysiloxanes with hexagonal structured morphology.[7] The method has utilized ordering imparted by the aminopropyl alkyl group.

Synthesis of bifunctionalized hybrid silica spheres with vinyl and aminopropyl groups through solvent-evaporation of siloxane solution through co-precipitation of fully condensed polyhedral oligomeric silsesquioxane and siloxane network was reported earlier.[8-9] Herein we report bent rod-like hybrid silica by drop-casting and drying of siloxane solution obtained from hydrolytic condensation of 3-aminopropyltriethoxysilane in ethanol/water mixture. The method is facile, without the use of surfactants or any catalyst and also other silane precursors.

Experimental

3-aminopropyltriethoxysilane (AS) was purchased from Aldrich Chemicals and absolute ethanol from s.d.Fine Chem Limited India. Siloxane solution was prepared by following the procedure reported elsewhere.[9] Typically, siloxane solution was prepared by diluting AS with the ethanol-water mixture (v/v = 14/1) to give a silane concentration of 0.45 M and aging the solution in a closed container at ambient temperature for a period over 7 days. Hybrid silica was prepared by casting the solution on a glass plate after diluting the siloxane solution in a 1:1 mole ratio with ethanol followed by evaporation of the solvent at ambient temperature and then drying at 80 °C.

Hybrid silica was characterized using Fourier Transform-Infra Red Spectroscopy (FT-IR), X-ray powder diffraction (XRD), and Scanning Electron Microscopy (SEM). FT-IR measurements were made on a Perkin-Elmer Spectrum one spectrophotometer in the range of 4000- 400 cm^{-1} using KBr pellets containing ca. 2 wt% sample. X-ray powder diffraction (XRD) data at 2θ between 2° and 20° were collected on a Philips X'pert Pro X-ray diffractometer equipped with a graphite monochromator and X'celerator detector. SEM images were taken in JEOL JSM-5600 LV scanning electron microscope using samples provided with a thin gold coating using JEOL JFC-1200 fine coater. UV-VISIBLE Spectra were recorded on a Perkin Elmer Lambda 365 spectrophotometer. Release studies were performed on the slow release of Rhodamine B from the hybrid silica.

Results and Discussion

The siloxane solution was clear and stable and a T-gel was obtained on concentrating the solution by slow evaporation of the solvent.[9] The solution when cast on a glass plate and allowed to dry at ambient temperature yielded bent rod-shaped silica with an average diameter of 200 nm as observed in SEM (Figure 1). AS in an alcohol-water mixture undergoes hydrolytic co-condensation without an external catalyst, owing to the internal catalytic activity of the basic alkyl amino group of AS which upon reacting with water produces nucleophilic OH^{-}. The pH of the solution was around 11. According to Voronkov, hydrolytic condensation of AS gives octa aminopropyl polyhedral oligomeric silsesquioxane (POSS) as the major product.[10] However, under basic conditions, the formation of POSS frameworks typically occurs with thermodynamic control because both formation and hydrolytic cleavage of Si-O-Si linkages

are facile.[9] The siloxane solution at equilibrium will contain a mixture of POSS and incompletely condensed intermediate species with a variety of linear, branched, or cyclic structures. Slow drying of such solutions generally gives T-gels due to an increase in solution concentration which shifts the equilibrium in a progressive manner to produce a siloxane network in the solution. Therefore one can expect the siloxane network self-assembled through H-bonding for the hybrid silica.

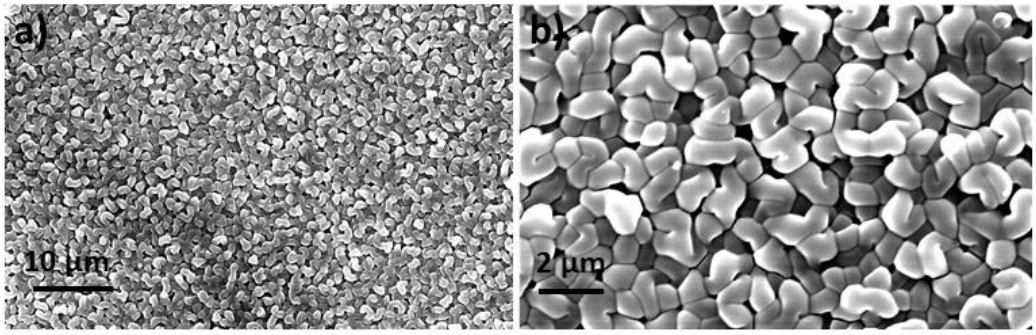

Figure 1. SEM micrographs of bent rod-shaped hybrid silica.

FTIR spectral features of the hybrid silica (Figure 2) showed bands due to aminopropyl group at 1500 cm^{-1} ($N\text{-}H_{bend}$), 3400 cm^{-1} ($N\text{-}H_{str}$), 2866 cm^{-1} and 2932 cm^{-1} ($C\text{-}H_{str}$)), Si-O-Si asymmetric stretching vibration at 1120 cm^{-1} and 1030 cm^{-1}, respectively due to cage-structured polyhedral oligomeric silsesquioxane (POSS) and branching/network siloxane.[9] The XRD of hybrid silica dried at 100 ºC (Figure. 3a) exhibited broad reflections at around 2θ of 8º and 20º which respectively, correspond to d-values of 10.1 Å and 4.4 Å. The peak at 10.1 indicated the presence of POSS in hybrid silica and the peak at 4.4 is due to siloxanes. In a previous paper, one of the authors demonstrated the synthesis of bifunctionalized hybrid silica spheres from mixtures of aminopropyltriethoxysilane and vinyltriethoxysilane using the same preparative technique.[9] However the presence of POSS in the former study was higher than in the latter study. It became evident that the POSS from aminopropyltriethoxysilane is more unstable.

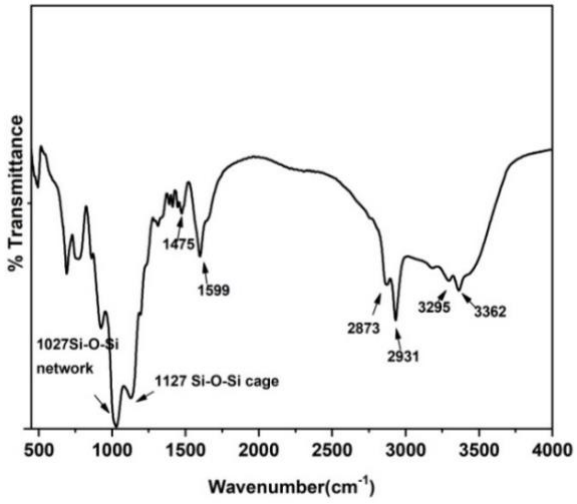

Figure 2. FT-IR spectrum of rod-shaped hybrid silica.

Thermogram of the hybrid silica indicated an initial heat loss of up to 100 degrees Celsius due to the loss of adsorbed water, followed by a significant weight loss at 400 degrees Celsius, possibly due to the loss of structural hydroxyls (Figure 3b). A char yield of 55 wt% was obtained at 800 ºC. It is proposed that rod-shaped hybrid silica is formed preferentially with aminopropyl groups exposed outwards to the bilayer. Siloxane network with hydroxyl groups interacting with aminopropyl groups on POSS forming nanodomains of POSS-siloxane aggregates, which then self-assemble into bent-rod shaped hybrid silica.

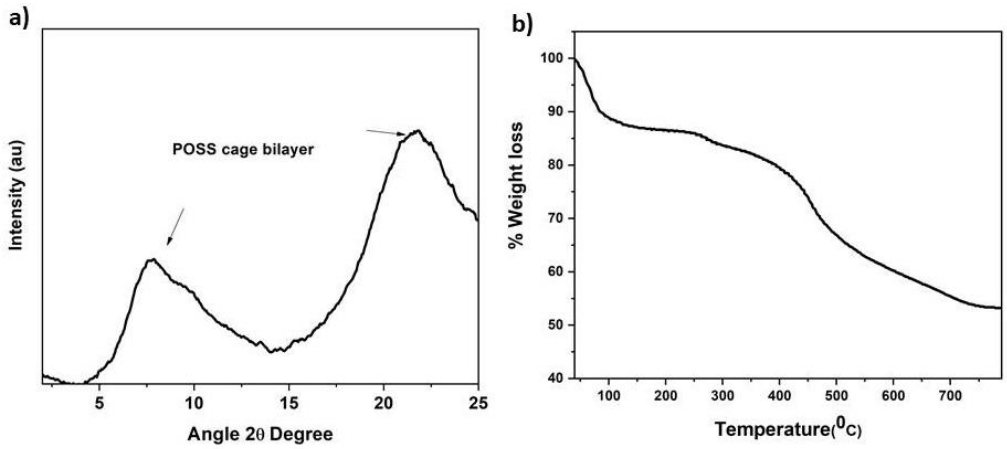

Figure 3a) X-ray diffractogram and b) thermogram of bent rod-shaped hybrid silica.

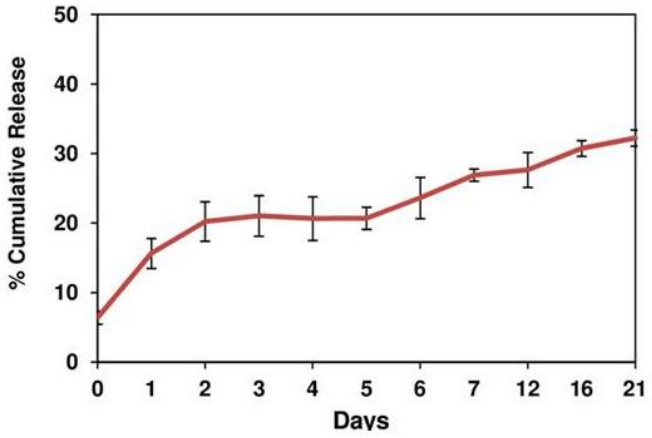

Figure 4. The release profile of Rhodamine B from hybrid silica into saline.

The use of the obtained morphology for controlled delivery application was evaluated by encapsulating it with Rhodamine B and studying the release of the dye in water for about 21 days by measuring the emission at 490 nm. A cumulative release of 30 percent was obtained in 21 days, indicating a slow release profile.

Conclusions

In conclusion, bent-rod-shaped hybrid silica was prepared through a surfactant-free auto-catalyzed hydrolytic condensation of 3-aminopropyltriethoxysilane in ethanol/water mixture, which contains both fully and partially condensed siloxanes. A short-range order of the siloxanes into a bilayer/two-dimensional arrangement was confirmed in the hybrid silica.

The release characteristic of Rhodamine B encapsulated in the hybrid silica indicated a slow and controlled release profile.

Reference

1. Endler, M. Borges. Silica, Hybrid Silica, Hydride Silica, and Non-Silica Stationary Phases for Liquid Chromatography. *Journal of Chromatographic Science.* 2015, 53, 580-584.
2. Srinivasan,s.; and Bowers, E.J. Integrated High Sensitivity Hybrid Silicon Magnetometer. *IEEE Photonics Technology Letters.*2014,26,13-15.
3. Davidson, M.; Ji, Y.; Leong, G.J.; Kovach, N.C.; Trewyn, B.G.; and Richards, R.M. Hybrid Mesoporous silica/ Noble metal Nanoparticle Materials- Synthesis and Catalytic Applications. *Chemistry of materials.* 2018,1,4386-4388.
4. Junior, J.A.; Abuçafy,M.P.; Manaia,E.B.; Silva,L.D.; -Andréo,B.G.C.; and Chiavacci,L.A. Drug Delivery Systems Obtained from Silica-Based Organic-Inorganic Hybrids. *Polymers.* 2016, 8,91 -94.
5. Reculusa, S.; Legrand,C.P.; Ravaine,S.; Mingotaud, C.; Duguet,E.; and Elodie -Lami,E.B.; Syntheses of Raspberrylike Silica/Polystyrene Materials. *Chemistry of Materials*. 2002, 14, 2354-2359.
6. Huh, S.; Wiench, J. W.; Trewyn, B. G.; Song, S.; Pruski, M.; Lin, V. S. Y.; Tuning of particle morphology and pore properties in mesoporous silicas with multiple organic functional groups. *Chem. Commun.* 2003, 2364-2365.
7. Kaneko, Y.; Iyi, N.; Kurashima, K.; Matsumoto,T.; FujitaT.; andi Kitamura,K. Hexagonal-Structured Polysiloxane Material Prepared by Sol−Gel Reaction of Aminoalkyltrialkoxysilane without Using Surfactants. *Chem. Mater*. 2004, 16, 3417–3423.
8. Chen, S.; Hayakawa, S.; Shirosaki, Y.; Fujii, E.; Kawabata, K.; Tsuru, K.; Osaka,A..Sol–Gel Synthesis and Microstructure Analysis of Amino-Modified Hybrid Silica Nanoparticles from Aminopropyltriethoxysilane and Tetraethoxysilane. *Journal of the American Ceramic Society*, 2009, 92, 2074-2082.
9. Nair, B. P.; and Pavithran, C. Bifunctionalized hybrid silica spheres by hydrolytic co-condensation of 3-aminopropyltriethoxysilane and vinyltriethoxysilane. *Langmuir*. 2009, 26, 730-733.
10. Voronkov, M. G.; and Lavrent'yev, V. I. Polyhedral oligosilsesquioxanes and their homo derivatives In Inorganic ring systems. *Inorganic Ring Systems*. 2005,5,199-236.

GREEN APPROACH OF SYNTHESIZING MAGNESIUM-BASED METAL ORGANIC-FRAMEWORK USING FLOWER EXTRACT OF CLITORIA TERNATEA AND ITS CORROSION STUDY

Lekshmy O[a], BeenaKumari K S [b*], Nayana Senan V[a], Sudha Devi R[a]

[a]Post Graduate and Research Centre, Mahatma Gandhi College, Thiruvananthapuram, Kerala, India, 695004
[b*]Department of Chemistry, All Saints' College, Thiruvananthapuram, Kerala, India 695007
E-mail: *beenagireesh@yahoo.co.uk*

Abstract

Recently, green synthesis of nano compounds has attracted much importance. In green approach, the products are manufactured using chemicals that reduce the use and generation of hazardous materials into the environment. In this area, green reagents such as plant extracts have been using to synthesize various products. The present study includes the microwave assisted synthesis of magnesium-based metal-organic framework using the flower extract of *Clitoria ternatea* as reducing agent. The MOF was characterized using the techniques FT-IR, PXRD, SEM, EDS and DLS.

Keywords: *Clitoria ternatea*, Metal-Organic Frameworks, SEM, EDS.

Introduction

Metal organic frameworks (MOFs) are well-organized self-assembled nano structures [1] with very high surface area [2], nano porosity [3] with tunable size and shape, consistent host-guest relations [4] etc. The structure makes the framework with metal ions and organic linker which undergo polymerization to form a long-extended construction. MOF forms co-ordination bond with bridging ligands such as di- and tricarboxylic acids. These ligands characteristically have rigid backbones. Examples are benzene-1,4-dicarboxylic acid (BDC or terephthalic acid), biphenyl-4,4′-dicarboxylic acid (BPDC), tricarboxylic acid, trimesic acid, etc. 1, 4-Benzenedicarboxylic acid is widely used as the ligands, due to its stability, flexibility and connectivity etc [5]. MOFs are multifunctional hybrid materials which offers extremelyvarious properties due to a wide variety of obtainable metal ions and organic linker molecules [6].

The synthesis of MOFs is determined by many features correlated to the reaction time, temperature, solvent used, nature of the metal ions and organic ligands, kinetics of the crystallization forming nucleation, crystal growth etc. Themost significant methods employed for the synthesis of MOFs are solvothermal [7], hydrothermal [8], sol-gel synthesis [9],

microwave assisted [10] etc. Green synthesis of metal organic frame work was also reported [11]. This is by using plant biomolecules which has various applications like sensing, CO_2 capture, bacteria-free nitrogen fixation, enhanced photosynthesis and photocatalysis etc.

The application of defensive anticorrosion coatings is one of the most significant approaches to recover the corrosion resistance of metals and alloys, which can successfully avoid their direct contact with corrosive media. Usually the shield coatings containing hazardous materials such as chromate etc. But during the prolonged service time, they are toxic and carcinogenic, and caused serious environmental pollution, hence it is required to develop eco-friendly coating materials [12]. So, the green mode of synthesis is focusing now-a-days.

The plant *Clitoria ternatea*, familiarly called as butterfly pea which is a decorative climber having blue or white flowers [13]. The species carrying blue flowers were used in this study for the synthesis of magnesium-based MOF. There had been no literature prevailing on the synthesis of magnesium-based MOF using the flower extract of *Clitoria ternatea*. Microwave method of synthesis was used to synthesis an ecological magnesium-based MOF using 1,4-benzenedicarboxylic acid and the flower extract of *Clitoria ternatea*. The flower extract act as a reducing agent in the synthesis of magnesium-based metal organic framework. The main compounds found in this flower are the pentacyclic triterpenoids such as taraxerol and taraxerone[14].

Materials and Methods

All chemicals and reagents used in this study are of AR grade. Merck A.R grade $MgSO_4.H_2O$ and Benzene dicarboxylic acid (BDC) were used in this study. Methanol used was from SRL, India make. The flowers of *Clitoria ternatea* were collected locally.

Preparation of *Clitoria ternatea*flower extract (CTFE)

About 5 g of flower was washed, dried and added to 30 mL of methanol. It was then digested using microwave for 15 minutes and a power of 450W. The digested liquid was cooled, decanted and filtered to produce the flower extract.

Formation of Mg-MOF

1:1 ratio of $MgSO_4.7H_2O$ and benzene dicarboxylic acid (BDC) acid had been finely pulverized by using a pestle and mortar. To this powdered mixture, add 15ml of methanol to make a paste. The paste was then mixed with 15ml of *Clitoria ternatea* flower extract and shake well for uniform mixing. It was then subjected to microwave irradiation for 15 minutes at a power of 450W. The microwave oven used for this study was of Samsung MS2 3F301E. The pinkish brown colored solution thus obtained was then filtered, washed using methanol and dried to obtain the Mg based MOF. This magnesium MOF was characterized by using different methods.

Characterization analysis of the prepared MOF

1. IR Spectral Analysis

Infrared spectroscopy (IR) is a technique based on the vibrations of the atoms in a molecule. The IR spectrum of the sample was recorded on SCHIMADZU DR 43 S Spectrometer using KBr pellets in the range of 400-5000 cm^{-1}.

2. Powder XRD Analysis

X-ray powder diffraction of the MOF the compound was taken by using Burker D8 Advance X-ray diffractometer. The particle size was calculated using Debye-Scherrer equation, $D=K\lambda/(\beta\cos\theta)$ where D is the crystalline size of nanoparticle, K represents the Scherrer constant (0.98), λ denotes the wavelength (1.54), β denotes the full width at half maximum (FWHM).

3. SEM Analysis

SEM analysis of the compounds were done by using FEI Nova Nano SEM 450 instrument.

4. EDX Elemental Analysis

Elemental analysis of the compounds was done by using energy dispersion spectroscopy using BrukerXflash instrument

5. DLS Analysis

Dynamic light scattering size distribution was performed using a Zeta Sizer.

Coating of prepared MOF on Copper rod

For corrosion studies, copper rod having dimensions of 1.5cm X 1.5cm X 0.1mm were selected. Drop casting method was adopted to adsorb the synthesized MOF on the surface of copper rod. After deposition, this rod was dipped in 3.5%NaCl solution for 72 hours and then dried in air. These samples were used for SEM analysis using FEI Nova Nano SEM 450 instrument.

Results and Discussion

Characterization of prepared MOF

1.IR Spectral Analysis

IR spectra of ligand and Mg based MOF is shown in figure1(a, b).

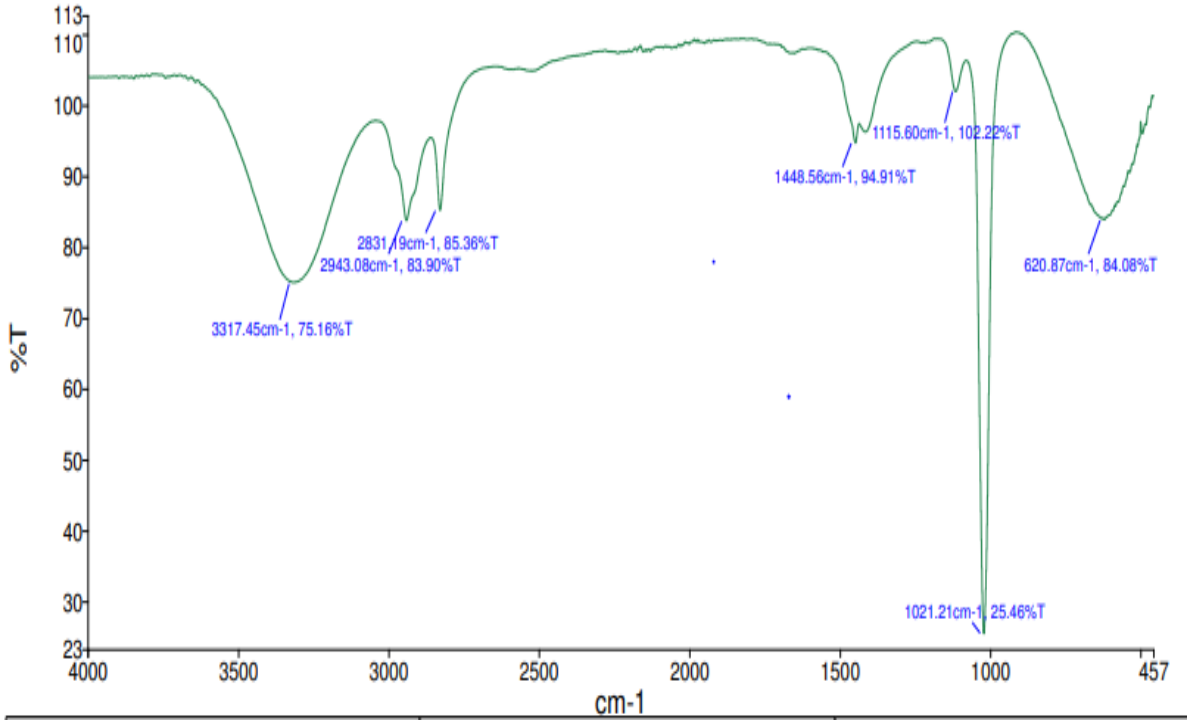

Figure 1(a). FT-IR spectrum of the ligand.

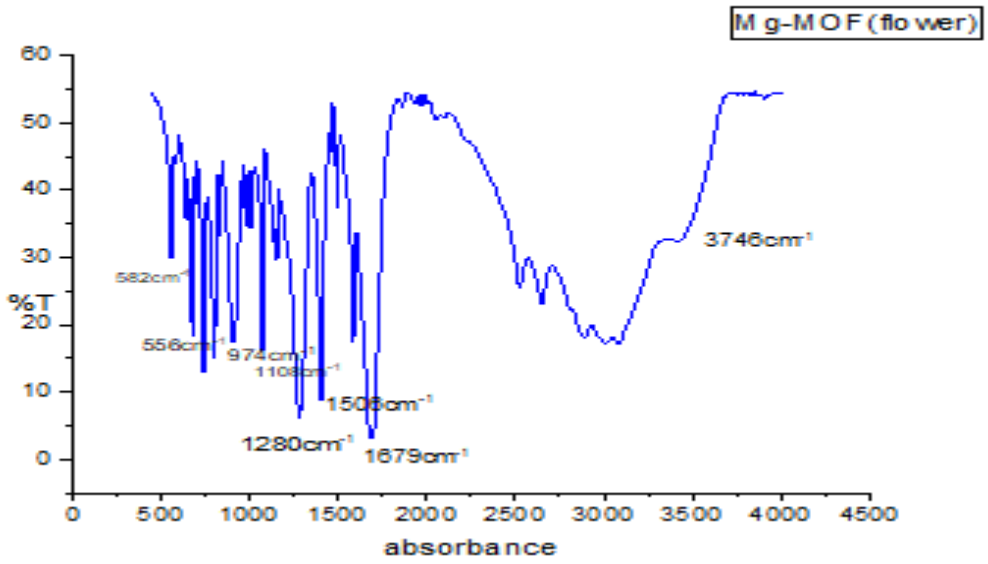

Figure 1(b). FT-IR spectrum of Mg-MOF (flower).

Table 1

Samples	Phenol (cm^{-1})	-CH stretching of alkanes (cm^{-1})	-COO bonded to metal (cm^{-1})	-COOH stretching (cm^{-1})	-CO stretching (cm^{-1})
Ligand	3317.45	2831.19	-	1448.56	-
Mg-MOF with flower extract	3746	2800	1679	1506	1108

Table 2 represents different peaks present in the FTIR spectra of the samples. Metal coordinated to the ligand was confirmed by the presence of an absorption band at 556 cm^{-1}. In Mg-MOF, a strong band was found at 1679cm^{-1} is due to -COOH stretching of benzene ring when metal coordinated to the ligand. There is an additional strong band in 3746cm^{-1} due to -OH stretching of phenol group present *Clitoria ternatea* flower extract. A strong band at 1506cm^{-1} is due to -COOH stretching and the band at 1108cm^{-1} is due to -C=O stretching of ligand. An additional band of 1280cm^{-1} denotes the C-N stretching of aliphatic primary amine of flower extract. A strong band in 974cm^{-1} region is due to OH bending of COOH. Metal coordinated to the ligand is confirmed by the presence of a strong band in 582-556cm^{-1} region. This indicates that the metal is bonded to carboxylic group of the ligand and also with amino and phenolic groups of the flower extract.[15]

2. Powder XRD Analysis

X-ray powder diffraction pattern of the MOF compound is shown in figure 2.

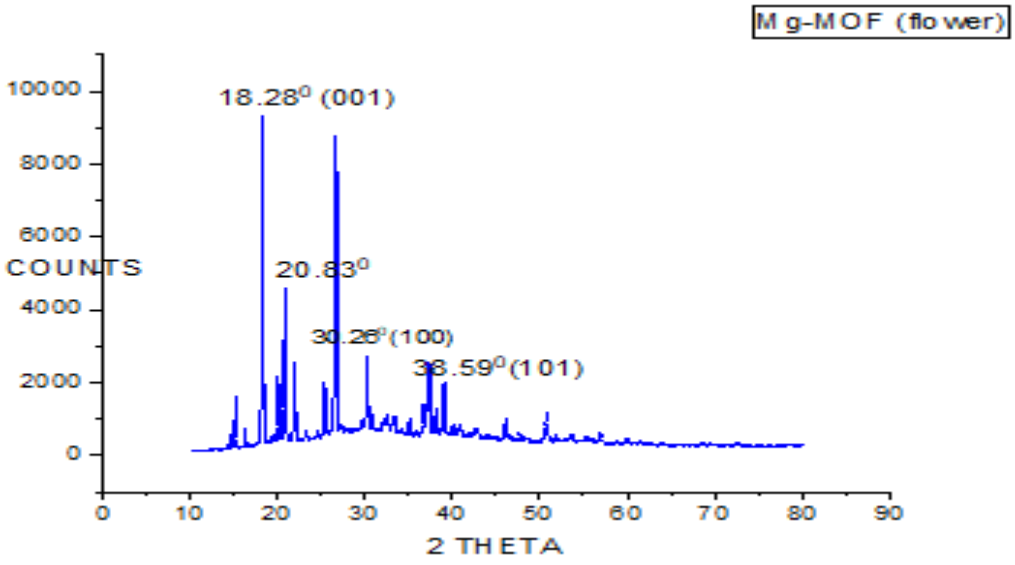

Figure 2. PXRD data of Mg-MOF.

The peaks at 2 θ values of 18.28° (001), 30.26 ° (100) and 38.59° (101) established the crystalline nature of flower extract (JCPDS data card no: 002-1207) [15]. The high intensity diffraction peaks at 20.83^0 is activated by the bio molecule from flower extract [17]. The peaks at 11.9^0 and 19.6^0 specifies the occurrence of Mg-MOF particles [18] The additional peaks were from the impurities which come into interaction with the desired MOF. The grain size was calculated based on Debye-Scherrer equation was 28.91 nm and exposed that the produced MOF was of nanometer in size [15].

3. SEM Analysis of prepared MOF

The size, spreading and morphology of the prepared MOF were studied by taking scanning electron microscopy photographs. Figure 3 shows the SEM image of synthesized Mg-MOF at a magnification of 750X.

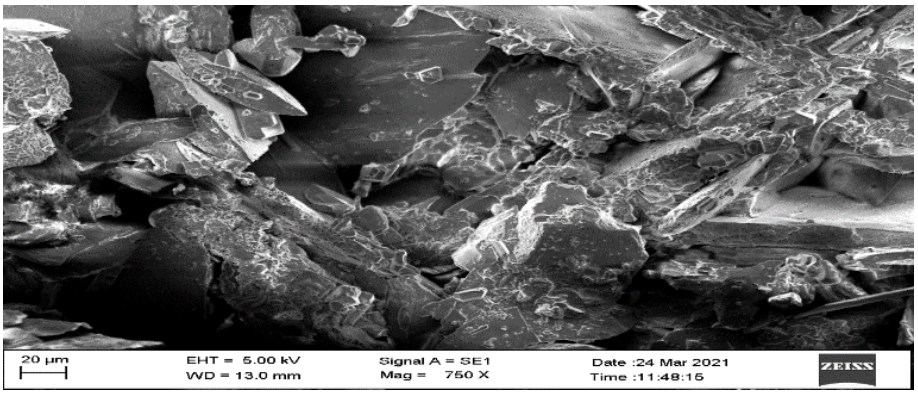

Figure 3. SEM analysis of MOF

The well dispersed MOF particles were seen in SEM images and the size of particle lies in between 50 to 200nm. SEM images also showed the porous nature of the synthesized Mg-MOF.

Energy Dispersive Spectroscopic Analysis (EDS)

The elemental analysis of metal organic framework of Mg was carried out using EDS elemental analysis method which is shown in figure 4.

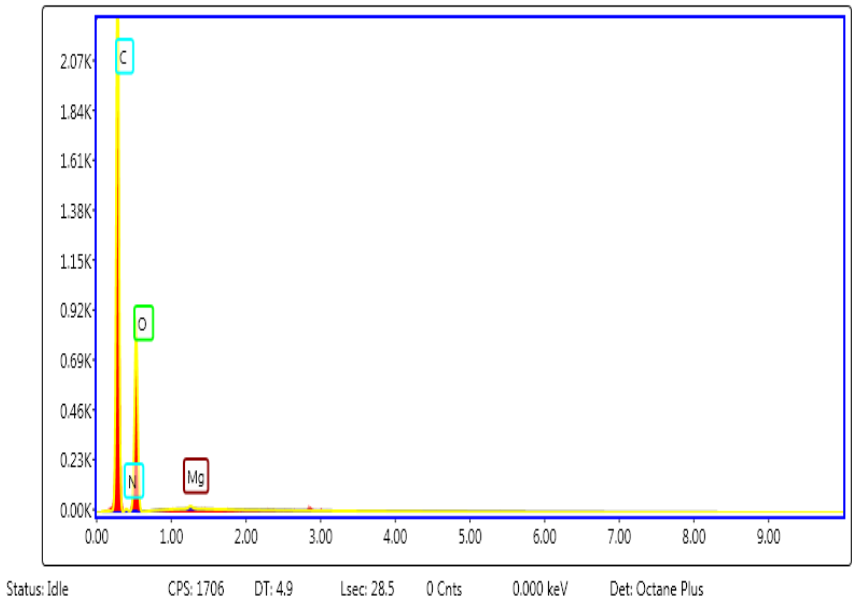

Figure 4. EDS data of Mg-MOF.

In EDS spectrum, the peak locations at 0.44, 0.615, 0.665,1.44 KeVrepresents the binding energies of the magnesium in MOF. The EDS spectra confirmedabout the successful synthesis of MOF.[16]

Dynamic Light Scattering Analysis

DLS is a technique used to determine particle size in colloidal solution. The particle size distribution of MOF is shown in figure 5.The mean particle size was 62.6nm confirming the nano meter size of synthesized MOF.

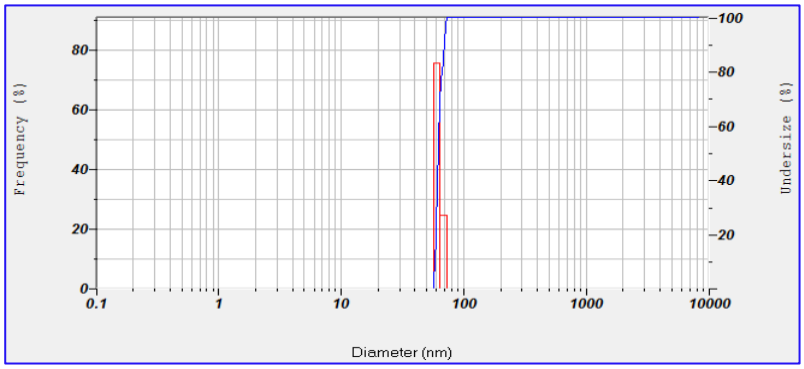

Figure 5. DLS of Mg -MOF.

The zeta potential graph of MOF is shown in figure 6. The scale of zeta potential signifies the degree of electrostatic repulsion among adjacent particles. Usually MOF particles have a surface charge that attracts a thin layer of ions of opposite charge and agglomerate. Nano particles with zeta potential values between -10 and +10 mV were considered roughly neutral in charge and had lesser tendency for agglomeration.

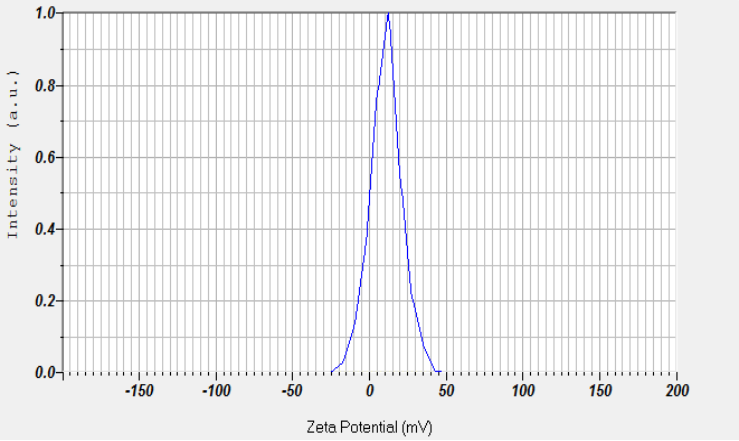

Figure 6. Zeta potential of Mg-MOF.

The manufactured MOF displayed a potential value of 10.8mV, and hence the particles will scatter in solution and resist aggregation.

SEM analysis of Coating on Copper rod

1. SEM Analysis of copper rod without MOF

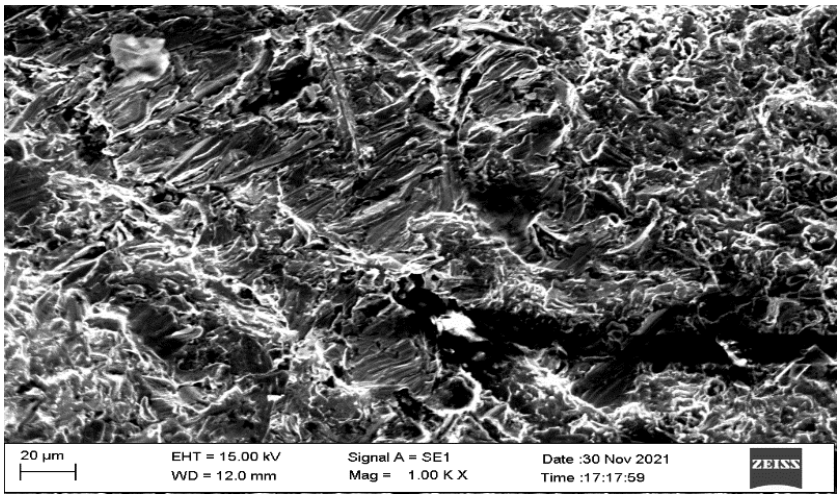

Figure 7. SEM analysis of copper rod without MOF

In figure 7. the SEM images represents the corroded copper rod nature without dipping in the solution. The corrosion deposits can be clearly seen in the images as agglomeration.

2. SEM Analysis of copper rod in blank solution

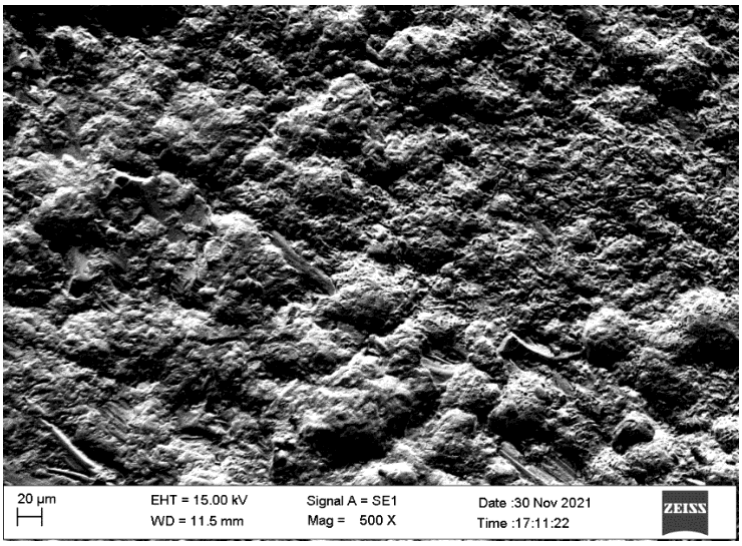

Figure 8. SEM analysis of copper rod in blank solution

In figure 8, represents the SEM images of copper rod in blank solution of 3.5%NaCl solution. The copper rod was dipped in 100ml NaCl for 72 hrs. The image shows the corrosion nature of copper rod.

3. SEM Analysis of copper rod in MOF NaCl solution

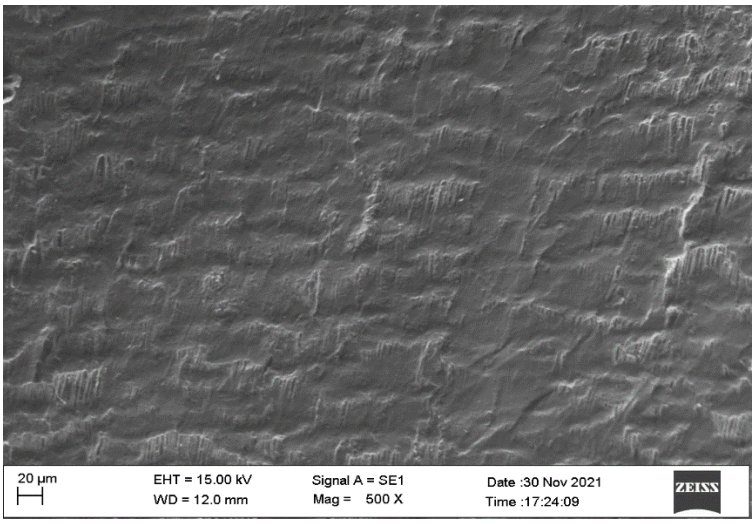

Figure 9. SEM analysis of copper rod in MOF solution

In figure 9, shows the SEM images of copper rod dipped in Mg-MOF dissolved in 3.5%NaCl solution for 72 hrs. There are no corrosion particles after dipping in the MOF solution reveals that the green synthesized MOF particle had adsorbed on the copper rod which act as a corrosion inhibitor.

Conclusion

Nanocrystalline Mg- MOF of 1,4- BDC and *Clitoria ternatea* flower extract was synthesized efficiently by means of microwave method. The synthesized MOF was characterized by using FT-IR, PXRD, SEM, EDS and dynamic light scattering studies. For corrosion studies, copper rod were selected. Drop casting method was adopted to adsorb the synthesized MOF on the surface of copper rod. These samples were used for surface analysis. The bonding of the metal to carboxylic group of the ligand as well as with amino and phenolic group of the flower extract was confirmed from FTIR data. The sharp peaks in the powder XRD patterns showed the crystalline nature of the synthesized MOF. The grain sizes calculated based on Debye Scherrer equation indicates that the synthesized MOF was of nanometer in size (28.91nm). SEM images confirmed the size of particle lies between 50 to 200nm. SEM analysis of deposited copper rod reveals that the prepared MOF had corrosion resistant property. The energy dispersive spectra showed the binding of metal to the ligand in the synthesized MOF. The DLS analysis showed that Mg-MOF is a nanosized material. The zeta potential value showed that the charge of prepared MOF is neutral and hence disperse in solution without showing a tendency for agglomeration and coagulation on standing. The flower extract added can increase the corrosion resistance of the prepared MOF.

Acknowledgement

Acknowledgement to Central Laboratory for Instrumentation and Facilitation (CLIF) and Department of chemistry, University of Kerala, Karyavattom Campus for providing the facility to conduct instrumental analysis

Reference

1. O. Shekhah, J. Liu, R. A. Fischer and C. Woll, Chemical Society Reviews., 40, 1081 (2011).
2. T. Ghanbari, F. Abnisa, W. Daud, and D. W. M. A. Wan, Sci.Tot.Environ., 707, 10, 13500 (2019).
3. S. Yang, V. V. Karve, A. Justin, I. Kochetygov, J. Espín, M. Asgari and W. L. Queen, Coordination Chemistry Reviews., 427, 213525 (2021).
4. Y. Y. Tong, Y. F Li, L. Sun, R. Yang, S. Zhang, Y. Fu and R. Chen, Separation Purification Technology., 250, 117142 (2020).
5. Rocío-Bautista, Taima-Mancera, Pasán, & Pino. (2019). Metal-Organic Frameworks in Green Analytical Chemistry. Separations, 6(3), 33. doi:10.3390/separations6030033
6. M. K. Buschbaum, F. Beuerle and C. Feldmann, Microporous Mesoporous Materials., 216, 171 (2015).
7. C. Qing, Y. Yiting, W. Liju, G. Zhiqi, Z. Yunchun, W. Dongmei and L. A. Chunxia, Journal of Inorganic and General Chemistry., 646, 437 (2020).
8. P. A. Ochoa, G. Givaja, P. J. S. Miguel, O. Castillo and F. Zamora, Inorganic Chemistry Communications., 10**,** 921 (2007).

9. D. Buso, K. M. Nairn, M. Gimona, A. J. Hill and P. Falcaro, Chem. Mater., 23, 929 (2011).
10. X. Wu, Z. Bao, B. Yuan, J. Wang, Y. Sun, H. Luo and S. Deng, Microporous Mesoporous Materials., 180:114 (2013).
11. J. J. Richardson and K. Liang, Nano. Micro. Small., 14, 1702958 (2017).
12. H. Zhu et al.Preparation of metal–organic framework films by electrophoretic deposition method, Mater. Lett. (2015)
13. Krithiga, N., Rajalakshmi, A., &Jayachitra, A. (2015). Green Synthesis of Silver Nanoparticles Using Leaf Extracts of Clitoriaternatea and Solanum nigrum and Study of Its Antibacterial Effect against Common Nosocomial Pathogens. Journal of Nanoscience, 2015, 1–8. doi:10.1155/2015/928204
14. Role of Crotalaria verrucosa L. extracts in synthesis of Zinc oxide nanoparticles M. Manokari1, Mahipal S. Shekhawat, Department of Botany, KanchiMamunivar Center for PG Studies, Pondicherry, India 2Department of Botany, MGGAC. Mahe, Pondicherry, India
15. John Sushma N, Prathyusha D, Swathi G, Madhavi T, Deva Prasad Raju B, Mallikarjuna K, Hak-Sung Kim (2016) Facile approach to synthesize magnesium oxide nanoparticles by using Clitoriaternatea—characterization and in vitro antioxidant studies. Applied Nanosience6: 437-444
16. K. Sreekanth Mahadeva, Jincheng Fan, Anis Biswas, K. S. Sreelatha, Lyubov Belova and K. V. Rao, Nanomaterials, 3, 486-497 (2013).
17. J. Z. Chan, R. Rasit Ali, K. Shameli, M.S.N. Salleh, K.X Lee and E.D. Mohamed Isa, IOP Conf.Ser:Mater.Sci.Eng, 808(2020).
18. T. K.N. Tran, H.L. Ho, H.V.Nguyen, B.T.Tran, T.T.Nguyen, P.Q.T. Bui and L.G.Bach, Open Chemistry, 20, 52-60 (2021).

EFFECT OF ZINC-CURCUMIN METAL COMPLEX ON THE CORROSION RESISTANCE OF COPPER IN 3.5% NaCl SOLUTION

Nayana Senan V[a], Beena Kumari K.S[*b], Lekshmy O[a]

[a]Post Graduate & Research Department of Chemistry, Mahatma Gandhi College, Kesavadasapuram, Trivandrum 695 004, Kerala, India

*[b,]*Department of Chemistry, All Saints' College, University of Kerala, Thiruvananthapuram, Kerala, India –695007*

beenagireesh@yahoo.co.uk

Abstract

Copper has been one of the most important materials in industry owing to its high electrical and thermal conductivities, mechanical workability, and its relatively noble properties. It is widely used in condenser pipes of ships, coastal power plant heat exchangers. Coating methods gets prior importance for the protection of metals and alloys against corrosion. Recently, the inhibition of copper corrosion in NaCl solutions by different types of inhibitor compound by spin coating method has been extensively studied. A zinc curcumin metal complex (Zn-CU) was prepared and its corrosion resistance towards copper corrosion in 3.5% NaCl solution for 3 days was studied. The corrosion resistance property of the synthesized compound was examined by potentiodynamic polarization, SEM and EDX. Metal complex coating on copper substrate was performed by spin coating technique using a nontoxic binder polyvinylpyrrolidone (PVP). Experimental investigations showed that Zn-CU/PVP reduces the copper corrosion and attains 85% inhibition efficiency.

Introduction

The properties of copper and its alloys, including their electrical, thermal, mechanical, and corrosion resistance, make them industrial materials with a wide range of uses. However, they are vulnerable to localised corrosion when oxygen, chlorides, sulphates, or nitrate ions are present (Fiala et al., 2007). Considering that the metallic corrosion process is normally electrochemical and it ordinarily begins at the surface, one promising approach for reducing it would be to develop a controllable physical barrier to corrosion in the form of films and coatings. Utilizing organic inhibitor coatings is one contemporary method for defending metals against corrosion caused by acids, bases, or neutrals (Bahari et al., 2020; Singh et al., 2013).They serve as a barrier or protective layer depending on the construction either as an insoluble chelate barrier created by chemisorption or produced by physisorption in the metal/electrolyte interphase (Antonijevic & Petrovic, 2008). The morphology (shape, branching, or conformation), aromaticity and conjugation, bonding strength to the metal substrate, the presence of heteroatomic nitrogen, oxygen, and/or sulphur, and the type and

number of bonding atoms or groups are some of the factors that affect an organic molecule's ability to inhibit metal corrosion. Other factors that affect the effectiveness of the inhibitor include temperature, pH, and stability in the aggressive environment. Many different approaches, including coating with polymers (M. Kendig et al., 2003) organic layers (Dahmani et al., 2021; X. Zhang et al., 2020) and other metals and alloys,(M. W. Kendig & Buchheit, 2003) have been developed to protect the copper surface. However, the existing coating technologies typically change the physical properties of copper, such as physical dimensions, appearance, and optical properties, due to the thickness of the coating, and often decrease the thermal and electrical conductivities. To overcome these drawbacks, intense effort is currently underway to create a thin coating with minimum changes in the physical and chemical properties of underlying metals. Recently, several reports have demonstrated that films formed by spin coating play a role of effective anti-corrosion barriers for electrochemical corrosion of metals (Ali Syed et al., 2015; Gore et al., 2019). In this work, a metal complex derived from Zinc Curcumin (Zn-CU) was coated on copper surface using polyvinyl pyrrolidone (PVP) as binder by spin coating method and tested for corrosion in 3.5% NaCl for 3 days. PVP is a non-toxic and eco-friendly water-soluble polymer utilized as a green corrosion inhibitor. Additionally, PVP has distinctive inhibition properties as it has an oxazole moiety (N-heterocycle). PVP displays good corrosion inhibition in alkaline solutions containing NaCl and in neutral solutions with a lower hydrogen evolution rate (Hourania et al., 2016; Hussein & Fekry, 2019). The aim of this work is to study the corrosion inhibition effect of Zinc Curcumin complex coating (Zn-CU) on copper in 3.5% NaCl solution using potentiodynamic polarization technique and by SEM/EDX.

Experimental Method

Materials Used

Curcumin longa was purchased from a supermarket. All chemicals and reagents were purchased from Sigma Aldrich. Copper sheet was purchased from an engineering shop.

Preparation of Turmeric extract

Locally available Curcuma longa rhizomes were collected and used as the starting material. The rhizomes were cleaned, dried and ground into powder. Then dried at 50^0C to a constant weight. The removal of lipids and oils from the extract is carried out by maceration technique. In this technique the dried turmeric powder was defatted twice using 30 mL hexane at 200 rpm at room temperature. Using 95% aqueous ethanol, the defatted residue was extracted and incubated for 2 hours by orbital shaker and concentrated at 50^0C under reduced pressure to remove the ethanol. The aqueous extract was then dried to remove the water content(Q. W. Zhang et al., 2018).

Extraction of Curcumin

Curcumin was extracted by Soxhlet extraction procedure. This procedure commonly used for the extraction of materials that are not water-soluble. The turmeric rhizomes were cleaned, parched in hot air oven at 105°C for 3 hrs. Parched turmeric rhizomes were crushed with mortar

and filtered to obtain uniform powder and stored in air tight containers. About 20g of the rhizome powder was weighed accurately and filled in a thimble. Then the thimble was put in the Soxhlet apparatus filled with acetone as the extraction solvent. The extraction procedure was carried out at 60^0C within 8 hrs. After the extraction process, acetone was removed from the extract using rotary evaporator. Then the residue was dried, weighed, and dissolved in 10 ml methanol for calculating the curcumin content using HPLC (Vetter et al., 2019).

Preparation of Zinc-Curcumin metal complex (Zn-CU complex)

4 milli molar solution of curcumin prepared by dissolving 1.473g of curcumin in 25ml of ethanol and heated for complete dissolution. 2 milli molar solution of zinc acetate dihydrate was prepared by dissolving 0.438g zinc acetate dihydrate in 20ml distilled water. The zinc acetate solution was slowly added to the ethanolic curcumin solution with constant stirring and refluxed for 3 hours. An orange red coloured precipitate formed was washed with 1:1 hot ethanol – water solution, dried under 60^0C in hot air oven and stored in silica desiccator. The yield was about 70%. This complex was completely soluble in DMSO partially soluble in DMF, methanol, ethanol and insoluble in water.

Characterisation of Zinc Curcumin metal complex (Zn-CU)

1. IR spectroscopy

IR spectroscopy of Curcumin and Curcumin–Zn (II) complex was performed on Perkin Elmer Spectrum 100 FTIR spectrophotometer by using a KBr disc. The spectral range was from 4000 to 550 cm^{-1}.

2. ^{1}H NMR spectroscopy

^{1}H NMR spectra of Curcumin and Zn-CU complex in DMSO-d_6 solution were recorded on PROBHD Z108618_0948 (PULPROG), 400 MHZ spectrometer. A 5 mm diameter NMR tube was used for this study.

CORROSION APPLICATION OF PREPARED METAL COMPLEX

1. Pre-treatment of the copper coupons

The copper coupons were cut into 40 x 20 x 2mm dimensions and polished with different grades of emery paper. The polished coupons were washed with soap solution and then with distilled water. It was dried using a filter paper and degreased with acetone. The dried coupons were stored in a desiccator for 30 minutes and used as electrodes for electrochemical studies. About $1cm^2$ surface area was exposed for the experiment. The test solution of 3.5% NaCl was prepared with distilled water.

2. Procedure of spin coating technique

About 100µL of the inhibitor solution with different concentrations of Zn-CU/PVP was spin coated on copper surface at a speed of 1000 rpm for 30s. The coated substrates were dried on a hot plate at 100 ^{0}C for 15 minutes. The dried substrates were tested for corrosion resistance studies in 3.5% NaCl medium for 3 days.

3. Potentiodynamic polarization study

The experiment was conducted in CHI6041E electrochemical system at 30^{0}C. The copper strips, platinum electrode and saturated calomel electrode were used as the working electrode, counter electrode, and reference electrode respectively. The pre-treated copper coupons were dipped in the test solution of 3.5% NaCl for 30 min to attain a steady state and the open circuit potential (OCP) was calculated (Habeeb et al., 2018). The cathodic and anodic Tafel curves were recorded with respect to the OCP value with a scanning rate of 1 mV/S^{-1}. The inhibition efficiency (η) from the potentiodynamic polarization measurement was given by the following equation:

$$\eta = \frac{i^0{}_{corr} - i_{corr}}{i^0_{corr}} \qquad (1)$$

where i^o_{corr} and i_{corr} are the corrosion current densities in the absence and presence of Zn-CU coating.

4. SEM evaluation

The FEI Nova Nano SEM 450 tool examined the morphology of coupons. The acceleration beam's energy was used at 20 keV. Analysing the morphology of the coated layer adsorbed on copper coupons is beneficial (Berrissoul et al., 2020).

5. EDX evaluation

By using a Bruker X Flash energy-dispersive X-ray spectrometer, the composition in the copper surface in 3.5% NaCl in the absence and presence of Zn-CU coating were measured.

Results And Discussion

Characterisation of Zinc Curcumin metal complex (Zn-CU)

1. IR spectroscopy

The FT-IR spectrum of curcumin is shown in Fig 1.

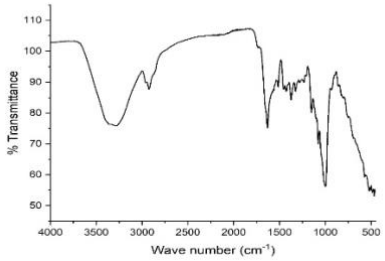

Fig 1. FT-IR spectrum of curcumin

The characterization of the complex was carried out using several techniques. To identify the functional groups, present in the curcumin ligand and its complex, FT-IR spectra were utilized. A stretching vibration at 1630 cm^{-1} and 1514 cm^{-1} corresponding to merging bands of (C=C) and (C=O) respectively. Peaks at 999 cm^{-1} and 1076 cm^{-1} in curcumin corresponded to the in-plane bending of aromatic C-CH and skeletal C-CH. Broadband shown at 3283cm^{-1} corresponds to the enolic –OH bond. The sharp band at 1425 cm^{-1} was associated with aromatic C=C stretching. Further, an intense medium band was observed at 1151 cm^{-1}, corresponding to the bending vibration of the phenolic group (C–O).

The FT-IR spectrum of Zn-CU complex is shown in Fig 2.

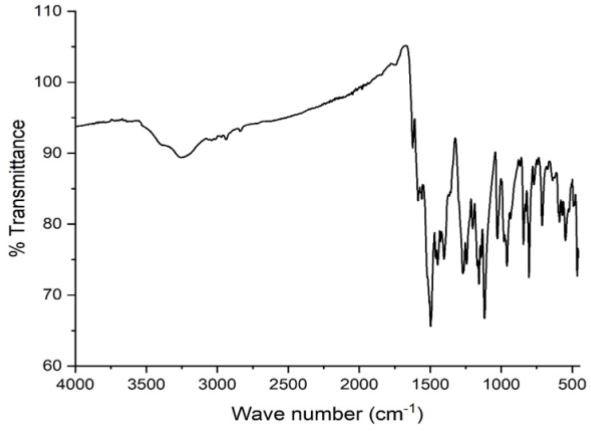

Fig 2. FT-IR spectrum of Zinc Curcumin complex

The (C=O) band of the curcumin shifted to the lower field from 1630 cm^{-1} to 1623 cm^{-1} (Refat et al.,2013). The enolic -OH band shifted to 3257 cm^{-1} from 3283 cm^{-1} in metal complex. It implies the conjugation of metal ion to the enolic -OH. A new band was observed

at 465 cm^{-1} in the complex corresponding to stretching frequency of (Zn–O). The benzoate trans–CH vibration was observed at 999 cm^{-1} for the pure curcumin ligand, which was shifted to 959 cm^{-1} for the Zn-CU complex (Kundu et al., 2013). The peaks at 2900-2800 cm^{-1} in both the curcumin ligand and complex was due to asymmetric CH stretching of either $–CH_3$ or $–OCH_3$ groups, which were present in both spectra.

2. ^{1}H NMR spectrum

The NMR spectrum for Zn-CU complex was performed using d_6 DMSO is shown in Fig 3.

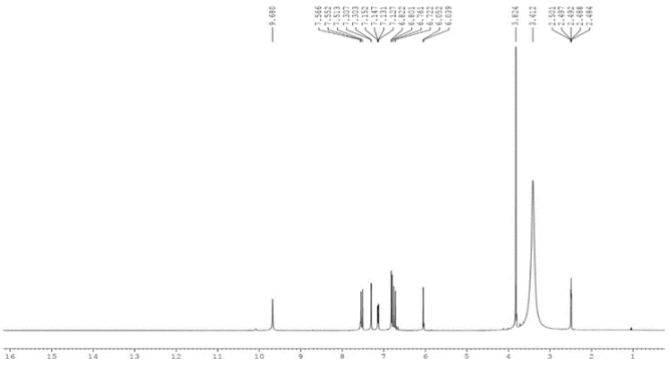

Fig 3. ^{1}H NMR spectrum of Zn-CU metal complex

The chemical shifts data δ (ppm) of the complex is given in Table 1 which was compared with the curcumin NMR spectrum from the literature (John et al 2005).

Table 1. Chemical shift values of Zn-CU complex

Type of Protons	**Chemical Shift (δ ppm)**	
	Curcumin	**Zn-CU Complex**
DMSO	2.517	2.501
H_2O (moisture)	3.365	3.412
6H ($-OCH_3$)	3.855	3.824
1H (C1)	6.073	6.039
1H (C3)	6.737	6.052
1H (C9)	6.825	6.761
1H (C10)	7.173	7.131
1H (C6)	7.338	7.303
1H (C4)	7.594	7.566
1H (-OH phenol)	9.82	9.68
1H (-OH enol)	16.45	_

From Table 1, it is evident that all protons of different carbon type in the complex were closely related to the free ligand except for the enolic proton. In the Zn-CU complex spectra, a low field signal for an intra-molecular hydrogen-bonded enolic proton at δ 16.45 ppm was missing, which indicates the contribution of carbonyl oxygen of enol in the formation of the complex (John et al 2005).

Corrosion Studies

\1. Potentiodynamic polarization study

Tafel curves of copper electrode in 3.5% NaCl in the absence and presence of Zn-CU complex coating are shown in Fig 4.

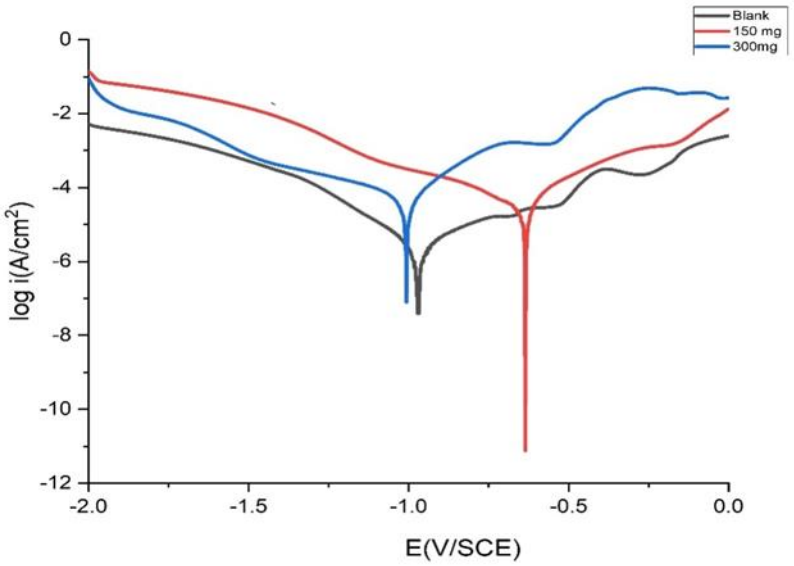

Fig 4. Tafel plot of coated and uncoated copper surfaces at 30 0C in 3.5% NaCl media.

This figure showed that the cathodic and anodic curves were different in the case of with and without Zn-CU coating. The E_{corr}, i_{corr}, η, βc and βa values, were obtained from Tafel curves. These parameters are given in Table 2.

Table 2. Corrosion parameters for uncoated and coated copper surface with Zn-CU/PVP.

Concentration (mg)	**E_{corr} (m V)**	**I_{corr} (µA cm^{-2})**	***β_a***	***β_c***	**IE (%)**
Uncoated copper	-972	44	635	149	0
Coated with150mg Zn-CU/PVP	-627	38.53	163	299	70
Coated with 300 mg Zn-CU/PVP	-1062	9.38	98	237	85

It was clear that the value of i_{corr} decreased in coated copper surface. This indicates the protective effect of inhibitor coating on copper which reduced the anodic dissolution. The corrosion inhibition efficiency attained a maximum of 85% at 300 mg/ L^{-1}.

2. SEM analysis

The surface study of copper after 3 days of immersion with and without coating was analysed by scanning electron microscopy. The SEM micrographs of copper surface after 3 days of immersion in 3.5% NaCl in the absence and presence of Zn-CU/PVP coating are shown in Fig 5.

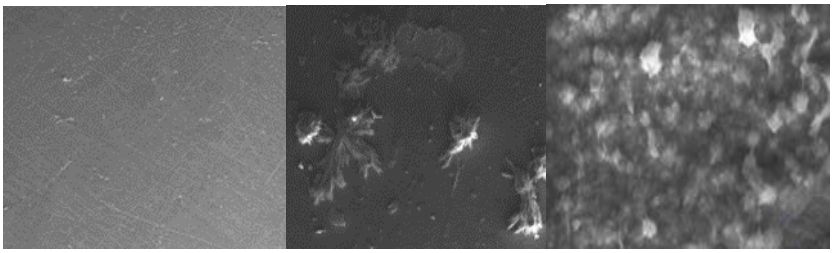

a b c

Fig 5. SEM micrographs of (a) polished copper, (b) after immersion without coating (c) coated with 300 mg Zn-CU/PVP in 3.5% NaCl solution for 3 days.

The Fig 5 (a) is the polished copper surface before coating, found smooth and showed some abrading scratches on the surface. Fig 5 (b) represents the damaged copper surface due to the corrosion attack by 3.5% NaCl solution. SEM images of coated copper surface after 3 days of immersion in NaCl solution with 300 mg Zn-CU/PVP complex is shown in Fig 5 (c). Fig 5 (c) shows the protective layer of coating on copper surface. The coated surface was not attacked by the corrosive media. From this it can be confirmed that the metal complex of zinc has potential ability to act as a better coating for the corrosion resistance of copper surface. A

good protective layer of Zn-CU/PVP complex efficiently inhibits corrosion of copper in neutral media.

3. EDX Analysis

EDX spectrum analysis was performed to identify the elemental composition of the coated layer formed on the copper surface is shown in Fig 6.

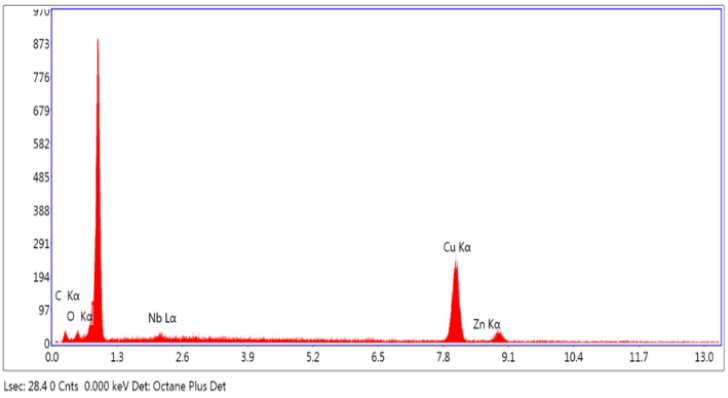

Fig 6. EDX spectra of coated copper surface with Zn-CU/PVP after 3 days of immersion in 3.5% NaCl.

This figure represents the spectrum of coated copper surface with 300 mg Zn-CU/PVP complex after the immersion in 3.5% NaCl solution for 3 days. Detection of C, O and Zn on this sample proved the better coating of Zn-CU complex on the surface of copper. The presence of C, O and Zn on the sample after 3 days of immersion in 3.5% NaCl confirmed the stability of Zn-CU/PVP layer on copper surface.

Conclusion

Synthesis of less toxic green anticorrosive coatings by incorporating plant and natural extracts are not only eco-friendly but also provide excellent corrosion prevention. This work mainly focussed on the synthesize of an eco-friendly metal complex of zinc by incorporating curcumin (Zn-CU). The synthesized compound was coated on copper surface using a binder PVP by spin coating method. Corrosion inhibition efficiency of Zn-CU increased with the concentration of metal complex. The corrosion resistance was up to 85% with 300 mg/ L^{-1} Zn-CU/PVP at 30^0C. The corrosion resistance property of Zn-CU metal complex in corrosive environment of 3.5% NaCl for copper has been tested by polarisation analysis, SEM and EDX. Electrochemical tests confirmed that Zn-CU complex showed better corrosion inhibition property. SEM supported by EDX confirmed the stability and elemental composition of coating on the copper surface.

Acknowledgements

We greatly acknowledged St. John's College, Anchal and Central laboratory for instrumentation and facilitation, Kariavattom for their help during the analysis of samples. We are very thankful to Government of Kerala for providing fellowship for doing this work.

References

1. Fiala, A., Chibani, A., Darchen, A., Boulkamh, A., & Djebbar, K. (2007). Investigations of the inhibition of copper corrosion in nitric acid solutions by ketene dithioacetal derivatives. *Applied Surface Science*, *253*(24), 9347–9356. https://doi.org/10.1016/j.apsusc.2007.05.066
2. Singh, B. P., Jena, B. K., Bhattacharjee, S., & Besra, L. (2013). Development of oxidation and corrosion resistance hydrophobic graphene oxide-polymer composite coating on copper. *Surface and Coatings Technology*, *232*, 475–481. https://doi.org/10.1016/J.SURFCOAT.2013.06.004
3. Bahari, H. S., Ye, F., Carrillo, E. A. T., Leliopoulos, C., Savaloni, H., & Dutta, J. (2020). Chitosan nanocomposite coatings with enhanced corrosion inhibition effects for copper. *International Journal of Biological Macromolecules*, *162*, 1566–1577. https://doi.org/10.1016/J.IJBIOMAC.2020.08.035
4. Antonijevic, M. M., & Petrovic, M. B. (2008). Copper Corrosion Inhibitors. A review. *Int. J. Electrochem. Sci* Vol. 3.
5. Kendig, M., Hon, M., & Warren, L. (2003) "Smart" Corrosion Inhibiting Coatings. *Progress in Organic Coatings* doi: 10.1016/S0300-9440(03)00137-1.
6. Dahmani, K., Galai, M., Ouakki, M., Cherkaoui, M., Touir, R., Erkan, S., Kaya, S., & El Ibrahimi, B. (2021). Quantum chemical and molecular dynamic simulation studies for the identification of the extracted cinnamon essential oil constituent responsible for copper corrosion inhibition in acidified 3.0 wt% NaCl medium. *Inorganic Chemistry Communications* Vol. 124. https://doi.org/10.1016/j.inoche.2020.108409.
7. Kendig, M. W., & Buchheit, R. G. (2003). Corrosion Inhibition of Aluminum and Aluminum Alloys by Soluble Chromates, Chromate Coatings, and Chromate-Free Coatings. *Corrosion*, *59*(5), 379–400. https://doi.org/10.5006/1.3277570.
8. Ali Syed, J., Lu, H., Tang, S., & Meng, X. (2015). Enhanced corrosion protective PANI-PAA/PEI multilayer composite coatings for 316SS by spin coating technique. *Applied Surface Science*, *325*(C), 160–169. https://doi.org/10.1016/j.apsusc.2014.11.021.
9. Hourania, M., Acta, H. A. Port (2016) Promotion of Copper Corrosion Inhibition by Application of a Square Wave Potential Regime to Copper Specimens in Polyvinylpyrrolidone Solutions. *Peacta.Org*, *34*(4), 267–275. https://doi.org/10.4152/pea.201604267
10. Zhang, Q. W., Lin, L. G., & Ye, W. C. (2018). Techniques for extraction and isolation of natural products: A comprehensive review. *Chinese Medicine (United Kingdom)*, *13*(1), 1–26. https://doi.org/10.1186/S13020-018-0177.
11. Vetter, W., Müller, M., Englert, M., & Hammann, S. (2019). Counter current chromatography-when liquid-liquid extraction meets chromatography. *Liquid-Phase Extraction* 289–325.https://doi.org/10.1016/B978-0-12-816911-7.00010-4.

12. Habeeb, H. J., Luaibi, H. M., Dakhil, R. M., Kadhum, A. A. H., Al-Amiery, A. A., &Gaaz, T. S. (2018). Development of new corrosion inhibitor tested on mild steel supported by electrochemical study. *Results in Physics*, *8*, 1260–1267. https://doi.org/10.1016/J.RINP.2018.02.015.

13. Berrissoul, A., Loukili, E., Mechbal, N., Benhiba, F., Guenbour, A., Dikici, B., Zarrouk, A., &Dafali, A. (2020). Anticorrosion effect of a green sustainable inhibitor on mild steel in hydrochloric acid. *Journal of Colloid and Interface Science*, *580*, 740–752. https://doi.org/10.1016/j.jcis.2020.07.073.
14. Refat, M.S. (2013) Synthesis and characterization of ligational behavior of curcumin drug towards some transition metal ions: Chelation effect on their thermal stability and biological activity. *Spectrochim. Acta Part A Mol. Biomol. Spectrosc.*, *105*, 326–337. https://doi.org/10.1016/j.saa.2012.12.041.
15. Kundu, S.; Nithiyanantham, U. (2013) In situ formation of curcumin stabilized shape-selective Ag nanostructures in aqueous solution and their pronounced SERS activity. *RSC Adv. 3*, 25278–25290. https://doi.org/10.1039/C3RA44471F.
16. Kong, L.; Priyadarsini, K.I.; Zhang, H.-Y. (2004) A theoretical investigation on intramolecular hydrogen-atom transfer in curcumin. *J. Mol. Struct. THEOCHEM, 684*, 111–116. https://doi.org/10.1016/j.theochem.2004.06.034.
17. John, V.D.; Krishnankutty, K. (2005) Synthesis, characterization and antitumour activities of some synthetic curcuminoid analogues and their copper complexes. *Transit. Met. Chem. 30,* 229–233. https://doi.org/10.1007/s11243-004-2632-z.

SYNTHESIS, CHARACTERISATION AND EPR SPECTRAL STUDIES OF COPPER(II) COMPLEXES OF *N*(4)-PHENYLSEMICARBAZONES

V.L. Siji[a], M. R. Sudarsanakumar[a,*]

[a] Department of Chemistry, All Saints' College, Thiruvananthapuram 695 007, Kerala, India

[a,]Department of Chemistry, Mahatma Gandhi College, Thiruvananthapuram 695 004, Kerala, India*

Abstract

Five copper(II) complexes $[Cu_2L^1{}_2(CH_3COO)_2]$ (**1**), $[Cu(HL^1)_2(NO_3)_2]$ (**2**), $[Cu(HL^2)_2(CH_3COO)_2]$ (**3**) and $[Cu(HL^2)_2(NO_3)_2]$ (**4**) have been synthesized and characterized by elemental analyses, molar conductance, magnetic susceptibility measurements, IR, electronic and EPR spectral studies. The IR spectral data suggests the involvement of oxygen and azomethine nitrogen in coordination to the central metal ion. The EPR spectra of complexes **1**, **2**, **3** and **4** in DMF solution at 77 K are axial with four hyperfine quartets in the parallel region could be resolved and a half field signal is observed at 1600 G for complex **3** which give evidence for its binuclear nature indicating a weak interaction between the two Cu(II) ions. Based on EPR studies, the spin Hamiltonian and bonding parameters have been calculated. The metal-ligand bonding parameters evaluated showed strong in-plane sigma and in-plane π bonding.

Keywords: Semicarbazones; Coordination compounds; EPR studies; Magnetic susceptibility measurements; Electronic spectra

Introduction

Semicarbazones are versatile ligands having π-delocalization of charge and configurational flexibility of the molecular chain that can give rise to a great variety of coordination modes.[1] Owing to the interest they generate through a variety of biological properties ranging from antitumoral, antibacterial, anticonvulsant, antiviral and antimalarial activities.[2-5] The biological activities of these ligands are considered to be their ability to form chelates with metals. Biological actions of metal complexes differ from those of either ligands or metal ions and increased or decreased biological activities are reported for several transition

metal complexes.[6] These materials have been used as drugs whose action is attributed to their ability to form metal complexes.[7]

Copper(II) complexes are interesting due to their biological roles and medicinal properties.[8] The copper complex of salicylaldehyde semicarbazone possessed pronounced antineoplastic properties against mammary carcinoma cells of the MCF-7 line.[9] The primary objective of this study has been to synthesize Cu(II) complexes of semicarbazones, where the semicarbazone ligands are coordinated in different fashions. The coordinating ability of semicarbazones is attributed to the extended delocalization of electron density over the NH−C(O)−NH−N═ system, which is enhanced by the substitution at the N^4 position.[10]

In continuation of our investigations on the complexing properties of N^4-phenyl semicarbazones, we synthesized two ligands benzaldehyde N^4-phenylsemicarbazone (HL^1) and acetone N^4-phenylsemicarbazone (HL^2) [11, 12]. Some complexes of these ligands have been reported recently. Here we report synthesis, spectral and EPR investigations of Cu(II) complexes of these two ligands. Through this paper, we could highlight some of the interesting features in the EPR spectra.

Experimental

Materials

N^4-phenylsemicarbazide (Sigma Aldrich), benzaldehyde (Merck) and acetone (Merck) were used as received. $Cu(NO_3)_2 \cdot 3H_2O$ and $Cu(CH_3COO)_2 \cdot H_2O$ were of analar grade and used as supplied. Solvent used was methanol (Merck) and used without further purification.

Synthesis of ligands

The synthesis of benzaldehyde-N^4-phenylsemicarbazone (HL^1) and acetone -N^4-phenylsemicarbazone (HL^2) [12] have been published by us earlier (Scheme 1). An equimolar mixture of N^4-phenylsemicarbazide (1 mmol) and benzaldehyde/acetone (1 mmol) was refluxed in methanol in presence of three to four drops of dilute acetic acid for 3 h (Scheme 2). On slow evaporation, colorless crystals of the compound separated out. It was filtered, washed with ether and dried over P_4O_{10} *in vacuo*. The compound was recrystallized from methanol.

HL^1: Yield: 75%; M.P.: 176-178 °C. Elemental Anal. Found (Calc.) (%): C, 70.24 (70.27); H, 5.45 (5.48); N, 17.72 (17.56). ^{1}H NMR (δ ppm in $CDCl_3$): 9.51 (1H, s), 8.13 (1H, s), 7.85 (1H, s), 7.09 – 7.58 (5H, m), 7.11-7.67 (5H, m). ^{13}C NMR (δ ppm in $CDCl_3$): C(8), 153.61; C(7), 141.78; C(9), 137.84; C(1), 133.66; C(11) & C(13), 130.02; C(12), 129.02; C(10) & C(14), 128.79; C(3) & C(5), 126.94 ; C(4), 123.54; C(2) & C(6), 119.68.

HL^2: Yield: 80%; M.P.: 152-154 °C. Elemental Anal. Found (Calc.) (%): C, 62.76 (62.80); H, 6.56 (6.87); N, 21.95 (21.98). ^{1}H NMR (δ ppm in $CDCl_3$): 8.04 (1H, s), 8.21 (1H, s), 7.02 – 7.52 (5H, m), 2.03 (3H, s), 1.90 (3 H, s), ^{13}C NMR (δ ppm in $CDCl_3$): C(4), 153.69; C(2), 147.72; C(5), 138.25; C(7) & C(9), 128.90; C(8), 123.10; C(6) & C(10), 119.36, C(3), 25.28; C(1), 16.52.

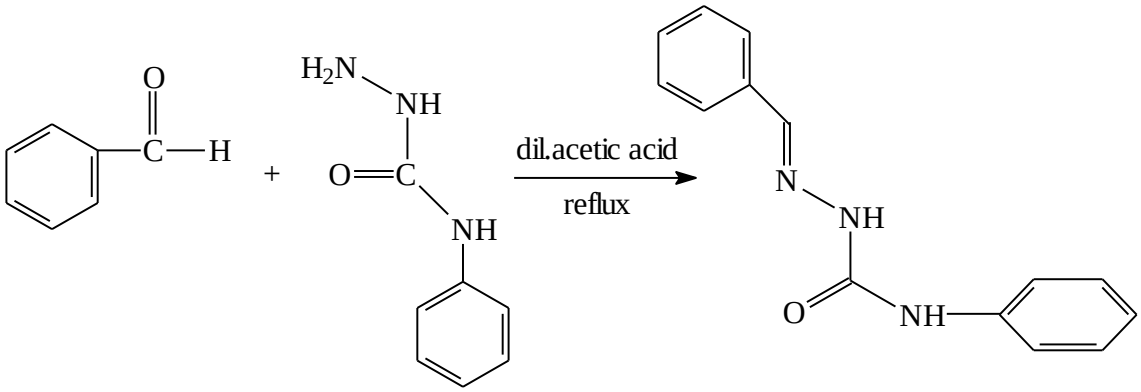

(Scheme 1)

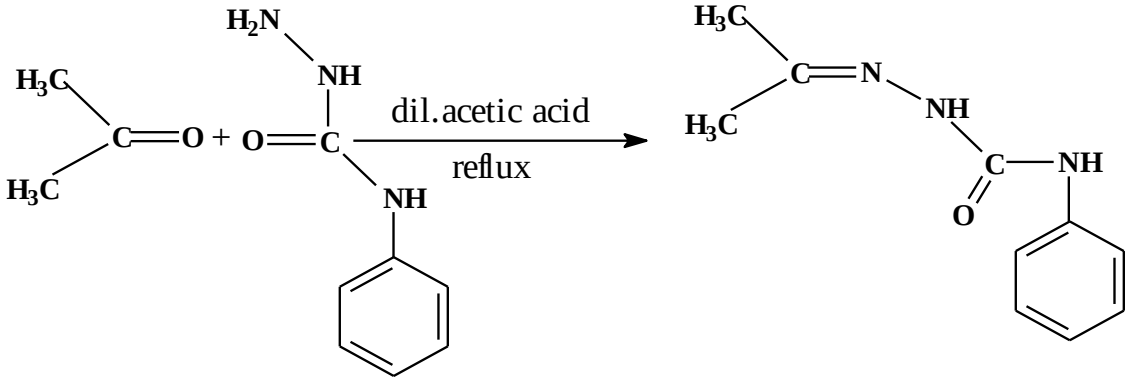

(Scheme 2)

Synthesis of complexes

*a. Synthesis of $[Cu_2L^1{}_2(CH_3COO)_2]$ (**1**) and $[Cu(HL^1)_2(NO_3)_2]$ (**2**)*

A solution of the ligand HL^1 (0.478 g, 2 mmol) in 20 ml of methanol was treated with methanolic solution of the appropriate salts (1 mmol). The solution was heated under reflux for 5 h. The resulting solution was allowed to stand at room temperature and after slow evaporation crystals separated out, which were collected, washed with methanol and finally with ether and dried over P_4O_{10} *in vacuo*.

$[Cu_2L^1{}_2(CH_3COO)_2]$ (**1**): Yield: 79 %, Color: green, M.P.: 216 °C, λ_m (methanol): 21 $ohm^{-1}cm^2mol^{-1}$, μ_{eff} (B.M.): 1.21, Elemental Anal. Found (Calcd.) (%): C, 53.15 (53.25); H, 4.27 (4.20); N, 11.61 (11.65)

$[Cu(HL^1)_2(NO_3)_2]$ (**2**): Yield: 75 %, Color: dark green, M.P.: 269 °C, λ_m (methanol): 13 $ohm^{-1}cm^2mol^{-1}$, μ_{eff} (B.M.): 1.81, Elemental Anal. Found (Calcd.) (%): C, 50.51 (50.49); H, 4.05 (3.94); N, 16.93 (16.83)

*b. Synthesis of $[Cu(HL^2)_2(CH_3COO)_2]$ (**3**)*and *$[Cu(HL^2)_2(NO_3)_2]$ (**4**)*

A solution of the ligand HL^2 (0.382 g, 2 mmol) in 20 ml of methanol was treated with methanolic solution of the appropriate salts (1 mmol). The solution was heated under reflux for 5 h. The resulting solution was allowed to stand at room temperature and upon slow evaporation crystals separated out, which were collected, washed with methanol and finally with ether and dried over P_4O_{10} *in vacuo*.

$[Cu(HL^2)_2(CH_3COO)_2]$ (**3**): Yield: 85%, Color: green, M.P.: 241 °C, λ_m (methanol): 15 $ohm^{-1}cm^2mol^{-1}$, μ_{eff} (B.M.): 1.85, Elemental Anal. Found (Calcd.) (%): C, 51.03 (51.10); H, 5.83 (5.73); N, 14.95 (14.90)

$[Cu(HL^2)_2(NO_3)_2]$ (**4**): Yield: 77 %, Color: dark green, M.P.: 224 °C, λ_m (methanol): 6 $ohm^{-1}cm^2mol^{-1}$, μ_{eff} (B.M.): 1.76, Elemental Anal. Found (Calcd.) (%): C, 42.20 (42.14); H, 4.69 (4.61); N, 19.61 (19.66)

Physical measurements

Elemental analyses of the ligands and their complexes were done on a Vario EL-III CHNS analyzer at SAIF, Cochin University of Science and Technology, Kochi, India. Infrared spectra were recorded on a Thermo Nicolet, Avator 370 spectrometer in the range 4000-400 cm^{-1} using KBr pellets. Electronic spectra in methanol were recorded on a Shimadzu UV-2450 UV – Vis. spectrophotometer. The molar conductances of the complexes in methanol (10^{-3} M) solution were measured at 298 K with a Systronics model 303 direct reading conductivity meter. Magnetic susceptibility measurements at room temperature were made using a PAR model 155 Vibrating Sample Magnetometer at 5 kOe field strength, at the Indian Institute of Technology, Roorkee, India. X-band EPR spectra of complexes in solid state at 298 K were recorded on a JEOL-JES-TE100 spectrometer, with diphenyl picryl hydrazine (DPPH) as the reference at Pondicherry University, Puducherry and at 77 K were recorded using DMF as a solvent at liquid nitrogen temperature on a Varian E-112 spectrometer using TCNE as the

standard with 100 kHZ modulation frequency and 9.1 GHz microwave frequency at SAIF, IIT, Bombay, India.

Results and discussion

All complexes were found to form readily from the reaction mixture of the appropriate salts and the ligand in hot methanol. Elemental analyses and conductivity data are in agreement with the empirical formula. In complex **1**, the semicarbazone deprotonate and chelate in the enol form, as proven by the IR spectral data. In complexes **2**, **3** and **4**, the ligand moieties are in the keto form. The molar conductivity values for 10^{-3} M methanol solutions of complexes suggest that these complexes are non-electrolytes. As expected these complexes are EPR active due to the presence of unpaired electron.

Magnetic susceptibilities

The magnetic moments of the Cu(II) complexes were calculated from the magnetic susceptibility measurements after applying the diamagnetic corrections. The Cu(II) complexes generally exhibit room temperature magnetic susceptibility as expected for an isolated d^9 transition metal center. The effective magnetic moment (μ_{eff}) values for all complexes except complex **1** fall in the range 1.76-1.85 B.M. very close to the spin only value for d^9 copper(II) complex.[15, 16] Magnetic moment value obtained for complex **1** is 1.21 B.M. which is in the range of 1.15-1.40 B.M., expected for a binuclear complex.[17] The low magnetic moment may be attributed to the presence of a strong antiferro-magnetic spin-spin interaction involving an oxygen bridged binuclear structure similar to those proposed for the Cu(II) complexes of analogous tridentate ligands.[18]

Infrared spectra

The tentative assignments of the important IR frequencies of the ligands and their complexes are presented in Table 1. The selected vibrational bands of the free ligand with its complexes give information about the ligating mode of the ligand upon complexation. The medium band at 3357 cm^{-1} and a strong band at 3375 cm^{-1} in the spectra of HL^1 and HL^2, assigned to $\nu(^4NH)$, shift to higher and lower energies.[19, 20] A medium band at 2917 cm^{-1} and 3196 cm^{-1} in the free ligands HL^1 and HL^2 respectively, due to $\nu(^2NH)$ vibration, is observed in the spectra of the complexes except complex **1**.. In complex **1**, the $\nu(^2NH)$ band disappears in the spectrum providing strong evidence for the ligand coordination to the Cu(II) ion in the deprotonated enol form and thus acting as uninegative ligand.[21,22] The ν(C=O) bands of semicarbazones are found to be shifted to lower frequencies in the other complexes. This indicates that the ligand coordinates to the metal in the keto form.[23] The appearance of a new band at 1242 cm^{-1} due to the coordination of the ν(C–O) enolic mode supports this observation. The ν(C=N) bands of semicarbazones are found to be shifted to lower frequencies in the complexes indicating coordination *via* the azomethine nitrogen.[24] In the spectrum of the complex **1**, the band corresponding to the newly formed N=C bond due to the enolization of

the ligand is present at *ca*. 1518 cm^{-1}.[25] The spectra of the complexes exhibit a systematic shift in the position of ν(N–N) bands in the region 1067-1186 cm^{-1}. The increase in the ν(N-N) value in the spectra of the complexes is due to the increase in double bond character, off-setting the loss of electron density *via* donation to the metal and it is confirmation of the coordination of the ligand through the azomethine.[26] It was further supported by the appearance of new bands at 415-445 cm^{-1}, assignable to ν(M–N) for these complexes.[27]

In complex **3**, the bands at 1555 cm^{-1} and 1314 cm^{-1} due to asymmetric and symmetric stretching suggest the presence of unidentate type of acetate group.[28] In the spectrum of the complex **1**, the bridging nature of acetate group linked with metal center. The asymmetric and symmetric stretching vibrations of the acetate group are observed at 1545 cm^{-1} and 1436 cm^{-1}.[29] The nitrato complexes **2** and **4** have two strong bands at 1448 cm^{-1} and 1283 cm^{-1} due to ν_4 and ν_1 respectively, with a separation of 165 cm^{-1} and a medium band at 1020 cm^{-1} due to ν_2 of the nitrate group. The above observations indicate the presence of terminal monodentate nitrate group.[25] ν_3, ν_5 and ν_6 are observed at 750, 701 and 824 cm^{-1} respectively.[30]

Electronic spectra

The electronic spectra are often very helpful in the evaluation of results furnished by other methods of structural investigation. The significant electronic spectral bands for the ligands and their complexes in methanol are presented in Table 2. The electronic spectra of semicarbazones show two well-defined bands in the UV region. The strong bands are at *ca*. 41,150 and 34,000 cm^{-1}. The former is assigned to the $\pi\rightarrow\pi^*$ and latter one is due to $n\rightarrow\pi^*$ electronic transitions of the semicarbazide moiety. [31] These bands are shifted upon complexation.

The electronic spectra of Cu(II) complexes are dominated by intense charge transfer bands. These intense bands cause the low energy bands to appear as weak shoulders. The charge transfer bands are observed at *ca*. 25,000 cm^{-1} and their broadness can be explained as being due to the combination of O→Cu and N→Cu LMCT transitions.[32] The charge transfer may occur from the P orbital of coordinated ketonic oxygen or nitrogen to the vacant d orbital of Cu(II). All the complexes exhibit a d-d band as weak shoulders in the visible region whose maximum of absorption lie in the visible region *ca*. 14,000 cm^{-1}.[33] The Cu(II) complexes with d^9 configuration is expected to experience Jahn-Teller distortion which leads to further splitting of the ^2Eg and $^2T_{2g}$ levels and give rise to three spin allowed transitions, $^2B_{1g}\rightarrow{}^2A_{1g}(\nu_1)$, $^2B_{1g}\rightarrow{}^2B_{2g}$ (ν_2) and $^2B_{1g}\rightarrow{}^2Eg$ (ν_s), which is expected to close in energy and generally appears as a broad band. It is very difficult to resolve it into separate three bands. The four lower orbitals are often so close together in energy that individual transfer there from to the upper d level cannot be distinguished and hence the single absorption band is observed. The spectra of the complexes are shown in Fig. 1.

EPR spectra of Cu(II) complexes

EPR spectra of the Cu(II) complexes in polycrystalline state at 298 K and in DMF at 77 K were recorded in the X band, using 100 kHz field modulation; g factors were quoted relative to the standard marker DPPH (g = 2.0036) and TCNE (g = 2.00277). The EPR parameters of the Cu(II) complexes are presented in Table 3.

The Cu(II) ion, with a d^9 configuration, has an effective spin of S = 1/2 couples with nuclear spin of ^{63}Cu (I = 3/2) and give rise to four hyperfine lines. In polycrystalline state, since it is magnetically concentrated the anisotropy may be lost. Dilution of the solid isolates the electron spin of the given complex from that of another paramagnetic molecule. In the absence of a magnetic field, the spin levels are doubly degenerate. In a magneticfield this degeneracy is lifted and the energy difference between these states is given by $E = h\nu = g\beta H$ where h is the Planck's constant, ν is the frequency, g is the Lande splitting factor (equal to 2.0023 for a free electron), β is the electronic Bohr magneton and H is the magnetic field. For the case of a $3d^9$ copper(II) ion the appropriate spin Hamiltonian assuming a B_{1g} ground state is given by.[34]

$$\hat{H} = \beta[g_{\parallel} H_z S_z + g_{\perp}(H_x S_x + H_y S_y)] + A_{\parallel} I_z S_z + A_{\perp} (I_x S_x + I_y S_y)$$

EPR spectra provide information about the coordination environment around Cu(II) complexes. The EPR spectra of complexes **2**, **3** and **4** in the polycrystalline state at 298 K (Fig. 2 and Fig. 3) show only one broad signal at g_{iso} = 2.103, 2.026 and 2.024, respectively. Such isotropic spectra consisting of one broad signal and hence only one g value, arises from extensive exchange coupling through misalignment of the local molecular axes between different molecules in the unit cell (dipolar broadening) and enhanced spin lattice relaxation. This type of spectra unfortunately give no information on the electronic ground state of the Cu(II) ions present in the complexes. However, the spectrum of complex **1** shows typical axial spectra with well defined $g_{\parallel}$ and $g_{\perp}$ features at values 2.261 and 2.083. The variation in the $g_{\parallel}$ and $g_{\perp}$ values indicates that the geometry of the compounds in the solid state is affected by the nature of the coordinating gegenions. The geometric parameter G, which is a measure of the exchange interaction between copper centers in the polycrystalline compound, is calculated using the equation

$$G = \frac{(g_{\square} - 2.0023)}{(g_{\perp} - 2.0023)} \text{ for axial spectra}$$

If G > 4, exchange interaction is negligible and if it is less than 4, considerable exchange interaction is indicated in the solid complex.[35, 36] The geometric parameter G for the complex **1** is found to be at 3.1 indicating that the g values obtained in the polycrystalline samples are near to the molecular g values which indicate that the unit cell of the compounds contain magnetically equivalent sites.[37-39] All complexes with $g_{\parallel} > g_{\perp} > 2.0023$ and G value falling with in this range are consistent with a $d_{x^2-y^2}$ ground state.

The EPR spectra of complexes **1**, **2**, **3** and **4** in the DMF solution at 77 K (Fig. 4-Fig. 7) are axial with four hyperfine lines in the parallel regions. For the spectra of the complexes in frozen DMF, the $g_{\|} > g_{\perp}$ values rules out the possibility of trigonal bipyramidal structures for which $g_{\perp} > g_{\|}$ is expected. In binuclear Cu(II) complexes the identification of Cu-Cu dipolar interaction is the most important application of the measurement of the EPR spectra. The zero field splitting parameter D give rise to transitions corresponding to $\Delta Ms = \pm 2$ due to Cu-Cu dipolar interaction. In the X-band spectra, $\Delta Ms = \pm 1$ transitions are associated with fields of *ca.* 3000 G, while the $\Delta Ms = \pm 2$ generate an absorption at the high field value of *ca*. 1500 G and the presence of this half field band is a useful criterion for dipolar interaction for the presence of some binuclear or polynuclear complex formation.[40] The EPR spectrum of the complex **1** in frozen DMF at 77 K (Fig. 4), exhibited a half field signal at 1600 G, which indicates a weak interaction between two copper(II) ions. The EPR parameters $g_{\|}$, $g_{\perp}$, g_{av}, $A_{\|}$ (Cu) and the energies of d-d transition were used to evaluate the bonding parameters α^2, β^2 and γ^2, which may be regarded as measures of the covalency of the in-plane σ bonds, in-plane π bonds and out-of-plane π bonds, respectively. The value of in-plane sigma bonding parameter α^2 was estimated from the following expression.

$$\alpha^2 = \frac{-A_{\|}}{0.036} + \left(g_{\|} - 2.00277\right) + \frac{3}{7}\left(g_{\|} - 2.00277\right) + 0.04$$

The orbital reduction factors $K_{\|} = \alpha^2\beta^2$ and $K_{\perp} = \alpha^2\gamma^2$ were calculated using the following expressions.[41]

$$K_{\|}^2 = \frac{\left(g_{\|} - 2.00277\right) E_{d-d}}{8\lambda_0}$$

$$K_{\perp}^2 = \frac{\left(g_{\perp} - 2.00277\right) E_{d-d}}{2\lambda_0}$$

where λ_0 is the spin orbit coupling constant and has the value –828 cm^{-1} for a copper(II) d^9 system. Hathaway *et al.* [42] has pointed out that for pure σ bonding $K_{\|} \approx K_{\perp} \approx 0.77$ and for in-plane π-bonding, $K_{\|} < K_{\perp}$, while for out-of-plane π-bonding $K_{\perp} < K_{\|}$. In all the complexes, it is observed that $K_{\|} < K_{\perp}$ which indicates the presence of significant in-plane π-bonding. Furthermore α^2, β^2 and γ^2 have values less than 1.0, which is expected for 100% ionic character of the bonds and become smaller with increasing covalent bonding. Therefore the evaluated values of α^2, β^2 and γ^2 of the complexes are consistent with both in-plane σ and in-plane π-bonding. The fact that the $g_{\|}$ values are less then 2.3 is an indication of significant covalent character to the M–L bond.[20, 27]

Conclusions

The analytical data correspond to the composition $[Cu_2L^1{}_2(CH_3COO)_2]$, $[Cu(HL^1)_2(NO_3)_2]$, $[Cu(HL^2)_2(CH_3COO)_2]$ and $[Cu(HL^2)_2(NO_3)_2]$.Conductance data show that the complexes are non-electrolytes in methanol. Infrared spectral data of nitrato complexes indicate monodentate nature of the nitrate group. Infrared spectral evidences establish the bidentate coordination of the ligands through keto/enol oxygen and azomethine nitrogen. EPR spectra of all the complexes in frozen DMF at 77 K are axial with four hyperfine lines in the parallel regions.

Acknowledgements

The authors are thankful to the SAIF, Cochin University of Science and Technology, Kochi, India for elemental analyses, IR and electronic spectral data, IIT, Roorkee for magnetic susceptibility measurements, SAIF, IIT, Mumbai and IIT, Puducherry, India for EPR spectral studies.

References

1. Li Q, Tang H, Li Y, Wang M, Wang L and Xia C G 2000 *J. Inorg. Biochem.* 78(2)167
2. Pandeya S N and Dimmock J P 1993 *Pharmazie* 48(9) 659
3. Beraldo H and Gambinob D 1993 *Mini Rev. Med. Chem*. 4(3) 659
4. Reena T A, Seena E B and Kurup M R P 2008 *Polyhedron* 27(17) 3461
5. Pandeya S N, Yogeeswari P and Stables J P 2000 *Eur. J. Med. Chem.* 35(10) 879
6. Yogeeswari P, Sriram D, Pandeya S N and Stables J P 2004 *Farmaco* 59(8) 609
7. Basuli F, Peng S M and Bhattacharya S 2001 *Inorg, Chem.* 40(6) 1126
8. Bauli F, Peng S M and Bhattacharya S 2000 *Inorg. Chem.* 39(6) 1120
9. Bauli F, Ruf M, Pierpont C and Bhattacharya S 1998 *Inorg. Chem*. 37(23) 6113
10. Casas J S, Garcia-Tasende M S and Sordo J 2000 *Coord. Chem. Rev*. 209(1) 197
11. Siji V L, Sudarsanakumar M R, Suma S and Kurup M R P 2010 *Spectrochim. Acta* 76A(1) 22
12. Siji V L, Sudarsanakumar M R and Suma S 2010 *Polyhedron* 29(9) 2035
13. Devereux M, McCann M, Leon V, Kelly R, Osheaa D and McKee V 2003 *Polyhedron* 22(24) 3187
14. Figgis B N and Lewis J 1964 *Prog. Inorg. Chem.* 6 37
15. Garg B S and Kurup M R P 1988 *Trans. Met. Chem.* 13(4) 309
16. Athappan P R and Rajagopal G 1996 *Polyhedron* 15(3) 527
17. Filipovic N, Borrmann H, Todorovic P, Borna M, Spasojevic V, Sladic D, Novakovic I and Andjelkovic K 2009 *Inorg. Chim. Acta* 362(6) 1996
18. Plesh G and Friebel C 1995 *Polyhedron* 14(9) 1185
19. E1-Sawaf A K, West D X, E1-Saied F A and E1-Babnasawy R M 1998 *Trans. Met. Chem.* 23(5) 649
20. Rapheal P F, Manoj E and Kurup M R P 2007 *Polyhedron* 26(4) 818
21. Tarafder M T H, Kasbollah A, Crouse K A, Ali A M, Yamin B M and Fun H –K 2001 *Polyhedron* 20(18) 2363

22. Reena T A, Seena E B and Kurup M R P 2008 *Polyhedron* 27(6) 1825
23. Siji V L, Sudarsanakumar M R and Suma S 2011 *Trans. Met. Chem.* 36(4) 417
24. Garg B S, Kurup M R P, Jain S K and Bhoon Y K 1988 *Trans. Met. Chem*. 13(2) 92
25. Nakamoto K 1977 *Infrared and Raman Spectra of Inorganic and Coordination Compounds* Part B, 5th ed., Wiley, Interscience, New York
26. Bindhu P, Kurup M R P and Satyakeerty T R 1998 *Polyhedron* 18(3-4) 321
27. Kala U L, Suma S, Kurup M R P, Krishnan S and John R P 2007 *Polyhedron* 26(7) 1427
28. Kurup M R P, Chandra S V and Muraleedharan K 2000 *J. Therm. Anal. Calorim.* 61(3) 909
29. Seguel V G, Rivas B L and Novas C 2005 *J. Chil. Chem. Soc*. 50(1) 401
30. Sathyanarayana D N 2004 *Vibrational Spectroscopy*, New Age International, New Delhi
31. Rao C R K and Zacharias P S 1997 *Polyhedron* 16(7) 1201
32. Joseph M, Kuriakose M, Kurup M,R,P, Suresh E, Kishore A and Bhat G 2006 *Polyhedron* 25(1) 61
33. John, R P, Sreekanth A, Rajakannan V, Ajith T A and Kurup M R P 2004 *Polyhedron* 23(16) 2549
34. Kivelsan D and Neiman R 1961 *J. Chem. Phys*. 35(1) 149
35. Maki A H and McGarvey B R 1958 *J. Chem. Phys*., 29(1) 31
36. Wasson J R and Trapp C 1969 J. Phys. Chem. 73(11) 3763
37. Proctor I M, Hathaway B J and Nicholts P 1968 *J. Chem. Soc. A* 1678
38. Jain S K, Garg B S and Bhoon Y K 1986 *Spectrochim. Acta* 42A(9) 959
39. Hathaway B J and Billing D E 1970 *Coord. Chem. Rev.* 5(2) 194
40. Mangalam N A, Sivakumar S, Kurup M R P and Suresh E 2010 *Spectrochim. Acta* 75 A(2) 686
41. Figgis B N 1996 *Introduction to Ligand Fields*, Interscience, New York
42. Hathaway B J, Wilkinson G, Gillard R D, Mc Cleverty J A (eds) 1987 *Comprehensive Coordination Chemistry*, Vol. 5, Pergamon, Oxford

Table 1. Selected infrared spectral assignments (cm^{-1}) for the ligands and their Cu(II) complexes.

Compound	ν(^{2}NH)	ν(^{4}NH)	ν(C=O)	ν(C=N)	ν(N=C)	ν(N=N)	ν(M=N)	ν(C=O)
HL^1	2917	3357	1708	1600	-	1032	-	-
$[Cu_2L^1{}_2(CH_3COO)_2]$ (**1**)	-	3299	-	1572	1508	1067	443	1242
$[Cu(HL^1)_2(NO_3)_2]$ (**2**)	3058	3313	1601	1567	-	1072	415	-
HL^2	3196	3375	1682	1591	-	1129	-	-
$[Cu(HL^2)_2(CH_3COO)_2]$(**3**)	3342	3397	1647	1566	-	1184	439	-
$[Cu(HL^2)_2(NO_3)_2]$ (**4**)	3218	3291	1665	1580	-	1185	445	-

Table 2. Electronic spectral assignments, λ (cm^{-1}) for the ligands and their Cu(II) complexes.

Compound	**π→π***	**n→π***	**LMCT**	**d-d**
HL^1	41, 150	34, 070	-	-
$[Cu_2L^1{}_2(CH_3COO)_2]$ (**1**)	37630	30950	25440	14100
$[Cu(HL^1)_2(NO_3)_2]$ (**2**)	37310	30860	25000	13320
HL^2	41, 150	33, 960	-	-
$[Cu(HL^2)_2(CH_3COO)_2]$ (**3**)	34600	30760	25770	16150
$[Cu(HL^2)_2(NO_3)_2]$ (**4**)	37300	30860	25010	14880

Table 3. EPR spectral assignments of Cu(II) complexes in polycrystalline state and in frozen DMF at 77 K.

	$[Cu_2L^1_2(CH_3COO)_2]$	**$[Cu(HL^1)_2(NO_3)_2]$**	**$[Cu(HL^2)_2(CH_3COO)_2]$**	**$[Cu(HL^2)_2(NO_3)_2]$**
Polycrystalline (298 K)				
$g_{\|}$	2.261	-	-	-
$g_{\perp}$	2.083	-	-	-
g_{iso}/g_{av}	2.142	2.103	2.024	2.026
G	3.206	-	-	-
DMF (77K)				
$g_{\|}$	2.202	2.219	2.299	2.203
$g_{\perp}$	2.061	2.065	2.086	2.061
g_{av}	2.108	2.115	2.157	2.132
$A_{\|}{}^a$	191.67	172.56	175.30	193.33
α^2	0.7897	0.7625	0.8589	0.8059
β^2	0.8212	0.8831	0.9407	0.8307
γ^2	0.8916	0.9475	0.9973	0.8976
$K_{\|}$	0.6512	0.6733	0.8080	0.6695
$K_{\perp}$	0.7041	0.7224	0.8566	0.7234

[a]A values are given in 10^{-4} cm^{-1}

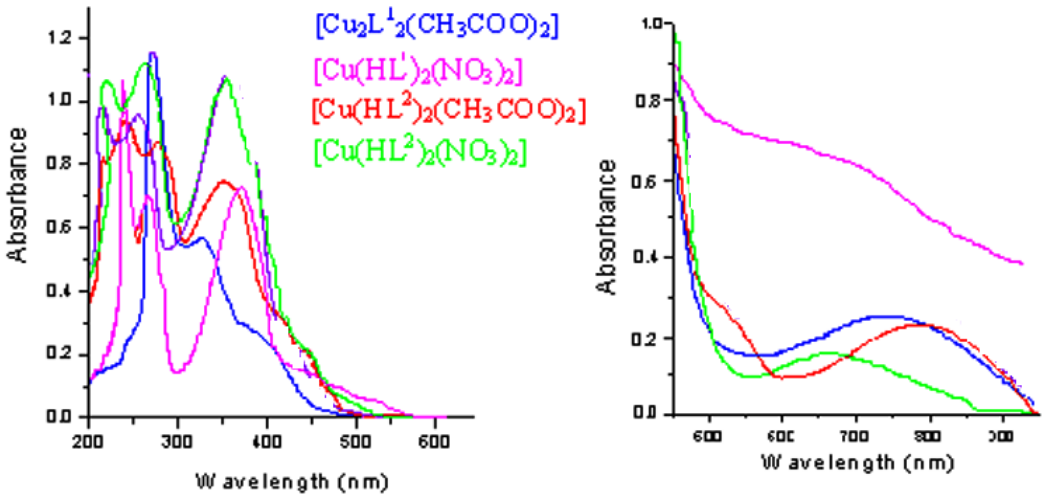

Fig. 1. Electronic spectra of Cu(II) complexes.

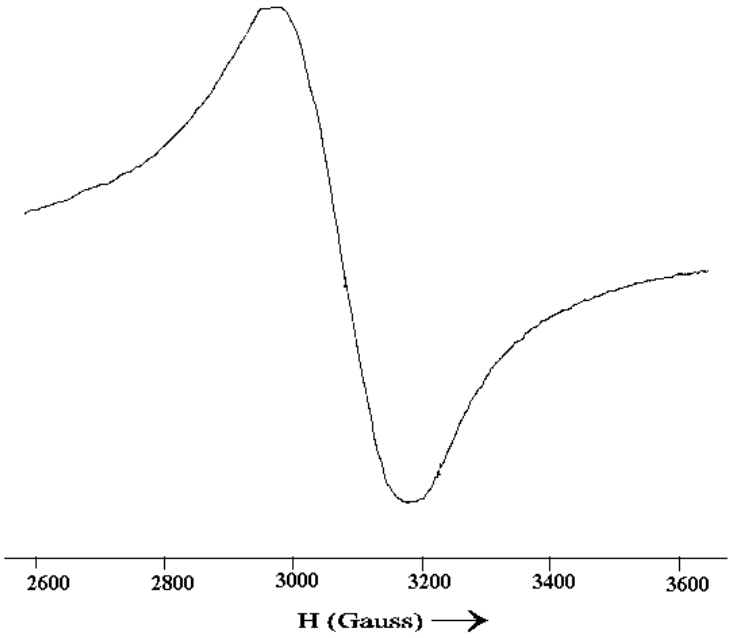

Fig. 2. EPR spectrum of $[Cu(HL^1)_2(NO_3)_2]$ in polycrystalline state at 298 K.

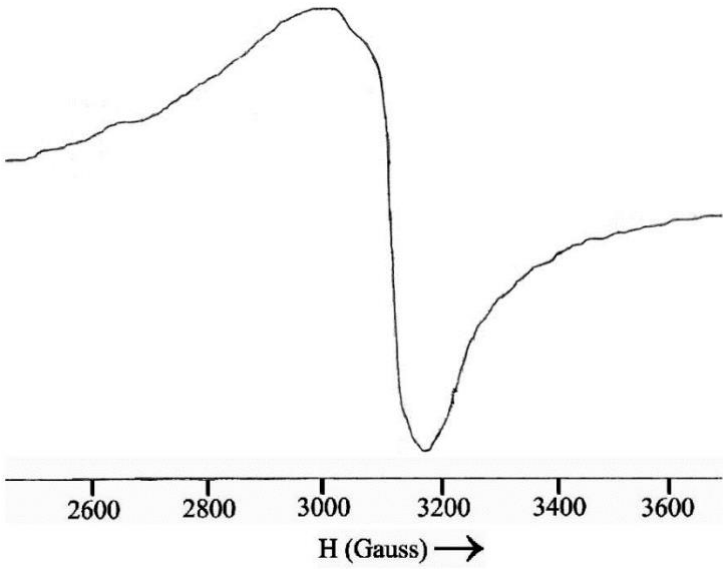

Fig. 3. EPR spectrum of $[Cu(HL^2)_2(CH_3COO)_2]$ in polycrystalline state at 298 K.

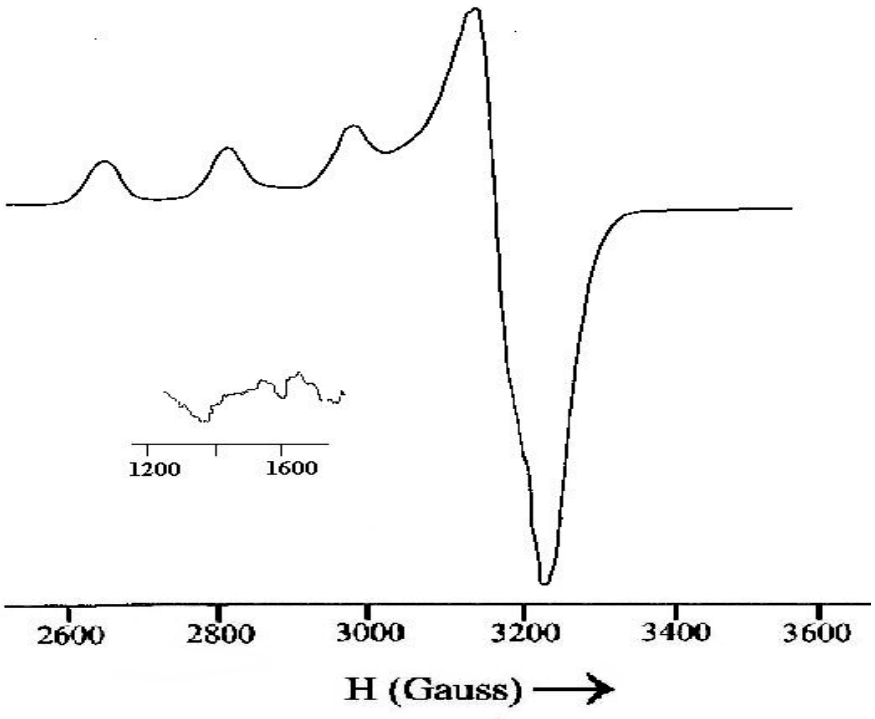

Fig. 4. EPR spectrum of $[Cu_2L^1_2(CH_3COO)_2]$ in DMF solution at 77 K.

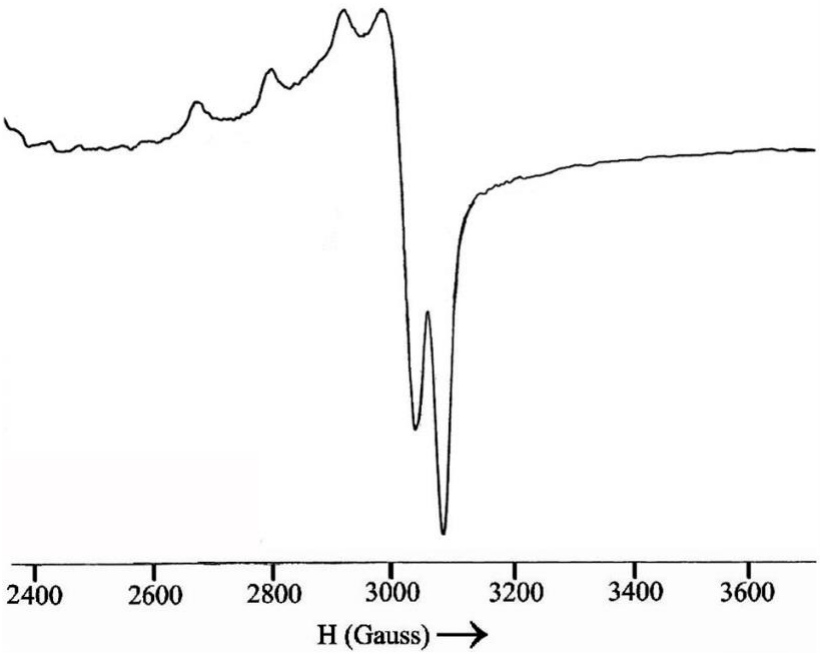

Fig. 5. EPR spectrum of $[Cu(HL^1)_2(NO_3)_2]$ in DMF solution at 77 K.

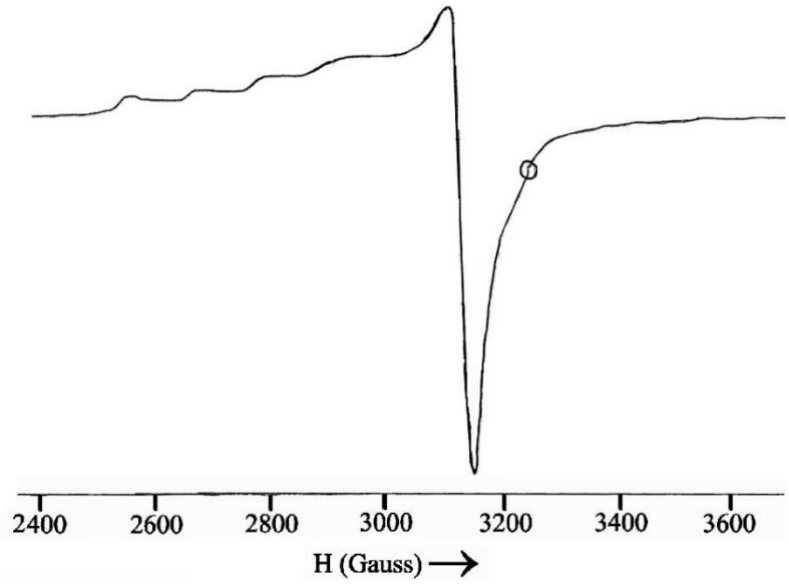

Fig. 6. EPR spectrum of $[Cu(HL^2)_2(CH_3COO)_2]$ in DMF solution at 77 K.

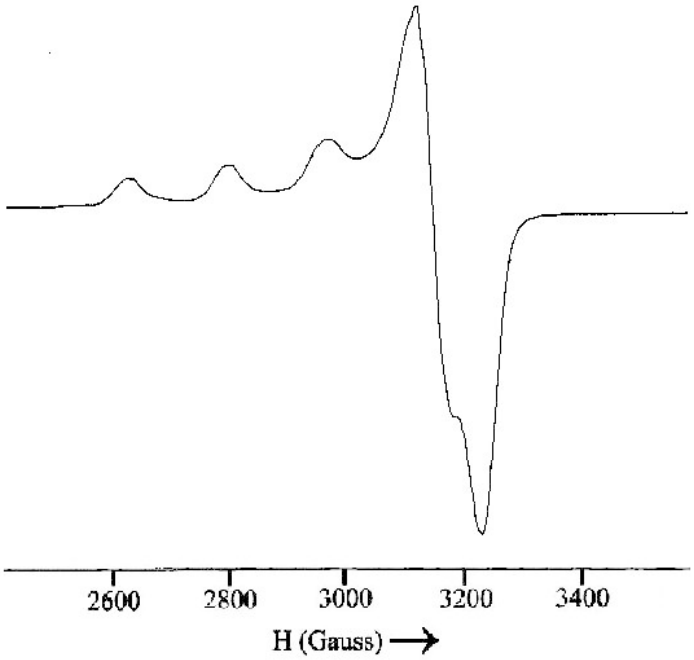

Fig. 7. EPR spectrum of $[Cu(HL^2)_2(NO_3)_2]$ in DMF solution at 77 K.

BIOLOGICAL ACTIVITY AND 3D MOLECULAR MODELING STUDIES OF Mn (II) COMPLEXES DERIVED FROM AMIDINOTHIOUREA DERIVATIVE

Suprabha S

Assistant Professor,
Department of Chemistry,
VTMNSS College, Dhanuvachapuram,
Thiruvananthapuram-695 034, Kerala, India
email: drsuprabhas@vtmnsscollege.ac.in, Telephone: 9446615992

Abstract

Mn(II) complexes with N-amidino-N^1-naphthylthiourea (L) have been synthesized. The physico chemical studies and spectral data reveals that the ligand acts as neutral bidentate and coordinates through S and N. An octahedral geometry has been suggested for all the complexes and are formulated as $[MnL_2X_2]$ where X = Cl^-, NO_3^-, NCS^-. $[MnL_2Cl_2]$ have been subjected to thermal decomposition and the 3D molecular modeling study. The *in-vitro* antimicrobial properties of the ligand in comparison to their metal complexes have been evaluated and it is observed that the complexes show more potent activity than the ligand.

Introduction

Amidinothiourea has several potential coordinating modes since it can act as an NN or SN donor ligand due to thiol-thioketo tautomerism[1,2]. Amidinothiourea and its derivatives are extremely important industrial and biological molecules. Recently research work on safe accelerators has gained interest worldwide and amidinothiourea derivatives are reported to be non-toxic and it is used in many pharmaceutical applications[3].

With the growing interest of amidinothiourea the present work was undertaken in order to investigate the ligational behaviour of amidinothiourea derivative viz. N-amidino-N^1-naphthylthiourea towards the metal ions Mn(II). In addition, the complexes are characterized and screened for their *in vitro* antimicrobial and antitumor activities.

Experimental

Materials. All the reagents and solvents used were of analytical grade quality obtained from commercial suppliers Fluka/Sisco Research Laboratories (India).

Synthesis of N-amidino-N^1-naphthylthiourea

The synthesis of ligand **c**onsists of 2 stages. First stage is the preparation of naphthyl-isothiocyanate, which was prepared by standard procedure[3]. Liquor ammonia (115 ml) was taken in a round bottom flask (500 ml) and CS_2 (55 ml) was added slowly. Naphthylamine was added slowly by shaking the mixture throughout. The crystalline product formed was filtered, dissolved in water (100 ml) and steam distilled with lead nitrate (200 g) dissolved in water (400 ml) for 3 h. The yellow oily liquid formed was extracted with ether.

In the second stage guanidine hydrochloride (0.1 mol) and NaOH (0.1 mol) were dissolved in CH_3CN (25 ml) to which naphthylisothiocyanate (0.1 mol) was added drop wise with constant stirring for about 2 h. It was diluted with water and precipitated solid was collected, recrystallised from hot water, dried and kept over anhydrous $CaCl_2$. The yield was about 75%, m.p. = 143 °C.

For $C_{12}H_{12}N_4S$

anal. calcd, %:	C, 58.90;	H, 4.82;	N, 23.01;	S, 13.08.
Found, %;	C, 59.01;	H, 4.90;	N, 22.95;	S, 13.11.

The ligand was characterized by elemental analysis IR and NMR spectra. The structure of the ligand is shown in Fig. 1.

Synthesis of metal complexes

A hot ethanolic solution (20 ml) of the required metal salts (0.001 mol) was mixed with a hot ethanolic solution (40 ml) of the ligand (0.002 mol). Immediate colour change with commencement of the separation of solid was observed in most cases. The contents were refluxed in a water bath for ~ 4 h, cooled, filtered, washed with ethanol and dried over anhydrous $CaCl_2$. The thiocyanate complexes were prepared by mixing metal salt (0.001 mol) and ligand (0.002 mol) with ~0.5 g of NH_4CNS and were refluxed for ~ 1h Fig. 2.

Analysis and physicochemical studies

The elemental analysis were performed using a LECO-CHN 600 Elemental Analyser at Central Drug Research Institute, Lucknow, India. Sulphur was estimated gravimetrically after decomposing the complex with nitric acid and a few drops of bromine water[4]. The halogen and thiocyanate were estimated by Volhard's method[4]. The metal content of the complexes were analysed using an atomic absorption spectrometer (GBC Avanta). IR spectra were recorded on a Schimadzu 8000 FT-IR spectrophotometer. The far IR spectra were recorded on a Polytec FIR 30 Fourier spectrometer using CsI disc. The electronic spectra were recorded on a Hitachi 320 UV-vis spectrophotometer.. The room temperature magnetic susceptibility measurements were made using a Guoy magnetic balance and the diamagnetic corrections for various atoms and structural units were computed from Pascal's constants[5,6]. Molar conductance measurements were carried out using 10^{-3} M solutions of the complexes in DMF at room temperature using a Thoshniwal conductivity meter with a dip type conductivity cell. The thermogravimetric analysis was carried out using a thermobalance of type Mettler Toledo STARe system.

Antimicrobial experiments

The antimicrobial activities of the ligand and the metal complexes against *E.coli*, *S.aureus*, *L.leishmanni* and *M.tuberculosis* were screened by resazurin assay method[7,8]. The bacterial culture was grown till their mid-log phase in the appropriate media (LB broth for *E.coli*, Nutrient broth for *S.aureus*, *L.leishmanni* and Middle brook 7H9 broth for *M.tuberculosis* H37 Rv). From this, the culture (50 µl) were added to fresh medium (450 µl) in 2 ml microcentrifuge tubes. The drugs (complexes) were prepared at a stock concentration of 2mg/ml in DMF. The drugs were tested at 10 µg/ml and 100 µg/ml concentrations. Control tubes had the same volumes of medium, bacterial culture and DMF without any drug. All the samples were taken in duplicates. The tubes were then kept for incubation at 37 °C for 7 days. After incubation 0.01% resazurin (20 µl) (Sigma, St. Louis, MO.USA) in water was added to each tube. The control tubes showed change of colour from blue to pink after 24 h at 37 °C. The complexes which prevented the change of colour of the dye were considered to be inhibitory to the microbes.

Results and Discussion

The ligand is expected to act as a potent bidentate due to thiol-thioketo tautomerism. Though various donor sites are present in the ligand it predominantly functions as SN donor ligand in the thiol form.

Formation of the metal complexes can be represented by the following general equations.

$$MX_2 + 2L \rightarrow [ML_2X_2]$$

M = Mn(II) and X= Cl^-, NO_3^-, NCS^-

All the complexes are stable at room temperature and possess good keeping qualities. They are non-hygroscopic solids and are insoluble in common organic solvents such as ethanol, benzene, chloroform and carbon tetrachloride. Formulation of these complexes has been done on the basis of elemental analysis, molar conductance and magnetic susceptibility measurements. The chemical analyses data are given in Table 1.

The molar conductance values in DMF (10^{-3} M solution) for the complexes fall ~ 10-50 Scm^2mol^{-1} showing their non-electrolyte nature[9].

In the present study Mn(II) complexes with NPTU show a magnetic moments around 5.9 BM. These values indicate high spin nature of Mn(II) complexes. Antiferromagnetic interaction can also be ruled out.

The binding mode of the ligand to metal ions was further elucidated by analysis of the IR spectra (Table 2) of the ligand and the metal complexes. The spectrum of the ligand shows a number of strong and weak bands in the region 3400-3100 cm^{-1} and these bands are assigned to N-H stretching vibrations[10,11]. A strong band ~ 1625 cm^{-1} is assigned to ν(C=N) and characteristic bands at 1490, 1300 and 940 cm^{-1} are due to NCS frequencies. The band at 890 cm^{-1} is

attributed to ν(C=S). In the complexes the absorption band due to ν(C=N) of the ligand is shifted to lower frequencies. The ν_3(NCS) band at 940 cm^{-1} in the ligand is considerably shifted to higher frequencies and ν(C=S) band at 890 cm^{-1} in the ligand is observed at lower frequencies in the complexes. These observations show that ligand behaves as bidentate and the metal ion is coordinated through the S and N atoms of the ligand in the thiol form. Moreover an additional band around 450 cm^{-1} is observed in the complexes which is due to metal-nitrogen coordination[12,13].

The occurrence of two strong bands in the nitrate complex of Mn(II) ~ 1520 cm^{-1} and 1430 cm^{-1} are attributed to ν_4 and ν_1 modes of vibrations of nitrate ions. The absence of ν_2 band ~1000 cm^{-1} shows that no ionic nitrate is present. Also the frequency separation ν_4-ν_1 ~ 100-200 cm^{-1} is reasonable to infer that nitrate group is coordinated monodentately[14,15]. The thiocyanate complexes of Mn(II) show a very strong band around 2070 cm^{-1} due to C-N stretching[16]. Bands with medium intensity ~ 830 cm^{-1} and δ (NCS) band near 490 cm^{-1} clearly indicate the N-coordinated nature of the thiocyanate group. Far infrared spectra of the metal complexes showed several absorption bands which were not observed in the ligand spectrum. The bands appearing around 320 cm^{-1} for the chloro complexe of Mn(II) are assignable to ν(M-Cl) stretching vibration[17].

The ground state term for the Mn(II) ion is ^6S and it is not split in presence of any ligand field but transforms into $^6A_{1g}$ state in an octahedral field. This is the only sextuplet state possible. Therefore, all the transitions to higher states are spin forbidden in an octahedral field (Jorgenson, 1962; Lever, 1984). Due to spin orbit coupling many spin forbidden transitions are shown by Mn(II) complexes. Some of the spin forbidden electronic transitions are $^6A_{1g} \rightarrow {}^4T_{1g}$, $^6A_{1g} \rightarrow {}^4T_{2g}$, $^6A_{1g} \rightarrow {}^4E_g$ and $^6A_{1g} \rightarrow {}^4A_{1g}$. These transitions are responsible for the pale pink colour of Mn(II) complexes. The newly synthesized Mn(II) complexes show a very intense band around 420 nm and a very faint shoulder around 500 nm. This intense peak may be attributed to the ligand absorption and the weak shoulder may be due to the overlapping of one spin forbidden d-d transition with the ligand absorption.

Thermal studies

The thermal decomposition behaviour of $[Mn(NPTU)_2Cl_2]$ is obtained from TG and DTG study. The complex shows a single stage decomposition. The TG-DTG curves of the complex are shown in Fig.3. The decomposition begins at 170 °C and is complete at 350 °C with a peak temperature of 290 °C. The mass loss in this stage is 86.20% which agrees with the combined loss of ligand and chlorido groups. The final residue of 12.82% corresponds to oxides of manganese.

Antimicrobial activity

The ligand and the metal complexes were screened for their antimicrobial activity by resazurin assay method. Resazurin is an oxidation-reduction indicator used for the evaluation of cell growth . It is a blue non-fluorescent and non-toxic dye that becomes pink and fluorescent when reduced to resorufin by oxidoreductases with in viable cells[18].

The results obtained are presented in Table 3. The increased activity of the metal chelates than the ligand can be explained on the basis of Overtone's concept and Tweedy's chelation theory[19-21]. The lipid membrane that surrounds the cell favours the passage of only lipid soluble materials. Hence lipophilicity is an important factor which controls the

antimicrobial activity. On chelation the polarity of the metal ion is reduced to a greater extent due to the overlap of the positive charge of the metal ion with the donor groups. Further, it increases the delocalisation of π-electrons over the whole chelate ring and hence enhance the liposolubility of the complexes. This increased liposolubility enhances the penetration of the complexes into the lipid membrane. Some important factors other than chelation which determine the activity are nature of the metal ion, nature of the ligand, coordinating sites, geometry of the complex, concentrations, hydrophilicity, steric and pharmacokinetic effects.

From the result it is clear that ligand shows no activity against the microbes. All the complexes are active against M-tuberculosis in 100 μg concentration Fig. 4. The chlorido and thiocyanato complexes are more active than nitrato complexes and are active against the microbes even in 10 μg/ml. This is because the bonding capacity of nitrate ion towards the central metal ion is greater than that of the chloride ion and the extent of metal ion available is decreased for the display of antibacterial activity.

3D Modelling

The possible 3D structures of Ligand and the complexe **$[Mn(NPTU)_2(NO_3)_2]$** were constructed using Modeling and Analysis software[45] CHEM Bio3D Ultra 11.0.

Conclusion

Ligands and most of the metal complexes were screened for their antibacterial, and antitubercular studies. The results reveals that some metal complexes are active against the microbes even in 10 μg/ml. The possible 3D structures of the ligand and their metal complexes(Fig. 5 & 6) were optimized by molecular mechanic calculations using Modeling and Analysis software.

Acknowledgement

Thanks to Dr R. Ajay Kumar, Department of Molecular Microbiology and Ruby John Anto, Molecular medicine and Cancer Research Division, Rajeev Gandhi Center for Biotechnology, Thiruvananthapuram, for providing facilities for the antimicrobial studies.

Table 1. Analytical data of the complexes

Complexes	Contents (found /calcd), %					Molar conductance Scm^{-2} mol^{-1}	μ_{eff}
	M	C	H	N	S		
$[MnL_2Cl_2]$	8.94/ 8.90	46.17/ 46.22	3.72/ 3.88	17.78/ 17.97	10.32/ 10.28	31	5.98
$[MnL_2(NO_3)_2]$	8.96/ 8.23	42.89/ 43.18	3.69/ 3.59	21.03/ 20.99	9.78/9. 59	35	5.88
$[MnL_2(NCS)_2]$	8.67/ 8.33	46.79/ 46.71	3.68/ 3.60	20.88/ 20.95	19.14/ 19.19	33	5.82

Table 2. IR spectral data of ligand and complexes

Ligand /complex	ν(N-H)	ν(C=N)	ν_1(NCS)	ν_2(NCS)	ν_3(NCS)	ν(C=S)	ν(M-N)	ν(M-Cl)	ν(M-NCS)	ν(NO_3)
L	3360	1638	1492	1325	955	895	-	-	-	
$[MnL_2Cl_2]$	3328	1621	1486	1290	961	864	522	325	-	
$[MnL_2(NO_3)_2]$	3322	1615	1483	1289	966	861	529	-	-	1528 (ν_4) 1432 (ν_1)
$[MnL_2(NCS)_2]$	3332	1619	1485	1285	969	864	530	-	480	

Table 3 Antimicrobial activity of ligand and its complexes (Resazurin assay method)

Ligand/Complex	Conc.µg/ml	Activity against			
		E.coli	*S.aureus*	*L.leishmanni*	*M.tuberculosis*
L	10	-	-	-	-
	100	-	-	-	-
$[MnL_2Cl_2]$	10	+	-	+	-
	100	+	+	+	+
$[MnL_2(NO_3)_2]$	100	-	+	-	+
$[MnL_2(NCS)_2]$	10	-	-	+	-
	100	+	+	+	+

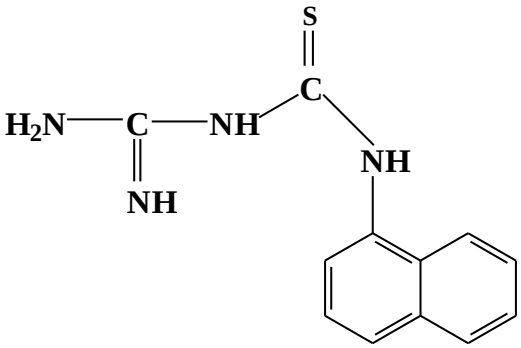

Fig.1

2D Structure of NPTU

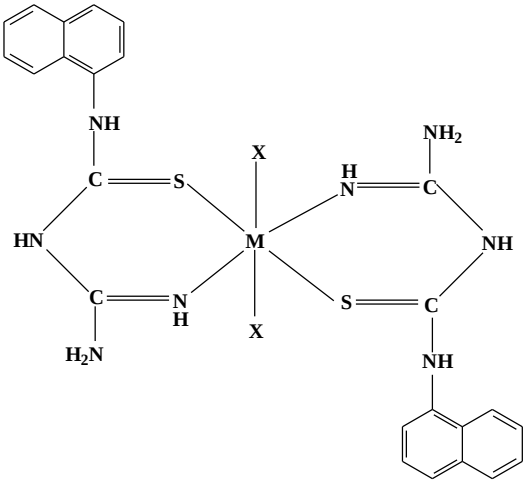

M=Mn(II)

X=Cl- ,NO3-, NCS-

Fig.2

2D Structure of metal complexes

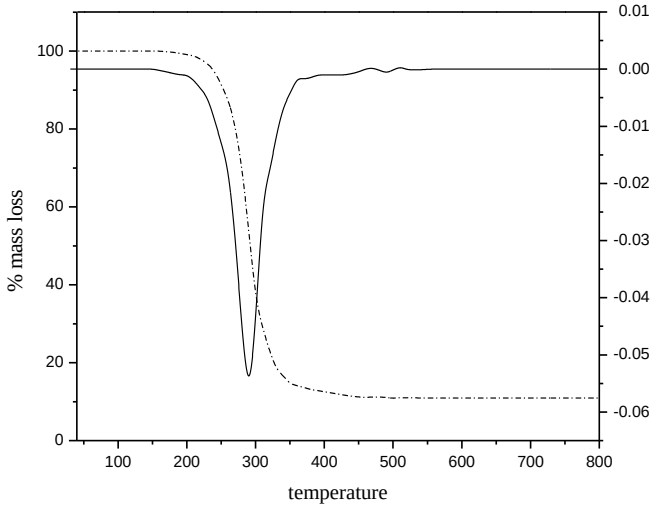

Fig.3

TG and DTG curves of $[MnL_2Cl_2]$

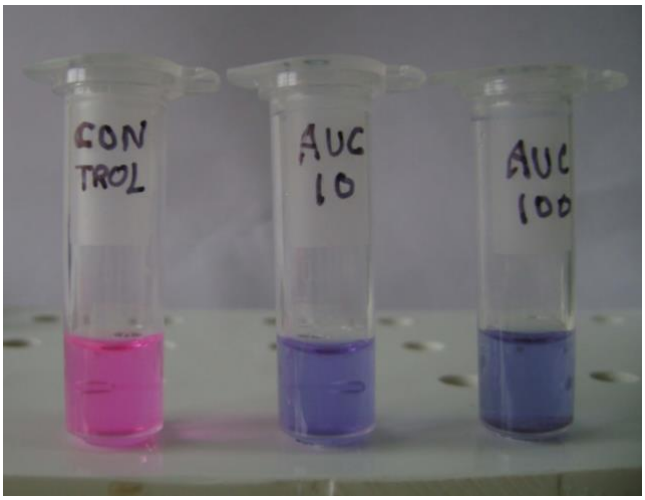

Fig.4

Antibacterial and antitubercular activity of $[MnL_2Cl_2]$

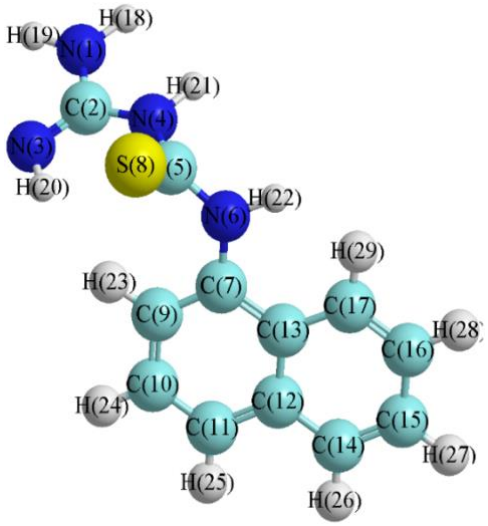

Fig.5

3D Molecular Structure of N-amidino-N^1-naphthylthiourea

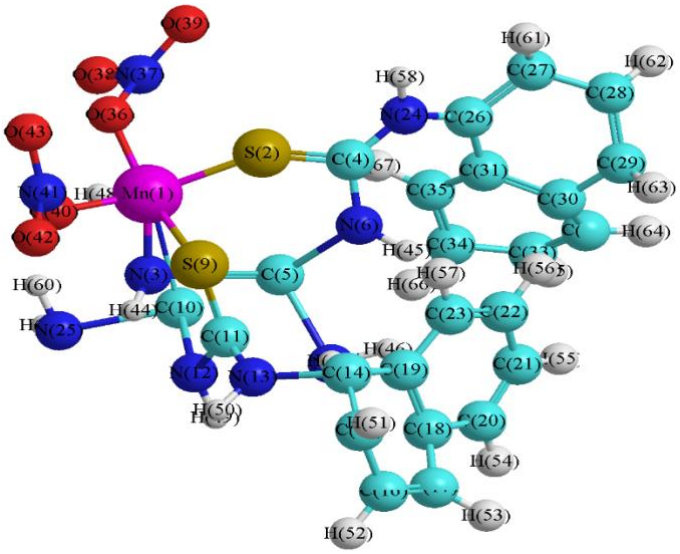

Fig.6

3D Molecular Structure of of $[Mn(NPTU)_2(NO_3)_2]$

References

1. Saha, C. R. and Roy, N. K., *J. Coord. Chem.*, 1983, vol. 12, p. 163.
2. Vilar, R., Mingos, D. M. P., White, A. J. P., et al., *Chem. Commun.*, 1999, p. 229.
3. Finar, I. L., *Organic Chemistry*, Vol I, Addison – Wesley Longman Inc., 1998.
4. Vogel, A. I., *A Text Book of Quantitative Chemical Analysis*, 6th Ed., Pearson Education, 1998.
5. Figgis, B. N., Lewis, J. and Wilkin, R. G. *Modern Coordination Chemistry*, New York, Interscience, 1960.
6. Dutta, R. L. and Syamal, A., *Elements of Magneto Chemistry*, New Delhi: East West Press, 1992, p.8.
7. Martin, A., Camacho, M., Portaels, F., et al., *Antimicrob. Agents Chemother*, 2003, vol. 47, p. 3616.
8. Banfi, E., Scialino, G. and Bragadin, C. M., *J. Antimicrob. Chemotherapy*, 2003, vol. 52, p. 796.
9. Geary, W. J., *Coord. Chem. Rev.*, 1971, vol. 7, p. 81.
10. Upadhyay, R. K., *J. Indian Chem. Soc.*, 1997, vol. 74, p. 535.
11. Sbirna, L. S., Muresan, V., Sbirna, S., et al., *J. Indian Chem., Soc.* 2005, p. 389.
12. Ferrero, J. R., *Low Frequency Vibrations of Inorganic and Coordination compounds*, New York: John Wileys, 1971.
13. Nakamato, K., *Infrared and Raman Spectra of Inorganic and Coordination Compounds*, New York: John Wiley, 1997.
14. Addison, C. C., Logan, N., Wall work, S. C., et al., *Quat. Rev. Chem. Soc.*, 1971, vol. 25, p. 289.
15. Ferraro, J. R., *J. Mol. Spectrosc.*, 1960, vol. 4, p. 99.
16. Bailey, R. A., Michelsen, T. W. and Mills, W. N. *J. Inorg. Nucl. Chem.*, 1971, vol. 33, p. 3206.
17. Kharodawala, M. J. and Rana, A. K. *Synth. React. Inorg. Met. Org. Chem.*, 2003, vol. 33, p. 1483.
18. Perrot, S., Dutetre-Catella, H., Martin, C., et al., Toxicol. Sci., 2003, vol. 72, p. 122.
19. Patel, N. H., Parekh, H. M. and Patel, M. N., *Phar. Chem. J.*, 2007, vol. 41, p. 78.
20. Chohan, Z. H., Shaikh, A. U., Naseer, M. M., et al., *J. Enz. Inhibit. Med. Chem.*, 2006, vol. 21, p. 771.
21. William, H. and Stephen, V., *Theory and Application of Microbiological Assay*, San Diego: Academic Press, 1989.

NIRMALA INDEX AND NIRMALA CHARACTERISTIC POLYNOMIALS OF GRAPHS

Deepa D [1*], Mathew Varkey T K [2]

[1,2] Department of Mathematics, TKM College of Engineering, Kollam, India.
[1] Assistant Professor, Department of Mathematics, VTM NSS College, Thiruvananthapuram.
***corresponding author: deeparajk@yahoo.co.in**

Abstract:

Topological indices are widely used in mathematical chemistry especially in isomer discrimination, chemical documentation, Quantitative Structure-Activity Re- lationships (QSAR), and Quantitative Structure-Property Relationships (QSPR). For a simple undirected graph G with n vertices and m edges, the Nirmala matrix N(G) is de- fined so that its $(i, j)^{th}$ entry is equal to $\sqrt{d_i + d_j}$ if the vertices i and j are adjacent and zero otherwise, where d_i denotes the degree of vertex v_i in G. In this paper we derive the Nirmala characteristic polynomial of different class of graphs.

Keywords: Nirmala Index, Nirmala characteristic polynomial.

MSC: 05C10,05C35,05C38

Introduction

Throughout this paper, we are considering only simple graphs (without loops and parallel edges). For a graph $G = (V, E)$, V denote the vertex set and E denotes the edge set.The degree of the vertex v in G is the number of edges incident on v and is denoted by d_v.Chemical graph theory is focused on finding topological indices, which are real num-bers related to a molecular structure, obtained through molecular graphs. Topological indices have important role in theoretical chemistry for QSPR and QSAR researches [18]

[12] [9][10][11][1].Topology of a molecule represented by the molecular graph, is an essen-tially non numerical mathematical object and various measurable properties of molecules are usually expressed by means of numbers. In order to link molecular topology to any molecular property,introduce numerical characteristics which is a graph invariant and is called topological index. Among all the topological indices the degree based and distance based topological indices such as Randic, Zagreb and Wiener indices have been used more considerably than any other topological indices in chemical and mathematical literature [7]

[16] [13] [17] [15] [14][3]. The first molecular descriptor or topological index is the Wiener index, introduced by H Wiener in 1947 to calculate the boiling points of paraffin [20] [19]. Since then, so many topological indices based on degree, distance, and neighbourhood degree sum have been defined. Estrada introduced the Estrada Index of molecular graphG and this

index has recently found applications in many areas such as quantifying the degree of folding of proteins and other long-chain bio-molecules, characterizing the general topological features of complex networks, measuring bipartivity of graphs etc. [14][8] The theory of graph spectra is a rapidly growing research area in the mathematical community. Spectral graph theory emerged in 1940s and the paper by Huckel is considered as the first paper where graph spectra appear through in an implicit form. The first mathematical paper on graph spectra appeared in 1957 and it was motivated by the membrane vibration problem which was tackled by solutions of partial differential equations. Since then, the topic graph spectra has emerged as a tool to solve many problems in almost all branches of sciences[4] [2][5]. The energy of graph , which is the sum of absolute values of eigenvalues, is one of the most important graph invariant. The plethora of problems addressed by several graph theorists opened another vast area of different matrices associated with a graph and the study of their spectra and energy. Given a graph G, the adjacency matrix

A is $n \times n$ matrix whose $(i,j)^{th}$ entry is 1 if $v_i v_j \in E(G)$ and zero otherwise. Thus A is a real symmetric matrix, its eigenvalues must be real and arranged in non-increasing order $\mu_1 \geq \mu_2 \geq ...\mu_n$ and the largest eigenvalue μ_1 is called the spectral radius of G.

The energy of a graph is introduced by Gutman and is defined as $\varepsilon'(G) = \sum_{i=1}^{n} |\mu_i(G)|$. In this paper, we study the Nirmala index from an algebraic point of view which is a natural phenomenon in mathematical chemistry. The Nirmala matrix $N(G)$ is defined so that its $(i,j)^{th}$ entry is equal to $d_i + d_j$ if the vertices i and j are adjacent and zero otherwise, where d_i denotes the degree of vertex v_i in G.The eigenvalues of $N(G)$ are denoted by $\lambda_1(G) \geq \lambda_2(G)....\lambda_n(G)$ where $\lambda_1(G)$ is called the Nirmala spectral radius of G. Herewe obtain some relationship between the energy of the graph and the Nirmala index, the Nirmala characteristic polynomial of different class of graphs.

Preliminaries

Here we point out some basic definitions and some lemmas used to derive the main results.

Definition 1. *[6] The diameter of a graph G is the maximum distance between any pairof vertices in G and is denoted by diam*(G).

Here we use the following notations for certain graphs and graph invariants.

$\Delta(G)$ and $\delta(G)$ denote the maximum and minimum vertex degrees in G. Let P_n, C_n, K_n, $K_{s,t}$ denote the path , cycle, complete graph with n vertices and complete bipartite graph with s+t vertices respectively.

Definition 2. *The First Zagreb index Z is defined as:*

$$Z = Z(G) = \sum_{i=1}^{n} d_i^2$$

Definition 3. *[15] Nirmala index N of G is defined as:*

$$N = N(G) = \sum_{ij \in E(G)} \sqrt{d_i + d_j}$$

Lemma 1. *[15] Let* $v_1 \geq v_2 \geq \ldots . v_n$ *be Nirmala eigenvalues of the graph G. Then* $\sum_{i=1}^{n} v_i = 0$ *and* $\sum_{i=1}^{n} v_i^2 = 2Z$

attained if and only if graph G is regular.

Lemma 3. *[15] If G is a graph on n vertices, with First Zagreb index Z(G), then Nirmala energy* $\varepsilon(G) \leq \sqrt{2nZ(G)}$.

Lemma 4. *[15] Let G be a graph on n vertices with Nirmala and first Zagreb indices N(G) and Z(G) respectively.*
Then

$$\varepsilon(G) \leq \frac{2N(G)}{n} + \sqrt{2(n-1)[Z(G) - (\frac{2N(G)}{n})^2]}$$

If G is bipartite, then

$$\varepsilon(G) \leq \frac{4N(G)}{n} + \sqrt{2(n-2)[Z(G) - 2(\frac{2N(G)}{n})^2]}$$

Lemma 5. *[6] If M is a non-singular square matrix, then*

$$det \begin{pmatrix} M & N \\ P & Q \end{pmatrix} = det(M)det(Q - PM^{-1}N).$$

3 Main Results

3.1 Relation between Energy of the graph $\varepsilon'(G)$ and Nirmala Index $N(G)$

In this section, we develop some results on the relation between energy of a graph by the adjacency spectrum and the Nirmala index.

Theorem 1. *If G is any graph, then* $\varepsilon'(G).\Delta(G) \geq N(G)$

Proof. Energy of an edge $e = (x, y)$ is

$$\varepsilon(e) = \frac{\varepsilon(x)}{d_x} + \frac{\varepsilon(y)}{d_y} > \frac{d_x}{d_x\Delta(G)} + \frac{d_y}{d_y\Delta(G)} > \frac{d_x + d_y}{\Delta(G)^2} > \frac{\sqrt{d_x + d_y}}{\Delta(G)}$$

Energy of the graph $\varepsilon'(G) = \sum_{e \in E(G)} \varepsilon(e) \geq \sum \frac{\sqrt{d_x + d_y}}{\Delta(G)} = \frac{N(G)}{\Delta(G)}$ □

Now we extend the the result for Complete graph and Complete bipartite graph in theorem 2 and 3.

Theorem 2. *For complete graph* $G = K_n$, $N(G) = \varepsilon'(G)\frac{n\sqrt{n-1}}{2\sqrt{2}}$

Proof.

$$\begin{aligned} N(G) &= \sum \sqrt{d_x + d_y} \\ &= \sum 2(n-1) \\ &= \frac{n(n-1)}{2}\sqrt{2(n-1)} \\ &= 2(n-1)\frac{n\sqrt{(n-1)}}{2\sqrt{2}} \\ &= \varepsilon'(G)\frac{n\sqrt{(n-1)}}{2\sqrt{2}} \end{aligned}$$

□

Theorem 3. *For a complete bipartite graph* $G = K_{n,n}$, $\varepsilon'(G) = \frac{N(G)^2}{n^2}$

Proof.

$$\begin{aligned} N(G) &= \sum \sqrt{d_x + d_y} \\ &= \sum \sqrt{n+n} \\ &= n^2\sqrt{2n} \\ &= n^2\sqrt{\varepsilon'(G)} \end{aligned}$$

Hence $\varepsilon'(G) = \frac{N(G)^2}{n^2}$ □

3.2 Nirmala characteristic polynomial of graphs

Here we derive the Nirmala characteristic polynomial of different class of graphs from Nirmala matrix.Also the Nirmala energy is derived.

Theorem 4. *For every $n \geq 5$, the Nirmala characteristic polynomial of the Path graph P_n satisfy $\phi_N(P_n, \lambda) = \lambda^2 \wedge_{n-2} - 6\lambda \wedge_{n-3} + 9\wedge_{n-4}$, where for every $k \geq 3$, $\wedge_k = \lambda \wedge_{k-1} - 4\wedge_{k-2}$ with $\wedge_1 = \lambda$ and $\wedge_2 = \lambda^2 - 4$. In addition the characteristic polynomial of P_2, P_3, P_4 are $\lambda^2 - 2, \lambda^3 - 6\lambda, \lambda^4 - 10\lambda^2 + 9$ respectively.*

Proof. It is easy to see that the Nirmala characteristic polynomial of P_2, P_3, P_4 are $\lambda^2 - 2, \lambda^3 - 6\lambda, \lambda^4 - 10\lambda^2 + 9$ respectively.Now for $k \geq 3$ consider k x k matrix

$$M_k = \begin{bmatrix} \lambda & -2 & 0 & \dots & \dots & 0 & 0 \\ -2 & \lambda & -2 & & & 0 & 0 \\ & & \cdot & & & \cdot & \\ 0 & 0 & 0 & & & \lambda & -2 \\ 0 & 0 & 0 & & & -2 & \lambda \end{bmatrix}$$

and let $\wedge_k = det(M_k)$.

One can easily check that $\wedge_k = \lambda \wedge_{k-1} - 4\wedge_{k-2}$ Now consider the path graph P_n

$$\phi_N(P_n, \lambda) = det(\lambda I - N(P_n))$$

$$= det \begin{bmatrix} \lambda & -\sqrt{3} & \dots & \dots & 0 & 0 \\ -\sqrt{3} & & & & & \\ & & \ddots & & & \\ 0 & 0 & 0 & & -\sqrt{3} & \lambda \end{bmatrix}$$

$$= \lambda det \begin{bmatrix} & M_{n-2} & \\ & & \\ & & -\sqrt{3} \end{bmatrix}$$

$$+ 3det \begin{bmatrix} 0 & \dots & -\lambda & \lambda \\ -\sqrt{3} & -2 & \dots & \dots & 0 & 0 \\ 0 & & & & & 0 \\ & & & & & \\ 0 & 0 & 0 & & -\sqrt{3} & \lambda \end{bmatrix}$$

$$= \lambda(\lambda \wedge_{n-2} - 3\wedge_{n-3}) - 3(\lambda \wedge_{n-3} - 3\wedge_{n-4})$$

$$= \lambda^2 \wedge_{n-2} - 6\lambda \wedge_{n-3} + 9\wedge_{n-4}$$

□

Theorem 5. *For every $n \geq 3$, the Nirmala characteristic polynomial of the Cycle C_n satisfy $\phi_N(C_N, \lambda) = \lambda \wedge_{n-1} -8 \wedge_{n-2} -2^{n+1}$, where for every $k \geq 3$, $\wedge_k = \lambda \wedge_{k-1} -4\wedge_{k-2}$ with $\wedge_1 = \lambda$ and $\wedge_2 = \lambda^2 - 4$*

Proof. Similar to the proof of the theorem 4, for every $k \geq 3$, we consider

$$M_k = \begin{bmatrix} \lambda & -2 & 0 & \dots & \dots & 0 & 0 \\ -2 & \lambda & -2 & & & 0 & 0 \\ \vdots & & \ddots & & & \ddots & \vdots \\ 0 & 0 & 0 & & & \lambda & -2 \\ 0 & 0 & 0 & & & -2 & \lambda \end{bmatrix}$$

and we obtain the required result. □

Theorem 6. *For $n \geq 2$, (i) The Nirmla characteristic polynomial of star graph $S_n = K_{1,n-1}$ is*

$$\phi_N(S_n, \lambda) = \lambda^{n-2}(\lambda^2 - n(n-1))$$

(ii) The Nirmala Energy of S_n is

$$\varepsilon(S_n) = 2\sqrt{n(n-1)}$$

Proof. The Nirmala matrix of $S_n = K_{1,n-1}$ is $N(S_n) = \begin{bmatrix} 0_{1*1} & J_{1*n-1} \\ J_{n-1*1} & 0_{n-1*n-1} \end{bmatrix}$

We have

$$det(\lambda I - N(S_n)) = det \begin{bmatrix} \lambda & -\sqrt{n}J_{1*n-1} \\ -\sqrt{n}J_{n-1*1} & \lambda I_{n-1} \end{bmatrix}$$

$$= \lambda det(\lambda I_{n-1} - \sqrt{n}J_{n-1*1}\tfrac{1}{\lambda}\sqrt{n}J_{1*n-1}$$

$$= \lambda det(\lambda I_{n-1} - \tfrac{n}{\lambda}J_{n-1}$$

$$= \lambda^{1-(n-1)} det(\lambda^2 I - nJ_{n-1})$$

The eigenvalues of J_{n-1} are $\begin{matrix} n-1 & 0 \\ 1 & n-2 \end{matrix}$

Therefore, eigenvalues of nJ_{n-1} are $\begin{matrix} n(n-1) & 0 \\ 1 & n-2 \end{matrix}$

Therefore, $\phi_N(S_n, \lambda) = \lambda^{n-2}(\lambda^2 - n(n-1))$ and $\varepsilon(S_n) = 2\sqrt{n(n-1)}$ □

Theorem 7. *For $n \geq 2$, (i) The Nirmala characteristic polynomial of complete graph K_n is*

$$\phi(K_n, \lambda) = (\lambda - \sqrt{2}(n-1)\sqrt{n-1})(\lambda + \sqrt{2(n-1)})^{n-1}$$

(ii) The Nirmala Energy of K_n is

$$\varepsilon(K_n) = 2\sqrt{2}(n-1)\sqrt{n-1} = [2(n-1)]^{\frac{3}{2}}$$

Proof. The Nirmala matrix of K_n is $N(K_n) = \sqrt{2(n-1)}(J - I)$

Therefore

$$\phi_N(K_n, \lambda) = det(\lambda I - \sqrt{2(n-1)}J + \sqrt{2(n-1)}I)$$
$$= det(\lambda + \sqrt{2(n-1)}I + \sqrt{2(n-1)}J)$$

Eigenvalue of J_n are

$$\begin{vmatrix} n & 0 \\ 1 & n-1 \end{vmatrix}$$

the eigenvalue of $\sqrt{2(n-1)}\,J_n$ are

$$\begin{vmatrix} n\sqrt{2(n-1)} & 0 \\ 1 & n-1 \end{vmatrix}$$

Therefore,

$$\phi_N(K_N, \lambda) = (\lambda - n\sqrt{2(n-1)} + \sqrt{2(n-1)})(\lambda + \sqrt{2(n-1)})^{n-1}$$

$$= (\lambda - \sqrt{2(n-1)}(n-1)(\lambda + \sqrt{2(n-1)})^{n-1}$$

$$= (\lambda - \sqrt{2}(n-1)^{\frac{3}{2}}(\lambda + \sqrt{2(n-1)})^{n-1}$$

and $\varepsilon(K_n) = [2(n-1)]^{\frac{3}{2}}$ □

Theorem 8. *For natural number $m, n \neq 1$, (i) the Nirmala characteristic polynomial of complete bipartite graph $K_{m,n}$ is*

$$\phi_N(K_{m,n}, \lambda) = \lambda^{m+n-2}(\lambda^2 - mn(m+n))$$

(ii) The Nirmala Energy of $K_{m,n}$ is $\varepsilon(K_{m,n}) = 2\sqrt{mn(m+n)}$

Proof. The Nirmala matrix of $K_{m,n}$ is $\sqrt{m+n}\begin{bmatrix} O_{m*m} & J_{m*m} \\ J_{n*m} & O_{n*n} \end{bmatrix}$

Using Lemma 5, we have

$$\det(\lambda I - N(K_{m,n})) = \det \begin{bmatrix} \lambda I_m & -\sqrt{m+n}J_{m\times n} \\ -\sqrt{m+n}J_{n\times m} & \lambda I_n \end{bmatrix}$$

$$= det(\lambda I_m) det(\lambda I_n - \sqrt{m+n}J_{n\times m}\tfrac{1}{\lambda} I_m \sqrt{m+n}J_{m\times n})$$

$$= \lambda^m det(\lambda I_n - \tfrac{(m+n)}{\lambda} mJ_n)$$

$$= \lambda^{m-n} det(\lambda^2 I_n - m(m+n)J_n)$$

The Eigenvalues of J_n are $\begin{matrix} n & 0 \\ 1 & n-1 \end{matrix}$ and therefore

eigenvalues of $m(m+n)J_n$ are $\begin{matrix} mn(m+n) & 0 \\ 1 & n-1 \end{matrix}$ Hence

$\phi_N(K_{m,n}, \lambda) = \lambda^{m+n-2}(\lambda^2 - mn(m+n))$ and $\varepsilon(K_{m,n}) = 2\sqrt{mn(m+n)}$ □

Conclusion

Through this paper, we found some relations connecting the energy of graphs with its adjacency spectra and the Nirmala index of that graph. The Nirmala energy associated with Nirmala matrix is derived for special class of graphs such as Path graph, Cycles, Star graph, Complete graph and Complete Bipartite graph. Nowadays, an organic investigation of chemical mixtures is high priced and demands modern apparatus to investigate these mixtures in laboratory. In this present scenario by the advantage of graph theory, espe- cially by the developments in topological indices, by studying the obvious atomic frames one can study the physicochemical properties such as heat of formation, enthalpy, infrared spectrum etc. , without using any laboratory equipment.

References

Alexandru T Balaban. *Chemical applications of graph theory*. Academic Press, 1976.

Ravindra B Bapat. *Graphs and matrices*, volume 27. Springer, 2010.

B BASAVANAGOUD and PRAVEEN JAKKANNAVAR. Neighbourhood degree matrix of a graph. *Electronic Journal of Mathematical Analysis and Applications*, 9(2):206–221, 2021.

John Adrian Bondy, Uppaluri Siva Ramachandra Murty, et al. *Graph theory with applications*, volume 290. Macmillan London, 1976.

DM Cvetcovic, M Doob, and H Sachs. Spectra of graphs. *Acad. Press, New York, San-Francisco, London*, 1980.

Dragoš M Cvetković, Michael Doob, and Horst Sachs. Spectra of graphs: theory and applications. *(No Title)*, 1980.

Mehdi Eliasi, Ali Iranmanesh, and Ivan Gutman. Multiplicative versions of first zagreb index. *Match-Communications in Mathematical and Computer Chemistry*, 68(1):217, 2012.

Ernesto Estrada, Juan A Rodríguez-Velázquez, and Milan Randić. Atomic branching in molecules. *International Journal of Quantum Chemistry*, 106(4):823–832, 2006.

A Graovac, I Gutman, and D Vukicevic. Mathematical methods and modelling for students of chemistry and biology. *Hum, Zagreb*, 2009.

I Gutman. Introduction to chemical graph theory. *Faculty of Science, Kragujevac*, 2003.

I Gutman. Mathematical methods in chemistry. *Prijepolje Museum, Prijepolje*, 2006.

I Gutman and B Furtula. Novel molecular structure descriptors–theory and applica-tions i, univ. *Kragujevac, Kragujevac*, 17, 2010.

Ivan Gutman. Geometric approach to degree-based topological indices: Sombor in- dices. *MATCH Commun. Math. Comput. Chem*, 86(1):11–16, 2021.

Ivan Gutman and Ernesto Estrada. Topological indices based on the line graph of the molecular graph. *Journal of chemical information and computer sciences*, 36(3):541– 543, 1996.

Ivan Gutman and Veerabhadrappa R Kulli. Nirmala energy. *Open Journal of Discrete Applied Mathematics*, 4(2):11–16, 2021.

Ivan Gutman, Emina Milovanović, and Igor Milovanović. Beyond the zagreb indices.

AKCE International Journal of Graphs and Combinatorics, 2018.

Izudin Redžepović. Chemical applicability of sombor indices. *Journal of the Serbian Chemical Society*, 2021.

Roberto Todeschini and Viviana Consonni. *Handbook of molecular descriptors*. John Wiley & Sons, 2008.

Harry Wiener. Structural determination of paraffin boiling points. *Journal of the American chemical society*, 69(1):17–20, 1947.

Harry Wiener. Relation of the physical properties of the isomeric alkanes to molecular structure. surface tension, specific dispersion, and critical solution temperature in aniline. *The Journal of Physical Chemistry*, 52(6):1082–1089, 1948.

EIGENVALUE AND SINGULAR VALUE DECOMPOSITION AND ITS APPLICATIONS

Aswathy C P

Department Of Mathematics, Al-Ameen College Edathala
Cpaswathy20@Gmail.Com
9847821216

Abstract

The paper entitled 'EIGENVALUE AND SINGULAR VALUE DECOMPOSITION AND ITS APPLICATIONS' is a review work of the paper 'A Singularly Valuable Decomposition: The SVD of a Matrix' by Dan Kalman, The American University, Washington, DC 20016. Singular value decompositions (SVD) have interesting and attractive algebraic properties and conveys important geometrical and theoretical insights about their linear transformation. The close connection between the singular value decomposition and the well-known theory of diagonalisation for symmetric matrices makes the topic immediately accessible. In this project, we have discussed Eigen Value Decomposition (EVD) and Singular Value Decomposition (SVD) and their applications. EVD is applicable for symmetric matrices whereas SVD is applicable for a real $m \times n$ matrix. If A is a symmetric real n×n matrix, there is an orthogonal matrix V and a diagonal matrix D such that $A = VDV^T$. Here the columns of V are eigenvectors for A and form an orthogonal basis for $\mathbb{R}^n$; the diagonal entries of D are the eigenvalues of A. For the SVD, an arbitrary real m×n matrix A. There are orthogonal matrices U and V and a diagonal matrix, denoted Σ, such that $A = U\Sigma V^T$. In this case, U is m×m and V is n×n, so that Σ is rectangular with the same dimensions as A. The diagonal entries of Σ, that is the $\Sigma_{ii} = \sigma_i$, can be arranged to be nonnegative and in order of decreasing magnitude. The positive ones are called the singular values of A. The columns of U and V are called the left and right singular vectors for A.

The analogy between the EVD for a symmetric matrix and SVD for an arbitrary matrix can be extended a little by thinking of matrices as linear transformations. For a symmetric matrix A , the transformation takes $\mathbb{R}^n$ to itself, and the columns of V define an especially nice basis.

We have explained the geometric interpretation of SVD and EVD. EVD can be used for computing higher powers of symmetric matrices and hence it can be used to solve difference equations. There are several applications for EVD such as Fibonacci numbers and Markov matrices. SVD also plays a major role in machine learning, Artificial intelligence etc. Generally, the SVD finds application in problems involving large matrices, with dimensions that can reach into the thousands. It is the existence of efficient and accurate computer algorithms for its computation that makes the SVD so useful in these applications. There is beautiful mathematics

involved in the derivation of the algorithms, and the subject is worth looking into. The SVD is an important tool in several different applications. Here we will present a detailed discussion of linear least squares. In general, SVD has wide range of applications. It also includes data compression and image compression, principal component analysis etc.

Introduction

In linear algebra, the singular value decomposition (SVD) is a factorization of a real or complex matrix. It generalizes the eigen decomposition of a square normal matrix with an orthonormal eigen basis to any m×n matrix . It is related to the polar decomposition. The singular value decomposition was originally developed by differential geometers, who wished to determine whether a real bilinear form could be made equal to another by independent orthogonal transformations of the two spaces acts on. Singular Value Decomposition (SVD) has various applications in machine learning, data analysis, image compression etc.

Eigenvalue Decomposition (Evd)

If A is a symmetric real n×n matrix, there is an orthogonal matrix V and a diagonal matrix D such that $A = VDV^T$. Here the columns of V are eigenvectors for A and form an orthogonal basis for $\mathbb{R}^n$; the diagonal entries of D are the eigenvalues of A. To emphasize the connection with the SVD, we will refer to VDV^T as the eigenvalue decomposition or EVD for A.

Singular Value Decomposition (Svd)

For the SVD, an arbitrary real m×n matrix A. There are orthogonal matrices U and V and a diagonal matrix, denoted Σ, such that $A = U\Sigma V^T$. In this case, U is m×m and V is n×n, so that Σ is rectangular with the same dimensions as A. The diagonal entries of Σ, that is the $\Sigma_{ii} = \sigma_i$, can be arranged to be nonnegative and in order of decreasing magnitude. The positive ones are called the singular values of A. The columns of U and V are called the left and right singular vectors for A.

How do we choose the bases $\{v_1, v_2, \ldots\ldots, v_n\}$ and $\{u_1, u_2, \ldots\ldots, u_m\}$ for the domain and range?

Consider $Av_i = \sigma_i u_i$ which is easily arranged. Select an orthonormal basis $\{v_1, v_2, \ldots\ldots, v_n\}$ for $\mathbb{R}^n$ so that the first k elements span the row space of A and the remaining n-k elements span the null space of A, where k is the rank of A. For 1 ≤ i ≤ k, define u_i to be a unit vector parallel to v_i , and extend this to a basis for $\mathbb{R}^m$. Relative to these bases, A will have a diagonal representation. But in general, although the v's are orthogonal, there is no reason to expect the $u's$ to be. The possibility of choosing the v- basis so that its orthogonality is preserved under A is the key point.

We show that the EVD of the n×n symmetric matrix A^TA provides just such a basis, namely, the eigenvectors of A^TA. Let $A^TA = DV^T$, with the diagonal entries λ_i of D arranged in non increasing order, and let the columns of V (which are eigenvectors of A^TA) be the orthonormal basis $\{v_1, v_2, \ldots\ldots, v_n\}$. Then

$$Av_i \,.\, Av_j = \left(A_{v_i}\right)^T \left(Av_j\right) = v_i^T A^T A v_j = v_i^T (\lambda_j v_j) = \lambda_j v_i v_j$$

So, the image set $\boldsymbol{\{Av_1, Av_2, \ldots\ldots, Av_n\}}$ is orthogonal, and the nonzero vectors in this set form a basis for the range of A. Thus, the eigenvectors of $A^T A$ and their images under A provide orthogonal bases allowing A to be expressed in a diagonal form.

To complete the construction, we normalize the vectors Av_i. The eigenvalues of $A^T A$ again appear in this step. Taking $i = j$ in the calculation above gives $|Av_i|^2 = \lambda_i$, which means $\lambda_i \geq 0$. Since these eigenvalues were assumed to be arranged in the non-increasing order, we conclude that $\lambda_1 \geq \lambda_2 \geq \cdots\cdots\cdots \geq \lambda_k \geq 0$ and since the rank of A equals k, $\lambda_i = 0$ for $i > k$. The orthonormal basis for the range is therefore defined by

$$u_i = \frac{Av_i}{\|Av_i\|} = \frac{1}{\sqrt{\lambda_i}} Av_i \,; 1 \leq i \leq k \,.$$

If $k < m$, we extend this to an orthonormal basis for $\mathbb{R}^m$. This completes the construction of the desired orthonormal bases for $\mathbb{R}^n$ and $\mathbb{R}^m$. Setting $\sigma_i = \sqrt{\lambda_i}$, we have $Av_i = \sigma_i u_i$ for all $i \leq k$. Assembling the v_i as the columns of matrix V and the u_i to the form U, this shows that $AV = U\sum$, where $\sum$ has the same dimension as A, has the entries σ_i along the main diagonal, and has all other entries equal to zero. Hence, $A = U\sum V^T$, which is the singular value decomposition of A.

In summary, an $m \times n$ real matrix A can be expressed as the product $U\sum V^T$, where V and U are orthogonal matrices and $\sum$ is a diagonal matrix. The matrix V is obtained from the diagonal factorization $A^T A = V^T$, in which the diagonal entries of D appear in non-increasing order; the columns of U come from normalizing the nonvanishing images under A of the columns of V and extending (if necessary) to an orthonormal basis for $\mathbb{R}^m$; the nonzero entries of $\sum$ are the respective square roots of corresponding diagonal entries of D.

The preceding construction demonstrates that the SVD exists, and gives some idea of what it tells about a matrix. The SVD encapsulates the most appropriate bases for the domain and range of the linear transformation defined by the matrix A. There is a relationship between these bases and the four fundamental subspaces associated with : the range and nullspace, and their orthogonal complements. It is the full picture provided by the SVD and these subspaces.

A Geometric Interpretation Of SVD

How A deforms space is to consider its action on the unit sphere in $\mathbb{R}^n$. An arbitrary element x of this unit sphere can be represented by $x = x_1 v_1 + x_2 v_2 + \cdots \ldots + x_n v_n$ with $\sum_{i=1}^{k} x_i^2 = 1$. The image is $Ax = \sigma_1 x_1 u_1 + \cdots \ldots . + \sigma_k x_k u_k$.

Letting $y_i = \sigma_i x_i$, we see the image of the unit sphere consists of the vectors

$y_1 u_1 + y_2 u_2 + \cdots \ldots + y_k u_k$, where $\frac{y_1^2}{\sigma_1^2} + \frac{y_2^2}{\sigma_2^2} + \cdots \ldots + \frac{y_k^2}{\sigma_k^2} = \sum_{i=1}^{k} x_i^2 \leq 1$.

If A has full column rank, so that $k = n$, the inequality is actually a strict equality. Otherwise, some of the x_i are missing on the right, and the sum can be anything from 0 to 1. This shows that A maps the unit sphere of $\mathbb{R}^n$ to a k-dimensional ellipsoid with semi-axes in the directions u_i and with the magnitudes σ_i. If $k = n$ the image is just the surface of the ellipsoid, otherwise it is the solid ellipsoid.

In summary, we can visualize the effect A as follows: it first collapses n-k dimensions of the domain, then distorts the remaining dimensions, stretching and squeezing the unit k-sphere into an ellipsoid, and finally embeds the ellipsoid in $\mathbb{R}^m$. This is illustrated for

$m = n = 3$ and $k = 2$.

As an immediate consequence, we see that $||A||$ the operator norm of A, defined as the maximum value of $|Av|$ for v on the unit sphere, is simply σ_1 , the largest singular value of A. Put another way, we have the inequality $|Ax| \leq \sigma_1|x|$, $\forall x \epsilon \mathbb{R}^n$, with the equality only when x is a multiple of v_1.

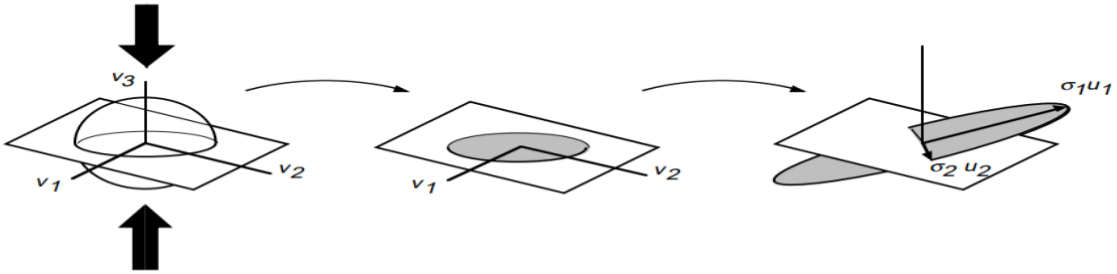

Applications Of Evd

Fibonacci Numbers

Fibonacci numbers 0,1,1,2,3,5,8,13, ...

You see the pattern: Every Fibonacci number is the sum of the two previous $F's$:

Fibonacci equation $F_{k+2} = F_{k+1} + F_k$.

That is the difference equation. It turns up in a most fantastic variety of applications, and deserves a book of its own. Leaves grow in a spiral pattern, and on the apple or oak you find five growths for every two turns around the stem. The pear tree has eight for every three turns, and the willow is 13:5. The champion seems to be a sunflower whose seeds chose an almost unbelievable ratio of $^{F_{12}}/_{F_{13}} = {}^{144}/_{233}$.

How could we find the 1000th Fibonacci number, without starting at F_o =0 and $F_1 = 1$ working all the way out to F_{1000}?

The goal is to solve the difference equation $F_{k+2} = F_{k+1} + F_k$. This can be reduced to a one-step equation $\boldsymbol{u_{k+1}} = \boldsymbol{Au_k}$. Every step multiplies $u_k = (F_{k+1}, F_k)$ by a matrix A:

$F_{k+2} = F_{k+1} + F_k$.

$F_{k+1} = F_{k+1}$

becomes $u_{k+1} = \begin{bmatrix} 1 & 1 \\ 1 & 0 \end{bmatrix} \begin{bmatrix} F_{k+1} \\ F_k \end{bmatrix} = Au_k$.

The one-step system $u_{k+1} = Au_k$ is easy to solve, It starts from u_0. After one step it produces $u_1 = Au_0$ Then u_2 is Au_1, which is A^2u_0. Every step brings a multiplication by A, and after k steps there are k multiplications:

The solution to a difference equation $\boldsymbol{u_{k+1} = Au_k}$ is $\boldsymbol{u_{k+1} = A^k u_0}$.

The real problem is to find some quick way to compute the powers A^k, and thereby find the 1000th Fibonacci number. The key lies in the eigenvalues and eigenvectors:

If A can be diagonalized, $A = S\Lambda S^{-1}$, then A^k, comes from Λ^k,:

$u_k = A^k u_0 = (S\Lambda S^{-1})(S\Lambda S^{-1}) \ldots (S\Lambda S^{-1})u_0 = S\Lambda^k S^{-1}u_0$.

The columns of S are the eigenvectors of A. Writing $S^{-1}u_0 = c$, the solution becomes

$$u_k = S\Lambda^k c = \begin{bmatrix} x_1 & \cdots & x_n \end{bmatrix} \begin{bmatrix} \lambda_1^k & & \\ & \ddots & \\ & & \lambda_n^k \end{bmatrix} \begin{bmatrix} c_1 \\ \vdots \\ c_n \end{bmatrix} = c_1\lambda_1^k x_1 + \cdots + c_n\lambda_n^k x_n$$

After k steps, u_k is a combination of the n "pure solutions" $\lambda^k x$. These formulas give two different approaches to the same solution $u_k = S\Lambda^k S^{-1}u_0$. The first formula recognized that A^k is identical with $\Lambda^k S^{-1}$, and we could stop there. The second approach brings out the analogy with a differential equation: **The pure exponential solutions $\boldsymbol{e^{\lambda it}x_i}$ are now the pure powers $\boldsymbol{\lambda_i^k x_i}$.**

In any specific example like Fibonacci's, the first step is to find the eigenvalues:

$A - \lambda I = \begin{bmatrix} 1-\lambda & 1 \\ 1 & -\lambda \end{bmatrix}$ has $\det(A - \lambda I) = \lambda^2 - \lambda - 1$

Two eigenvalues $\lambda_1 = \frac{1+\sqrt{5}}{2}$ *and* $\lambda_2 = \frac{1-\sqrt{5}}{2}$

The second row of $A - \lambda I$ is $(1, -\lambda)$. To get $(A - \lambda I)x = 0$, the eigenvector is $x = (\lambda, 1)$.The first Fibonacci numbers $F_0 = 0$ and $F_1 = 1$ go into u_0 and $S^{-1}u_0 = c$.

$S^{-1}u_0 = \begin{bmatrix} \lambda_1 & \lambda_2 \\ 1 & 1 \end{bmatrix}^{-1} \begin{bmatrix} 1 \\ 0 \end{bmatrix}$ gives $c = \begin{bmatrix} \frac{1}{(\lambda_1 - \lambda_2)} \\ \frac{-1}{(\lambda_1 - \lambda_2)} \end{bmatrix} = \frac{1}{\sqrt{5}} \begin{bmatrix} 1 \\ -1 \end{bmatrix}$.

Those are the constants in $u_k = c_1\lambda_1^k x_1 + c_2\lambda_2^k x_2$. Both eigenvectors x_1 and x_2 have second component 1. That leaves $F_k = c_1\lambda_1^k + c_2\lambda_2^k$ in the second component of u_k :

Fibonacci numbers $F_k = \frac{1}{\sqrt{5}}[(\frac{1+\sqrt{5}}{2})^k - (\frac{1-\sqrt{5}}{2})^k]$

This is the answer we wanted. $F_{1000} =$ = nearest integer to $\frac{1}{\sqrt{5}}(\frac{1+\sqrt{5}}{2})^{1000}$

Applications Of SVD

Principal Component Analysis

Principal Component Analysis (PCA) is one of the central uses of the SVD, providing a data-driven, hierarchical coordinate system to represent high dimensional correlated data. It is a dimensionality reduction method that is often used to reduce the dimensionality of large data sets, by transforming a large set of variables into a smaller one that still contains most of the information in the large set. Reducing the number of variables of a data set naturally comes at the expense of accuracy but the trick in dimensionality reduction is to trade a little accuracy for simplicity, because smaller data sets are easier to explore and visualize and make analysing data much easier and faster for machine learning algorithms without too much variables to process.

Linear Least Squares

The general context of a linear least squares problem is this: we have a set of vectors which we wish to combine linearly to provide the best possible approximation to a given vector. If the set of vectors is $\{a_1, a_2, \cdots, a_n\}$ and the given vector is b, we seek coefficients $x_1, x_2, \cdots, x_n$ which produce a minimal error

$$\left| b - \sum_{i=1}^{n} x_i a_i \right|$$

The problem can arise naturally in any vector space, with elements which are sequences, functions, solutions to differential equations, and so on. As long as we are only interested in linear combinations of a finite set $\{a_1, a_2, \cdots, a_n\}$, it is possible to transform the problem into one involving finite columns of numbers. In that case, define a matrix A with columns given by the a_i and a vector x whose entries are the unknown coefficients x_i. Our problem is then to choose x minimizing $|b - Ax|$. As in earlier discussions, we will denote the dimensions of A by m and n, meaning in this context that the a_i are vectors of length m. There is a geometric interpretation to the general least squares problem. We are seeking an element of the subspace S spanned by the $a_i$which is closest to b. The solution is the projection of b on S and is characterized by the condition that the error vector (that is, the vector difference between b and its projection) should be orthogonal to S. Orthogonality to S is equivalent to orthogonality to each of the a_i. Thus, the optimal solution vector x must satisfy $a_i \cdot (Ax - b) = 0$ for all i. Equivalently, in matrix form, $A^T (Ax - b) = 0$. Rewrite the equation as $A^T Ax = A^T b$, a set of equations for the x_i generally referred to as the *normal equations* for the linear least squares problem. Observe that the independence of the columns of A implies the invertibility of $A^T A$. Therefore, we have $x = (A^T A)^{-1} A^T b$.

References

The SVD of a Matrix' by Dan Kalman, The American University, Washington, DC 20016

David C. Lay, *Linear Algebra and its Applications*, Addison–Wesley, Reading, MA, 1994.

Stephen J. Leon, *Linear Algebra with Applications*, 4th edition, Macmillan, New York, 1994.

Cliff Long, Visualization of matrix singular value decomposition, *Mathematics Magazine*, vol 56, no 3, pp161-167, May 1983.

I. J. Good, Some applications of the singular decomposition of a matrix, *Techno metrics*, vol 11, no 4, pp 823-831, Nov 1969.

SUM OF POWER n DIVISOR CORDIAL LABELING FOR SUBDIVISION OF PATH AND STAR RELATED GRAPHS

***†P. Preetha Lal and ‡M. Jaslin Melbha**

†Research Scholar, Department of Mathematics, Women'sChristian College, Nagercoil, Tamil Nadu, India

‡Assistant Professor, Department of Mathematics, Women'sChristian College, Nagercoil, Tamil Nadu, India
Affiliated to Manonmaniam Sundaranar University, Abishekapatti,Tirunelveli - 627 012

Abstract

A sum of Power n divisor cordial labeling of a graph G with vertex set V is a bijection $f: V \to \{1,2,3,\dots,|V(G)|\}$ such that an edge uv is assigned the label 1 if 2 divides $(f(u)+f(v))^n$ and 0 otherwise. The number of edges labeled with 0 and the number of edges labeled with 1 differ atmost 1. A graph with a sum of power n divisor cordial labeling is called a sum of power n divisor cordial graph. We establish in this paper that subdivision that subdivision of some path and star related graphs are sum of power n divisor cordial graphs.

Keywords: Sum of power n, subdivision, path, star

Introduction:

Let $G = (V, E)$ be a (p, q) graph with $p = |V(G)|$ vertices and $q = |E(G)|$ edges, where $V(G)$ and $E(G)$ denote the vertex set and edge set of the graph. In this paper, we consider the graphs which are simple, finite and undirected. For graph theoretic terminology and notations we refer to Harary [2]. The concept of graph labeling was introduced by Rosa [5] in 1967. A detailed survey of graph labeling is available in Gallian [1]. The concept of sum divisor cordial labeling has been introduced by Lourduswamy et al [4]. Jaslin Melbha and Preetha lal introduced the concept of sum square divisor cordial labeling [3]. In this paper we investigate the subdivision of some path and star related graphs are sum of power n divisor cordial graphs. We will provide brief summary of definitions and other information which are necessary for the present investigation.

Preliminaries

Definition 1.1. $Sp(P_m, K_{1,n})$ is a graph in which the root of the star $K_{1,n}$ is attached at one end of the path P_m.

Definition 1.2. $P_n \otimes S_m$ is a graph obtained from a path P_n by attaching root of a star S_m at every pendent vertex of P_n.

Definition 1.3. A subdivision graph $S(G)$ of a graph G is a graph that can be obtained from G by subdividing each edge of G exactly once.

Definition 1.4. A sum of Power n divisor cordial labeling of a graph G with vertex set V is a bijection $f: V \to \{1,2,3,\dots,|V(G)|\}$ such that an edge uv is assigned the label 1 if 2 divides $(f(u)+f(v))^n$ and 0 otherwise. The number of edges labeled with 0 and the number of edges labeled with 1 differ atmost 1. A graph with a sum of power n divisor cordial labeling is called a sum of power n divisor cordial graph.

Main Results

Theorem 2.1. The subdivision graph $S(P_n)$ of the graph P_n is sum of power n cordial graph.

Proof: Let P_n be a path with consecutive vertices $\alpha_1, \alpha_2, \dots, \alpha_n$. Let $\{a_1, a_2, \dots, a_{n-1}\}$ be the new vertices which subdivide the edges $\alpha_i\alpha_{i+1}$. Define a function $f: V(G) \to \{1, 2, \dots, |V(G)|\}$ by $f(\alpha_i) = i\,; 1 \le i \le n$, $f(a_i) = \alpha_n + i\,; 1 \le i \le n-1$. Then the induced edge labels are **Case (i)** For an odd number of n, $f^*(\alpha_i a_i) = 0\,; 1 \le i \le n-1$, $f^*(a_i\alpha_{i+1}) = 1; 1 \le i \le n-1$.

Case (ii) For an even number of n, $f^*(\alpha_i a_i) = 1\,; 1 \le i \le n-1$, $f^*(a_i\alpha_{i+1}) = 0\,;$ $1 \le i \le n-1$.

From both the cases, we observe that $e_f(0) = n-1$ and $e_f(1) = n-1$. Thus $|e_f(0) - e_f(1)| \le 1$. Hence the subdivision of the path is sum of power n divisor cordial graph.

Example 2.2. $S(P_6)$ is sum of power n divisor cordial graph as shown in the figure.

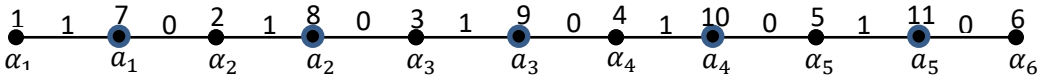

Figure 2.1

Theorem 2.3. The subdivision graph $S(K_{1,n})$ of the star $K_{1,n}$ is sum power n divisor cordial graph.

Proof: Let (V_1, V_2) be the partition of $K_{1,n}$ with $V_1 = \{\alpha\}$ and $V_2 = \{\alpha_i : 1 \le i \le n\}$. Let $\{a_i : 1 \le i \le n\}$ be the new vertices which subdivide the edges $\alpha\alpha_{i+1}$. The resulting graph is $S(K_{1,n})$. Define a function $f: V(G) \to \{1, 2, \dots, |V(G)|\}$ by $f(\alpha) = 1$, $f(\alpha_i) = 2i\,; 1 \le i \le n$, $f(a_i) = 2i+1\,; 1 \le i \le n$. Then the induced edge labels are $f^*(\alpha a_i) = 1\,; 1 \le i \le n$, $f^*(a_i\alpha_i) = 0\,; 1 \le i \le n$. We observe that $e_f(0) = n$ and $e_f(1) = n$. Thus $|e_f(0) - e_f(1)| \le 1$. Hence the graph $S(K_{1,n})$ is sum of power n divisor cordial graph.

Example 2.4. $S(K_{1,4})$ is sum of power n divisor cordial graph as shown in the figure.

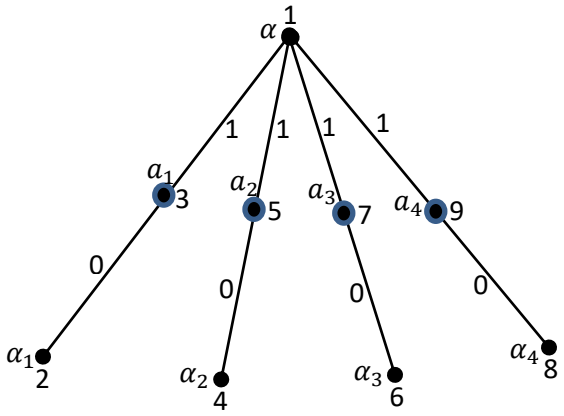

Figure 2.2

Theorem 2.5. The subdivision graph $SS_p(P_n, K_{1,n})$ is sum of power n divisor cordial graph if n is odd.

Proof: Let $\alpha_1, \alpha_2, \dots, \alpha_n$ be the vertices of the path P_n and $\beta_1, \beta_2, \dots, \beta_n$ be the vertices of the star $K_{1,n}$. Now the root of the star $K_{1,n}$ is attached at one end of the path P_n. Thus, the resultant graph is $S_p(P_n, K_{1,n})$. Let $\{\gamma_i : 1 \le i \le n\}$ be the new vertices which subdivide the edges $\alpha_i\alpha_{i+1}$ and let $\{\delta_i : 1 \le i \le n\}$ be the new vertices which subdivide the edges $\alpha_n\beta_i ; 1 \le i \le n$. Define a function $f: V(G) \to \{1, 2, \dots, |V(G)|\}$ by $f(\gamma_i) = i ; 1 \le i \le n-1$,n$f(\delta_i) = n - 1 + i ;$ $1 \le i \le n, f(\alpha_i) = \delta_n + 2i - 1; 1 \le i \le n, f(\beta_i) = \delta_n + 2i;\ 1 \le i \le n$. Then the induced edge labels are $f^*(\alpha_{2i}\gamma_{2i}) = 1; 1 \le i \le \left\lfloor \frac{n}{2} \right\rfloor$, $f^*(\gamma_{2i}\alpha_{2i+1}) = 1; 1 \le i \le \left\lfloor \frac{n}{2} \right\rfloor, f^*(\alpha_{2i-1}\gamma_{2i-1}) = 0 ;$ $1 \le i \le \left\lfloor \frac{n}{2} \right\rfloor$, $f^*(\gamma_{2i-1}\alpha_{2i}) = 0 ; 1 \le i \le \left\lfloor \frac{n}{2} \right\rfloor$, $f^*(\alpha_n\delta_{2i-1}) = 0 ; 1 \le i \le \left\lceil \frac{n}{2} \right\rceil$, $f^*(\alpha_n\delta_{2i}) =$ $1 ; 1 \le i \le \left\lfloor \frac{n}{2} \right\rfloor$, $f^*(\delta_{2i-1}\beta_{2i-1}) = 1 ; 1 \le i \le \left\lceil \frac{n}{2} \right\rceil$, $f^*(\delta_{2i}\beta_{2i}) = 0 ;\ 1 \le i \le \left\lfloor \frac{n}{2} \right\rfloor$. We observe that, $e_f(0) = 2n$ and $e_f(1) = 2n$. Thus $|e_f(0) - e_f(1)| \le 1$. Hence the graph $SS_p(P_n, K_{1,n})$ is sum of power n divisor cordial graph.

Example 2.6. The graph $SS_p(P_5, K_{1,5})$ is sum of power n divisor cordial graph.

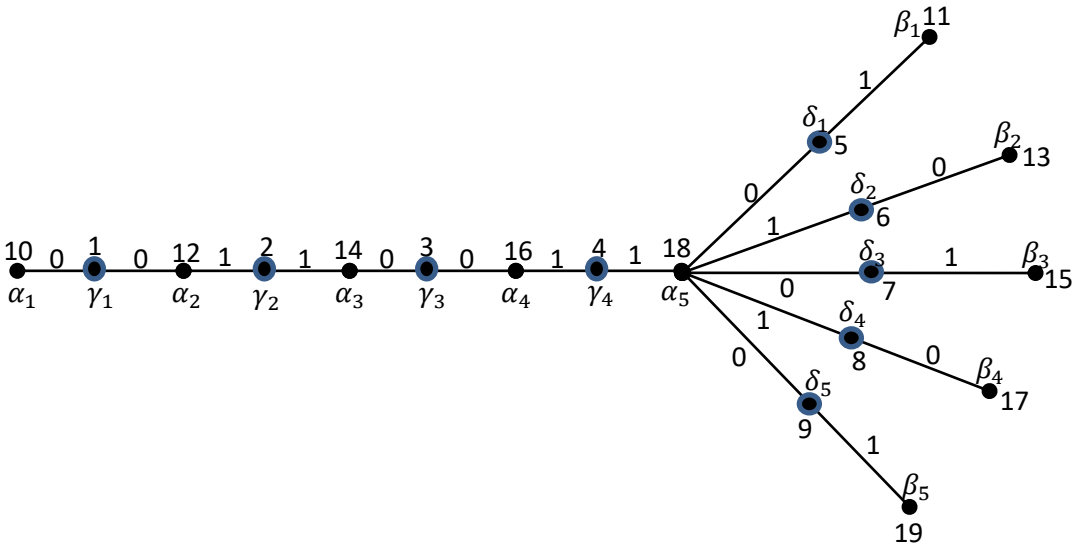

Figure 2.3.

Result:

From the graph $SS_p(P_n, K_{1,n})$,

i)If $n = m$, the condition satisfied, if $n \neq m$, the condition fails.

ii)For an odd number of n, the graph is sum of power n divisor cordial graph. For an even number of n, the graph is not satisfied with the condition.

Theorem 2.7. The subdivision graph $S(P_n \otimes S_m)$; n, m are even is sum of power n divisor cordial graph.

Proof: Let $\{A_i : 1 \leq i \leq n\}$ be the vertex of the path P_n and let $\{A'_i: 1 \leq i \leq n-1\}$ be the vertices of P_n. Which subdivide the edges $\alpha_i\alpha_{i+1}$ and let $\{B_i, C_i, D_i, \dots, Z_i : 1 \leq i \leq m\}$ be the vertices of S_m and let $\{b_i, c_i, d_i, \dots, z_i ; 1 \leq i \leq m\}$ be the vertices of the star which subdivide the edges $\{A_1B_i, A_2C_i, A_3D_i, \dots, A_nZ_i : 1 \leq i \leq m\}$. Define a function $f: V(G) \to \{1, 2, \dots, |V(G)|\}$ by $(b_i) = i ; 1 \leq i \leq m$, $f(c_i) = b_m + i ; 1 \leq i \leq m$, …, $f(z_i) = y_m + i ; 1 \leq i \leq m$, $f(B_i) = \alpha_1 + ni ; 1 \leq i \leq m$, $f(C_i) = \alpha_2 + ni ; 1 \leq i \leq m$, . . . , $f(Z_i) = \alpha_n + ni ; 1 \leq i \leq m$, $f(A_i) = z_m + i ; 1 \leq i \leq m$, $f(A'_i) = Z_m + i ; 1 \leq i \leq n-1$. Then the induced edge labels are $f^*(A_1b_{2i-1}) = 1 ; 1 \leq i \leq \frac{m}{2}$, $f^*(A_2c_{2i}) = 1 ; 1 \leq i \leq \frac{m}{2}$, . . . , $f^*(A_nz_{2i}) = 1 ; 1 \leq i \leq \frac{m}{2}$, $f^*(b_{2i-1}B_{2i-1}) = 1 ; 1 \leq i \leq \frac{m}{2}$, $f^*(c_{2i}C_{2i}) = 1 ; 1 \leq i \leq \frac{m}{2}$, . . . , $f^*(z_{2i}Z_{2i}) = 1 ; 1 \leq i \leq m-2$,$f^*(A_iA'_i) = 1 ; 1 \leq i \leq n-1$,$f^*(A_1b_{2i}) = 0 ;$ $1 \leq i \leq \frac{m}{2}$, $f^*(A_2c_{2i-1}) = 0 ; 1 \leq i \leq \frac{m}{2}$, …, $f^*(A_nz_{2i-1}) = 0 ; 1 \leq i \leq \frac{m}{2}$, $f^*(b_{2i}B_{2i}) = 0 ; 1 \leq i \leq \frac{m}{2}$, $f^*(c_{2i-1}C_{2i-1}) = 0 ; 1 \leq i \leq \frac{m}{2}$, . . . , $f^*(z_{2i}Z_{2i}) = 0 ; 1 \leq i \leq \frac{m}{2}$, $f^*(A'_iA_{i+1}) = 0 ; 1 \leq i \leq \frac{m}{2}$. We observe that $e_f(0) = \frac{nm}{2} + n - 1$ and $e_f(1) = \frac{nm}{2} + n - 1$. Thus $|e_f(0) - e_f(1)| \leq 1$. Hence the graph $S(P_n \otimes S_m)$ is sum of power n divisor cordial graph.

Example 2.8. The graph $S(P_4 \otimes S_4)$ is sum of power n divisor cordial graph as shown in the figure.

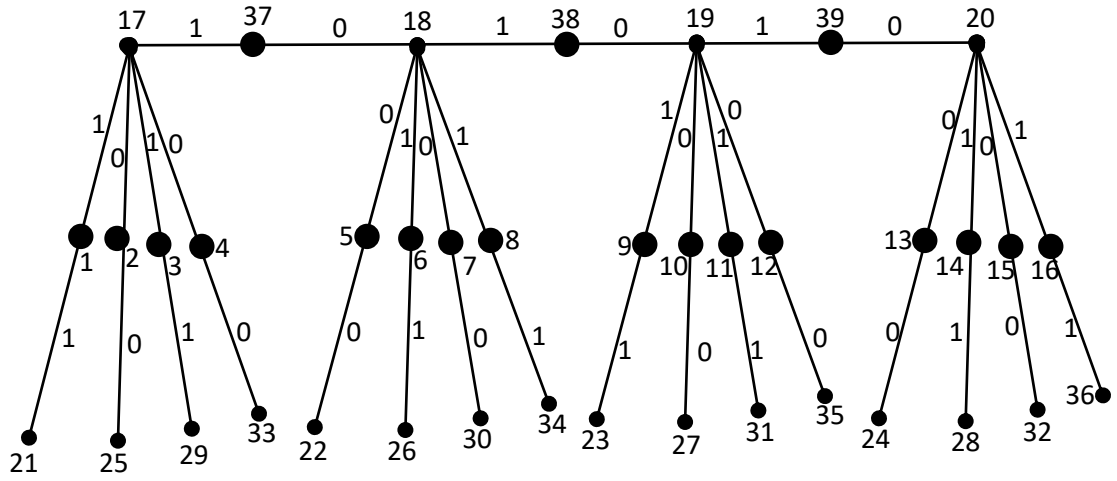

Figure 2.4.

Result:

For the graph $S(P_n \otimes S_m)$, n and m should be even otherwise the condition is not satisfied.

Conclusion:

The study of labeled graph is important due to its diversified applications. In this paper, we found some new results of subdivision of path and star related graphs are sum of power n divisor cordial graphs.

References:

J. A. Gallian, A dynamic survey of graph labeling, The Electronics Journal of Combinatorics (2012).

F. Harary, Graph Theory, Narosa Publishing House Reading, New Delhi (1998).

M. Jaslin Melbha and P. Preetha lal, Sum square divisor cordial labeling of theta graph, International Journal of non-linear analysis and applications, accepted for Publication.

A. Lourdusamy, F. Patrick, Sum Divisor Cordial Graphs, Proyecciones (Antofagasta) 35(1) (2016) 119-136.

A. Rosa, On Certain Valuation of the Vertices of a Graphs, Theory of Graphs Internet Symposium, Rome, July (1996) Gordom and Brcach N. Y and Dunod Paris (1967) 349-355.

Path related mean square cordial graphs, International Journal of Emerging Technologies in Engineering Research (IJETER) Volume 2, Issue 3, October (2015).

THE MOLECULAR-GRAPH BASED STRUCTURAL DESCRIPTORS OF BROAD-SPECTRUM ANTIVIRAL DRUGS USED IN COVID-19 TREATMENT

Fayis Thazhethe Palliyali[1], Mathew Varkey T.K[2]

[1,2]Department of Mathematics, TKM College of Engineering, APJ Abdul Kalam Technological University, Kollam, Kerala, India.

Abstract

Although several putative therapeutic agents are clinically trialed, the efficacy is not approved yet for the prevention or treatment for the ongoing pandemic to ensure the quality of life of infected patients after curing the illness, namely side effects. In this unprecedented situation, the identification and optimization of lead compound will be a crucial step in drug discovery which is largely resolved by the computational methods. it is important to find appropriate representation of putative therapeutic agents against COVID-19 using molecular descriptors to obtained a structural-activity relationship in computer aided drug discovery.

Keywords: Covid-19, Potential drug molecules, Arithmetic-geometric index, harmonic mean index

Introduction

Historically, nothing has killed more human beings than infectious diseases. Starting from the well documented first pandemic, the Justinian Plague in 541AD[1], that likely contributed to the decline of the Neolithic population of western Eurasia[2]to the recent COVID-19, pandemics have been a continuous threat that inflicts an insurmountable toll on human life and suffering.

On December 2019, an unprecedented outbreak of contagious viral pneumonia of mysterious aetiology was reported in Wuhan city of Hubei province, the People's Republic of China[3,4] .Wuhan is the most crowded sprawling capital city of Hubei province and a major transportation hub in the heartland of China with inhabitants exceeding 11 million. In early January 2020, the Chinees Centre for Disease Control and Prevention (China CDC) identified the causative pathogen[5], Severe Acute Respiratory Syndrome Corona Virus 2 (SARS-CoV-2), is a single-stranded positive-sense RNA virus belongs to the genus *Betecoronavirus* of the family *Coronovirdae*[6]. Subsequently, The World Health Organization (WHO) named the disease caused by SARS-CoV-19 as COVID-19. The rapid dissemination of SARS-CoV-2, which clasped the entire glob has reached the WHO to declare the outbreak to be a public health emergency of International Concern and a pandemic on 11th March 2020.

The escalating mortality and morbidity of the ongoing pandemic[7]have placed the researchers in a deluge to find an efficacious drug targeting SARS-CoV-2. Moreover, the designing of a new drug is expensive and time-consuming and the crisis should not lower the scientific standards [8]. In this extremity, the repurposing of existing drugs will be a logical approach since it has already been found to be sufficiently safe in preclinical models and humans if early-stage trials have been completed[9]. Although, in experimental repurposing, the identification of a lead compound from a wide range of chemical library and the optimization are the most critical stage in finding an efficacious drug, which is highly resolved with rapidly advancing computer – assisted techniques and the tools [10].

Quantitative structure−activity relationship (QSAR), is a major and matured part of computational tool applied to retrieve information correlating to lead discovery and optimization and also to understand the chemical-biological mechanism of existing drugs [11], more robustly with the help of molecular graph-based structural descriptors (Topological indices) [12]. The IUPAC defined the topological index as a numerical value associated with the chemical constitution for correlation of chemical structure with various physical properties, chemical reactivity or biological activity [13]. This paper will discuss the most familiar degree based topological indices of promising molecular structures G [14] against Covid-19. This non-empirical real valued function f: G→R^+ mapping the potential drug molecules [15] will help in QSAR models for the selection and design of structural analog with improved activity and finally into drug candidates.

Let G be a graph of order n and minimum degree $\delta(G) \geq \varphi$. Let $V(G)$ be the $vertex\ set$ and $E(G)$ be the $edge\ set$ of G, respectively. The degree of a vertex u in G is the number of edges incident to it. Let $\mu_{r,s}$ be the number of edges joining the vertices of degree r and s.

Based on the ratio of and arithmetical mean geometrical mean, a new molecular descriptor is proposed, called *Arithmetic-geometric index* [16] and it is defined as

$$AG(G) = \sum_{\varphi \leq r \leq s \leq n-1} \frac{r+s}{2\sqrt{rs}} \mu_{r,s}$$

Very recently a new topological index is defined, named *harmonic mean index* [17]formulated by

$$H_{MI}(G) = \sum_{\varphi \leq r \leq s \leq n-1} \frac{2rs}{r+s} \mu_{r,s}$$

Remdesivir

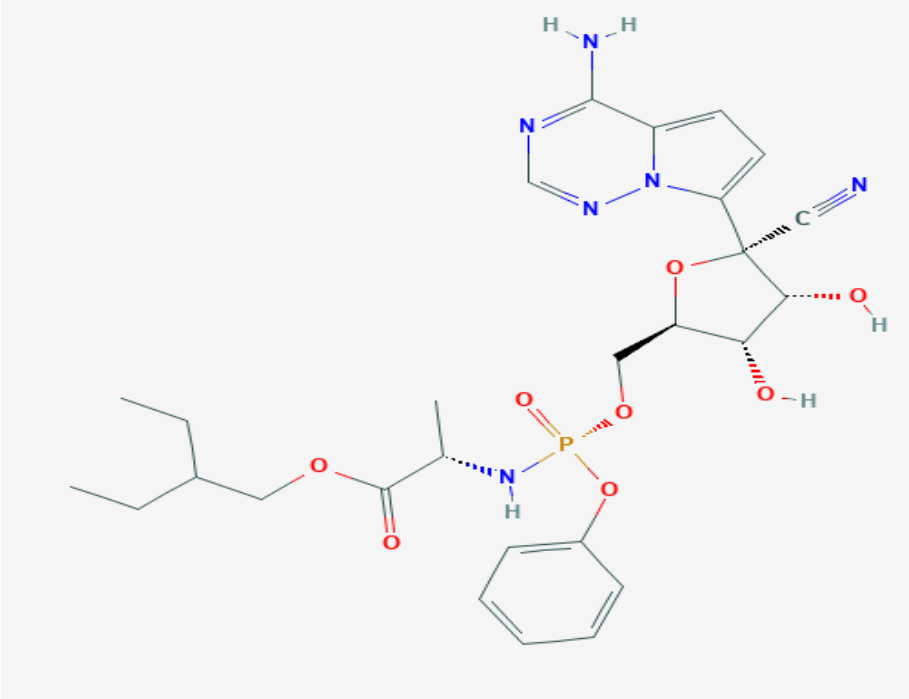

Fig.1 Chemical structure of Remdesivir [1]($C_{27}H_{35}N_6O_8P$)

Remdesivir (GS-5734) is an investigational broad-spectrum antiviral drug originally developed to treat Ebola virus infection[18] . Recently, it has been recognized as a potential antivirus against a wide variety of RNA viruses, including Middle East respiratory syndrome coronavirus (MERS-CoV) and Severe Acute Respiratory Syndrome Coronavirus (SARS-CoV) [19], which are phylogenetically identical to SARS-CoV-2[20]. Remdesivir is also being researched for its antiviral activity against SARS CoV-2 and the result shows that it is highly effective in controlling the COVID-19 in vitro [15,21,22].

Table 1: Edge partition of Remdesivir graph based on degrees of end vertices of each edge

(r, s)	$(1,2)$	$(1,3)$	$(1,4)$	$(2,2)$	$(2,3)$	$(2,4)$	$(3,3)$	$(3,4)$
Number of edges joining the e vertices of degree r and s, $\mu_{r,s}$	3	5	1	9	14	5	6	2

Theorem 1.1: For the molecular graph $G_1$of Remdesivir the Harmonic mean index, $H_{MI}(G_1) = \frac{21607}{210}$

Proof: Let G_1be the molecular graph of Remdesivir.

[1] National Center for Biotechnology Information. PubChem Database. Remdesivir, CID=121304016, https://pubchem.ncbi.nlm.nih.gov/compound/121304016 (accessed on January 15, 2021)

Harmonic mean index, $H_{MI}(G_1) = \sum_{\varphi \le r \le s \le n-1} \frac{2rs}{r+s} \mu_{r,s}$

By using edge partition of G_1 given in Table 1

$$H_{MI}(G_1) = 2\left(\frac{1\times2}{1+2} \times 3 + \frac{1\times3}{1+3} \times 5 + \frac{1\times4}{1+4} + \frac{2\times2}{2+2} \times 9 + \frac{2\times3}{2+3} \times 14 + \frac{2\times4}{2+4} \times 5 + \frac{3\times3}{3+3} \times 6 + \frac{3\times4}{3+4} \times 2\right)$$

$$\Rightarrow H_{MI}(G_1) = \frac{21607}{210}$$

Theorem 1.2: For the molecular graph $G_1$of Remdesivir the Arithmetic-geometric index,

$$AG(G_1) = \frac{65}{4} + 6\sqrt{2} + \frac{9\sqrt{3}}{2} + \frac{35}{\sqrt{6}}$$

Proof: Let G_1be the molecular graph of Remdesivir.

Arithmetic-geometric index, $AG(G_1) = \sum_{\varphi \le r \le s \le n-1} \frac{r+s}{2\sqrt{rs}} \mu_{r,s}$

By using edge partition of G_1 given in Table 1

$$AG(G_1) = \frac{3}{2\sqrt{2}} \times 3 + \frac{4}{2\sqrt{3}} \times 5 + \frac{5}{2\sqrt{4}} + \frac{4}{2\sqrt{4}} \times 9 + \frac{5}{2\sqrt{6}} \times 14 + \frac{6}{2\sqrt{8}} \times 5 + \frac{6}{2\sqrt{9}} \times 6 + \frac{7}{2\sqrt{12}} \times 2$$

$$\Rightarrow AG(G_1) = \frac{65}{4} + 6\sqrt{2} + \frac{9\sqrt{3}}{2} + \frac{35}{\sqrt{6}}$$

Chloroquine

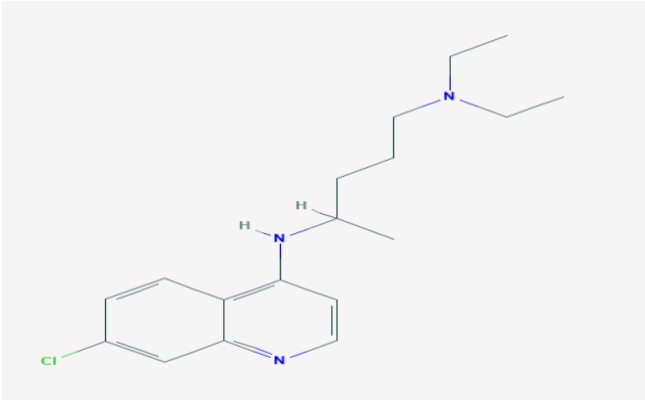

Fig.2 Chemical structure of Chloroquine[2]($C_{18}H_{26}ClN_3$)

Chloroquine, is a 9-aminoquinoline discovered in 1934, a low coast and widely prescribed antimalarial, autoimmune disease drug, has recently been recognized as a potential broad-spectrum antiviral drug including SARS-CoV [23,24]. The recent studies demonstrate that chloroquine is potentially clinically applicable against the SARS-CoV-2[15,25].

[2] National Center for Biotechnology Information. PubChem Database. Chloroquine, CID=2719, https://pubchem.ncbi.nlm.nih.gov/compound/2719#section=Structures (accessed on January 15, 2021)

Table 2: Edge partition of chloroquine graph based on degrees of end vertices of each edge

(r,s)	$(1,2)$	$(2,2)$	$(1,3)$	$(2,3)$	$(3,3)$
Number of edges joining the vertices of degree r and s, $\mu_{r,s}$	2	5	2	12	2

Theorem 2.1: For the molecular graph $G_2$of chloroquine the Harmonic mean index, $H_{MI}(G_2) = \frac{757}{15}$

Proof: Let G_2be the molecular graph of choloquine.

Harmonic mean index, $H_{MI}(G_2) = \sum_{\varphi \le r \le s \le n-1} \frac{2rs}{r+s}\mu_{r,s}$

By using edge partition of G_2 given in Table 2

$$H_{MI}(G_2) = 2\left(\frac{1\times2}{1+2} \times 2 + \frac{2\times2}{2+2} \times 5 + \frac{1\times3}{1+3} \times 2 + \frac{2\times3}{2+3} \times 12 + \frac{3\times3}{3+3} \times 2\right) = \frac{757}{15}$$

Theorem 2.2: For the molecular graph $G_2$of chloroquine the Arithmetic-geometric index,

$$AG(G_2) = \frac{3}{\sqrt{2}} + \frac{4}{\sqrt{3}} + 5\sqrt{6} + 7$$

Proof: Let G_2be the molecular graph of choloquine.

Arithmetic-geometric index, $AG(G_2) = \sum_{\varphi \le r \le s \le n-1} \frac{r+s}{2\sqrt{rs}}\mu_{r,s}$

By using edge partition of G_2 given in Table 2

$$AG(G_2) = \frac{3}{2\sqrt{2}} \times 2 + \frac{4}{2\sqrt{4}} \times 5 + \frac{4}{2\sqrt{3}} \times 2 + \frac{5}{2\sqrt{6}} \times 12 + \frac{6}{2\sqrt{9}} \times 2$$

$$\Rightarrow AG(G_2) = \frac{3}{\sqrt{2}} + \frac{4}{\sqrt{3}} + 5\sqrt{6} + 7$$

Hydroxychloroquine

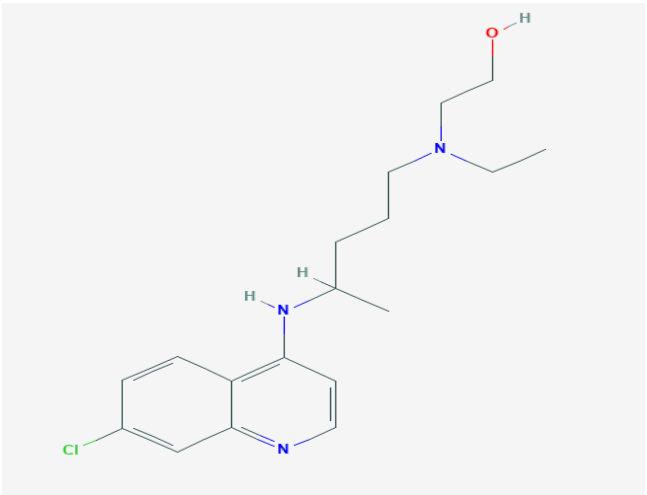

Fig.3 Chemical structure of Hydroxychloroquine[3] ($C_{18}H_{26}ClN_3O$)

Hydroxychloroquine is a 4-aminoquinoline and it is a derivative of chloroquine that has both antimalarial and anti-inflammatory activities. Hydroxychloroquine is being studied to prevent and treat coronavirus disease 2019.

Table 3: Edge partition of hydroxychloroquine graph based on degrees of end vertices of each edge

(r, s)	$(1, 2)$	$(2, 2)$	$(1, 3)$	$(2, 3)$	$(3, 3)$
Number of edges joining the vertices of degree r and s, $\mu_{r,s}$	2	6	2	12	2

Theorem 3.1: For the molecular graph $G_3$of hydroxychloroquine the Harmonic mean index,

$H_{MI}(G_3) = \frac{787}{15}$

Proof: Let G_3be the molecular graph of hydroxychloroquine.

Harmonic mean index, $H_{MI}(G_3) = \sum_{\varphi \le r \le s \le n-1} \frac{2rs}{r+s} \mu_{r,s}$

By using edge partition of G_3 given in Table 3

$H_{MI}(G_3) = 2\left(\frac{1\times2}{1+2} \times 2 + \frac{2\times2}{2+2} \times 6 + \frac{1\times3}{1+3} \times 2 + \frac{2\times3}{2+3} \times 12 + \frac{3\times3}{3+3} \times 2\right) = \frac{787}{15}$

Theorem 3.2: For the molecular graph $G_3$of hydroxychloroquine the Arithmetic-geometric index,

$AG(G_3) = \frac{3}{\sqrt{2}} + \frac{4}{\sqrt{3}} + 5\sqrt{6} + 8$

Proof: Let G_3be the molecular graph of hydroxychloroquine.

Arithmetic-geometric index, $AG(G_3) = \sum_{\varphi \le r \le s \le n-1} \frac{r+s}{2\sqrt{rs}} \mu_{r,s}$

By using edge partition of G_3 given in Table 3

$AG(G_3) = \frac{3}{2\sqrt{2}} \times 2 + \frac{4}{2\sqrt{4}} \times 6 + \frac{4}{2\sqrt{3}} \times 2 + \frac{5}{2\sqrt{6}} \times 12 + \frac{6}{2\sqrt{9}} \times 2$

$\Rightarrow AG(G_3) = \frac{3}{\sqrt{2}} + \frac{4}{\sqrt{3}} + 5\sqrt{6} + 8$

[3] National Center for Biotechnology Information. PubChem Database. Hydroxychloroquine, CID=3652

https://pubchem.ncbi.nlm.nih.gov/compound/3652 (accessed on January 15, 2021)

Lopinavir

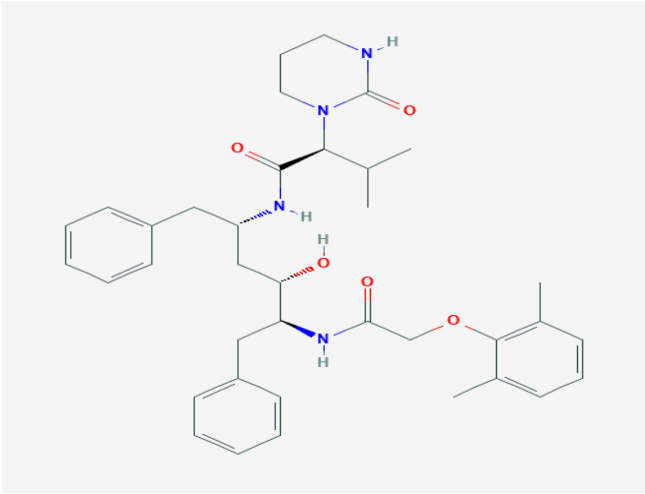

Fig.4 Chemical structure of Lopinavir[4] ($C_{37}H_{48}N_4O_5$)

Lopinavir is an antiretroviral protease inhibitor used in combination with ritonavir in the therapy and prevention of human immunodeficiency virus (HIV) infection and the acquired immunodeficiency syndrome (AIDS).

Table 4: Edge partition of Lopinavir graph based on degrees of end vertices of each edge

(r,s)	$(1,3)$	$(2,2)$	$(2,3)$	$(3,3)$
Number of edges joining the vertices of degree r and s, $\mu_{r,s}$	8	14	20	7

Theorem 4.1: For the molecular graph $G_4$of Lopinavir the Harmonic mean index, $H_{MI}(G_4) = 109$

Proof: Let G_4be the molecular graph of Lopinavir.

Harmonic mean index, $H_{MI}(G) = \sum_{\varphi \le r \le s \le n-1} \frac{2rs}{r+s}\mu_{r,s}$

By using edge partition of G_4 given in Table 4

$$\Rightarrow H_{MI}(G_4) = 2\left(\frac{2\times2}{2+2} \times 14 + \frac{1\times3}{1+3} \times 8 + \frac{2\times3}{2+3} \times 20 + \frac{3\times3}{3+3} \times 7\right) = 109$$

Theorem 4.2: For the molecular graph $G_4$of Lopinavir the Arithmetic-geometric index,

[4] National Center for Biotechnology Information. PubChem Database. Lopinavir, CID=92727

https://pubchem.ncbi.nlm.nih.gov/compound/Lopinavir (accessed on January 15, 2021)

$$AG(G_4) = \frac{16}{\sqrt{3}} + \frac{50}{\sqrt{6}} + 21$$

Proof: Let G_4be the molecular graph of Lopinavir

Arithmetic-geometric index, $AG(G) = \sum_{\varphi \le r \le s \le n-1} \frac{r+s}{2\sqrt{rs}} \mu_{r,s}$

By using edge partition of G_4 given in Table 4

$$AG(G_4) = \frac{4}{2\sqrt{4}} \times 14 + \frac{4}{2\sqrt{3}} \times 8 + \frac{5}{2\sqrt{6}} \times 20 + \frac{6}{2\sqrt{9}} \times 7$$

$$\Rightarrow AG(G_4) = \frac{16}{\sqrt{3}} + \frac{50}{\sqrt{6}} + 21$$

Ribavirin

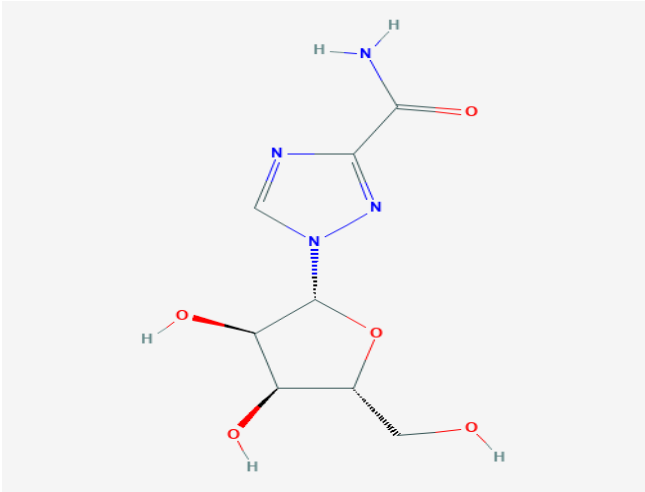

Fig.5 Chemical structure of Ribavirin[5] ($C_8H_{12}N_4O_5$)

Ribavirin is a nucleoside analogue and antiviral agent used in therapy of chronic hepatitis C and other flavivirus infections. it is an inhibitor of HCV polymerase and possesses a broad spectrum of activity against DNA and RNA viruses. Ribavirin is a potential antiviral drug that can be used for the treatment of Covid-19 [26,27]

Table 5: Edge partition of ribavirin graph based on degrees of end vertices of each edge

(r,s)	$(1,2)$	$(2,2)$	$(1,3)$	$(2,3)$	$(3,3)$
Number of edges joining the vertices of degree r and s, $\mu_{r,s}$	1	1	4	7	5

[5] National Center for Biotechnology Information. PubChem Database. Ribavirin, CID=37542

https://pubchem.ncbi.nlm.nih.gov/compound/Ribavirin (accessed on January 15, 2021)

Theorem 5.1: For the molecular graph $G_5$of ribavirin the Harmonic mean index, $H_{MI}(G_5) = \frac{617}{15}$

Proof: Let G_5be the molecular graph of ribavirin

Harmonic mean index, $H_{MI}(G) = \sum_{\varphi \le r \le s \le n-1} \frac{2rs}{r+s} \mu_{r,s}$

By using edge partition of G_5 given in Table 5

$$H_{MI}(G_5) = 2\left(\frac{1\times2}{1+2} + \frac{1\times3}{1+3} \times 4 + \frac{2\times2}{2+2} + \frac{2\times3}{2+3} \times 7 + \frac{3\times3}{3+3} \times 5\right) = \frac{617}{15}$$

Theorem 5.2: For the molecular graph $G_5$of ribavirin the Arithmetic-geometric index,

$$AG(G_5) = 6 + \frac{3}{2\sqrt{2}} + \frac{8}{\sqrt{3}} + \frac{35}{2\sqrt{6}}$$

Proof: Let G_5be the molecular graph of ribavirin

Arithmetic-geometric index, $AG(G) = \sum_{\varphi \le r \le s \le n-1} \frac{r+s}{2\sqrt{rs}} \mu_{r,s}$

By using edge partition of G_5 given in Table 5

$$AG(G_5) = \frac{3}{2\sqrt{2}} + \frac{4}{2\sqrt{3}} \times 4 + \frac{4}{2\sqrt{4}} + \frac{5}{2\sqrt{6}} \times 7 + \frac{6}{2\sqrt{9}} \times 5$$

$$\Rightarrow AG(G_5) = 6 + \frac{3}{2\sqrt{2}} + \frac{8}{\sqrt{3}} + \frac{35}{2\sqrt{6}}$$

Fevipiravir

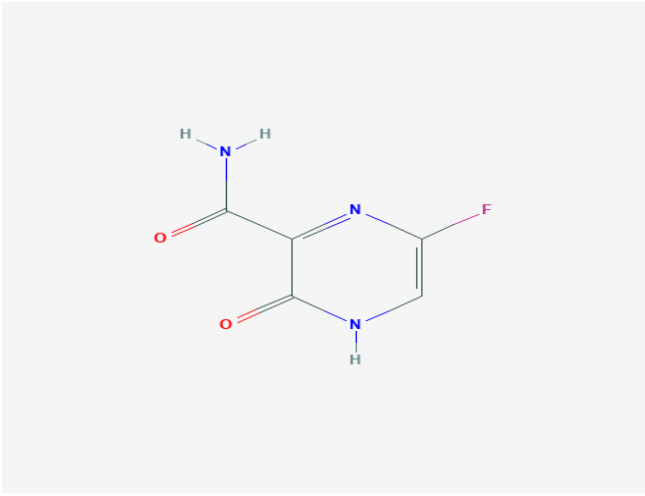

Fig.6 Chemical structure of Fevipiravir[6]($C_5H_4FN_3O_2$)

[6] National Center for Biotechnology Information. PubChem Database. Ribavirin, CID=492405

https://pubchem.ncbi.nlm.nih.gov/compound/Favipiravir (accessed on January 15, 2021)

Favipiravir is a broad-spectrum oral antiviral drug that selectively inhibits RNA-dependent RNA polymerase (RdRp) and the viral replication phase of SARS-CoV-2 and is being studied in multiple ongoing international clinical trials [28,29]

Table 6: Edge partition of Fevipiravir graph based on degrees of end vertices of each edge

(r, s)	(1,3)	(2,2)	(2,3)	(3,3)
Number of edges joining the vertices of degree r and s, $\mu_{r,s}$	4	1	4	2

Theorem 6.1: For the molecular graph $G_6$of Fevipiravir the Harmonic mean index, $H_{MI}(G_6) = \frac{118}{5}$

Proof: Let G_6be the molecular graph of Fevipiravir

Harmonic mean index, $H_{MI}(G) = \sum_{\varphi \le r \le s \le n-1} \frac{2rs}{r+s} \mu_{r,s}$

By using edge partition of G_6 given in Table 6

$$H_{MI}(G_6) = 2\left(\frac{1\times3}{1+3} \times 4 + \frac{2\times2}{2+2} + \frac{2\times3}{2+3} \times 4 + \frac{3\times3}{3+3} \times 2\right) = \frac{118}{5}$$

Theorem 6.2: For the molecular graph $G_6$of Fevipiravir the Arithmetic-geometric index,

$$AG(G_6) = 3 + \frac{8}{\sqrt{3}} + \frac{10}{\sqrt{6}}$$

Proof: Let G_6be the molecular graph of Fevipiravir

Arithmetic-geometric index, $AG(G) = \sum_{\varphi \le r \le s \le n-1} \frac{r+s}{2\sqrt{rs}} \mu_{r,s}$

By using edge partition of G_6 given in Table 6

$$AG(G_6) = \frac{4}{2\sqrt{3}} \times 4 + \frac{4}{2\sqrt{4}} + \frac{5}{2\sqrt{6}} \times 4 + \frac{6}{2\sqrt{9}} \times 2$$

$$\Rightarrow AG(G_6) = 3 + \frac{8}{\sqrt{3}} + \frac{10}{\sqrt{6}}$$

Conclusion

The most prominent and the recent degree based topological indices discussed in this study which mapping the potential molecular structures against SARS-CoV-2 will help the QSAR models for the selection and design of new structural analogues. We anticipate these new structural analogues of existing potential drug molecules with improved activity will be a promising drug against the ongoing pandemic.

Reference:

J. C. Russell, Demogr. J. C. Russell, Demogr. 5, 174 (1968). 5, 174 (1968).

N. Rascovan, K. G. Sjögren, K. Kristiansen, R. Nielsen, E. Willerslev, C. Desnues, and S. Rasmussen, Cell 176, 295 (2019).

H. Lu, C. W. Stratton, and Y. W. Tang, J. Med. Virol. 92, 401 (2020).

C. Huang, Y. Wang, X. Li, L. Ren, J. Zhao, Y. Hu, L. Zhang, G. Fan, J. Xu, X. Gu, Z. Cheng, T. Yu, J. Xia, Y. Wei, W. Wu, X. Xie, W. Yin, H. Li, M. Liu, Y. Xiao, H. Gao, L. Guo, J. Xie, G. Wang, R. Jiang, Z. Gao, Q. Jin, J. Wang, and B. Cao, Lancet 395, 497 (2020).

Z. Wu and J. M. McGoogan, JAMA - J. Am. Med. Assoc. 323, 1239 (2020).

A. E. Gorbalenya, S. C. Baker, R. S. Baric, R. J. de Groot, C. Drosten, A. A. Gulyaeva, B. L. Haagmans, C. Lauber, A. M. Leontovich, B. W. Neuman, D. Penzar, S. Perlman, L. L. M. Poon, D. V. Samborskiy, I. A. Sidorov, I. Sola, and J. Ziebuhr, Nat. Microbiol. 5, 536 (2020).

E. Dong, H. Du, and L. Gardner, Lancet Infect. Dis. 20, 533 (2020).

A. J. London and J. Kimmelman, Science (80-.). 368, 476 (2020).

S. Pushpakom, F. Iorio, P. A. Eyers, K. J. Escott, S. Hopper, A. Wells, A. Doig, T. Guilliams, J. Latimer, C. McNamee, A. Norris, P. Sanseau, D. Cavalla, and M. Pirmohamed, Nat. Rev. Drug Discov. 18, 41 (2018).

S. J. Y. Macalino, V. Gosu, S. Hong, and S. Choi, Arch. Pharm. Res. 38, 1686 (2015).

C. Hansch, D. Hoekman, and H. Gao, Chem. Rev. 96, 1045 (1996).

E. Estrada and E. Uriarte, Curr. Med. Chem. 8, 1573 (2012).

U. Of and A. Chemistry, 69, 1975 (1975).

S. H. Basha, J. PeerScientist 2, e1000013 (2020).

M. Wang, R. Cao, L. Zhang, X. Yang, J. Liu, M. Xu, Z. Shi, Z. Hu, W. Zhong, and G. Xiao, Cell Res. 30, 269 (2020).

V. S. Shegehalli and R. Kanabur, J. Comput. Math. Sci. 6, 19 (2015).

G. S. Singh and N. J. Koshy, Int. J. Res. Eng. Sci. Manag. 2, 3 (2020).

T. K. Warren, R. Jordan, M. K. Lo, A. S. Ray, R. L. Mackman, V. Soloveva, D. Siegel, M. Perron, R. Bannister, H. C. Hui, N. Larson, R. Strickley, J. Wells, K. S. Stuthman, S. A. Van Tongeren, N. L. Garza, G. Donnelly, A. C. Shurtleff, C. J. Retterer, D. Gharaibeh, R. Zamani, T. Kenny, B. P. Eaton, E. Grimes, L. S. Welch, L. Gomba, C. L. Wilhelmsen, D. K. Nichols, J. E. Nuss, E. R.

Nagle, J. R. Kugelman, G. Palacios, E. Doerffler, S. Neville, E. Carra, M. O. Clarke, L. Zhang, W. Lew, B. Ross, Q. Wang, K. Chun, L. Wolfe, D. Babusis, Y. Park, K. M. Stray, I. Trancheva, J. Y. Feng, O. Barauskas, Y. Xu, P. Wong, M. R. Braun, M. Flint, L. K. McMullan, S. S. Chen, R. Fearns, S. Swaminathan, D. L. Mayers, C. F. Spiropoulou, W. A. Lee, S. T. Nichol, T. Cihlar, and S. Bavari, Nature 531, 381 (2016).

T. P. Sheahan, A. C. Sims, R. L. Graham, V. D. Menachery, L. E. Gralinski, J. B. Case, S. R. Leist, K. Pyrc, J. Y. Feng, I. Trantcheva, R. Bannister, Y. Park, D. Babusis, M. O. Clarke, R. L. MacKman, J. E. Spahn, C. A. Palmiotti, D. Siegel, A. S. Ray, T. Cihlar, R. Jordan, M. R. Denison, and R. S. Baric, Sci. Transl. Med. 9, (2017).

N. Petrosillo, G. Viceconte, O. Ergonul, G. Ippolito, and E. Petersen, Clin. Microbiol. Infect. (2020).

J. Grein, N. Ohmagari, D. Shin, G. Diaz, E. Asperges, A. Castagna, T. Feldt, G. Green, M. L. Green, F.-X. Lescure, E. Nicastri, R. Oda, K. Yo, E. Quiros-Roldan, A. Studemeister, J. Redinski, S. Ahmed, J. Bernett, D. Chelliah, D. Chen, S. Chihara, S. H. Cohen, J. Cunningham, A. D'Arminio Monforte, S. Ismail, H. Kato, G. Lapadula, E. L'Her, T. Maeno, S. Majumder, M. Massari, M. Mora-Rillo, Y. Mutoh, D. Nguyen, E. Verweij, A. Zoufaly, A. O. Osinusi, A. DeZure, Y. Zhao, L. Zhong, A. Chokkalingam, E. Elboudwarej, L. Telep, L. Timbs, I. Henne, S. Sellers, H. Cao, S. K. Tan, L. Winterbourne, P. Desai, R. Mera, A. Gaggar, R. P. Myers, D. M. Brainard, R. Childs, and T. Flanigan, N. Engl. J. Med. 2327 (2020).

W. C. Ko, J. M. Rolain, N. Y. Lee, P. L. Chen, C. T. Huang, P. I. Lee, and P. R. Hsueh, Int. J. Antimicrob. Agents 55, 105933 (2020).

A. Savarino, J. R. Boelaert, A. Cassone, G. Majori, and R. Cauda, Lancet Infect. Dis. 3, 722 (2003).

E. Keyaerts, L. Vijgen, P. Maes, J. Neyts, and M. Van Ranst, Biochem. Biophys. Res. Commun. 323, 264 (2004).

J. Gao, Z. Tian, and X. Yang, Biosci. Trends (2020).

I. F. N. Hung, K. C. Lung, E. Y. K. Tso, R. Liu, T. W. H. Chung, M. Y. Chu, Y. Y. Ng, J. Lo, J. Chan, A. R. Tam, H. P. Shum, V. Chan, A. K. L. Wu, K. M. Sin, W. S. Leung, W. L. Law, D. C. Lung, S. S in, P. Yeung, C. C. Y. Yip, R. R. Zhang, A. Y. F. Fung, E. Y. W. Yan, K. H. Leung, J. D. Ip, A. W. H. Chu, W. M. Chan, A. C. K. Ng, R. Lee, K. Fung, A. Yeung, T. C. Wu, J. W. M. Chan, W. W. Yan, W. M. Chan, J. F. W. Chan, A. K. W. Lie, O. T. Y. Tsang, V. C. C. Cheng, T. L. Que, C. S. Lau, K. H. Chan, K. K. W. To, and K. Y. Yuen, Lancet 395, 1695 (2020).

J. S. Khalili, H. Zhu, N. S. A. Mak, Y. Yan, and Y. Zhu, J. Med. Virol. 92, 740 (2020).

E. A. Coomes and H. Haghbayan, J. Antimicrob. Chemother. 75, 2013 (2020).

Q. Cai, M. Yang, D. Liu, J. Chen, D. Shu, J. Xia, X. Liao, Y. Gu, Q. Cai, Y. Yang, C. Shen, X. Li, L. Peng, D. Huang, J. Zhang, S. Zhang, F. Wang, J. Liu, L. Chen, S. Chen, Z. Wang, Z. Zhang, R. Cao, W. Zhong, Y. Liu, and L. Liu, Engineering 5 (2020).

INTUITIONISTIC ANTI FUZZY BG-IDEALS IN BG-ALGEBRA

R.Rashma[1], K.R.Sobha[2]

[1]Research scholar,Reg.No:21113182092001
Sree Ayyappa college for Women,Chunkankadai,Nagercoil-629001, TamilNadu, India.
[2]Assistant Professor, Department of Mathematics, Sree Ayyappa College for Women, Chunkankadai, Nagercoil.
[Affiliated to Manonmaniam Sundaranar University, Abishekapatti, Tirunelveli-627012, Tamil Nadu, India.]
1rashmamariagiri@gmail.com
2vijayakumar.sobha9@gmail.com

Abstract

In this Paper, we introduce the concept of intuitionistic anti fuzzy BG-ideals in BG-algebra and we have discussed some of its algebraic properties.

Keywords:BG-algebra, Anti fuzzy subalgebra,Intuitionistic anti fuzzy subalgebra, Lower level subset, Anti fuzzy BG-Ideal, Intuitionistic Anti fuzzy BG-Ideal.

Introduction

In 1965,Zadeh [20] introduced the notion of a fuzzy set and fuzzy subset of a set as a method for representing uncertainty in real physical world.Since then its application have been growing rapidly over many disciplines.As a generalization of this,intuitionistic fuzzy subset was defined by K.T.Atanassov in 1986..K.Iseki and Jun et al. introduced three classes of abstract algebra: BCI-algebras, BH-algebras and BCK-algebra respectively.Further, the notion of intuitionistic fuzzy ideals was introduced by Jun and Kim in BCK-algebra.Neggers and H.Kim introduced the notion of B-algebra and d-algebra which is another generalization of BCK-algebra, and they also investigated several relation between d-algebra and BCK-algebra as well as some other interesting relation between d-algebra and oriented digraph.Ahn and Lee studied fuzzy subalgebra of BG-algebra.Fuzzy set give a degree of membership of an element in a given set, while intuitionistic fuzzy set give both degree of membership and nonmembership.Both degree belong to the interval [0,1], and their sum should not exceed 1.

Preliminaries

Definition 1

A BG-algebra is a non-empty set X with a constant 0 and a binary operation '*' satisfying the following axioms

(i) $x * x = 0$

(ii) $x * 0 = x$

(iii)$(x * y) * (0 * y) = x \ \ \forall\, x, y \in X$.

Definition 2

Let μ be a fuzzy set in BG-algebra.Then μ is called an anti fuzzy subalgebra of X if $\mu(x * y) \leq max\{\mu(x), \mu(y)\}$ for all $x, y \epsilon X$.

Definition 3

Let (μ_A, γ_A) be a Intuitionistic fuzzy set in BG-algebra.Then (μ_A, γ_A) is called an Intuitionistic anti fuzzy subalgebra of X if

$$\mu_A(x * y) \leq max\{\mu_A(x), \mu_A(y)\}$$

$$\gamma_A(x * y) \geq min\{\gamma_A(x), \gamma_A(y)\} \text{ for all } x, y \epsilon X.$$

Definition 4

An intuitionistic fuzzy set μ_A in X is called an intuitionistic Anti fuzzy BG-Ideal of *X* if it satisfies the following inequalities:

(i) $\mu_A(0) \leq \mu_A(x)$

(ii) $\mu_A(x) \leq max\{\mu_A(x * y), \mu_A(y)\}$

(iii) $\mu_A(x * y) \leq max\{\mu_A(x), \mu_A(y)\}$

(iv) $\gamma_A(0) \geq \gamma_A(x)$

(v) $\gamma_A(x) \geq min\{\gamma_A(x * y), \gamma_A(y)\}$

(vi) $\gamma_A(x * y) \geq min\{\gamma_A(x), \gamma_A(y)\} \forall\, x, y \epsilon X$

Theorem 5

If (μ_A, γ_A) is an Intuitionistic Anti fuzzy BG-Ideal of X that $(\mu_A)_t$ and $(\gamma_A)_t$ is a BG-Ideal of X for all $t \epsilon [0,1]$.

Proof:

Let (μ_A, γ_A) be Intuitionistic Anti fuzzy BG-Ideal of *X* and $x, y \epsilon X$.

If $x, y\epsilon((\mu_A)_t, (\gamma_A)_t)$.

Then $\mu_A(0) \leq \mu_A(x) \leq t$ implies $0\epsilon(\mu_A)_t \forall\ t\epsilon[0,1]$

Let $x * y\epsilon(\mu_A)_t$ and $y\epsilon(\mu_A)_t$.

Therefore $\mu_A(x * y) \leq t$ and $\mu_A(y) \leq t$.

Now $$\mu_A(x) \leq max\{\mu_A(x * y), \mu_A(y)\}$$
$$\leq max\{t, t\}$$
$$\leq t$$

Hence $\mu_A(x) \leq t$.That is, $x\epsilon(\mu_A)_t$

Let $x\epsilon(\mu_A)_t$,$y\epsilon X$.Choose y in X Such that $\mu_A(y) \leq t$.

Since $x\epsilon(\mu_A)_t$ implies $\mu_A(x) \leq t$.

We know that, $\mu_A(x * y) \leq max\{\mu_A(x), \mu_A(y)\}$
$$\leq max\{t, t\}$$
$$\leq t$$

$\mu_A(x * y) \leq t$ implies $x * y\epsilon(\mu_A)_t$.

Also

Let γ_A be Intuitionistic Anti fuzzy BG-Ideal of X and $x, y\epsilon X$.

If $x, y\epsilon(\gamma_A)_t$.

Then $\gamma_A(0) \geq \gamma_A(x) \geq t$ implies $0\epsilon(\gamma_A)_t \forall\ t\epsilon[0,1]$

Let $x * y\epsilon(\gamma_A)_t$ and $y\epsilon(\gamma_A)_t$.

Therefore $\gamma_A(x * y) \geq t$ and $\gamma_A(y) \geq t$.

Now $\gamma_A(x) = min\{\gamma_A(x * y), \gamma_A(y)\}$
$$\geq min\{t, t\}$$

Hence $\gamma_A(x) \geq t$.That is, $x\epsilon(\gamma_A)_t$

Let $x\epsilon(\gamma_A)_t$,$y\epsilon X$.Choose y in X Such that $\gamma_A(x) \geq t$.

Since $x\epsilon(\gamma_A)_t$ implies $\gamma_A(y) \geq t$.

We know that, $\gamma_A(x * y) \geq min\{\gamma_A(x), \gamma_A(y)\}$
$$\geq min\{t, t\}$$

$\gamma_A(x * y) \geq t$ implies $x * y \epsilon (\gamma_A)_t$.

Hence$((\mu_A)_t, (\gamma_A)_t)$is a BG-Ideal of X .

Theorem 6

Let X be a BG-algebra $t\epsilon[0,1]$ and $((\mu_A)_t, (\gamma_A)_t)$is a BG-Ideal of X then (μ_A, γ_A) is an Intuitionistic Anti fuzzy BG-Ideal of X.

Soln

Let $((\mu_A)_t, (\gamma_A)_t)$ be a BG-Ideal of X.

Let $x, y \epsilon ((\mu_A)_t$.Then , $\mu_A(x) \leq t$ and $\mu_A(y) \leq t$

Let $\mu_A(x) = t_1$ and $\mu_A(y) = t_2$

Without loss of generality

Let $t_1 \leq t_2$.Then $x \epsilon (\mu_A)_{t_2}$.Now $x \epsilon (\mu_A)_{t_2}$ and $y \epsilon X$ implies $x * y \epsilon (\mu_A)_{t_2}$

That is, $\mu_A(x * y) \leq t_2$

$= max\{t_1, t_2\}$

$= max\{\mu_A(x), \mu_A(y)\}$

$\mu_A(x * y) \leq max\{\mu_A(x), \mu_A(y)\}$

Now let $\mu_A(0) = \mu_A(x * x)$

$\leq max\{\mu_A(x), \mu_A(y)\}$

$= \mu_A(x)$

$\mu_A(0) \leq \mu_A(x)$

Further $\mu_A(x) = (\mu_A(x * y) * (0 * y))$

$\leq max\{\mu_A(x * y), \mu_A(0 * y)\}$

$\leq max\{\mu_A(x * y), \max\{\mu_A(0), \mu_A(y)\}$

$\leq max\{\mu_A(x * y), \mu_A(y)\}$

Clearly this can be proved for maximal condition also,

That is

$\gamma_A(x * y) \geq min\{\gamma_A(x), \gamma_A(y)\}$

$\gamma_A(0) \geq \gamma_A(x)$

$$\gamma_A(x) \geq min\{\gamma_A(x * y), \gamma_A(y)\}$$

Hence (μ_A, γ_A) is an Intuitionistic Anti fuzzy BG-Ideal of X.

Definition 7

Let $f: X \to Y$ be a mapping of BG-algebra and (μ_A, γ_A) be a Intuitionistic fuzzy in Y then $(\mu_A^f, \gamma_A^f) = A^f$ is the pre-image of (μ_A, γ_A) under f is

$$\mu_A^f(x) = \mu_A(f(x))$$

$$\gamma_A^f(x) = \gamma_A(f(x)) \; \forall x \epsilon X$$

Theorem 8

Let $f: X \to Y$ be a homomorphism of BG-Algebra.If $A = (\mu_A, \gamma_A)$ is an Intuitionistic Anti fuzzy BG-Ideal of Y.Then $(\mu_A^f, \gamma_A^f) = A^f$ is an Intuitionistic Anti fuzzy BG-Ideal of X.

Proof:

For any $x \epsilon X$ we have

$\mu_A^f(x) = \mu_A(f(x)) \geq \mu_A(0) = \mu_A(f(0)) = \mu_A^f(0)$ And

$\gamma_A^f(x) = \gamma_A(f(x)) \leq \gamma_A(0) = \gamma_A(f(0)) = \gamma_A^f(0) \forall x, y \in X$

Let $x, y \epsilon X$,then

$$max\{\mu_A^f(x * y), \mu_A^f(y)\} = max\{\mu_A(f(x * y)), \mu_A(f(y))\}$$
$$= max\{\mu_A(f(x) * f(y)), \mu_A(f(y))\}$$
$$\geq \mu_A(f(x))$$
$$= \mu_A^f(x)$$

$$min\{\gamma_A^f(x * y), \gamma_A^f(y)\} = min\{\gamma_A(f(x * y)), \gamma_A(f(y))\}$$
$$= min\{\gamma_A(f(x) * f(y)), \gamma_A(f(y))\}$$
$$\leq \gamma_A(f(x))$$
$$= \gamma_A^f(x)$$

$$max\{\mu_A^f(x), \mu_A^f(y)\} = max\{\mu_A(f(x)), \mu_A(f(y))\}$$
$$= max\{\mu_A(f(x) * f(y))\}$$
$$\geq \mu_A(f(x * y))$$

$$= \mu_A^f(x * y)$$

$$min\{\gamma_A^f(x), \gamma_A^f(y)\} = min\{\gamma_A(f(x)), \gamma_A(f(y))\}$$

$$\leq min\{\gamma_A(f(x) * f(y))\}$$

$$\leq \gamma_A(f(x * y))$$

$$= \gamma_A^f(x * y)$$

Hence (μ_A^f, γ_A^f) is an Intuitionistic Anti fuzzy BG-Ideal of X.

Theorem 9

Let $f: X \to Y$ be a epimorphism of BG-Algebra.If.Then $(\mu_A^f, \gamma_A^f) = A^f$ is an Intuitionistic Anti fuzzy BG-Ideal of X. then $A = (\mu_A, \gamma_A)$ is an Intuitionistic Anti fuzzy BG-Ideal of Y.

Proof:

Let $y \epsilon Y$, By hypothesis there exist $x \epsilon X$ such that $f(x) = y$,

then $\mu_A(y) = \mu_A(f(x))$

$$\geq \mu_A^f(x)$$

$$= \mu_A^f(0)$$

$$= \mu_A(f(0))$$

$$= \mu_A(0)$$

$$\mu_A(y) \geq \mu_A(0)$$

Similiarly $\gamma_A(y) \leq \gamma_A(0)$

Let $x, y \epsilon Y$, By hypothesis there exist $a, b \epsilon X$ such that $f(a) = x$ and $f(b) = y$.It follows that

$$\mu_A(x) = \mu_A(f(a))$$

$$= \mu_A^f(a)$$

$$\leq max\{\mu_A^f(a * b), \mu_A^f(b)\}$$

$$= max\{\mu_A(f(a * b)), \mu_A(f(b))\}$$

$$= max\{\mu_A(f(a) * f(b)), \mu_A(f(b))\}$$

$$= max\{\mu_A(x * y), \mu_A(y)\}$$

Similiarly, $\gamma_A(x) \geq min\{\gamma_A(x * y), \gamma_A(y)\}$

$$\mu_A(x * y) = \mu_A(f(a) * f(b))$$

$$= \mu_A(f(a * b))$$

$$= \mu_A^f(a * b)$$

$$\leq max\{\mu_A^f(a), \mu_A^f(b)\}$$

$$= max\{\mu_A(f(a)), \mu_A(f(b))\}$$

$$\leq max\{\mu_A(x), \mu_A(y)\}$$

$$\gamma_A(x * y) \geq min\{\gamma_A(x), \gamma_A(y)\}$$

Hence (μ_A, γ_A) is an Intuitionistic Anti fuzzy BG-Ideal of Y.

References

S. S. Ahn and H. D. Lee, Fuzzy Subalgebras of Bg-Algebras, Communication of the Korean Mathematical Society 19 (2004) 243-251.

K. T. Atanassov , On Intuitionistic Fuzzy Sets Theory, Published by SpringerVerlag Berlin Heidelberg, 2002. Journal of New Theory 27 (2019) 01-10 10

K. T. Atanassov, More on intuitionistic Fuzzy Sets, Fuzzy sets and systems 33(1) (1989) 37-45.

K. T. Atanassov, Intuitionistic Fuzzy Sets, VII ITKR's Session, Sofia,(Deposed in Central Sci. - Techn. Library of Bulg. Acad. of Sci., 1697/84) (1983)(in Bulg).

C. S. Hoo, Fuzzy ideals of BCI and Mv-algebras, fuzzy sets and system 62 (1994) 111-114.

Q. P. Hu and X. Li, On proper BCH-algebras, Mathematica JaponicaInternational Society for Mathematical Sciences Japonica 30 (1985) 659–661.

Q. P. Hu and X. Li, On BCH-algebras, Mathematics Seminar notes 11 (1983) 313-320.

K. Iseki, On BCI-algebras, Math. Seminar Notes 8 (1980) 125-130.

Y. B. Jun and K. H. Kim, Intuitionistic fuzzy ideals of BCK- algebras, International Journal of Mathematics and Mathematical Sciences 24(12) (2000) 839-849.

Y. B. Jun, E. H. Roh and H. S. Kim, On BH-algebras, Scientiae Mathematicae Japonicae Online1 (1998) 347-354.

K. H. Kim, Intuitionistic Fuzzy Ideals of Semigroups, Indian Journal of Pure and Appllied Mathematics Math. 33(4) (2002) 443-449.

C. B. Kim and H.S. Kim, On BG-algebras, Demonstratio Mathematica 41(3) 497-505.

J. Meng and Y. B. Jun, BCK-algebras, Kyung Moon Sa. Co., Seoul, (1994).

R.Muthuraj, M.Sridharan and P. M. Sitharselvam, Fuzzy BG-Ideals in BG-Algebra, International Journal of Computer Applications 2 (2010) 26-30.

Neggers and H. S. Kim, On B-algebras, Mathematiˇcki Vensik, 54 (2002) 21-29.

Neggers and H. S. Kim, On -d-Algebras, Mathematica Slovaca 49(1999) 19-26.

A. Rosenfield, Fuzzy Groups, J. Math. Anal. Appl. 35 (1971) 512-517.

M. W. Rysiawa, Anti Fuzzy filters of pseudo-BL-algebras, Commentations Mathematicae 51(2) (2011) 155-165.

T. Senapati, M. Bhowmik, M. Pal, Intuitionistic fuzzifications of ideals in BG-algebras, Mathematical Aeterna 2(9) (2012) 761-778.

L. A. Zadeh, Fuzzy sets, Inform. Control. 8 (1965) 338-353

DOMESTIC SOLID WASTE MANAGEMENT: A CASE STUDY AT DHANUVACHAPURAM

Dr. Gayathri Elayidam U

Assistant Professor in Zoology
VTM NSS College, Dhanuvachapuram

Introduction

In recent times, a closer observation would indicate that many regions have turned out to be garbage dumps that existed uncontaminated a few years ago. Over and above, growing consumption has led to increased production of waste in both rural and urban areas. Community wakefulness and fear of pollution in their locality prevented the local bodies to identify sites for waste disposal that are suited for public interest in most cities and towns in Kerala.

Greater than before waste levels would mount in a deteriorating state of nature's health that would also upset the well-being of organisms. This increasing waste level may be due to a lack of proper and efficient solid waste management besides awareness amongst the public. The environmental and public health risks that arise due to inadequate waste disposal have been well-documented (Schertenleib & Meyer, 1992). The re-emergence of certain infectious diseases like Dengue fever has been proven to be a result of poor solid waste management in some Latin American countries. In this case, the vector, *Aedes aegypti* mosquito, was found to breed in discarded artificial or plastic containers that can hold rainwater (Leontsini, 1995; Rigau-Perez et al, 1998).

Solid Waste is defined as any unwanted or discarded materials that arise from human activity and that are not free-flowing (WHO Expert Committee 1971). It can be either biodegradable or non-biodegradable. Waste formed in urban areas and rural areas or different seasons may be different in composition. Domestic-generated waste has become a severe concern in the management of any solid waste whether municipal or rural. Domestic waste will be the primary waste and most of the waste produced will fall into this category. It has become an important issue, particularly considering the delicate environment. The categorization of solid waste according to its physical and recyclable composition is the initial step necessary for the efficacious implementation of an integrated waste management system. It should ensure that the domestic waste produced is sorted into appropriate classifications before disposal. To achieve this, waste must be stored in separate containers depending on whether they are biodegradable, non-biodegradable or toxic

The rural milieu of Dhanuvachapuram propelled to embark on this survey on domestic solid waste management in its areas.

The objectives are

- to evaluate the quantity and composition of household solid waste
- to identify opportunities for waste recycling in detailed composition
- to examine the habit of households on recyclable waste discharge
- the household attitudes toward good waste management
- the household behaviours toward recycling activities

Materials and Methods

Two-stage survey of households was conducted for the dry season and rainy season. One member of each household who was within the age bracket of 18-74 years was selected to be interviewed. The questionnaire design consists of sections like Household Solid Waste Management; Concerns about Solid Waste Management; Willingness to Participate; Solid Waste Management Attitude Scale.

A survey with a face-to-face interview during the period of the waste generation survey was conducted to draw out the current household habits for waste discharge/storage activities and collection services at households and to identify the problems of the HSW management system. The household behaviours for recyclable waste discharge were also examined. Households were used to collect, store, and sell recyclable wastes, except for plastic packaging and bags; some recycling activities were implemented with high participation of households. The household attitudes toward good waste management and the household behaviours on recycling activities were evaluated. This study also analyzed relations between household behaviours and relevant factors such as education level, urbanization level, income, age, gender, and working status.

Results

The result found that significant correlations were mainly found for education level and urbanization level in all relevant factors. The effects of household attitudes and household behaviours on household solid waste generation in detailed composition were also considered. The household solid waste generation rate per capita per day was positively correlated with the population density and urbanization level.

Table1. Showing garbage disposal in rural areas of Dhanuvachapuram

Most of the respondents (40.0%) reported that most of their household garbage is piled in the yard, while some (25.88) store theirs in an open container, a few (17.64) in closed containers and others (16.88) stored in plastic bags. Burning constituted the major method of household garbage disposal by respondents (76.47%). Very few of the respondents made use of other methods such as composting, recycling, reuse, use of garbage trucks, etc.

	Burn	Bury	Dump	Recycle	Reuse	Compost	Others
Food waste	4.70%	18.29%	36.47%	-	-	11.76%	31.76%
Yard trimmings	76.47%	4.70%	16.47%	-	-	2.35%	1.17%
Paper/ cardboard	52.94%	-	-	47.05%	-	-	-
Plastic	61.17%	2.35%	10.58%	25.88%	-	-	-
Metal	-	-	10.58%	25.88%	-	-	-
Glass	-	21.17%	67.05%	11.76%	-	-	-

Fig 1. Graph showing means for storing household waste

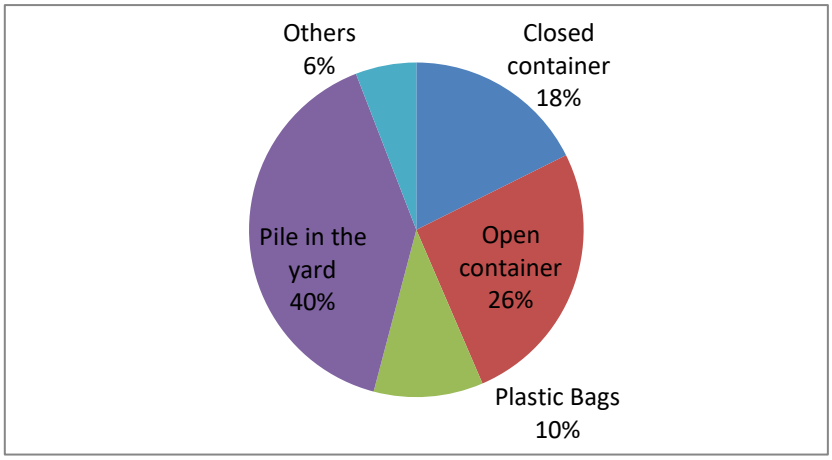

It is obvious that a great number of respondents (80%) are concerned about the current state of the natural environment but have a shallow knowledge of what constitutes the natural environment. A percentage of respondents (22.35%) considered cutting down trees to be the major issue that affects the environment. This was closely followed by household garbage (21.17%). Then come pesticides and herbicides (20%), factories (14.11%), dangerous solid waste (10.58%), automobile exhaust (10.5%), the person (8.23%), sewage pollution (3.52%), etc.

Fig 2. A major issue affecting the environment

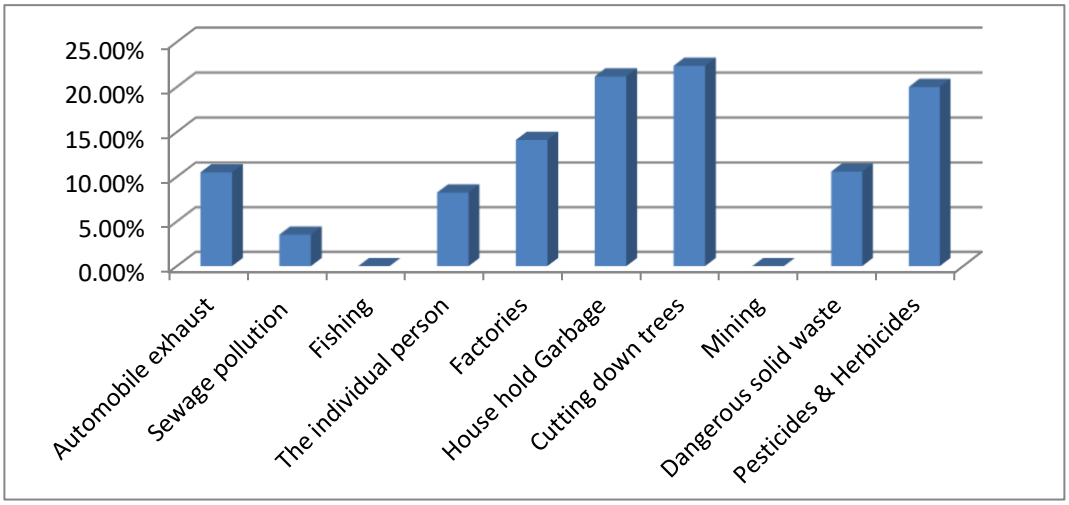

Generally, most respondents showed concern about issues of solid waste management. All respondents (100%) were concerned about diseases related to improper waste storage and disposal and only a few (11.76%) were not concerned about the health risk related to burning garbage.

Fig3. Graph showing how concerned the respondents are over various factors

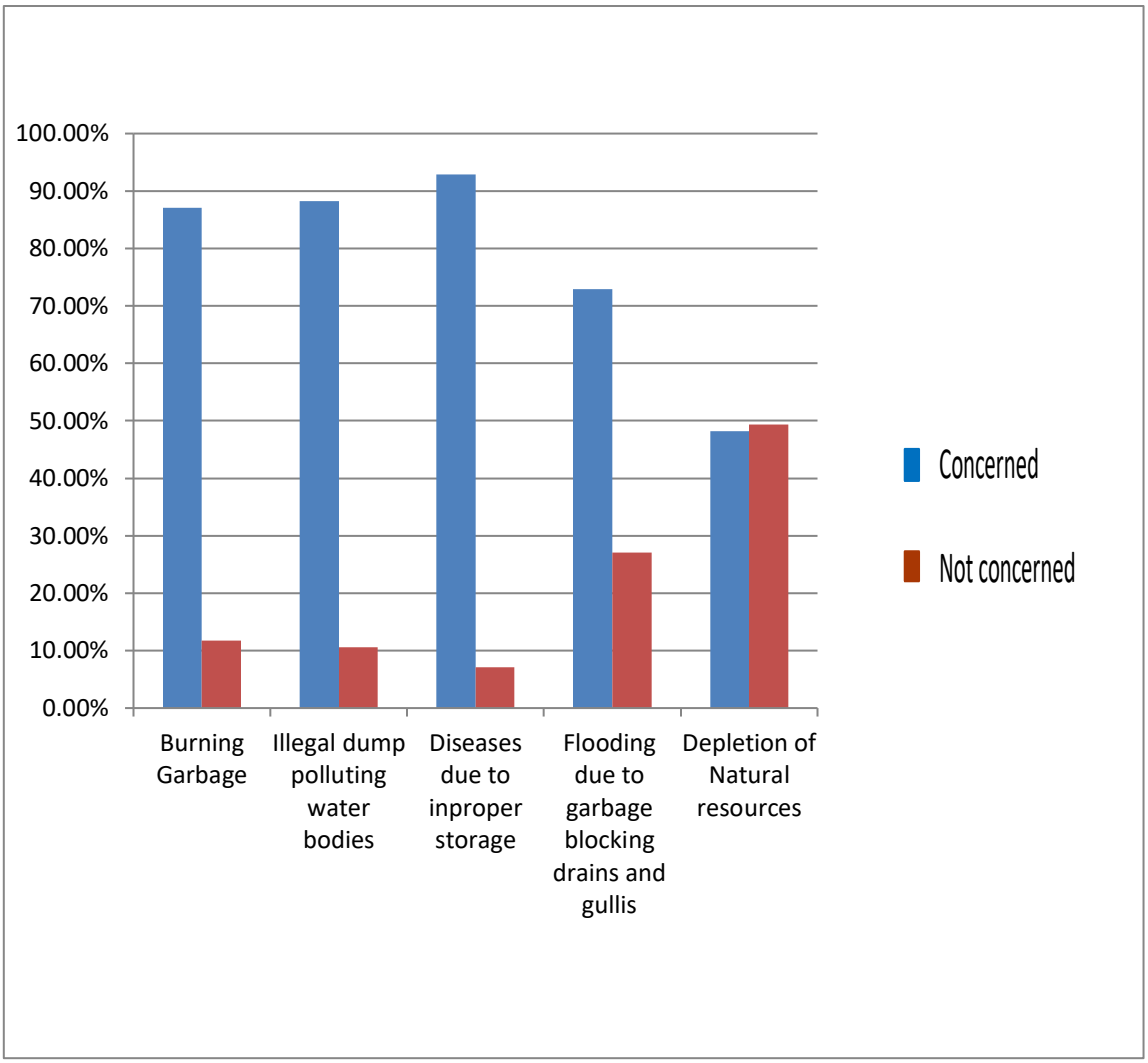

It is obvious that generally, a greater percentage of respondents are willing to participate in efforts aimed at reducing waste, recycling and composting household garbage and were willing to get more information on how to reduce garbage.

Table 2. Showing the degree of awareness among respondents

	Yes	No
Composting	97.64%	2.35%
Recycling	92.94%	7.05%
Willing to separate	90.58%	9.41%
Willing to pay	34.11%	65.88%
Willing to participate	81.17%	18.82%
Return the plastic bottles	56.47%	43.52%
Willing to purchase less	82.35%	16.47%
More information	63.52%	36.47%
Willing to carry to collecting center	82.35%	17.64%
Building the Community Skiff	74.11%	25.88%
Maintenance of the Skiff	74.11%	25.88%

Most respondents (63.52%) also agreed that environmental education should be taught in schools and that public education about proper garbage management is a way to fix the garbage crisis. Most of the respondents (87.05%) were against the burning of garbage.

Many of the respondents were willing to participate in recycling and composting programs if they were given adequate orientation. Some residents are already involved in composting and recycling (81.17%).

This survey has been able to indicate the current household solid waste management as a case study. The residents are generally concerned about the environment but are not doing enough to reduce, recycle and reuse the household garbage they generate. The natural environment requires protection to remain healthy for all of its inhabitants. Protecting and bringing about a healthy and sustainable environment requires the collective efforts of the public, the environmental health authorities, and the private sector. Let us all remember these three big words about 'waste': Reduce, Recycle, and Reuse**.**

The solid waste management program will also incorporate a public awareness program aimed at educating and sensitizing the importance of managing garbage. The main focus will be to ensure that proper ethics are conducted when it comes to throwing away the garbage. Most people are not aware of local solid waste management problems and how daily consumption and lifestyle patterns contribute to these problems. Asking people about their buyer preferences and waste disposal habits accomplishes three things: 1) Data can be collected to document consumer habits that contribute to waste disposal problems; 2) the people being interviewed focus their attention on the issue; and 3) the group conducting the survey becomes more aware of public attitudes toward waste and waste management.

References:

Golit (2001). Sustainable Cities and Benefits. *Regional Policy and Development, Series 9.* London*:* Mitshire Kingsley publishers.

MufeedSharholy, Kafeel Ahmad, GauharMahmood, R.C. Trivedi (2008). Municipal solid waste management in Indian cities – A review Waste Management Vol. 28 (2) 459–467

Neha Gupta, Krishna Kumar Yadav, Vinit Kumar (2015) A review on current status of municipal solid waste management in India Journal of Environmental Sciences 08/*2015*; DOI:10.1016/j.jes.2015.01.034

PhucThanhNguyen (2010). A study on evaluation methodologies for household solid waste management toward a sustainable society in Vietnam. Journal of Vietnamese environment http://ousar.lib.okayama-u.ac.jp/file/41448/K004242.pdf

Schertenleib, R., & Meyer, W. (1992).Municipal solid waste management in DC's: Problems and issues; need for future research. *IRCWD News (No. 26).*

DIVERSITY STUDY OF SOIL ARTHROPODS IN TWO DIFFERENT SITES - CHITHARA OILPALM PLANTATION AND KILIMANOOR RUBBER PLANTATION WITH SPECIAL REFERENCE TO COLLEMBOLA

Shibina A S, Arya S, Salini B S, Adhira M Nayar

Postgraduate Department of Zoology and Research Centre,
Mahatma Gandhi College Trivandrum

Abstract

The diversity of soil Arthropods special reference to collembola were studied for a period of six months from January 2022 to June 2022 in two selected sites. The selected sites include oilpalm plantation, Chithara and rubber plantation, Kilimanoor. From the study a total of 23 collembolans collected along with other soil organisms. There were 7different genus of collembolans which belonged to 2 orders and 4 families. Diversity and distribution of soil arthropods and collembolans in two sample sites also recorded. The physical and chemical parameters of soil such as soil pH, soil temperature, soil moisture, organic carbon, available nitrogen, available phosphorus, available potassium etc were analysed and recorded. The soil factors vary during the different months of the study. These also influence the diversity of collembola. The highest number of collembolans was collected from site A and order Entomobryomorpha has a dominance because high number of collembolans collected from this order. The soil factors have a main role in the diversity and distribution of collembolans. The other soil arthropods also collected along with collembolans. Collembolans are important soil arthropods. They involved in organic matter decomposition, nutrient cycling, biological regulations etc. They increase the soil fertility. Collembolans play an Important role in soil ecosystem.

Introduction

Biodiversity is the key factor of the structure and function of ecosystem (Lee, 1991 and Wall et al. 2005). Soil is extremely dynamic, complex and highly heterogenous system that allows the development of large number of ecological habitats, home of an array of live organisms and perform important functions for the ecosystem (Gardi and Jeffery, 2009). Soil is one of the most valuable resources on this planet. Soil is a living dynamic and critical point of the terrestrial ecosystem that supports several forms of life.

Soils are non-renewable natural resource vital for the productivity in the terrestrial environment (Lavelle, 1996). Also, soil is one of the most essential and diverse natural habitats of the biodiversity on earth. From the food we eat, to the clothes we wear, our existence is inextricably linked to the fate of our soils. Soil is a complex and fragile medium, an amalgamation of water, air, minerals and organic matter. About half of the volume of any soil consists of pore

spaces containing varying proportions of air and water, while the other half is principally the mineral component, comprised of weathered parent bedrock and deposited minerals.

The soil arthropods measuring up to 10mm in length can be considered as micro arthropods and considered to be members of soil mesofauna. Soil biota increases the surface area available for bacterial and fungal activities and converts humic substances to organic matter. Organic matter mixes with mineral part of soil and it forms the upper layer of soil. So micro arthropods play a role in soil maturation. The species interaction also performs vital functions in a soil system. Soil is considered as a living tissue and the seat of biological activities due to the presence of soil fauna. Soil biota perform numerous activities like mixing, mounting, forming voids, regulating soil erosion, regulating water movement and air in soil, regulating plant and animal litter, regulating nutrient cycling, etc. soil fauna is also used to provide soil quality indicators. Soil fauna (micro fauna – protozoa, bacteria, meso fauna – Acarina, symphyla, collembola, Diplura and macro fauna – chilapoda, Coleoptera, Orthoptera, Hymenoptera) interactions perform vital functions in number of biological processes. The most abundant of soil meso fauna are Acari and Collembola, which together constitute 72 to 97% of total arthropod fauna of Indian soils (Wall work, 1976).

The distribution of micro arthropods can be influenced by soil moisture percentage, pore space, oxygen saturation deficits, temperature variations, floods, cropping cultivation, organic matter percentage, litter, nematode populations, man and animal disturbances, soil type, and texture, predation and feeding habitats among others (Christiansen, 1970; Rahim, 2008). Soil temperature, soil moisture, nutrient concentration was important in variation in number and community composition of micro arthropods (Tousignant and Coderre, 1992). The physiochemical factors of soil such as temperature, moisture, P^H, and compaction which change from layer to layer in soil leads to vertical stratifications and changes the vertical distribution of soil fauna (Bardgett, 2005). The temperature and moisture content of soil, rainfall showed significant positive correlation with total soil micro arthropod population i.e., the edaphic and climatic factors affect the dynamics of micro arthropods.

Any land uses affect the soil fauna. The degradation of soil biota reduces the soil biodiversity. The soil arthropods play vital role in soil biodiversity. These are play their important roles in soil formation, nutrient cycles and maintaining soil fertility (Edwards et al.). The soil arthropods mainly include the insects such as springtails, beetles, ants, crustaceans such as sowbugs, Arachnids such as spiders and mites, myriapods such as centipedes and millipedes and scorpions. These are very important functioning of an ecosystem and perform different functions.

Collembola,commonly known as springtails, are small and primitively wingless insects (Lubbock, 1873). Collembola belong to the subclass Apterygota represents one of the two subclass of insects and consists of four orders – Collembola (springtails), Diplura, Proturan and Thysanura (silver fish or bristle tails). They are the smallest, but most successful animals. They are very tiny and abundant animals in the world. Most of the Collembolans are only few millimeters long. They are minute insects. The body is distinctly divided into head, thorax, abdomen. The head bears a pair of four segmental antenna, ecto – gnathus mouthparts within a pouch and one to several pairs of lateral ocelli form an eye patch. Springtails are the one of the significant soils mesofauna (Singh and Singh, 1975). They have very wide global distribution.

They are present in every habitat and continent including Antarctica (Block, 1884) and high altitude of Himalayas (Yossi, 1966). They are found in vast numbers in almost all habitats from seashore to top of mountains (Fjellberg, 1998). Their diversity is very notable and constitutes the second highest mesofauna after Acarina (Yadav and Singh, 2009). Collembolans are most important groups in soil mesofauna, mainly because of their importance in soil genesis, dynamics and evolution (Palacias – Vargas, 1985). They feed on organic matters consequently influence the process of decomposition and mineralization (Culik and Filho, 2003). Hence, they play their role in pedo – ecosystems (Palacios – Vargas, 1985). The majority of springtails are carnivores and eat nematodes, rotifers and even others springtails also. They are ideal bioindicators (Stork and Eggleton, 1992 and Zeppelini et al.,2009). Collembola have significant influences on soil microbial ecology and fertility and thus through influence on microorganisms, decomposition and nutrient cycling (Culik and Filho, 2003). These are the major organisms in soil fauna, through plant litter decomposition they forming soil micro structure. They are the hosts of many parasitic protozoa, Nematoda, Trematoda and pathogenic bacteria and in turn are attacked by different predators.

More than 6500 species of Collembola are known throughout the world and these are only a small part of the still undescribed species. Collembolans are the most important microarthropods in the soil. They involved in different process such as decomposition of organic matter, nutrient cycling, biological regulation, soil structure, etc. Springtails play very vital role in soil ecosystem.This study focuses on the;

Diversity of soil arthropods collected from two different ecosystem with special reference to order collembola.

Analysis of physical and chemical factors that affect the distribution of collembolans.

Materials And Methods

Study Area

The project was conducted on 2 different sites; oil plantation, Chithara and rubber plantation, Kilimanoor. Chithara oil plantation is a large agricultural land. The total area is 1615.70Ha, comprising of four divisions planted with both imported and indigenous material from Thodupuzha developed by CPCRI Regional Station, Palod. The total population of palm is 213396. Chithara oil palm area has oil temperature range between 30 – 32℃ during day and 23 – 24℃ during night. The relative humidity is about 86%.

The rubber plantation taken for project study located at Malayamadom, near Kilimanoor town. The total area of rubber plantation is about 5 acres contain 1500 rubber trees. The area has a minimum temperature of 25℃ during night and a maximum of 34℃ during day with a relative humidity of 82%. From the two different sites the sample were collected in the month from January 2022 to June 2022.

Site A: The first site was oil palm Chithara, lying at coordinates 8.8264°N, 76.9177°E. The soil sample is collected in a polythene cover.

Site B: The second site was rubber plantation at Kilimanoor lying at coordinates 8.7701°N, 76.8808°E.

All the samples were collected in polythene bags. The samples required for nutrient analysis was collected using V method.

1. **Faunal Sampling**

The soil was collected from two different sites by digging out the land. Soil sample was taken in polythene bags. For nutrient analysis the soil taken separately using V method. The soil organisms were collected using different methods like hand picking, using Berlese funnel and aspirator, etc. The equipments and materials used include brush, needle, forceps, Berlese funnel, aspirator, alcohol etc.

2. **Physicochemical parameters of soil:**

The soil temperature was determined by using thermometer at a depth of 5 cms.Soil moisture was determined by Oven – Dry method. A soil suspension was prepared in a beaker, one part of the soil was mixed with five parts of distilled water and shaken well, and allowed to rest for 1 hour. P^H of this solution were recorded using digital pH meter.

Organic carbon content of soil was determined by Rapid titration method (Blackley, 1939). Available phosphorus is commonly extracted using (Bray and Kurtz, 1945). The available potassium in soil is extracted and was determined using flame photometer. Available nitrogen in soil is determined by Alkaline permanganate method.

Observations and Results

From the study a total of 42 arthropods were collected from two study sites. Out of these 23 individuals were collembolans. The soil arthropod population showed changes from January to June and from one site to other during the study period. The highest number of soil arthropods collected from oil palm plantation at January and least number of arthropods collected during March. In total 23collembolans collected, there were 8different genus of collembolans which belonged to two orders and four families.

Site A contained 25 individuals in which 16 were collembolans. Site B contained 17 individuals in which 7were collembolans. Site A has the highest number of collembolans Out of these 23collembolans family Entomobryidea had highest number of individuals followed by isotomidae and paronellidae within the order Entomobryomorpha, majority belonged to family Entomobryidea. The second dominant order was poduromorpha.

The two study sites, soil factors show variations during the different months of the study period. The different factors such as soil temperature, soil pH, soil moisture, organic carbon, available nitrogen, available phosphorus, available potassium etc. Were analyzed and recorded. Site A (oil palm plantation) and site B (rubber plantation) had a temperature range 28-32 degree Celsius. Site A had an optimum range of pH of 6.4. In site B had soil pH of 4.6. The moisture content of the soil of two sites shows wide variations. The highest number of collembolans are seen in moderate moisture content.

The highest number of collembolans was collected from site A and lower number from site B. The highest number of collembolans collected belongs to order Entamobryomorpha.The other soil organisms also obtained from the study sites such as isopods, ants, earthworm, spider, diptura, mite, beetle, millipedes, termites, centipeds, etc.

Site B had highest moisture content compared to site A. So, site B had lower number of collembolans. The soil collected from site A had high organic carbon content, available nitrogen, available phosphorus, available potassium and had an optimum moisture content and temperature. So high number of collembolans are collected from siteA.

PLATE – I

Family Entomobryidea

Lepidocyrtus

Lepidocyrtoides

Willowsia

PLATE – II

Dicranorchesella

Family Isotomidae

Isotomiella

PLATE – III

Family paronellidae

Salina

Family Neanuridae

Bilobella

Diversity and distribution of soil arthropods and collembolans in different sampling site.

Sampling site	Number of arthropods collected	Number of other arthropods collected	Number of collembola collected
Site A	25	9	16
Site B	17	10	7

GRAPH

Graph showing the comparison of diversity of collembolans and other soil arthropods from two sampling sites.

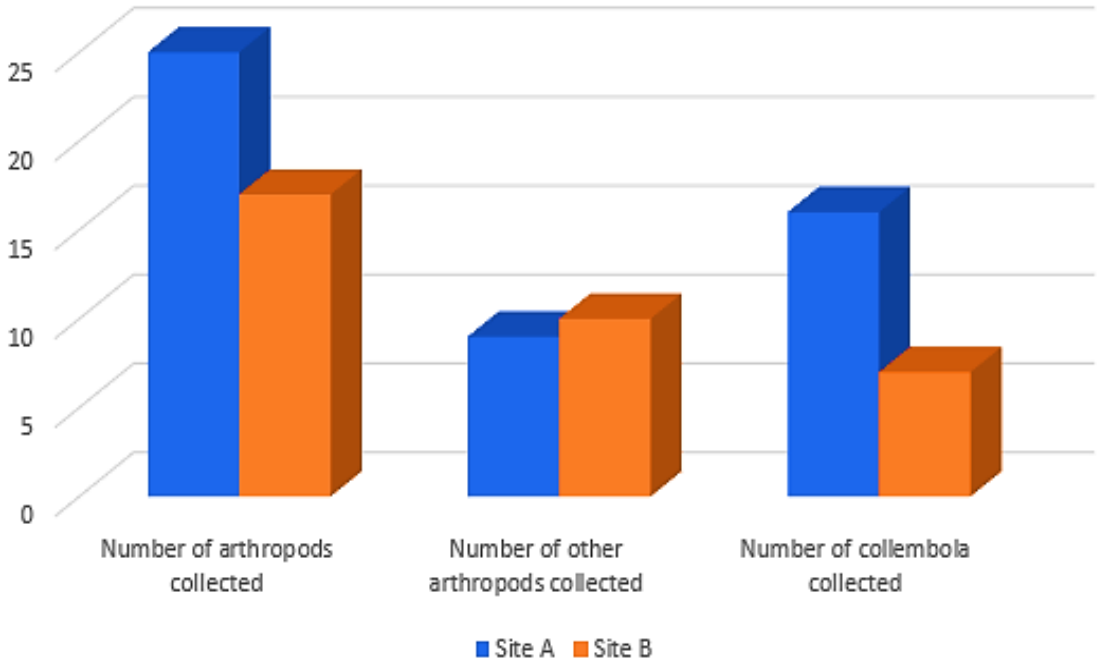

Order wise distribution of collembolans

Collembolan orders	Number of organisms from each order	
	Site A	Site B
Order Poduromorpha	6	2
Order Entomobryomorpha	10	5
Order Symphypleona	0	0
Order Neelipleona	0	0

Pie diagram showing order wise distribution of collembolans

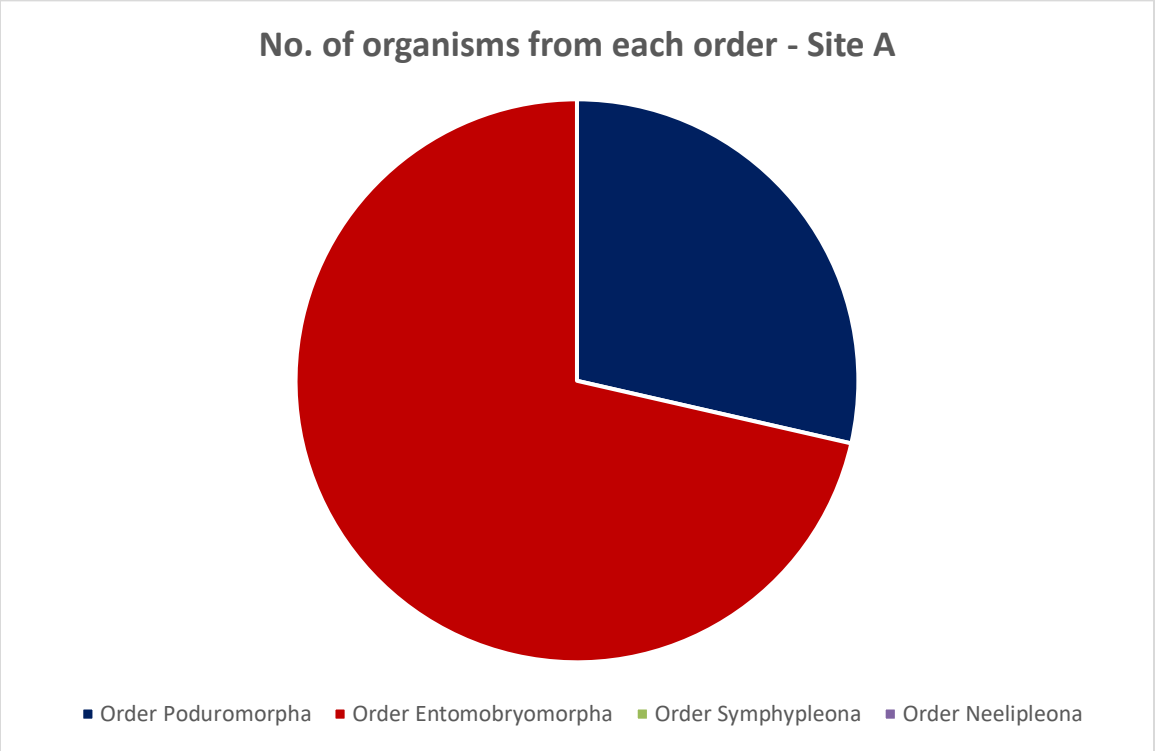

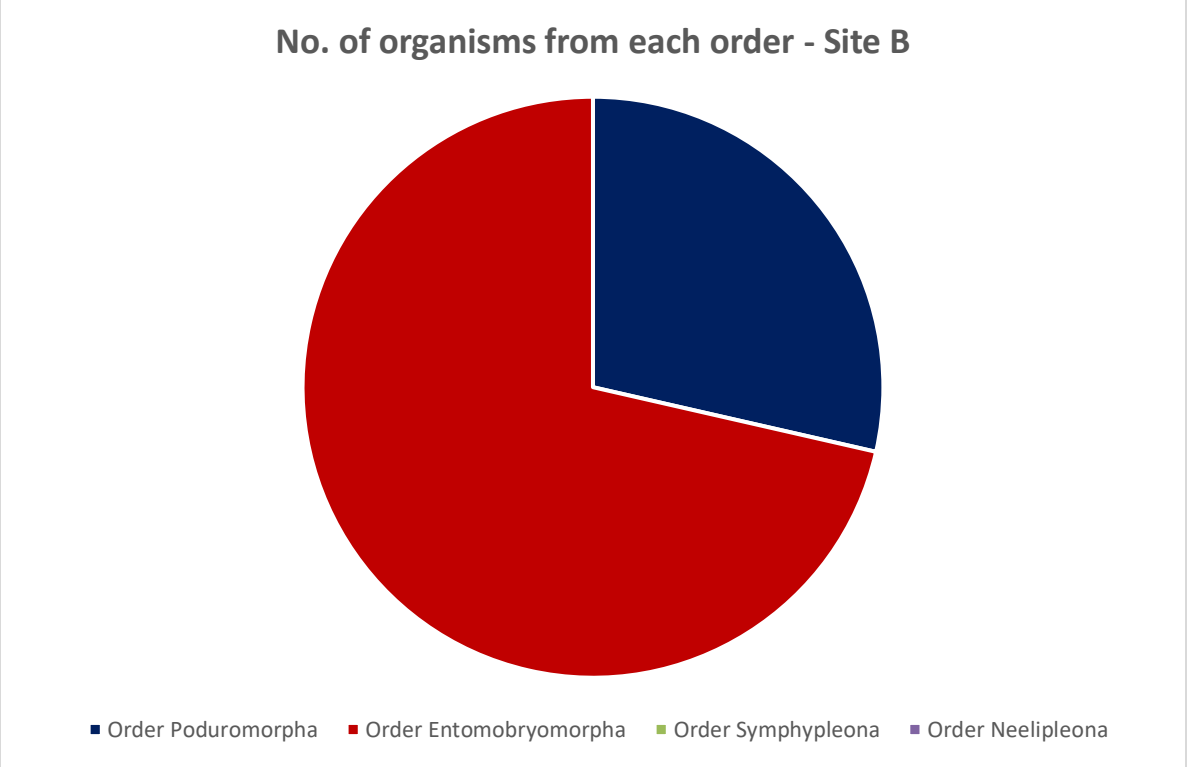

Physical and chemical parameters of soil sample taken from different sites

Sampling site	Month	Soil temperature (°C)	Soil moisture (%)	Soil P^H	Organic carbon (g/Kg)	Available phosphorus (Kg/ha)	Available nitrogen (Kg/ha)	Available potassium (Kg/ha)
Site A	Jan	28	7.426	6.0	7.01	15.85	314.44	172.6
	Feb	29	7.135	5.9	7.12	14.93	317.92	168.82
	Mar	31	6.811	6.2	6.98	14.89	318.56	171.47
	Apr	30	6.896	6.5	6.64	15.76	320.2	169.08
	May	30	6.957	7.1	6.27	15.02	313.04	169.11
	June	29	7.235	6.8	7.25	14.85	313.6	170.24
Site B	Jan	29	12.985	4.1	1.55	11.97	270.21	99.53
	Feb	30	12.826	4.5	1.82	12.31	269.7	100.16
	Mar	32	10.926	4.8	1.48	11.83	264.51	102.46
	Apr	31	10.983	4.7	0.97	11.94	266.59	98.85
	May	30	11.335	5.1	1.09	12.96	271.01	100.74
	June	30	13.246	5.4	1.52	12.83	266.56	100.8

Discussion

From the study, the physical and chemical parameters of the soil highly influence the diversity collembolans. The high number of collembolans are collected from site A oil palm plantation. The pH level of the soil in the site A was 6.45 and higher value of organic carbon, available nitrogen, available phosphorus, available potassium compared to the site B. Site B was a rubber plantation has lower number of collembolans. The soil pH in site B was 4.6 and had a high level of moisture content. The different factors such as soil temperature, soil pH, organic carbon, available nitrogen, available phosphorus, available potassium etc. were analysed.

Site A had an optimum pH and site B has the soil pH of 4.6. In this study pH of the soil has no influence on the collembolan diversity. The studies of Ghosh and Roy (2005), Bhagawati et al. (2008) also reported that pH did not exhibit any direct influence on collembolan diversity. Soil moisture content also affect the collembolans, they greatly seen in soil with moderate moisture content. The site B had a higher moisture content compared to Site A and lower number of collembolans. The high number of collembolans are observed in site A with a optimum level of soil moisture content. It clearly reveals that soil moisture content highly influence the collembolan diversity... There is a negative correlation between the collembolan diversity and soil moisture. Battacharya and Ray Choudhuri (1979), Hazra (1978) also reported that soil

moisture acted as pivotal factors for growth and development of collembolans. The maximum diversity of collembolans was observed during January and least in March, where the temperature was high the soil temperature shows a negative correlation with arthropod population.

Different physicochemical properties revealed strong significant positive correlation of collembolan diversity. The organic carbon (%) exhibits a strong positive correlation with soil arthropod population. The significant increase in collembolan population due to sudden increase of soil organic matter has also been studied earlier Hazra and Battacharya,2003., Ghosh and Roy ,2005, Santos et al., (2018) which might be due to decomposition and conversion of available leaf or other litters to organic matter in the soil which served as a source sufficient food and provide a healthy ecological niche for many arthropods. Dhillon and Gibson also made similar studies and reported that higher concentration of organic matter and availability of sufficient amount of moisture content influence the growth and survival of collembolans. The chemical parameters such as available nitrogen, available phosphorus and available potassium also influence the collembolan diversity. But the constant use of chemical pesticides, insecticide and fertilizers negatively affect the soil organisms. So, this leads to decrease the number of soil organisms. The physical and chemical parameters of soil such as soil moisture, soil pH, soil temperature, organic carbon, available nitrogen, available phosphorus, available potassium etc played pivotal roles in controlling the diversity of collembolans.

A total of 42 soil arthropods were collected in which 23 collembolans belonged to 2 order and 4 families. Large number of collembolans were collected belonged to order Entomobryomorpha. In this order Entomobryidea family contain high number of individuals.

The individuals in order Entomobryomorpha were present in two study sites. Order symphypleona and Neelipleona was not collected from the two sites. Other soil arthropods also collected from the study sites. From the study it is clear that an optimum temperature and moisture content positively affect the collembolan diversity. The high organic content in the soil has also influence the diversity of collembolans

References

Abbas, M.J. and H. Parwez (2012) Impact of adaphic factors on the diversity of soil microarthropods in an agricultural ecosystem at Aligrah. Indian J. Fund.Appl. Life. Life Sci.2:185-191.

Ashrof, M. (1971) Influence of environmental factors on collembolan.Rev.Ecol. Biol.sol.,8(2):231-252.

Badejio, M.A and Van straallen, N.M. (1993). Seasonal abundance of springtails in two contrasting environment.

Hazra, A.K and Mandal, G.P. (2007) Pictorial Handbook on Indian collembolan.

Hazra, A.K. Ecology of collembola in deciduous forest floor of Birbhum district, West Bengal in relation to soil moisture.

Hopkins, S.P: Biology of the springtails (Insecta: Collembola).

Imms, A. D. (1912) on some collembola from India, Burma and Ceylon with catalogue of the Oriental species of order. Proc.Zool. Soc.Lond;82.

Kaneda, S., Kaneko, N., (2008) Collembolan feeding on soil affect carbon and nitrogen mineralization by their influence on microbial and nematode activities. Biol.fertility soils.

Mandal G P, Hazra A K. (2009) The diversity of collembola (Hexapoda) from East and North East India with some notes of their Ecology. Record of zoological survey of India.

Mandal, G P. Checklist of Indian collembola,2010. (Insecta: Apterygota). http://zsi.gov.in /checklist/collembola.pdf 2010.

Mandal, GP., Suman, K.K. Studies on diversity and distribution of soil Microarthropods fauna with special reference to collembola in sajnekhali wildlife sanctuary, south 24 PGS, WestBengal.Rec. Zool.Surv. India.2014.

Mitra SK. Studies on the genus Dicranocentroides. Imms,1912 (collembola: Entomobryidea: paronellidae) from India.

Nijima, K. (1971). Seasonal changes in the collembolan populations in a warm temperate forest of Japan.

Parisi V., Menta C., Gardi C., Jacomini C., Mozzanica E (2005) Microarthropod communities as a tool to assess soil quality and Biodiversity

Prabhoo N.R (1971) Bark and moss inhabiting collembola of South India.

Prabhoo N.R(1971) soil and litter collembola of South India.

Prabhoo, N.R (1976) soil Microarthropods of virgin forest and adjoining tea field in the western Ghats in Kerala.

Prabhoo NR. Soil and litter collembola of South India.

Raghuraman M., Yadhav R S., Singh J. (2010) Biodiversity of collembola at Varanasi.

Rusek J. (1998) Biodiversity of collembolan and their functional role in the ecosystem.

Verma D, Paliwal A K (2010) Effects of springtails community on plant growth. Biol Forum Int J 2(2):70-72.

Wallwork J.A. (1976) The distribution and diversity of soil fauna.

Yadav RS., Singh J. (2009) Biodiversity of soil arthropods under Mango (Mangifera indica L.) orchard ecosystem in Varanasi, Ranchi, Jharkhand. Environment and ecology.

Yadav RS. (2017) First records of collembola and their diversity measurement from BAU Ranchi, Jharkhand. Journal of Entomology and zoology studies.

Yosii R. (1966) Collembola of Himalaya: journals of college of arts and science, Chiba University.

PHYTOCHEMICAL INVESTIGATION AND IN VITRO CONSERVATION OF HIBISCUS HISPIDISSIMUS GRIFF. -AN ETHNOMEDICINAL PLANT OF KERALA.

Pradeesh S[1*], Archa J [2] and Aswathi Krishna K. U.[3]

***PG and Research, Department of Botany, Mahatma Gandhi College, Kesavadasapuram,**

Thiruvananthapuram - 695 011.

Corresponding author – Ph. 7994625618, email – *pradeeshnair10@gmail.com*

Abstract

Plants are the primary resource upon which animals including human race depend on their nutritional and energy requirements. Bio-prospectors in search of chemical constituents in production of curative substances or drugs often find plants as the potential source. Phytochemicals comprising primary and secondary plant metabolites play key role in curative properties attributed to a particular plant. Hibiscus hispidissimus Griff. of the family Malvaceae is a wild species of Hibiscus used by tribal people of Kerala for treating various diseases and for culinary purpose in other countries. Present study aimed to conduct phytochemical, nutritional, antioxidant and anticancer analysis in fresh sample and methanolic extract of leaves and in vitro conservation of Hibiscus hispidissimus. The plant exhibits sufficient characteristics related to claims of its therapeutic properties. Crude methanolic leaf extract is used for preliminary phytochemical analysis. Phytochemicals such as reducing sugar, flavonoids, alkaloids, tannins, terpenoids, steroids, saponins and anthraquinones were qualitatively analyzed. Phytochemicals detected in the study can have direct or indirect effect on properties attributed to the plant. Quantitative phytochemical analysis showed higher amount of total carbohydrate, total proteins in addition to considerable amount of reducing sugar, starch and pigments like chlorophyll-a and chlorophyll-b. Total polyphenol and superoxide dismutases were present in higher amounts, satisfying its use as potential source of antioxidants. Anticancer analysis of crude methanolic leaf extract in EAC (Ehrlich's Ascites carcinoma) and DLA (Dalton's Lymphoma Ascites) showed higher cytotoxicity in EAC compared to DLA against standard revealing promising anticancer effects of the leaf extract. In vitro conservation of different explants on MS (Murashige and Skoog) medium supplemented 2 mg/L BAP (Benzyl amino purine) showed bare survival capacity of nodal explant with axillary bud. Present study evaluated various nutritional, medicinal and regenerative aspects of the plant H. hispidissimus, exhibiting diverse potentialities of the plant and provide supporting information for its use as an ethnomedicinal plant.

Keywords: *Hibiscus hispidissimus*, Malvaceae, EAC, BAP, DLA and *in vitro* conservation.

Introduction

Plants have established its relevance in nutritional, medicinal as well as therapeutic aspects of human life. The secondary metabolites of plants serve as defense mechanisms against predation by many microorganisms, insects and herbivores (Maitra, 2015) and are also found to be therapeutically active. According to WHO, around 21,000 plant species have the potential for being used as medicinal plants. Consuming of diets which are rich in fruits, greens and vegetables can reduce risk of heart disease, stroke and cancer (Gaziano, 1999). Plants have efficient enzymatic and non-enzymatic antioxidant defense systems to avoid toxic effects of free radicals. Enzymatic antioxidants include superoxide dismutase (SOD), glutathione peroxidase (GPx) and catalase (CAT) that are active within the cells to remove free radicals such as super oxides and peroxides (POD) before formation of free radicals in combination of metal ions. About 13 million people get affected by cancer every year and approximately 60% people die in the developing countries due to cancer (Jemal *et al*., 2011). Phytochemicals such as tannins and saponins in pulses also have anticarcinogenic effects (Mudryj *et al*., 2014). *In vitro* tissue culture is an effective tool for the production of bioactive compound because the amount of secondary metabolites produced in this technique can be higher than those produced by parent plants in addition to production of new compounds (Rao *et al*., 2002).

Hibiscus hispidissimus belonging to the family Malvaceae is a climber commonly found in hotter regions of South Asian subcontinent comprising India and Sri Lanka. Its roots, infused in water, make a cooling drink during hot climatic conditions. The whole plant, roots, leaves, tender leaves and fruits are used in treatments for various ailments such as fever, ulcers, pustules, cysts, abscess, gangrene, oedema, inflammation, orthopaedic disorders, fractures, snake bites, filarial oedema and urinary tract related diseases. However, no much scientific validation has been made for this species for its medicinal uses. To address this lacuna, the present study was carried out for qualitative phytochemical analysis, evaluation of anticancer property of the crude methanol extract in DLA and EAC cell line and *in vitr*o conservation of plant. In future *H. hispidissimus* is important natural source of developing new drugs. So have select the present plant for this study.

Materials and Methods

Collection and Preparation of Sample for Phytochemical Analysis

The plant *Hibiscus hispidissimus* were collected as fresh from Pachamala, Thiruvananthapuram district of Kerala. For sample preparation, fresh leaves were separated, shade dried, ground well using mechanical blender to fine powder and transferred into air tight containers for further analysis.

Preparation of Plant Extract

The dried plant materials were extracted with methanol for 8 hours by soxhelt apparatus and extract obtained as green, black solid respectively. After which, the residues were transferred to pre-weighted sample container for storage and later used for phytochemical screening. The

different phytochemicals like reducing sugar, flavonoids, alkaloids, tannins, terpenoids, steroids, saponins and anthraquinones were tested.

Extraction from Plant Parts

The fine powder was used for extraction by methanol solvent. Fifty grams of sample powder kept into the soxhlet apparatus for distillation. Methanol was taken in the round bottom flask. The apparatus was kept over heating mantle and heated for 8 hours at 70°C. After completing the process, extract was collected in a beaker and was kept in oven at 37°C-40°C. The crude concentrated extract was again weighted and used for further biochemical analysis and anticancer analysis by using DLA and EAC cell lines.

Phytochemical Screening

Phytochemical analysis of plant extract was done as described by Harborne (Harborne,1977). The different phytochemicals like reducing sugar, flavonoids, alkaloids, tannins, terpenoids, steroids, saponins and anthraquinones were tested.

Biochemical analysis

The fresh leaves of *Hibiscus hispidissimus* were used for the nutritional and antioxidant analysis and experiment was repeated thrice to confirm the result. The analysis was preformed following standard methods for estimation of reducing sugar (Miller, 1972), total carbohydrate (Hedge and Hofreiter, 1962), total protein (Lowry *et al*., 1951), chlorophyll (Witham *et al*., 1971). starch (Thayumanavan and Sadasivam, 1984) and antioxidant like proline (Bates *et al*., 1973), lycopene (Zakaria *et al*.,1979), carotenoids (Bendich and Olson, 1989), total polyphenol (Eom *et al*., 2008), polyphenol oxidase (Esterbauer *et al*.,1991) superoxide dismutase (Gong *et al., 2005*) and Lipid peroxide (Ewa, 2006).

Result and Discussion

Fresh leaves of *Hibiscus hispidissimus* were studied for its nutritional and antioxidant properties. Crude methanolic leaf extract were used for the preliminary phytochemical investigation and *in vitro* anticancer analysis. The different explants of the plant were used to carry out *in vitro* conservation.

Table 1: Preliminary Phytochemical Evaluation of *H. hispidissimus*

Sl No:	Phytochemicals	Methanol extract of *H. hispidissimus*
1	Reducing sugar	+++
2	Flavonoids	+++
3	Alkaloids	+
4	Tannins	++
5	Terpenoids	+++
6	Steroids	+
7	Saponins	++
8	Anthraquinones	-

Preliminary phytochemical analysis of methanolic leaf extract of *H. hispidissimus* showed presence of reducing sugar, flavonoids, alkaloids, tannins, terpenoids, steroids and saponins. Anthraquinones were not detected (Table.1).

Quantitative Analysis

Nutritional Evaluation

The roots, leaves and the whole plant of *H. hispidissimus* were used by ancient Sri Lankans for culinary purposes including preparation of herbal gruel, drinks, mallow (a dish with mixture of vegetables), salad and curry (Gunatilaka *et al*., 2013). Reducing sugar plays an important role in the central metabolic pathways and help in the production of secondary metabolites that enhance the medicinal properties of plants (Deepa and Sumit, 2020). Reducing sugar from the aerial plant parts were extracted and analysed by Dinitrosalycylic acid method and the results were found to be high (0.986 mg g-1) as shown in Fig. 1. Carbohydrates are macronutrients present in plants that forms major constituents of human diet that can be metabolized to yield energy (Pradeesh and Praveena, 2020). The amount of carbohydrate in *H. hispidissimus* was found to be higher (27.508 mg g -1) as shown in Fig. 2. Proteins are highly complex substance that is present in all living organisms. Proteins are of great nutritional value and are directly involved in the chemical processes essential for life (Pradeesh and Praveena, 2020). Estimation of protein from the leaves of *H. hispidissimus* was done by Lowry's method and the result was found to be higher (30.816 mg g-1) as shown in Fig. 2. Chlorophyll is the natural pigment molecule widely distributed in photosynthetic plants, algae and cyanobacteria. It has a similar structure to hemoglobin molecule with presence of porphyrin ring but with a central atom of magnesium instead of iron. It plays crucialrole in photosynthesis. Dietary chlorophyll derivative has the ability to scavenge long lived free radicals such as DPPH and ABTS (Mishra *et al*., 2011). The estimation of Chlorophyll in *H. hispidissimus* was carried out using Arnon's method with a result of high content of chlorophyll-a (0.89 mg g-1), chlorophyll-b (0.817 mg g-1) and total chlorophyll (1.621 mg g-1) as shown in in Fig. 3. Starch is the reserve food material of plants which serve as storage of energy and carbon source. Commercial productionof starch can be done by degradation of starch. It is used as thickening agents in sauces and as colloidal stabilizers in salad dressings (Manthey and Xu, 2009). The amount of starch in *H. hispidissimus* was found to be higher (0.791 mg g-1) as shown in Fig. 4. The nutritional analysis of leaves of *H. hispidissimus* showed the presence of high amount of reducing sugar, carbohydrate, protein, chlorophyll-a, chlorophyll-b, total chlorophyll and starch.

Evaluation of Antioxidant Properties

Evaluation of enzymatic and non-enzymatic antioxidants in *H. hispidissimus* can help in understand the therapeutic potential of the plant in terms of its antioxidant properties. Present study evaluated non-enzymatic antioxidants like proline, lycopene, carotenoids and polyphenols and enzymatic antioxidants such as superoxide dismutases (SOD), polyphenol oxidase (PPO), amylase and lipid peroxidase (LPX) by standard estimation methods. Proline is an amino acid

molecule that plays important role in physiological as well ascellular processes (cell proliferation, cell death and gene expression) in plants. Since it can actas signaling molecule, proline catabolism in mitochondria is linked to oxidative respiration andit gives out energy for growth resumed after stress (Szabados and Arnould, 2010). The amount of proline in *H. hispidissimus* was estimated (0.526 mg g-1) and is shown in Fig. 5. Lycopene comprises the most important class of carotenoids which at physiological concentration have the potential to act against cancerous cells and its proliferation. It interfereswith growth factor receptor signaling and cell cycle progression in prostate cancer cells withouttoxic effects and cell apoptosis (David and Lu, 2002). The estimated amount of lycopene in methanolic leaf extract of *H. hispidissimus* (0.418 mg g-1) is shown in Fig. 5. Carotenoids are widely distributed lipophilic pigment molecules with antioxidant property. They act as antenna molecules in capturing light and in transfer of energy to chlorophyll molecules during photosynthesis. The estimated amount of carotenoids in *H. hispidissimus* is 0.416 mg g-1 as shown in Fig. 5. Polyphenols are bioactive molecule broadly divided into two classes (flavonoids and phenolic acids). The phytochemical estimation revealed that the total polyphenol content in *H. hispidissimus* is 0.991 mg g-1 as shown in Fig. 5.

Superoxide dismutase (SOD) are metalloenzymes catalyzing dismutation or reaction of superoxide radicals. Intracellular SOD may play key role protection of cancer cells against reactive oxygen species generated by anticancer drugs and radiation (Shingo *et al*., 1994). The amount of superoxide dismutases in *H. hispidissimus* is 1.992 mg g-1 as shown in Fig. 6. Polyphenol oxidases (PPO) mediated reactions play important role in alteration of colour, flavor, texture and nutritional values of fruit and vegetable crops. PPO plays a major role in the development of brown pigments in plants. It is also responsible for the functions including defense, cell differentiation and somatic embryogenesis (Constabel and Barbehenn, 2008). The estimated amount of enzymatic antioxidant polyphenol oxidase in *H. hispidissimus* is 0.972 mg g-1 as shown in Fig. 6. Amylase play important role in inducing growth of embryo by the breakdown of starch to sugar in the seeds (Pradeesh and Swapna, 2018). The estimated amount of enzymatic antioxidant amylases in *H. hispidissimus* is 0.986 mg g-1 as shown in Fig. 6. Free radicals such as H_2O_2 attacks unsaturated fatty acids producing lipid hydroperoxides and further occurrence of chain reactions changes lipid structure and organization of cell membrane in the process of lipid peroxidation. Peroxidase enzymes (stress enzymes) are haeme-containing enzymes that can oxidize various substrates using H_2O_2 that prevent its accumulation under metabolism during stress conditions thereby preventing lipid peroxidation (Pradeesh and Swapna, 2018). The result revealed that the amount of enzymatic antioxidant lipoperoxide in *H. hispidissimus* is 0.981 mg g-1 as shown in Fig. 6.

Plants have been used for medicinal purposes since the beginning of human history and are the basis of modern medicine. Most chemotherapeutic drugs for cancer treatment are molecules identified and isolated from plants or their synthetic derivatives. Many compounds isolated from plants are being vigorously tested for their anticancer properties and that showed specificity towards cancer cells. They can induce cell death and inhibit the growth of tumors (Michal *et al*., 2014). Present study evaluated *in vitro* anticancer activity of *H. hispidissimus* leaf methanolic extract. Anticancer effect was analysed using Dalton's Lymphoma Ascites (DLA) and Ehrlich Ascites Carcinoma (EAC) cell lines. Viability was determined by Trypan blue exclusion method. The viable cell suspension 1×10^6 cells in 0.1 ml was added in the tubes containing various

concentrations (100, 500 and 1000 µg/ml) of test compounds and the volume was made up to 1 ml using phosphate buffer saline (PBS). The mixtures were incubatedfor 3 hours at 37˚C and were added with 2 drops of Trypan blue dye. Dead cells take up the blue colour of the dye while the live cells do not. Reduction in the viable cell count and increased non-viable cancer cell count towards normal in tumor host suggest antitumour effect against EAC and DLA cells in mice. Cyclophosphamide is used as standard anticancer compound. The result obtained from anticancer study revealed that the methanol extract of *H.hispidissimus* showed 46.2, 72.8, 84.9% cytotoxicity in EAC compared to 42.9, 69.3, 80.6% cytotoxicity in DLA at concentrations of 100, 500 and 1000 µg/ml. Result obtained in the present study demonstrated that the methanol extract of leaf of *H. hispidissimus* exhibits *in vitro* anticancer activity against DLA and EAC cell lines. The leaf extracts showed concentration dependent cytotoxicity which was found to be effective against solid tumor induced by DLA and ascites tumor induced by EAC (Fig.7).

Long term conservation *in vitro*, is an important aspect of plant tissue culture. Elite germplasm of various rare and endangered species have been conserved *in vitro* (Martin and Pradeep, 2003). *In vitro* conservation of *H. hispidissmus* was carried out with explants such as leaf, petiole, node with axillary bud and terminal bud in MS medium supplemented with 2 mg/L BAP (Plate. 1). Results revealed that nodal explant with axillary bud possess comparatively higher survival chance (10 days in medium) and direct organogenesis (6 days after inoculation) than other explants used. Node with axillary bud and node with terminal budwere less vulnerable to fungal infection in the first week. All the explants were subsequently infected by 11th day, node with axillary bud being the last to get infected.

Conclusion

Present study revealed that *H. hispidissimus* has high amount of nutritional factors like reducing sugar, carbohydrates, protein, pigments and starch. The non-enzymatic and enzymatic antioxidants like proline, lycopene, total polyphenol, superoxide dismutase and polyphenol oxidase were also found to be higher. The plant extract was found to be effective against DLA induced solid tumour and EAC induced ascites tumour. This may be used to the development of effective therapeutic approaches towards the prevention or treatments of various types of cancer in human beings. The leaves of *H. hispidissimus* has sufficient nutrients, antioxidants and *in vitro* anticancer activity also. *In vitro* conservation of the nodal explant of *H. hispidissimus* was done with different explants (leaf, stem, node with axillary bud and node with terminal bud). Explant were inoculated in Murashigi and Skooge (MS)medium supplemented with BAP and the culture was maintained by fungal infection one week after inoculation. Node with axillary bud show more survival capacity by few days in the culture compared to their explants used. This generated information on phytochemical, nutritional, and medicinal characteristicsand therapeutic potential of *H. hispidissimus* provide scientific proof for identifying the plant bio resource and its effective utilization in the future. The behavior of plant in culture can provide basis for future conservational strategies and aid in selection of suitable explant of the plant for future studies. In brief the wild species of *H. hispidissimus* fits its claims of nutritional and medicinal properties which satisfy its use as an ethnomedicinal plant by tribal communities of Kerala.

Acknowledgement

The authors are grateful to Dr. T. S. Swapna, Associate Professor, Department of Botany, University of Kerala, Kariyavattom, Thiruvananthapuram for necessary support and the Amala Cancer Hospital and Research Centre, Amala Nagar, Thrissur, for *in vitro* anticancer activity analysis.

Fig. 1. Reducing sugar in leaves of *H. hispidissimus*

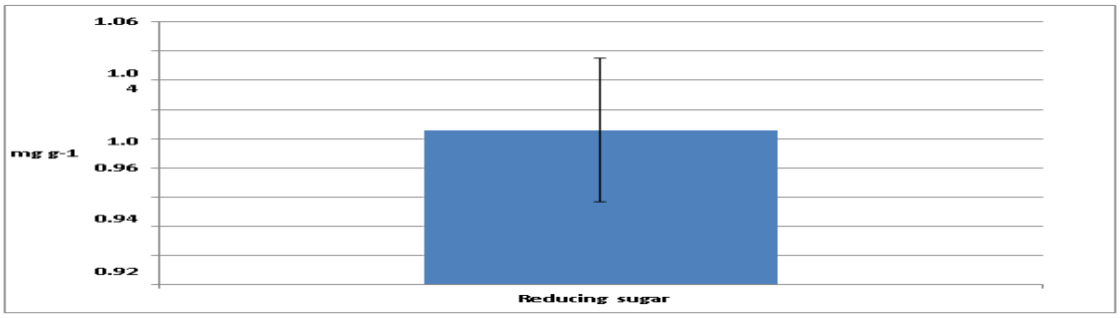

Fig. 2. Total carbohydrates and Total protein in leaves of *H. hispidissimus*

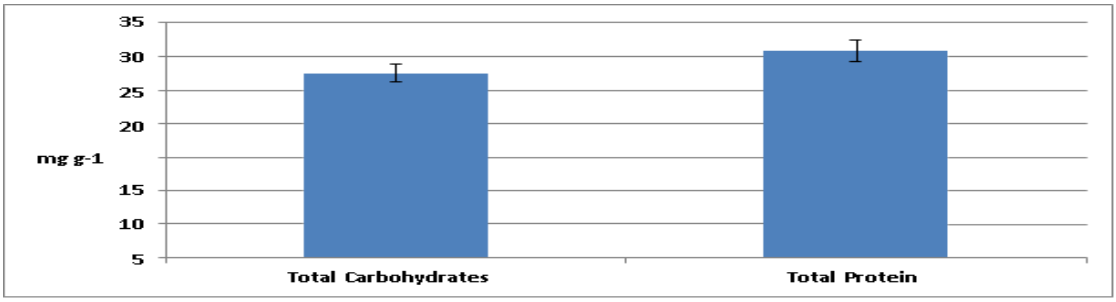

Fig. 3. Pigments in leaves of *H. hispidissimus*

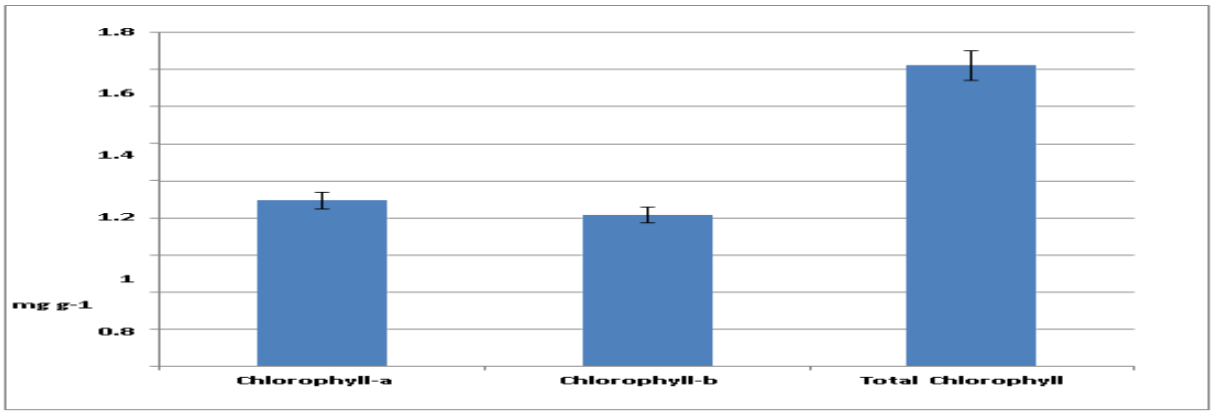

Fig. 4. Starch in leaves of *H. hispidissimus*

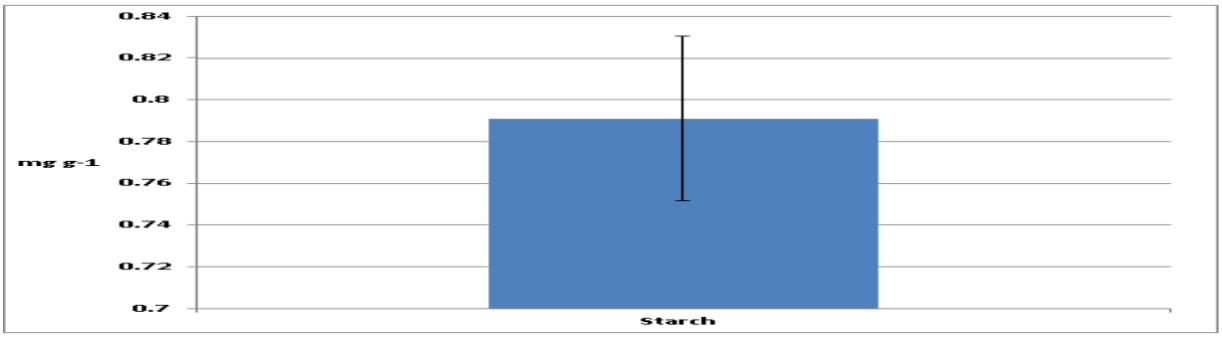

Fig. 5. Non-Enzymatic Antioxidant in Leaves of *H. hispidissimus*

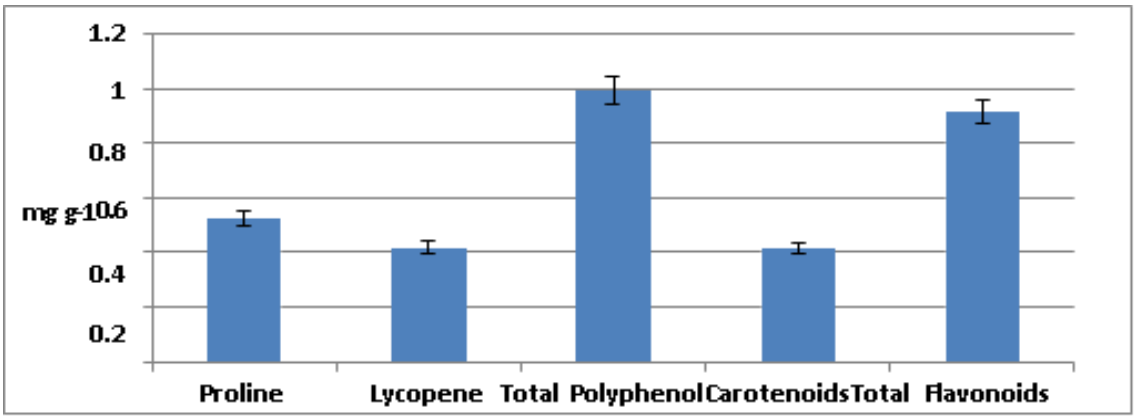

Fig. 6. Enzymatic Antioxidants in Leaves of *H. hispidissimus*

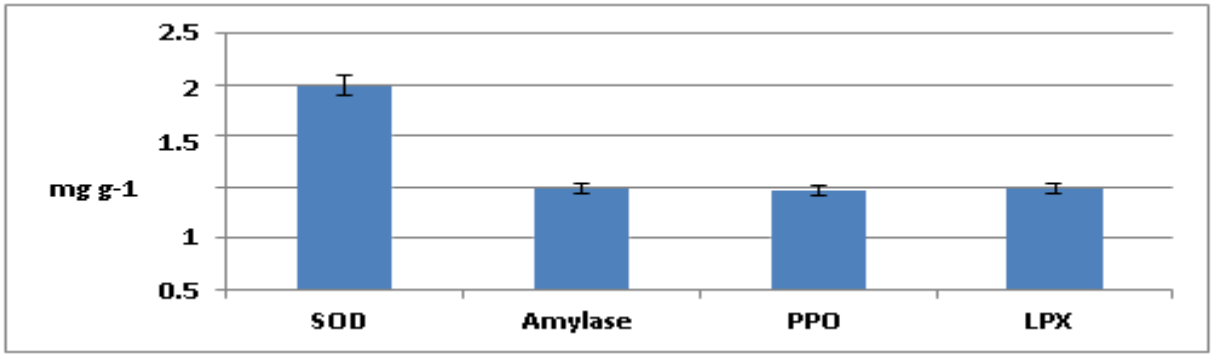

Fig. 7. *In vitro* anticancer activity in leaves of *H. hispidissimus*

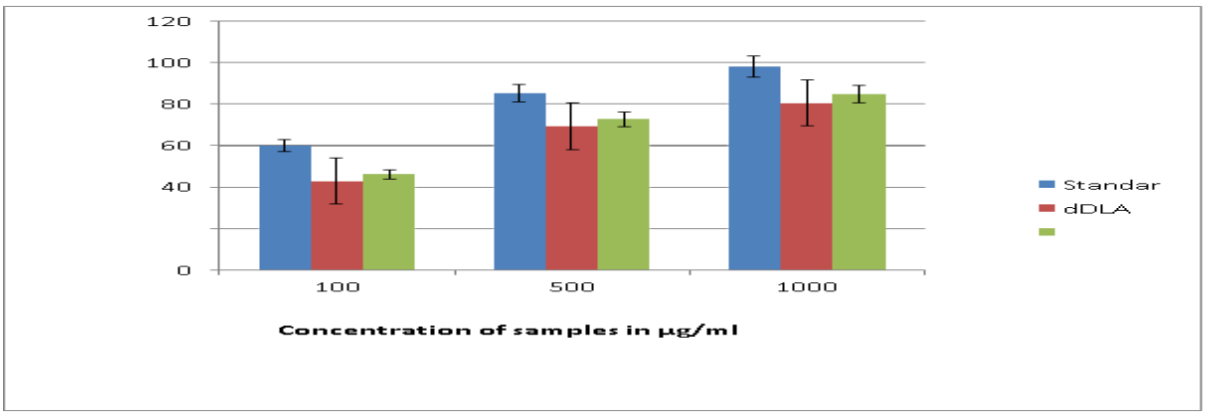

Plate 1. Node with axillary bud showing shooting (Organogenesis)

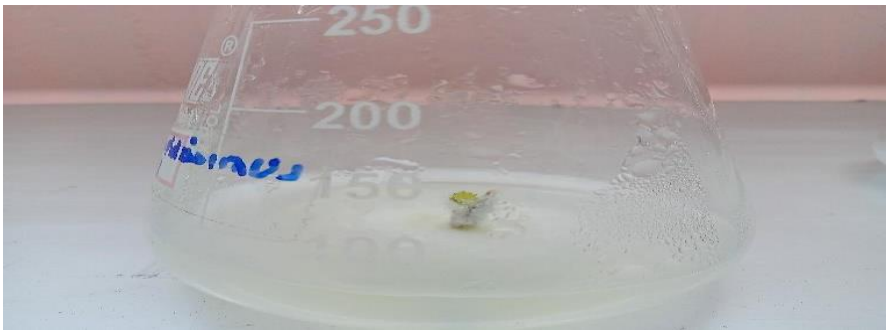

Refferences

Bates, L. S., Waldren, R. P. and Teare, I. D. 1973. Rapid determination of free prolinefor water stress studies. *Plant soil.* 39: 205-207.

Bendich, A. D. and Olson, J. A. (1989). Biological actions of carotenoids 1. The FASEB journal. 3(8): 1927-1932.

Constabel C.P. and Barbehenn R. (2008). Defective roles of polyphenol oxidase in plants. J. Intro Plant Resist Herbi. 8(12):253-270.

Deepa Khatri and Sumit B.B. (2020). Reducing sugar, total phenolic content and antioxidant potential of Nepalese plants. Int J Biomed Res. 10(55): 1-10.

David, Heber. and Lu, Q. Y. (2002). Overview of mechanisms of action of lycopene.

Experimental biology and medicine. 227(10): 920-923.

Eom, S. H., Park, H. J., Jin, C. W., Kim, D. O., Seo, D. W. and Jeong, Y. H. (2008). Changes in antioxidant activity with temperature and time in *Chrysanthemum indicum* L. teas during elution processes in hot water. *Food Science and Biotechnology.* 17: 408-412.

Estebauer, H., Dieber, R. M., Striegl, G. and Waeg, G. 1991. Role of Vitamin-E in preventing the oxidation of low density lipoprotein. *American Journal of Clinical Nutrition.* 53: 314-321.

Fijesh, Vijayan P. Study of anticancer activity of selected medicinal plants with specialreference to *Hibiscus furcatus* and *Ophiorrhiza species*. (Doctoral dissertation, Amala cancer research centre, Mahatma Gandhi University): 150-155.

Gaziano, J. M. (1999). Antioxidant vitamins and cardiovascular disease. Proceedings of the Association of American Physicians. 111(1): 2-9.

Gong, H., Zhu, X., Chen, K., Wang, S. and Zhang, C. (2005). Silicon alleviates oxidative damage of wheat plants in pots under drought. *Plant Science.* 169: 313-321.

Gunatilaka, H, D, P., Ediriweera, E, R, H, S, S., Weerasinghe, K, D, C, M. (2013). Useof Hibiscus furcatus (Napiritta) in treatment of various diseases. Natural solution for health challenges. 2: 97.

Hedge J.E., Hofreiter B.T. (1962). In: Methods in Carbohydrate Chemistry. (Eds. Whistler R L and Be Miller J N). Academic Press, New York; p. 17: 420.

Harborne J.B. (1977). Phenolic glycosides and their natural distribution in the biochemistry of phenolic compounds. Academic Press, New York, London; p. 152-16

Jemal, A., Siegel, R., Ward, E. and Brawley, O. (2011). Cancer statistics, 2011: the impact of eliminating socioeconomic and racial disparities on premature cancer deaths. *CA: a cancer journal for clinicians*. 61(4): 212-236.

Kumar, Vinay. (2020). Standardization and antidiabetic effect of some indigenous medicinal plants. (Doctoral dissertation, Dr. A.P.J. Abdul kalam Technical University):2-8.

Lowry, O. H., Rosebrough, N. J., Farr. A. L. and Randall. R. J. (1951). Protein measurement with folin phenol reagent. *Journal of Biological Chemistry.* 193: 265-275.

Maitra, S. (2015). Evaluation of pharmacological and antimicrobial activities of potential plant constituents. (Doctoral dissertation, Jadavpur University): 4-8.

Manthey, F. A. and Xu, Y. (2009). 2 Glycobiology of Foods: Food Carbohydrates— Occurrence, Production, Food Uses, and Healthful Properties. *Advances in food biochemistry*: 23.

Martin, K.P. and A.K. Pradeep, 2003. Simple strategy for the *in vitro* conservation of *Ipsea malabarica* an endemic and endangered orchid of the Western Ghats of Kerala, India. Plant Cell Tissue Organ Cult., 74: 197-200.

Michal L., Elisha S., Sarah S., Helena P., Elaine S. and Haya L.G. (2014). Evaluating medicinal plants for anticancer activity. Scienti World Journal. 31(1): 100-110

Miller, G. L. (1972). Use of Dinitrosalycylic acid reagent for determination of reducingsugars. *Analytical chemistry*. 31: 426-428.

Mishra, V. K., Bacheti, R. K. and Husen, A. (2011). Medicinal uses of chlorophyll: A critical overview. Chlorophyll: Structure, function and medicinal uses: 177-196.

Mudryj, A. N., Yu, N. and Aukema, H. M. (2014). Nutritional and health benefits of pulses. Applied Physiology, *Nutrition, and Metabolism*. 39(11): 1197-1204.

Pradeesh S. and Praveena P. (2020). Phytochemical investigation and in vitro anticancer activity of Sesbania grandiflora (L.) Pers. – A wild leafy vegetable of Southern Western Ghats. J. Advances in Biol Sci. 7(1&2): 49-53.

Pradeesh, S. and Swapna, T.S. (2018). *In vitro* studies and phytochemical evaluation of *Bidens biternata*. LAP LAMBERT, Academic Publishing: 64-105.

Rao, S. R. and Ravishankar, G. A. (2002). Plant cell cultures: chemical factories of secondary metabolites. *Biotechnology advances*, 20(2): 101-153.

Shingo, Y., Sakurada, S. and Nagumo, M. (1994). Role of intracellular SOD in protecting human leukemic and cancer cells against superoxide and radiation. *Free Radical Biology and Medicine*. 17(5): 389-395.

Thayumanavan, B. and Sadasivam, S. (1984). Physico chemical basis for the preferential uses of certain rice varieties. Q*uality Plant Foods for Human Nutrition.* 34:253.

Witham, F. H., Blaydes, D. F. and Devlin. R. M. (1971). Experiments in Plant Physiology, Van-Nostrand Reinhold Company, New York, USA. 245.

Zakaria, H., Simpson, K., Brown P. R., and Krotulovic, A. 1979. Use of reversed phaseHPLC analysis for the determination of provitamin-A, carotenes in tomatoes. *Journal of Chromatography*. 176: 109-117.